Elastic Wave Radiation from Borehole Seismic Sources in Anisotropic Media

by

Wenjie Dong

M.S., Colorado School of Mines (1989)
B.S., University of Geological Sciences, China (1985)

Submitted to the Department of Earth, Atmospheric, and Planetary Sciences
in partial fulfillment of the requirements for the degree of

Doctor of Philosophy

at the

MASSACHUSETTS INSTITUTE OF TECHNOLOGY

December 1993

Signature of Author ....
Department of Earth, Atmospheric, and Planetary Sciences
December 14, 1993

Certified by ..
M. Nafi Toksöz
Professor of Geophysics
Thesis Supervisor

Accepted by ....
Thomas H. Jordan
Chairman
Department of Earth, Atmospheric, and Planetary Sciences

Elastic Wave Radiation from Borehole Seismic Sources in Anisotropic Media

by

Wenjie Dong

Submitted to the Department of Earth, Atmospheric, and Planetary Sciences
on December 14, 1993, in partial fulfillment of the
requirements for the degree of
Doctor of Philosophy

Abstract

This thesis is concerned with wave radiation and propagation from borehole seismic sources in homogeneous and inhomogeneous anisotropic media, with focus on the investigation of borehole influence on downhole source radiation.

First, numerically feasible dynamic and static Green's functions in transversely isotropic media are obtained in dyadic form by evaluating in general a 2-D inverse Laplacian operator involved in previous dynamic Green's function expressions. This evaluation is of particular importance for the later BEM implementation because of off-centered sources. The final dyadic form is similar to that of the isotropic dyadic Green's function, therefore, it lends itself to easy analytical and numerical manipulations. The dynamic Green's function is expressed through three scalar quantities characterizing the propagation of SH, P-SV, and P-SV-SH waves. The static Green's function has the same dyadic form as the dynamic Green's function and the three corresponding scalar functions are derived. From the dynamic Green's function, displacements due to vertical, horizontal, and explosive sources are explicitly given. The singular properties of the Green's functions are addressed through their surface integrals within the limits of coinciding receiver and source. The singular contribution is shown to be $-1/2$ when the static stress Green's function is integrated over a half elliptical surface. These results are directly applicable to the later BEM implementation.

Following the discussion of Green's functions, analytical radiation patterns of three typical downhole seismic sources in transversely isotropic (TI) media are obtained through asymptotic evaluation of displacement integrals. The radiation patterns are expressed in terms of the slowness components of a particular point on the slowness surface of the medium. This particular point, known as the saddle point of the displacement integrals, is easily determined by geometric arguments based on the slowness and wave surfaces of the TI medium. Since the saddle point determines

ray direction, the radiation patterns can be readily incorporated into existing ray modeling codes to account for borehole source effects. The analytical results show that borehole source radiation patterns are independent of the source frequency if the product of frequency with borehole radius is much smaller than the sound speed of the borehole fluid. This independence is true for most crosshole experiments with source frequency up to 1 kHz. Numerical test results show that the anisotropy effect on P-wave pattern is relatively moderate. On the contrary, its effect on the S-wave pattern is prominent even for low degrees of P and S wave anisotropy. In the isotropic limit, previous analytical results for isotropic medium are recovered. For sources in cased borehole, casing and cement affect both wave amplitudes and radiation patterns.

In Chapter 4, a modeling technique based on the boundary element method is established for modeling source radiation from open or cased boreholes in layered TI media. The axis of symmetry of TI layers is assumed to be parallel with the borehole axis. Under this assumption, the problem is significantly simplified because the element discretization of the borehole remains one dimensional. For open boreholes, three equivalent sources on each element are assumed to represent the boundary effects on the inner fluid and the outer solid. Three boundary conditions set up a system of equations for the equivalent sources on all elements. Once the sources are known, displacements in the solid and pressure in the fluid are obtained. For cased boreholes, the method treats borehole fluid, and casing and cement as a cylindrically layered isotropic medium. In this case, the boundary conditions to be satisfied at the borehole wall are four (continuity of the normal and tangential displacements and stresses). Thus, more computation is required to solve the system of equations. The implementation of the method is illustrated through several examples.

Using the technique developed in Chapter 4, a Cross-well hydrophone data set is analyzed in Chapter 5. Two other modelings, one with no boreholes and one with a receiver borehole only, are used for comparison. The results show that synthetic and real data agree with each other very well only when the source borehole is included in the modeling. The importance of the source borehole stems from the fact that the local geology contains high-contrast sedimentary rocks. Since most of the source energy travels along the source borehole as a tube wave, at high-contrast interfaces tube-to-shear wave conversion is no longer a negligible secondary effect. In fact, as the data and the modeling results suggest, shear waves due to tube wave conversion are even stronger than the primary shear waves. The data and the modeling results also illustrate that, when sandwiched between high velocity layers, a low velocity channel traps tube wave-converted energy and guides it to the receiver borehole to excite tube waves.

Finally, two special borehole sources are modeled analytically and numerically. For the Downhole Orbital Vibrator, actual rotation of a radial force is incorporated into a mathematical expression for the source. By using this source and the Green's functions, the three displacement components in isotropic and TI media are provided. Their numerical evaluation shows that the source may be useful in detecting shear

wave anisotropy. For a drill-bit source, the BEM technique of Chapter 4 is extended to model its radiation pattern. Results suggest that borehole has little effect on drill-bit radiation.

Thesis Supervisor: M. Nafi Toksöz
Title: Professor of Geophysics

To my parents, Shuangyi and Xiuge,

for their love and sacrifice,

which made this accomplishment possible.

Acknowledgments

I would like to thank my advisor, Nafi Toksöz, for providing a stimulating research environment at the Earth Resources Lab. His encouragement, advice, and guidance led to this immensely rewarding thesis research, despite its clear difference from my background on seismic migration and inversion. Every conversation with Nafi during the past few years was an enjoyable and encouraging one. His enthusiasm for new research topics is surpassed only by his breathe of knowledge and depth of insight. Another person from whom I benefited the most is Michel Bouchon. Discussions with him on the nitty-gritty of the boundary element method were particularly beneficial. His extensive knowledge on wave theory was a ready source of consultation.

Many people contributed to my education at MIT, directly or indirectly. I thank Denis Schmitt and Bata Mandal for technical discussions on some of the topics in the thesis. Arthur Cheng and Roger Turpening have always been sources of help, consultation, fruitful discussions. Interactions with Toru Takahashi on the Buckhorn crosshole data set are particularly appreciated. Tom Jordan, being a widely recognized researcher, is also a great teacher. The two courses taken with him were very enjoyable and had broadened my perception of geophysics. Ted Madden's scientific attitude and breathe of knowledge set an excellent example for newcomers to science research. From my experience with him, it is indeed a tough act to follow. Sara Brydges, Naida Buckingham, Liz Henderson, Sue Turbak, Al Taylor, and Jane Maloof have been very helpful in practical matters and paper works at ERL.

Fellow students and ERL research staff made my stay pleasant. The two ERL computer junkies, Ted Charrette and Joe Matarese, have always been ready to help. Carol Caravana, Bob Cicerone, Karl Ellefsen, Jack Foley, Rick Gibson, Sergio Kostek, Jung Mo Lee, Randy Mackie, Jeff Meredith, Burch Oral, Ed Reiter, Bill Rodi, Arcangelo Sena, Craig Schultz, Xiaoming Tang, and Delaine Thompson were friendly. Fellow Chinese students and scholars, Ningya Cheng, Chengbin Peng, Xiaomin Zhao, Zhenya Zhu, Yingping Li, Jie Zhang, Tiepeng Zhou, and Weiqun Shi, provided re-

liable friendship and many laughing materials during lunch hours. Bob Greaves, Matthijs Haartsen, Matthias Imhof, and Refael Katzman have shared with me many interesting discussions about science, life, and society.

Outside MIT, I like to acknowledge the discussions and interactions on other research topics with Terry Young, Bob Keys, Mark Willis, Keh Pann, and Stan Laster of Mobil, with Herb Swan, T.K. Kan, Ken Tubman, and Lee Kuo of ARCO, with Norman Bleistein, Ken Larner, Art Wegleign, Wafik Beydoun, John Minear, John Queen, and Jon Gaston. I thank Sven Treitel for being on my thesis committee.

I also thank Priscilla and Ned Tebbetts for their friendship and for the stories about MIT in the 40's. Hopefully, I've picked up a little of Ned's tremendous pride on being a MIT alumnus.

Most of all, I'm deeply grateful to my wife, Qing Tang, for her unconditional love and sacrifice throughout this endeavor. I'm also indebted to my parents, my brother and sister, for their consistent love over the years.

This research was supported by a grant from the U.S. Department of Energy, contract #DE-FG02-89ER14084. The author also held a SEG Foundation Scholarship award for two years. The crosshole data used in the thesis were provided by OYO corporation and Western Kentuky Petroleum Company.

Contents

Chapter 1

Introduction

The dynamics of elastic wave is a fine subject for investigation and I am sorry to pass from it now for a time. —Lord Kelvin.

1.1 Objectives

Over the last decade, the geophysical community developed a new seismic imaging technique: *Crosshole Tomography.* This technique closely resembles the more familiar X-ray medical imaging method. In seismic crosshole tomography, however, sources are excited in one borehole and seismic waves are recorded in an adjacent borehole. These recorded signals are analyzed to obtain the structure or inhomogeneity of the medium between the two boreholes. When wave traveltimes are the only data used in the analysis, the method is often referred to as *Traveltime Tomography.* Because of its robustness and simplicity in data requirement, it is by far the most widely used tomography technique. In the meantime, demands for using seismic amplitude information to estimate medium attenuation and to improve tomographic images, have prompted geophysicists to look into techniques such as *Attenuation Tomography* and *Diffraction Tomography.*

One of the major difficulties concerning these techniques is the lack of understand-

ing of the seismic signatures radiated from various seismic sources placed downhole. It is of great importance to have this understanding due to the following reasons:

- Removal of the source signature is necessary in both attenuation tomography and diffraction tomography.
- The source signature also affects time-picking for various wave arrivals in traveltime tomography.
- Borehole source radiation is a complicated wave phenomena. Some other waves beside body P and S waves may exist in the data. They have to be identified before any processing.

Works dealing with this problem have all concentrated on infinite boreholes in infinite homogeneous isotropic media. As more and more sophistication is introduced into the tomography techniques, such as anisotropy and variable background, complicated source signatures result. The purpose of this thesis research, therefore, is to investigate the source borehole effect on downhole source radiation in homogeneous and heterogeneous *anisotropic* media. The problem is studied through analytical approximation and numerical modeling of wave radiation from various downhole sources in different downhole conditions.

1.2 Background

An explosion source in a homogeneous isotropic elastic medium excites only P waves. Though ideally a true statement, actual man-made seismic sources in surface and borehole seismic experiments can hardly be treated as ideal point sources. In a surface seismic survey using dynamite sources, shot holes are typically drilled to couple the source to the ground. In a borehole seismic survey, specially designed downhole sources are operated inside boreholes that are hundreds of meters deep and are commonly fluid-filled. Typical borehole sources include *volume* sources (such as

dynamite and air-gun), *radial* sources (such as bender and cavity resonator), and *vertical* sources (such as wall-clamped vertical vibrators). Special sources include the downhole orbital vibrator and the drill-bit. Regardless of the type of sources and experiments, wave radiation from these sources is affected by the presence of the borehole.

In simulating radiation from a dynamite explosion in shot holes for a surface seismic survey, Heelan (1953) presented a theoretical study of wave radiation from a cylindrical source of finite length, with all its surfaces subjected to symmetric lateral and tangential stresses. This work was the first to achieve an analytical solution for a downhole source of finite size in an empty borehole. One major conclusion of this study was that radial stresses applied to the wall of the borehole produce shear waves beamed at a 45° direction from the borehole axis. Combining Heelan's solution with an elementary tube wave propagating along a source hole, White and Sengbush (1963) added the effect of fluid to their considerations.

Lee and Balch (1982) obtained a close-form solution for the volume point source radiation problem in an infinitely long fluid-filled borehole embedded in a homogeneous isotropic medium. This study identified the existence of a tube wave pole and investigated the influence of borehole fluid on the body wave radiation patterns. They found that the effect of fluid on the shear wave radiation pattern is much more dramatic than the effect on the compressional wave pattern. When tube wave velocity is close to (but smaller than) shear wave velocity, the effect is substantial. When shear wave velocity is much higher than tube wave velocity, the effect can be basically neglected. Their study did not treat the radiation pattern of the shear waves when shear wave velocity of the formation is less than about 1.4 km/s.

The theoretical radiation characteristics of downhole sources in high velocity or hard formation rocks have been verified by the experiments of Riggs (1955) and Fehler and Pearson (1981, 1984). However, experiments performed in low velocity or soft sediments such as that of White and Sengbush (1963) and de Bruin and Huizer (1989)

showed poor agreement with Heelan's prediction. By exciting a source in a fluid-filled cased hole, de Bruin and Huizer (1989) observed secondary arrivals moving out at velocities higher than the formation shear velocity. They attributed this phenomenon to the influence of tube waves and the generation of conical wavefronts.

The reason that no shear wave radiation pattern could be determined for soft sediments and the hypothesis of de Bruin and Huizer were explained by Meredith (1990) and Meredith *et al.* (1993) in detail. It was concluded that shear wave radiation into low velocity sediments is affected by the radiation from tube waves in a source borehole due to the generation of Mach waves or borehole conical waves. The physics and propagation of Mach waves were illustrated by explicit evaluation of the residue of a tube wave pole. Using a Thomson-Haskell algorithm, Meredith (1990) also calculated the near-field patterns of several sources in a radially layered medium. The far field patterns were evaluated by the method of stationary phase and proved identical to those of Heelan (1953) and Lee and Balch (1982). Field data compared well with analytic predictions. Winbow (1991) and Gibson (1993) studied the radiation of borehole sources in a cased and cemented borehole in a homogeneous isotropic medium. Winbow (1991) concluded that 99% of an explosion source energy is trapped by the borehole as tube waves.

The aforementioned works concentrated on the radiation of sources in infinite boreholes. Over the past several years, noticeable effort was made to utilize drill-bit vibration as a seismic source. The literature on this subject is, at most, scarce. Wave propagation along drill-strings and presure waves inside drilling fluid were studied by Lee (1991) using analytical models and field test data. He suggested that instead of the traditionally used unit harmonic displacement, or unit force at the bit, a unit harmonic relative displacement source placed between rock and drill-bit be used to simulate the motion of a tri-cone bit. The preliminary characterization and usage of recorded seismic signals while drilling were discussed by Rector (1990).

Roughly during the same time period, substantial efforts over acoustic logging

problems led to tremendous progress in the understanding of waves inside a fluid-filled borehole. Wavefields inside a borehole that are due to a point source on the axis of a fluid-filled borehole in an isotropic medium were considered by Ingram (1963) and Cheng and Toksöz (1981). Using contour and numerical integration, Ingram (1963) identified those parts of the solutions which represented refracted arrivals, multiply reflected conical waves, a surface wave along the cylindrical boundary, and a wave that decays in the axial direction. Cheng and Toksöz (1981) arrived at the solution by studying the propagation and dispersion characteristics of guided waves using dispersion curves. They also obtained full waveform acoustic logs by discrete wavenumber integration. Other studies include the works of Greenfield (1978), Tsang and Rader (1979), White (1960, 1965, 1983), Schmitt and Bouchon (1985), and Bouchon and Schmitt (1989).

The previous works dealt with radiation and propagation problems in a homogeneous isotropic medium. The isotropy assumption for earth materials is only a first order approximation. Elastic anisotropy in sedimentary rocks has long been observed and studied by many researchers. The causes for this anisotropy have generally been classified into three categories: fine layering, oriented minerals, and oriented cracks due to regional stress. The anisotropic effect of periodic, or fine lamination of isotropic layers, has been thoroughly studied (e.g., Postma, 1955; Backus, 1962; Berryman, 1979; Levin, 1979). Fine layering results in an overall transversely isotropic (TI) medium. Oriented vertical cracks in the rock produce azimuthal anisotropy or vertical transverse-isotropy (VTI) (e.g., Crampin, 1984). Regional stress acting on isotropic rocks causes anisotropy because of closing of cracks (Nur and Simmons, 1969; Lo *et al.*, 1986; Gibson and Toksöz, 1990). The analysis and application of anisotropy in exploration seismology have been described by Crampin (1985), Thomsen (1986), Winterstein (1986), Larner (1993), Larner and Cohen (1993), Robertson and Corrigan (1983), White and Tongtaow (1981), Schmitt (1989), and Ellefsen (1990), among others. Theoretical studies of wave propagation and radiation from seismic sources

can be found in Musgrave (1954), Buchwald (1959), Fedorov (1968), Takeuchi and Saito (1972), Ben-Menahem and Sena (1990), Mandal and Toksöz (1990), and Mandal (1991).

Papers on numerical modeling of crosshole data in a layered medium include Kurkjian *et al.* (1992), Track *et al.* (1992), and Bouchon (1993). In Kurkjian *et al.*, a moving source and moving receiver mechanism is used to approximate the effect of source and receiver boreholes. The difficulty with the finite difference method (Track *et al.*, 1992) is mainly associated with the large scale difference between borehole diameter and formation extent. The ability to calculate the far field is limited. Bouchon (1993) proposed a boundary element technique to model wave propagation from borehole sources in layered isotropic media. This method overcomes the scale problem in finite difference methods. It is semi-analytic and is ideally suited to model borehole source radiation problems. In Chapter 4, the method is described and extended to include anisotropy and cased boreholes.

1.3 Scope of the Thesis

The subject of this thesis is pursued in five chapters. Chapter 2 contains the study of Green's functions in transversely isotropic media and their singular properties. An unified treatment for the dynamic and static cases is presented through solving the wave and equilibrium equations by an extended Kupradze method (Kupradze, 1979). This solution technique is a general one and can be regarded as an alternative to that used in Ben-Menahem and Sena (1990). Of particular importance in the boundary element method is the availability of a workable Green's function. Using the governing equations for SH and for *quasi* P-SV waves, the involvement of a 2-D inverse Laplacian is removed without limiting it to special cases. This led to a numerically feasible form of the dynamic Green's function, that is valid for general sources at arbitrary locations. The singular properties of the static function, which are the same

as those of the dynamic function, are studied through their surface integration. The results of this chapter are directly applicable in the BEM implementation in Chapter 4.

In Chapter 3, the radiation problem is considered for a fluid-filled borehole penetrating a homogeneous TI medium along its symmetry axis. Displacement potentials in both the fluid and the TI formation are used to derive displacement integrals. The displacement potentials in a TI medium are easily obtainable from the Green's function developed in Chapter 2. Far-field radiation patterns of three borehole sources are derived through asymptotic approximation of the displacement integrals. The anisotropy effect on the radiation patterns is investigated using a test medium. The results suggest that the S wave pattern is subject to dramatic change from its isotropic limit, even for low degrees of anisotropy. Then, Mach wave phenomena and radiation from cased borehole are discussed. The availability of the radiation patterns in terms of ray parameters enable direct incorporation into existing ray-tracing codes to account for the source borehole effect.

In Chapter 4, the boundary element method is used to model wave radiation from an open or cased borehole in a layered TI medium, whose symmetry axis is along the borehole axis. The BEM technique and implementation procedures are presented first. Then, as part of the element surface integration requirement, the displacements and stresses for ring sources are presented. The isotropy and TI results are given together for the purpose of comparison. Wave propagation in horizontally layered TI media and in cylindrically layered isotropic media is discussed with particular attention as to how they could be included in the BEM algorithm. Bench-Mark examples are provided to illustrate the implementation. The comparison of BEM results with those from the discrete wavenumber method validates the implementation procedures.

In Chapter 5, the BEM modeling technique of Chapter 4 is used to analyze a real crosshole data set from Buckhorn, Illinois. The site geology and experiment setup are described first. Then, we review a previous tomography analysis of the data set

using traveltime methods. Because the data are recorded by hydrophone in a receiver borehole, some theoretical aspects of the receiver borehole effect are also reviewed. To identify wave types in the data, three types of modeling are employed: without boreholes, with a receiver borehole only, and with a source borehole only. The two models without the source borehole can explain only those waves that, in one way or another, are related to the direct P and S waves. Once the source borehole is included in the model, all events in the data are explained.

In Chapter 6, two special downhole sources, a downhole orbital vibrator and a drill-bit, are modeled. A mathematical model for the orbital vibrator is provided, and the displacements in isotropic and TI media are calculated. The results show the 3-D nature of the source. More interestingly, the results seem to suggest that the source might be useful in detecting shear wave anisotropy using a single displacement component, namely, the horizontal displacement. A drill-bit source is modeled by vertical forces exerted on the bottom of a borehole. A modified BEM technique, that includes the borehole bottom, is used in the modeling.

Finally, the main results of this research are summarized in Chapter 7.

Chapter 2

Dynamic and Static Green's Functions in Transversely Isotropic Elastic Media

2.1 Introduction

Wave propagation from various seismic sources placed inside a fluid-filled borehole embedded in a layered transversely isotropic medium is of great interest and importance to geophysicists dealing with crosshole, vertical seismic profiling, and acoustic logging data. In simulating wave propagation in this geometry, ordinary numerical techniques, such as the finite difference method and the finite element method, encounter computational difficulties because of the significant scale difference between the borehole diameter and the formation extent. A technique (Bouchon, 1993; Dong *et al.*, 1992) perfectly suited to this kind of geometry is the boundary element method (BEM). It is a semi-analytical method because the only discretization occurs at the borehole boundary and the propagation of waves is realized through the use of the dynamic Green's function. This technique also requires the static Green's function to regularize the boundary surface integral when the source and the receiver coincide.

These essential requirements of the Green's functions in the BEM technique motivate this work.

Although plane wave propagation in TI media has been studied by many workers (e.g. Musgrave, 1954; Fedorov, 1968; Crampin, 1985; among others), the literature on the static and dynamic Green's functions of the TI medium are scarce at best. Among the existing papers, most provide the solution in component and numerical forms. Pan and Chou (1976) presented an explicit solution of the equilibrium equation in terms of displacement and stress components for vertical and horizontal forces. In their solution procedure, three displacement potentials and an assumed solution form with unknown coefficients were used. Buchwald (1959) solved the wave equation for three strains: $\left(\frac{\partial u_y}{\partial x} - \frac{\partial u_x}{\partial y}\right)$, $\frac{\partial u_z}{\partial z}$ and $\left(\frac{\partial u_x}{\partial x} + \frac{\partial u_y}{\partial y}\right)$. The far-field approximation of these strains were given using a stationary phase approximation. Other workers (White, 1982; Mandal and Toksöz, 1990) employed numerical methods to study the radiated waveforms of a line source, a vertical and a horizontal point force, and an explosion source. Kazi-Aoual *et al.* (1988) devised an algorithm using the Kupradze method (Kupradze, 1979) for calculating the dynamic Green's function. In Kazi-Aoual *et al.* (1988), the dynamic Green's function is expressed as the cofactor matrix of a symmetric matrix of differential operators operating on a single scalar. The scalar is represented by the Hankel transform. Ben-Menahem and Sena (1990) and Sena (1992) extended the work of Buchwald and obtained the dynamic Green's tensor in the form of the Hankel transform by recovering the displacement vector from the three strains. This extension is significant because a fairly simple dynamic Green's tensor is given in terms of dyadic notation. However, due to the presence of a 2-D inverse Laplacian operator in the expression, this Green's function does not lend itself easily to the kinds of numerical and analytical manipulations required by the BEM method.

This chapter presents an unified treatment of the dynamic and static Green's functions. We first describe an alternative derivation of the dynamic Green's function,

which solves the wave equation for general source distribution by using a modified Kupradze method. This serves as an introduction and a review for later developments. The static Green's function is then defined by deriving its related quantities. The term in the Green's functions that involves the inverse Laplacian is evaluated without limiting it to special cases. The final form of the Green's functions is valid for arbitrary sources at arbitrary locations, which is critical for the BEM technique. The dynamic Green's function is then applied to obtain the displacements for three basic sources. Finally, the static Green's function is used to compute the singular contribution when integrating the dynamic stress function over a boundary surface in the limit of the source coinciding with the receiver.

2.2 The Dynamic Green's Function

In a Cartesian coordinate system (x, y, z) with unit vector $(\hat{x}, \hat{y}, \hat{z})$, let $\mathbf{u} = (u_x, u_y, u_z)$ and $\mathbf{F} = (F_x, F_y, F_z)$, respectively, be the displacement vector and external body force of a transversely isotropic medium characterized by the five independent elastic stiffness constants, c_{11}, c_{13}, c_{33}, c_{44}, and c_{66}. The frequency domain wave equation in terms of the displacement components for a transversally isotropic medium can be written in the following form

$$\begin{aligned}
c_{11}\frac{\partial^2 u_x}{\partial x^2} + c_{66}\frac{\partial^2 u_x}{\partial y^2} + c_{44}\frac{\partial^2 u_x}{\partial z^2} + (c_{11}-c_{66})\frac{\partial^2 u_y}{\partial x \partial y} + (c_{13}+c_{44})\frac{\partial^2 u_z}{\partial x \partial z} + \rho\omega^2 u_x &= -F_x, \\
c_{11}\frac{\partial^2 u_y}{\partial y^2} + c_{66}\frac{\partial^2 u_y}{\partial x^2} + c_{44}\frac{\partial^2 u_y}{\partial z^2} + (c_{11}-c_{66})\frac{\partial^2 u_x}{\partial x \partial y} + (c_{13}+c_{44})\frac{\partial^2 u_z}{\partial y \partial z} + \rho\omega^2 u_y &= -F_y, \qquad (2.1) \\
c_{33}\frac{\partial^2 u_z}{\partial z^2} + c_{44}\left(\frac{\partial^2 u_z}{\partial x^2} + \frac{\partial^2 u_z}{\partial y^2}\right) + (c_{13}+c_{44})\frac{\partial}{\partial z}\left(\frac{\partial u_x}{\partial x} + \frac{\partial u_y}{\partial y}\right) + \rho\omega^2 u_z &= -F_z.
\end{aligned}$$

In the above equation, the relation $c_{12} = c_{11} - 2c_{66}$ is used. These equations can be easily compared with those in White (1983), where Love's notation for the elastic constants is used. Grouping the first two equations together in terms of transverse displacement, $\mathbf{u}_t = u_x\hat{x} + u_y\hat{y}$, and rewriting the third equation, we obtain

$$c_{66}\nabla_t^2\mathbf{u}_t + c_{44}\frac{\partial^2 \mathbf{u}_t}{\partial z^2} + (c_{11}-c_{66})\nabla_t\nabla_t\cdot\mathbf{u}_t + (c_{13}+c_{44})\frac{\partial}{\partial z}\nabla_t u_z + \rho\omega^2\mathbf{u}_t = -\mathbf{F}_t, \qquad (2.2)$$

$$c_{44}\nabla_t^2 u_z + c_{33}\frac{\partial^2 u_z}{\partial z^2} + (c_{13}+c_{44})\frac{\partial}{\partial z}\nabla_t \cdot \mathbf{u}_t + \rho\omega^2 u_z = -F_z \quad (2.3)$$

where, $\mathbf{F}_t = F_x\hat{x} + F_y\hat{y}$. A similar to solving the elastic wave equation for the isotropic case, where the curl and divergence are taken on both sides of the equation, Equations (2.2) and (2.3) can be solved by taking the transverse curl and the transverse divergence on both sides.

Following Buchwald (1959), and taking the transverse curl, defined as $\nabla_t \times = [\nabla - \frac{\partial}{\partial z}\hat{z}]\times$, of Equation 2.2, one obtains

$$c_{66}\nabla_t^2 \nabla_t \times \mathbf{u}_t + c_{44}\frac{\partial^2}{\partial z^2}\nabla_t \times \mathbf{u}_t + \rho\omega^2 \nabla_t \times \mathbf{u}_t = -\nabla_t \times \mathbf{F}_t. \quad (2.4)$$

The gradient terms disappeared because $\nabla_t \times \nabla_t u = 0$. By virtue of Green's superposition theorem, the solution of this equation in terms of the transverse curl of $\mathbf{u}_t$ is

$$\nabla_t \times \mathbf{u}_t = \int_V g(\mathbf{x},\mathbf{x}')\,\nabla_t' \times \mathbf{F}_t'\,d\mathbf{x}', \quad (2.5)$$

where $\mathbf{x} \doteq (x,y,z)$ is the receiver location, and $\mathbf{x}' \doteq (x',y'z')$ is the source location. $g(\mathbf{x},\mathbf{x}')$ is the Green's function of the scalar wave equation

$$c_{66}\nabla_t^2 g + c_{44}\frac{\partial^2 g}{\partial z^2} + \rho\omega^2 g = -\delta(\mathbf{x}-\mathbf{x}'). \quad (2.6)$$

This function is readily obtained following transformation $s = \sqrt{c_{66}/c_{44}}\,z$ and $\delta(az) = \delta(z)/a$. If $e^{-i\omega t}$ dependence is assumed for the wavefield, this Green's function is

$$g(\mathbf{x},\mathbf{x}') = \frac{e^{ik_0 R}}{4\pi\sqrt{c_{44}c_{66}}R}, \quad (2.7)$$

where, $R = \sqrt{(x-x')^2 + (y-y')^2 + c_{66}/c_{44}(z-z')^2}$ is the modified distance from the source to the receiver and $k_0 = \omega/\sqrt{c_{66}/\rho}$ is the wave number. In the isotropic limit, $c_{66} = c_{44} = \mu$, and g reduces to the scalar shear wave Green's function.

Taking the transverse divergence of Equation 2.2 and the z derivative of Equation 2.3, one obtains two coupled equations (Buchwald 1959),

$$\left(c_{11}\nabla_t^2 + c_{44}\frac{\partial^2}{\partial z^2}\right)\nabla_t \cdot \mathbf{u}_t + (c_{13}+c_{44})\nabla_t^2\frac{\partial u_z}{\partial z} + \rho\omega^2\nabla_t \cdot \mathbf{u}_t = -\nabla_t \cdot \mathbf{F}_t, \quad (2.8)$$

$$\left(c_{44}\nabla_t^2 + c_{33}\frac{\partial^2}{\partial z^2}\right)\frac{\partial u_z}{\partial z} + (c_{13}+c_{44})\frac{\partial^2}{\partial z^2}\nabla_t \cdot \mathbf{u}_t + \rho\omega^2\frac{\partial u_z}{\partial z} = -\frac{\partial F_z}{\partial z}. \quad (2.9)$$

These equations can be solved using an extended version of the Kupradze method (Kupradze, 1979; Kazi-Azoual *et al.*, 1988) outlined for an isotropic medium. First, we rewrite the coupled equation in a matrix form

$$\begin{bmatrix} L_z & (c_{13}+c_{44})\nabla_t^2 \\ (c_{13}+c_{44})\frac{\partial^2}{\partial z^2} & L_t \end{bmatrix} \begin{bmatrix} \nabla \cdot \mathbf{u}_t \\ \frac{\partial u_z}{\partial z} \end{bmatrix} = \begin{bmatrix} -\nabla_t \cdot \mathbf{F}_t \\ -\frac{\partial}{\partial z} F_z \end{bmatrix}, \tag{2.10}$$

where

$$L_t = c_{44}\nabla_t^2 + c_{33}\frac{\partial^2}{\partial z^2} + \rho\omega^2, \tag{2.11}$$

$$L_z = c_{11}\nabla_t^2 + c_{44}\frac{\partial^2}{\partial z^2} + \rho\omega^2. \tag{2.12}$$

In the Kupradze method, the unknowns of the system are expressed in terms of the cofactor matrix of the original symmetric matrix operating on a single scalar. The system is greatly simplified because the product of a symmetric matrix and its cofactor matrix results in an identity matrix scaled by the determinant of the original matrix. This method no longer applies in our case due to the loss of symmetry of the matrix in Equation 2.10. Kazi-Aoual *et al.* (1988) can still apply the Kupradze method because they solve Equation 2.1, which is symmetric when written in matrix form. Instead of the cofactor matrix, the adjoint of the original matrix must be used for the nonsymmetric system. The adjoint of a matrix is defined as the transpose of its cofactor matrix. The product of a matrix with its adjoint is the identity matrix scaled by its determinant. Following this method, we assume

$$\begin{bmatrix} \nabla_t \cdot \mathbf{u}_t \\ \frac{\partial u_z}{\partial z} \end{bmatrix} = \int_V \begin{bmatrix} L_t & -(c_{13}+c_{44})\nabla_t^2 \\ -(c_{13}+c_{44})\frac{\partial^2}{\partial z^2} & L_z \end{bmatrix} \phi(\mathbf{x},\mathbf{x}') \begin{bmatrix} \nabla_t' \cdot \mathbf{F}_t' \\ \frac{\partial}{\partial z'} F_z' \end{bmatrix} d\mathbf{x}'. \tag{2.13}$$

Substituting Equation 2.13 into Equation 2.10, we obtain

$$\left[L_t L_z - (c_{13}+c_{44})^2 \frac{\partial^2}{\partial z^2}\nabla_t^2\right] \phi(\mathbf{x},\mathbf{x}') = -\delta(\mathbf{x}-\mathbf{x}'). \tag{2.14}$$

Similar equation is given in Ben-Menahem and Sena (1990) and Sena (1992). The scalar equation (2.14) is solved by Ben-Menahem and Sena (1990) using the pow-

erful Fourier transform method. Using the same method, Kazi-Azoual *et al.* (1988) evaluates a six order equation instead. In the following the derivation of ϕ is reviewed.

Defining the 3-D spatial Fourier transform as follows,

$$\mathbf{FT}\{f(\mathbf{x})\} = \int_{-\infty}^{\infty} dz \int_{-\infty}^{\infty} dy \int_{-\infty}^{\infty} dx f(\mathbf{x}) e^{-i[k_x(x-x')+k_y(y-y')+k_z(z-z')]}, \tag{2.15}$$

and applying it to Equation 2.14, one has

$$\phi(k_x, k_y, k_z, \omega) = \frac{-1}{(c_{11}k^2 + c_{44}k_z^2 - \rho\omega^2)(c_{44}k^2 + c_{33}k_z^2 - \rho\omega^2) - (c_{13} + c_{44})^2 k^2 k_z^2}, \tag{2.16}$$

where, $k^2 = k_x^2 + k_y^2$ is the transverse or horizontal wavenumber. To return to the spatial coordinates, one takes the inverse transform first, then changes the rectangular space $(x - x', y - y', z - z')$ and wavenumber (k_x, k_y, k_z) domain into cylindrical coordinates (D, θ_D, z) and (k, θ_k, k_z). Integration over θ_k produces a zeroth order Bessel function of the first kind, i.e, $2\pi J_0(kD) = \int_0^{2\pi} d\theta_k e^{ikD\cos(\theta_k - \theta_D)}$. The final result is

$$\phi(\mathbf{x}, \mathbf{x}', \omega) = \frac{-1}{(2\pi)^2 c_{33} c_{44}} \int_0^{\infty} k J_0(kD) dk \int_{-\infty}^{\infty} dk_z \frac{e^{ik_z(z-z')}}{(k_z^2 - \nu_a^2)(k_z^2 - \nu_b^2)}. \tag{2.17}$$

In this equation, $D = \sqrt{(x - x')^2 + (y - y')^2}$, and ν_a^2 and ν_b^2 represent the two roots of the denominator in (2.16), corresponding to *quasi-P* and *quasi-SV* waves, respectively. After regrouping terms, the equation for the denominator is

$$\begin{aligned} c_{33}c_{44}k_z^4 &+ [(c_{11}c_{33} - c_{13}^2 - 2c_{13}c_{44})k^2 - (c_{33} + c_{44})\rho\omega^2]k_z^2 \\ &+ (c_{44}k^2 - \rho\omega^2)(c_{11}k^2 - \rho\omega^2) = 0, \end{aligned} \tag{2.18}$$

whose roots are

$$\nu_b^2 = \frac{(c_{33} + c_{44})\rho\omega^2 - (c_{11}c_{33} - c_{13}^2 - 2c_{13}c_{44})k^2 + \sqrt{Ak^4 + Bk^2 + C}}{2c_{33}c_{44}}, \tag{2.19}$$

$$\nu_a^2 = \frac{(c_{33} + c_{44})\rho\omega^2 - (c_{11}c_{33} - c_{13}^2 - 2c_{13}c_{44})k^2 - \sqrt{Ak^4 + Bk^2 + C}}{2c_{33}c_{44}}, \tag{2.20}$$

where,

$$A = (c_{11}c_{33} - c_{13}^2)[c_{11}c_{33} - (c_{13} + 2c_{44})^2],$$

$$
\begin{aligned}
B &= -2\rho\omega^2(c_{33}-c_{44})[c_{11}c_{33}-(c_{13}+2c_{44})^2], \\
&\quad +4\rho\omega^2 c_{44}(c_{13}+c_{44})(c_{13}+2c_{44}-c_{33}) \qquad (2.21)\\
C &= (c_{33}-c_{44})^2\rho^2\omega^4.
\end{aligned}
$$

To calculate the k_z integral properly, one should notice that the integrand has four poles at $k_z = \pm\nu_a$ and $k_z = \pm\nu_b$. Moreover, for a real ω, these four poles lie on the real k_z axis, rendering the integral undefined. However, if a complex ω is assumed, these poles are off the real axis, and the integral is well-defined. If we assume $Im[\nu_a] > 0$ and $Im[\nu_b] > 0$, then for $z - z' > 0$, we have to close the contour in the upper half of the k_z plane. By Cauchy's theorem, the real axis integration is equivalent to 2π times the residue of poles at $k_z = \nu_a$ and $k_z = \nu_b$. Similarly, for $z - z' < 0$, the integral is equal to the pole contribution at $-\nu_a$ and $-\nu_b$. The combined result valid for all $z - z'$ is

$$
\phi(\mathbf{x},\mathbf{x}',\omega) = \frac{-i}{4\pi c_{33}c_{44}}\int_0^\infty \frac{1}{\nu_b^2-\nu_a^2}\left(\frac{e^{i\nu_b|z-z'|}}{\nu_b}-\frac{e^{i\nu_a|z-z'|}}{\nu_a}\right)kJ_0(kD)dk. \qquad (2.22)
$$

Once g and ϕ are determined, we obtain the transverse curl, the transverse divergence, and the z derivative of the displacement vector, $\mathbf{u}$. These quantities are

$$
\begin{aligned}
\nabla_t \times \mathbf{u}_t &= \int_V g(\mathbf{x},\mathbf{x}')\nabla_t' \times \mathbf{F}_t' d\mathbf{x}', \qquad (2.23)\\
\nabla_t \cdot \mathbf{u}_t &= \int_V L_t\phi(\mathbf{x},\mathbf{x}')\nabla_t'\cdot\mathbf{F}_t' d\mathbf{x}' - (c_{13}+c_{44})\int_V \nabla_t^2\phi(\mathbf{x},\mathbf{x}')\frac{\partial F_z'}{\partial z'}d\mathbf{x}', \qquad (2.24)\\
\frac{\partial u_z}{\partial z} &= \int_V L_z\phi(\mathbf{x},\mathbf{x}')\frac{\partial F_z'}{\partial z'}d\mathbf{x}' - (c_{13}+c_{44})\int_V \frac{\partial^2\phi(\mathbf{x},\mathbf{x}')}{\partial z^2}\nabla_t'\cdot\mathbf{F}_t' d\mathbf{x}'. \qquad (2.25)
\end{aligned}
$$

Now, a few vector identities and integration by parts can be used to recover the total displacement vector. Using vector identity $g\nabla_t' \times \mathbf{f}' = \nabla_t' \times (g\mathbf{f}') - \nabla_t' g \times \mathbf{f}'$ in (2.23) and noticing that $\nabla_t' g = -\nabla_t g$, we have

$$
\begin{aligned}
\nabla_t \times \mathbf{u}_t &= \int_V \{\nabla_t' \times [g(\mathbf{x},\mathbf{x}')\mathbf{F}_t'] + \nabla_t g(\mathbf{x},\mathbf{x}')\times\mathbf{F}_t'\}\, d\mathbf{x}' \\
&= \int_V \nabla_t g(\mathbf{x},\mathbf{x}')\times\mathbf{F}_t' d\mathbf{x}'. \qquad (2.26)
\end{aligned}
$$

In (2.26), since the integrand of the first integral is in a differential form, the integral can be evaluated at the boundary surface of the volume. This results in zero because

$\mathbf{F}_t$ is a body force and not supported at the boundary surface. Applying $\phi\nabla_t \cdot \mathbf{f} = \nabla_t \cdot (\phi\mathbf{f}) - \nabla_t\phi \cdot \mathbf{f}$ and Green's theorem to the first integral of (2.24) by noticing that the surface integral is zero again because $\mathbf{F}_t$ is not supported on the surface ($\mathbf{F}$ is a volume source), and using integration by parts to the second integral, we obtain

$$\nabla_t \cdot \mathbf{u}_t = \int_V \nabla_t L_t \phi(\mathbf{x}, \mathbf{x}') \cdot \mathbf{F}'_t \, d\mathbf{x}' - (c_{13} + c_{44}) \int_V \nabla_t^2 \frac{\partial \phi(\mathbf{x}, \mathbf{x}')}{\partial z} \hat{z} \cdot \mathbf{F}' \, d\mathbf{x}'. \tag{2.27}$$

Similarly, for (2.25), we have

$$\frac{\partial u_z}{\partial z} = \int_V \frac{\partial}{\partial z} L_z \phi(\mathbf{x}, \mathbf{x}') \hat{z} \cdot \mathbf{F}' \, d\mathbf{x}' - (c_{13} + c_{44}) \int_V \frac{\partial^2}{\partial z^2} \nabla_t \phi(\mathbf{x}, \mathbf{x}') \cdot \mathbf{F}'_t \, d\mathbf{x}'. \tag{2.28}$$

Using the identity $\nabla_t^2 \mathbf{u}_t = \nabla_t \nabla_t \cdot \mathbf{u}_t - \nabla_t \times \nabla_t \times \mathbf{u}_t$, the total displacement vector can be recovered as

$$\begin{aligned}
\mathbf{u} &= \mathbf{u}_t + u_z \hat{z} \\
&= \frac{1}{\nabla_t^2} [\nabla_t \nabla_t \cdot \mathbf{u}_t - \nabla_t \times \nabla_t \times \mathbf{u}_t] + \hat{z} \int \frac{\partial u_z}{\partial z} dz \\
&= \int_V \frac{\nabla_t \nabla_t}{\nabla_t^2} L_t \phi(\mathbf{x}, \mathbf{x}') \cdot \mathbf{F}' \, d\mathbf{x}' - (c_{13} + c_{44}) \int_V \nabla_t \frac{\partial}{\partial z} \phi \hat{z} \cdot \mathbf{F}' \, d\mathbf{x}' \\
&\quad - \int_V \frac{1}{\nabla_t^2} \nabla_t \times (\nabla_t g(\mathbf{x}, \mathbf{x}') \times \mathbf{F}'_t) d\mathbf{x}' \\
&\quad + \int_V L_z \phi(\mathbf{x}, \mathbf{x}') \hat{z}\hat{z} \cdot \mathbf{F}' \, d\mathbf{x}' - (c_{13} + c_{44}) \int_V \frac{\partial}{\partial z} \hat{z} \nabla_t \phi \cdot \mathbf{F}' \, d\mathbf{x}' \\
&= \int_V \left[g\bar{\mathbf{I}} + \hat{z}\hat{z}(L_z\phi - g) - (c_{13} + c_{44}) \frac{\partial}{\partial z} (\nabla_t \hat{z} + \hat{z} \nabla_t) \phi + \frac{\nabla_t \nabla_t}{\nabla_t^2} (L_t \phi - g) \right] \cdot \mathbf{F}' d\mathbf{x}'.
\end{aligned} \tag{2.29}$$

In the above derivation, the following identities have been used:

$$\begin{aligned}
\nabla_t \times (\nabla_t g \times \mathbf{F}'_t) &= \nabla_t \nabla_t g \cdot \mathbf{F}'_t - \nabla_t^2 g \mathbf{F}'_t, \\
\bar{\mathbf{I}} &= \bar{\mathbf{I}}_t + \hat{z}\hat{z}, \\
\mathbf{F}_t &= \bar{\mathbf{I}}_t \cdot \mathbf{F}, \\
\frac{1}{\nabla_t^2} \nabla_t^2 &= 1.
\end{aligned}$$

The last equation in the above says that the displacement field can be determined for any kind of source by convolving the source with a certain function then integrating over the source volume. This is exactly the statement of Green's superposition

theorem, and this certain function (the integrand) is just the Green's function for the wave equation. Thus, the dynamic Green's function (tensor), denoted by $\overline{\mathbf{G}}$ and expressed in dyadic form, is

$$\overline{\mathbf{G}} = g\bar{\mathbf{I}} + \hat{z}\hat{z}(L_z\phi - g) - (c_{13} + c_{44})\frac{\partial}{\partial z}(\nabla_t\hat{z} + \hat{z}\nabla_t)\phi + \frac{\nabla_t\nabla_t}{\nabla_t^2}(L_t\phi - g). \qquad (2.30)$$

The meanings of L_t, L_z, g and ϕ in the above equation are defined in Equations (2.11), (2.12), (2.7) and (2.22), respectively. Comparing Equation 2.30 with the separate forms (eqns. 80 and B36) in Ben-Menahem and Sena (1990), one can verify that they are equivalent.

The inverse Laplacian operator, $\frac{1}{\nabla_t^2}$, does not have simple form except for fields or sources with z-axis symmetry. With the z-axis symmetry, this operator (Ben-Menahem and Sena, 1990; Sena, 1992) is

$$\nabla_t^2 u = \frac{1}{r}\frac{\partial}{\partial r}\left(r\frac{\partial u}{\partial r}\right) \longleftrightarrow \frac{1}{\nabla_t^2}u = \int\frac{dr}{r}\int rudr. \qquad (2.31)$$

Even in this special case, the inverse Laplacian incurs coordinate (r) integration with respect to Bessel functions, which usually is not an easy task. For off-centered sources which will be encountered in the BEM method, the above is no longer valid, and an alternative is required. As shown later, in general this inverse Laplacian operator can in fact be replaced by integration over z.

Even with ∇_t^{-2} in Equation 2.30, the isotropic Green's function can be obtained. In the isotropic limit, $c_{11} = c_{33} = \lambda + 2\mu$, $c_{13} = \lambda$ and $c_{44} = c_{66} = \mu$,

$$A = 0,\ \ B = 0,\ \ C = (\lambda+\mu)^2\rho^2\omega^4,\ \ \nu_b^2 = \frac{\rho\omega^2}{\mu} - k^2,\ \ \nu_a^2 = \frac{\rho\omega^2}{\lambda+2\mu} - k^2. \qquad (2.32)$$

Using the Sommerfeld representation for a point source, ϕ is simplified to

$$\phi = \frac{-1}{(\lambda+\mu)\rho\omega^2}(g_\beta - g_\alpha) = \frac{-1}{(\lambda+\mu)\rho\omega^2}\left(\frac{e^{ik_\beta R}}{4\pi R} - \frac{e^{ik_\alpha R}}{4\pi R}\right), \qquad (2.33)$$

where g_β and g_α are the scalar Green's function of the scalar wave equations

$$\nabla^2 g_\beta + \frac{\rho\omega^2}{\mu}g_\beta = -\delta(\mathbf{x}-\mathbf{x}'),\quad \nabla^2 g_\alpha + \frac{\rho\omega^2}{\lambda+2\mu}g_\alpha = -\delta(\mathbf{x}-\mathbf{x}'). \qquad (2.34)$$

These two equations can be used to simplify $L_t\phi$ and $L_z\phi$ at any point, *including the source point.* We then have

$$L_z\phi = \frac{g_\beta}{\mu} - \frac{1}{\rho\omega^2}\frac{\partial^2(g_\alpha - g_\beta)}{\partial z^2}, \quad L_t\phi = \frac{g_\beta}{\mu} - \frac{1}{\rho\omega^2}\nabla_t^2(g_\alpha - g_\beta). \tag{2.35}$$

With these results and $g = g_\beta/\mu$ from (2.7), the Green's function becomes

$$\overline{\mathbf{G}} = \frac{1}{\mu}g_\beta\bar{\mathbf{I}} + \frac{1}{\rho\omega^2}\left[\left(\frac{\partial}{\partial z}\nabla_t\hat{z} + \frac{\partial}{\partial z}\hat{z}\nabla_t\right) + \hat{z}\hat{z}\frac{\partial^2}{\partial z^2} + \nabla_t\nabla_t\right](g_\beta - g_\alpha) \tag{2.36}$$

$$= \frac{1}{\rho\omega^2}\left[k_\beta^2 g_\beta\bar{\mathbf{I}} + \nabla\nabla(g_\beta - g_\alpha)\right], \tag{2.37}$$

which is exactly the dynamic Green's function for the isotropic elastic medium (Kupradze, 1963; Ben-Menahem and Singh, 1981).

2.3 The Static Green's Function

To determine the singular behavior of the dynamic Green's function when a field point approaches the source point, the static case must be considered because it is required to regularize the surface integrals of the dynamic Green's function (Kupradze, 1963). Following the procedure of the previous section and setting the frequency to zero ($\omega = 0$), one finds that the static Green's function has the same form as (2.30) except that L_t, L_z, g and ϕ must be redefined. Operators L_t and L_z stay the same as in Equations. (2.11) and (2.12) with $\omega = 0$, while more work is required in order to obtain g and ϕ. In the static limit, Equations (2.6) and (2.14) become

$$c_{66}\nabla_t^2 g + c_{44}\frac{\partial^2 g}{\partial z^2} = -\delta(\mathbf{x} - \mathbf{x}'), \tag{2.38}$$

$$\left[c_{33}c_{44}\frac{\partial^4}{\partial z^4} + (c_{11}c_{33} - c_{13}^2 - 2c_{13}c_{44})\nabla_t^2\frac{\partial^2}{\partial z^2} + c_{11}c_{44}\nabla_t^4\right]\phi = -\delta(\mathbf{x} - \mathbf{x}'). \tag{2.39}$$

The solution of the first equation is

$$g = \frac{\nu_g}{4\pi c_{66}}\frac{1}{R_g}; \quad R_g = \sqrt{(x - x')^2 + (y - y')^2 + \nu_g^2(z - z')^2}. \tag{2.40}$$

where, $\nu_g = \sqrt{c_{66}/c_{44}}$. The second equation can be factorized into

$$c_{33}c_{44}\nu_a^2\nu_b^2\left(\nabla_t^2 + \frac{1}{\nu_a^2}\frac{\partial^2}{\partial z^2}\right)\left(\nabla_t^2 + \frac{1}{\nu_b^2}\frac{\partial^2}{\partial z^2}\right)\phi = -\delta(\mathbf{x}-\mathbf{x}'), \tag{2.41}$$

where, ν_a^2 and ν_b^2 are the negative counterparts of the solutions of equation

$$c_{33}c_{44}\nu^4 + (c_{11}c_{33} - c_{13}^2 - 2c_{13}c_{44})\nu^2 + c_{11}c_{44} = 0, \tag{2.42}$$

i.e.,

$$\nu_a^2 = \frac{(c_{11}c_{33} - c_{13}^2 - 2c_{13}c_{44}) + \sqrt{(c_{11}c_{33} - c_{13}^2)[c_{11}c_{33} - (c_{13}+2c_{44})^2]}}{2c_{33}c_{44}}, \tag{2.43}$$

$$\nu_b^2 = \frac{(c_{11}c_{33} - c_{13}^2 - 2c_{13}c_{44}) - \sqrt{(c_{11}c_{33} - c_{13}^2)[c_{11}c_{33} - (c_{13}+2c_{44})^2]}}{2c_{33}c_{44}}. \tag{2.44}$$

In order to be a solution of (2.41), ϕ must satisfy

$$\left(\nabla_t^2 + \frac{1}{\nu_b^2}\frac{\partial^2}{\partial z^2}\right)\phi = \frac{\nu_a}{4\pi c_{33}c_{44}\nu_a^2\nu_b^2}\frac{1}{R_a}, \tag{2.45}$$

$$\left(\nabla_t^2 + \frac{1}{\nu_a^2}\frac{\partial^2}{\partial z^2}\right)\phi = \frac{\nu_b}{4\pi c_{33}c_{44}\nu_a^2\nu_b^2}\frac{1}{R_b}, \tag{2.46}$$

where,

$$R_a = \sqrt{(x-x')^2 + (y-y')^2 + \nu_a^2(z-z')^2},$$

$$R_b = \sqrt{(x-x')^2 + (y-y')^2 + \nu_b^2(z-z')^2}.$$

In arriving at the above equations, we employed the transformations $s_a = \nu_a(z-z')$, $s_b = \nu_b(z-z')$, and $\delta(s/c) = c\delta(s)$, and the Poisson's equation

$$\nabla^2\frac{1}{4\pi R} = -\delta(\mathbf{x}-\mathbf{x}'), \tag{2.47}$$

where, $R = \sqrt{(x-x')^2 + (y-y')^2 + (z-z')^2}$. From Equations (2.45) and (2.46), we obtain

$$\frac{\partial^2\phi}{\partial z^2} = \frac{1}{4\pi c_{33}c_{44}(\nu_b^2 - \nu_a^2)}\left[\frac{\nu_b}{R_b} - \frac{\nu_a}{R_a}\right], \tag{2.48}$$

$$\nabla_t^2\phi = \frac{1}{4\pi c_{33}c_{44}(\nu_b^2 - \nu_a^2)}\left[\frac{1}{\nu_a R_a} - \frac{1}{\nu_b R_b}\right]. \tag{2.49}$$

Assuming ν_a and $\nu_b > 0$ (or $Re[\nu_a]$ and $Re[\nu_b] > 0$), integration over z yields

$$\frac{\partial \phi}{\partial z} = \frac{\mathrm{sgn}(z-z')}{4\pi c_{33}c_{44}(\nu_b^2 - \nu_a^2)}\{\ln[R_b + \nu_b|z-z'|] - \ln[R_a + \nu_a|z-z'|]\}, \tag{2.50}$$

and

$$\begin{aligned}\phi = \frac{1}{4\pi c_{33}c_{44}(\nu_b^2 - \nu_a^2)}\{ & \quad |z-z'|\ln[R_b + \nu_b|z-z'|] - \tfrac{R_b}{\nu_b} \\ & - \quad |z-z'|\ln[R_a + \nu_a|z-z'|] + \tfrac{R_a}{\nu_a} \quad \}.\end{aligned} \tag{2.51}$$

Except for the absolute value, this expression is the same as the assumed solution form in Pan and Chou (1976) (Eq. 19). The absolute value of $z - z'$ is necessary because for ν_a or $\nu_b > 0$, and $z - z' = -R_a/\nu_a$ or $-R_b/\nu_b$, (2.51) yields a finite solution, instead of infinity when the absolute value sign is absent.

The isotropic limit cannot be obtained from the above expression for ϕ. This is because at the limit, $\nu_a = \nu_b = 1$, and (2.41) reduces to

$$\mu(\lambda + 2\mu)\left(\nabla_t^2 + \frac{\partial^2}{\partial z^2}\right)^2 \phi = -\delta(\mathbf{x} - \mathbf{x}'). \tag{2.52}$$

Using the identity $\nabla^2 R = \frac{2}{R}$, the solution for this equation is

$$\phi = \frac{1}{8\pi c_{33}c_{44}} R. \tag{2.53}$$

Substitution of this ϕ and g into (2.30) yields the isotropic static Green's function (Love, 1944), i.e.,

$$\overline{\mathbf{G}} = \frac{1}{4\pi\mu R}\overline{\mathbf{I}} - \frac{\lambda + \mu}{8\pi\mu(\lambda + 2\mu)}\nabla\nabla R.$$

2.4 Simplification: Calculation of $\frac{\nabla_t \nabla_t}{\nabla_t^2}(L_t\phi - g)$

The last term in the dynamic Green's function (Eq. 2.30) is a valid but very abstract expression. Its precise meaning is hard to define in general. Even for special cases, numerical calculation of the Green's function renders integration of Bessel functions with respect to spatial coordinates. This, along with the integration over wave

numbers, may present many numerical difficulties. For far-field approximation as in Ben-Menahem and Sena (1990), operator ∇_t^{-2} presents no problem because of the $\frac{1}{r^2}$ factor preceding the r integrals (see the reference). In the borehole BEM problem, the near-field is of critical importance, and the exact meaning of ∇_t^{-2} is required. In the following, we show a method to evaluate the last term in Equation 2.30 for general source geometry.

Before we proceed, let's understand why $\frac{1}{\nabla_t^2}$ disappears in the isotropic case (Equation 2.37). As seen from (2.35), $L_t\phi$ cancels out g and leaves $-\frac{1}{\rho\omega^2}\nabla_t^2(g_\alpha - g_\beta)$. This cancels out the inverse Laplacian. To obtain (2.35), the two independent scalar wave equations in (2.34) for the P and S waves are used. In the case of transverse isotropy, one no longer has two separate scalar wave equations for the *quasi-P* and *quasi-S* waves. Instead, one has a fourth order scalar equation (2.14) for the $P-SV$ waves and a second order equation (2.6) for the SH wave. Equation 2.14 indicates the inevitable involvement of operator L_z in the calculation. This suggests that $L_z(L_t\phi - g)$ be computed first, rather than $(L_t\phi - g)$ alone.

From equations (2.14) and (2.6), a simple manipulation yields

$$L_z(L_t\phi - g) = \nabla_t^2\left[(c_{13}+c_{44})^2\frac{\partial^2\phi}{\partial z^2} - (c_{11}-c_{66})g\right]. \tag{2.54}$$

Because L_z is a linear operator, the above result suggests that $L_t\phi - g = \nabla_t^2\psi$, where ψ is an unknown function to be determined. Thus, we obtain

$$\frac{\nabla_t\nabla_t}{\nabla_t^2}(L_t\phi - g) = \nabla_t\nabla_t\,\psi, \tag{2.55}$$

and

$$L_z\psi = (c_{13}+c_{44})^2\frac{\partial^2\phi}{\partial z^2} - (c_{11}-c_{66})g. \tag{2.56}$$

Now that we have got rid of the inverse Laplacian, what is left to do is to determine ψ by solving the inhomogeneous equation (2.56), where the differential operator L_z is defined by Equation 2.12.

The right hand side of (2.56) has the form of the Hankel transform because

$$\frac{\partial^2\phi}{\partial z^2} = \frac{i}{4\pi c_{33}c_{44}}\int_0^\infty \frac{1}{\nu_b^2-\nu_a^2}\left(\nu_b\, e^{i\nu_b|z-z'|} - \nu_a\, e^{i\nu_a|z-z'|}\right) kJ_0(kD)dk, \tag{2.57}$$

$$g = \frac{i}{4\pi c_{44}} \int_0^\infty \frac{e^{i\nu_c|z-z'|}}{\nu_c} k J_0(kD) dk, \tag{2.58}$$

where, ν_a and ν_b are defined in Equations (2.19) and (2.20), and $\nu_c = \sqrt{(\rho\omega^2 - c_{66}k^2)/c_{44}}$. This suggests that the solution ψ should also be in the form of the Hankel transform. i.e.,

$$\psi = \frac{i}{4\pi} \int_0^\infty f(z,z')\, k J_0(kD) dk. \tag{2.59}$$

Substituting this solution form and Equations (2.57) and (2.58) into (2.56), we obtain the following ordinary differential equation for $f(z,z')$

$$\begin{aligned} \frac{d^2 f(z,z')}{dz^2} + \nu_z^2 f(z,z') &= p(z,z') \\ &= \frac{S_1}{\nu_b^2 - \nu_a^2}\left[\nu_b e^{i\nu_b|z-z'|} - \nu_a e^{i\nu_a|z-z'|}\right] - \frac{S_2}{\nu_c} e^{i\nu_c|z-z'|} \end{aligned} \tag{2.60}$$

In arriving at the above equation, the following definitions and identities were used,

$$\nu_z^2 = \frac{c_{11}}{c_{44}}\left(\frac{\rho\omega^2}{c_{11}} - k^2\right), \quad S_1 = \frac{(c_{13}+c_{44})^2}{c_{33}c_{44}^2}, \quad S_2 = \frac{c_{11}-c_{66}}{c_{44}^2}, \tag{2.61}$$

$$\begin{aligned} \nabla_t^2 J_0(kD) &= \nabla_t^2 \sum_{m=0}^{\infty} \epsilon_m J_m(kr_0) J_m(kr) \cos m(\theta - \theta_0) \\ &= \sum_{m=0}^{\infty} \epsilon_m J_m(kr_0) \nabla_t^2 [J_m(kr) \cos m(\theta - \theta_0)] \\ &= \sum_{m=0}^{\infty} \epsilon_m J_m(kr_0) \left[\frac{1}{r}\frac{\partial}{\partial r}\left(r\frac{\partial J_m(kr)}{\partial r}\right) - \frac{m^2}{r^2} J_m(kr)\right] \cos m(\theta - \theta_0)] \\ &= \sum_{m=0}^{\infty} \epsilon_m J_m(kr_0) [\, -k^2 J_m(kr)\,] \cos m(\theta - \theta_0)] \\ &= -k^2 J_0(kD). \end{aligned} \tag{2.62}$$

For the second identity, the addition theorem (Watson, 1944) of Bessel's functions was used.

Equation 2.60 can be solved with the aid of the Green's function for this ordinary differential equation. This Green's function, denoted by $q(z,z'')$, and satisfying the continuity condition of q and discontinuity condition of $\frac{\partial q}{\partial z}$ at the source level $z = z''$, is

$$q(z,z'') = \frac{e^{i\nu_z|z-z''|}}{2i\nu_z}. \tag{2.63}$$

Using Green's theorem on (2.60), we obtain

$$f(z,z') = \int_{-\infty}^{\infty} q(z,z'')\, p(z'',z')dz''. \tag{2.64}$$

When $p(z'',z')$ (defined in (2.60)) is substituted into the above equation, there are three integrals of the type $\int_{-\infty}^{\infty} e^{i\nu_1|z-z''|}e^{i\nu_2|z''-z'|}dz''$. This type of integral is readily computed by dividing the integral into three sub-domain integrals: $\int_{-\infty}^{\infty} = \int_{-\infty}^{z'} + \int_{z'}^{z} + \int_{z}^{\infty}$ for $z > z'$ and $\int_{-\infty}^{\infty} = \int_{-\infty}^{z} + \int_{z}^{z'} + \int_{z'}^{\infty}$ for $z < z'$. The final result is

$$\int_{-\infty}^{\infty} e^{i\nu_1|z-z''|}e^{i\nu_2|z''-z'|}dz'' = \frac{2i}{\nu_1^2-\nu_2^2}\left[\nu_1 e^{i\nu_2|z-z'|} - \nu_2 e^{i\nu_1|z-z'|}\right]. \tag{2.65}$$

Using this result in (2.64), we obtain

$$\begin{aligned} f(z,z') = \quad & \frac{1}{\nu_z}\left[\frac{S_2}{\nu_z^2-\nu_c^2} - \frac{S_1\nu_z^2}{(\nu_z^2-\nu_a^2)(\nu_z^2-\nu_b^2)}\right]e^{i\nu_z|z-z'|} \\ - \quad & \frac{S_1\nu_a}{(\nu_b^2-\nu_a^2)(\nu_z^2-\nu_a^2)}e^{i\nu_a|z-z'|} \\ + \quad & \frac{S_1\nu_b}{(\nu_b^2-\nu_a^2)(\nu_z^2-\nu_b^2)}e^{i\nu_b|z-z'|} - \frac{S_2}{\nu_c(\nu_z^2-\nu_c^2)}e^{i\nu_c|z-z'|}. \end{aligned} \tag{2.66}$$

The above seems to suggest four types of propagating waves. However, a closer examination of the first term of $f(z,z')$ shows that it vanishes altogether. This result agrees with the physics that only three kinds of waves exist in a TI medium, ν_a part for *quasi*-P wave, ν_b part for *quasi*-SV wave, and ν_c part for the SH wave. Thus, the final result is

$$\begin{aligned} f(z,z') = \quad & - \quad \frac{S_1\nu_a}{(\nu_b^2-\nu_a^2)(\nu_z^2-\nu_a^2)}e^{i\nu_a|z-z'|} \\ & + \quad \frac{S_1\nu_b}{(\nu_b^2-\nu_a^2)(\nu_z^2-\nu_b^2)}e^{i\nu_b|z-z'|} - \frac{S_2}{\nu_c(\nu_z^2-\nu_c^2)}e^{i\nu_c|z-z'|}. \end{aligned} \tag{2.67}$$

Substituting this result back into (2.59) and using (2.55), one obtains a meaningful and numerically feasible form for the originally abstract term. It can be easily implemented on a computer.

In the isotropic limit,

$$S_1 = \frac{(\lambda+\mu)^2}{\mu^2(\lambda+2\mu)}; \quad S_2 = \frac{\lambda+\mu}{\mu^2}; \quad \nu_b^2-\nu_a^2 = \rho\omega^2\frac{\lambda+\mu}{\mu(\lambda+2\mu)};$$

$$\nu_c^2 = \nu_b^2 = \rho\omega^2/\mu - k^2; \quad \nu_z^2 - \nu_a^2 = \frac{\lambda+\mu}{\mu}\nu_a^2;$$
$$\nu_z^2 - \nu_b^2 = \nu_z^2 - \nu_c^2 = -\frac{\lambda+\mu}{\mu}k^2,$$

then

$$f(z,z') = \frac{1}{\rho\omega^2}\left(\frac{e^{i\nu_b|z-z'|}}{\nu_b} - \frac{e^{i\nu_a|z-z'|}}{\nu_a}\right), \tag{2.68}$$

and, using the Sommerfeld integral, we have

$$\psi = \frac{i}{4\pi}\int_0^\infty f(z,z')\; kJ_0(kD)dk = \frac{g_\beta - g_\alpha}{\rho\omega^2}, \tag{2.69}$$

which agrees with the result of (2.36).

For the static case, Equations (2.48) and (2.49) yield

$$L_t\phi = \frac{1}{4\pi c_{33}c_{44}(\nu_b^2 - \nu_a^2)}\left\{\frac{c_{44} - c_{33}\nu_a^2}{\nu_a}\frac{1}{R_a} - \frac{c_{44} - c_{33}\nu_b^2}{\nu_b}\frac{1}{R_b}\right\}. \tag{2.70}$$

ν_a^2 and ν_b^2 are now defined by Equations (2.43) and (2.44). $1/R_a$, $1/R_b$ satisfy

$$\left[\nabla_t^2 + \frac{1}{\nu_i^2}\partial_z^2\right]\frac{1}{R_i} = -\frac{4\pi}{\nu_i}\delta(\mathbf{x}-\mathbf{x}'), \tag{2.71}$$

where, subscript i represents a, b, or g. A manipulation of (2.71), with the fact that operators $\frac{\partial^2}{\partial z^2}$ and $\frac{1}{\nabla_t^2}$ commute in cylindrical coordinates, yields

$$\begin{aligned}\frac{1}{\nabla_t^2}\frac{1}{R_i} &= -\int\frac{\nu_i^2}{R_i}d^2z - \frac{4\pi\nu_i}{\nabla_t^2}\int\delta(\mathbf{x}-\mathbf{x}')d^2z \\ &= -\nu_i|z-z'|\ln[R_i + \nu_i|z-z'|] + R_i - \frac{4\pi\nu_i}{\nabla_t^2}\int\delta(\mathbf{x}-\mathbf{x}')d^2z. \end{aligned}\tag{2.72}$$

In calculating $\frac{1}{\nabla_t^2}(L_t\phi - g)$, the second term in (2.72) drops out due to cancellation, and we obtain

$$\begin{aligned}\psi &= \frac{1}{\nabla_t^2}(L_t\phi - g) \\ &= \frac{c_{44} - c_{33}\nu_b^2}{4\pi c_{33}c_{44}(\nu_b^2 - \nu_a^2)\nu_b}\{\nu_b|z-z'|\ln[R_b + \nu_b|z-z'|] - R_b\} \\ &\quad -\frac{c_{44} - c_{33}\nu_a^2}{4\pi c_{33}c_{44}(\nu_b^2 - \nu_a^2)\nu_a}\{\nu_a|z-z'|\ln[R_a + \nu_a|z-z'|] - R_a\} \\ &\quad +\frac{\nu_g}{4\pi c_{66}}\{\nu_g|z-z'|\ln[R_g + \nu_g|z-z'|] - R_g\}. \end{aligned}\tag{2.73}$$

It is interesting to note from the above calculations that the inverse Laplacian is essentially removed by integration over z. The end result of z integration is basically to introduce amplitude weighting for different waves. The computations are based on operator manipulation and therefore the results are valid for any source geometry.

2.5 Displacements for Three Basic Sources

Before we proceed to calculate the displacements, we summarize the results of the previous sections. The dynamic and static Green's function in transversely isotropic media can be expressed in the following single dyadic form

$$\overline{\mathbf{G}} = g\bar{\mathbf{I}}_t + \hat{z}\hat{z}L_z\phi - (c_{13}+c_{44})(\nabla_t\hat{z} + \hat{z}\nabla_t)\frac{\partial\phi}{\partial z} + \nabla_t\nabla_t\psi. \tag{2.74}$$

For the dynamic case, L_z, g, ϕ, and ψ are defined in Equations (2.12), (2.7) or (2.58), (2.22), and (2.59) plus (2.67), respectively. For the static case, these symbols are defined in Equations (2.12) with $\omega = 0$, (2.40), (2.51), and (2.73).

Practically, we now have all the tools necessary to solve wave propagation and scattering problems in a TI medium. As the basic applications of Green's functions, we calculate the displacements produced by vertical, horizontal and explosive point sources.

2.5.1 Vertical point force

For a vertical point force (parallel to the symmetry axis) at the origin, $\mathbf{F}(\mathbf{x}) = \hat{z}\delta(\mathbf{x})$. Using the Green theorem, we obtain

$$\mathbf{u} = \int_V \overline{\mathbf{G}}(\mathbf{x},\mathbf{x}')\cdot\mathbf{F}(\mathbf{x}')d\mathbf{x}' = \hat{z}L_z\phi - (c_{13}+c_{44})\nabla_t\frac{\partial\phi}{\partial z}. \tag{2.75}$$

The displacement vector does not depend on g, indicating that a point force along the symmetry axis does not excite SH waves. Writing out in components, we have

$$U_r = \frac{\mathrm{sgn}(z)}{4\pi}\int_0^\infty S_{ab}k^2J_1(kr)\left[e^{i\nu_b|z|} - e^{i\nu_a|z|}\right]dk, \tag{2.76}$$

$$U_z = \frac{i}{4\pi}\int_0^\infty kJ_0(kr)\left[S_b e^{i\nu_b|z|} - S_a e^{i\nu_a|z|}\right]dk, \tag{2.77}$$

where,

$$S_{ab} = \frac{c_{13}+c_{44}}{c_{33}c_{44}(\nu_b^2-\nu_a^2)}, \quad S_a = \frac{\nu_a^2-\nu_z^2}{c_{33}(\nu_b^2-\nu_a^2)\nu_a}, \quad S_b = \frac{\nu_b^2-\nu_z^2}{c_{33}(\nu_b^2-\nu_a^2)\nu_b}.$$

2.5.2 Horizontal point force

For a point force at the origin and directed along an isotropic plane (say along $\hat{x}$), $\mathbf{F}(\mathbf{x}) = \hat{x}\delta(\mathbf{x})$. The displacement vector is

$$\mathbf{u} = g\hat{x} - (c_{13}+c_{44})\frac{\partial^2\phi}{\partial x\partial z}\hat{z} + \nabla_t\frac{\partial\psi}{\partial x}. \tag{2.78}$$

Now g is included in the final expression, indicating that a horizontal point force excites all three waves: *SH*, *quasi-P*, and *quasi-SV*. In their components, the displacements are

$$U_r = \frac{i\cos\varphi}{4\pi}\int_0^\infty kJ_0(kr)\left[T_a e^{i\nu_a|z|} - T_b e^{i\nu_b|z|}\right]dk + \frac{i\cos\varphi}{4\pi}\int_0^\infty f(z,0)\,k^2\frac{J_1(kr)}{r}dk, \tag{2.79}$$

$$U_\varphi = \frac{i\sin\varphi}{4\pi c_{44}}\int_0^\infty kJ_0(kr)\frac{e^{i\nu_c|z|}}{\nu_c}dk + \frac{i\sin\varphi}{4\pi}\int_0^\infty f(z,0)\,k^2\frac{J_1(kr)}{r}dk, \tag{2.80}$$

$$U_z = \frac{\mathrm{sgn}(z)}{4\pi}\cos\varphi\int_0^\infty S_{ab}k^2J_1(kr)\left[e^{i\nu_a|z|} - e^{i\nu_b|z|}\right]dk. \tag{2.81}$$

The azimuthal angle φ is measured from the x-axis in the $x-y$ plane. S_{ab} is the same as defined before, and T_a and T_b are

$$T_a = \frac{S_1\nu_a k^2}{(\nu_b^2-\nu_a^2)(\nu_z^2-\nu_a^2)}, \quad T_b = \frac{S_1\nu_b k^2}{(\nu_b^2-\nu_a^2)(\nu_z^2-\nu_b^2)}.$$

The second terms in U_r and U_φ represent the near-field part of the wave field. In the far-field, only the first terms contribute. However, in the BEM modeling of downhole sources, these near terms are crucial in satisfying the boundary conditions. The above simple forms allow easy computation of the near-field.

2.5.3 Explosive point source

For an explosive point source at the origin, the displacement vector is obtained by taking the divergence of the Green's function with respect to the source coordinates. Since $\nabla = -\nabla'$ for functions g, ϕ, and ψ, we have

$$\mathbf{u} = -\hat{z}\frac{\partial}{\partial z}(L_z\phi) - \nabla_t(L_t\phi) + (c_{13}+c_{44})(\nabla_t^2\hat{z} + \frac{\partial}{\partial z}\nabla_t)\frac{\partial\phi}{\partial z}. \tag{2.82}$$

In the above, $L_t\phi = \nabla_t^2\psi + g$ is used. The curl of $\mathbf{u}$ is

$$\nabla\times\mathbf{u} = \nabla_t\times\hat{z}\frac{\partial}{\partial z}\left[(c_{13}+2c_{44}-c_{11})\nabla_t^2 + (c_{33}-c_{13}-2c_{44})\frac{\partial^2}{\partial z^2}\right]\phi. \tag{2.83}$$

For an explosive source in a transversely isotropic medium, the curl of the displacement field is not zero. This implies that the explosive source excites not only the *quasi-P* but also the *quasi-SV* waves. In the isotropic limit, $c_{11} = c_{33} = c_{13} + 2c_{44}$, the curl of the displacement field due to an explosive source is zero, indicating that only the compressional wave exists. The two displacement components are

$$U_r = \frac{i}{4\pi}\int_0^\infty \left[(S_{ab}\nu_a + T_a)e^{i\nu_a|z|} - (S_{ab}\nu_b + T_b)e^{i\nu_b|z|}\right]k^2J_1(kr)dk, \tag{2.84}$$

$$U_z = \frac{\mathrm{sgn}(z)}{4\pi}\int_0^\infty \left[(S_b\nu_b - S_{ab}k^2)e^{i\nu_b|z|} - (S_a\nu_a - S_{ab}k^2)e^{i\nu_a|z|}\right]kJ_0(kr)dk \tag{2.85}$$

In the isotropic limit, $S_{ab}\nu_b + T_b = 0$ and $S_b\nu_b - S_{ab}k^2 = 0$. SV wave contribution to the displacements vanishes. The displacements reduce to the gradient of ϕ.

2.5.4 Numerical evaluation in two media

The above displacement integrals are evaluated in two particular TI media. The first medium (Mesaverde sandstone - Ben-Menahem and Sena, 1990) has a density of 2870 kg/m^3 and the following elastic constants (in 10^9Pa): $c_{11} = 50$, $c_{33} = 45$, $c_{13} = -8.6$, $c_{44} = 24.6$, and $c_{66} = 26.6$. The parameters of the second medium (plexiglas-aluminum - White, 1982) are: ρ=1950 kg/m^3, $c_{11} = 51.8$, $c_{33} = 21.4$, $c_{13} = 13.0$, $c_{44} = 3.65$, and $c_{66} = 14.1$. The first medium is only slightly anisotropic, while the second medium is extremely anisotropic. The displacements are calculated

at receivers placed circularly around the sources. For the case of the horizontal force, the receiver array makes a 45^o azimuthal angle with the $x - z$ plane. The radius of the receiver array is 75 m for the first medium and 30 m for the second. The calculated displacements are then rotated to the spherical coordinates. The resulting radial, tangential, and azimuthal components are plotted in a way to show both the amplitudes and phase fronts.

Figures 2-1, 2-2 and 2-3, and 2-4, respectively, show the displacements due to vertical, horizontal ($\hat{x}$), and explosive point sources in the first medium. The phase fronts of the P, SV, and SH waves are almost circular. The P and SH (Azimuthal component in Figure 2-3) waves travel a little faster in the horizontal direction than in the vertical direction. The SV wave travels faster in the 45^o direction. That the P and SV waves sustain large amplitudes in wide angle range (Figure 2-1) suggests large lobes in the radiation pattern. Figure 2-4 shows the existence of SV waves for an explosion in the medium. If examined carefully, this SV wave exhibits two lobes in each quadrant. A similar pattern can also be seen for the vertical force (Figure 2-1). However, this phenomenon is absent for the case of the horizontal force.

Figures 2-5 to 2-8 show the displacements in the second medium. One immediate observation is the triplication of SV waves. Although the magnitude of one branch is significantly smaller than the other two, the three branches of SV wave are clearly seen on Figure 2-6, where the point force is in the isotropic plane. If the source is a point force along the symmetry axis or an explosion, one branch of the triplication disappears. The vertical force result agrees with the calculation of White (1982) for a line source approximated by a borehole along the symmetry axis. White (1982) also demonstrated the difference in energy fall-off for the *quasi-P* and *quasi-SV* waves. Amplitude decays as -1 power of distance for the P wave, and as -0.8 for the SV waves near the triplication. The results of this subsection support this observation.

2.6 Surface Integral of the Green's Functions

In the boundary element method, integration of the Green's function over boundary surfaces is a necessary calculation. However, the Green's function is singular when receiver and source coincide. The displacement Green's function has a first order singularity which is removable when integrated over the surface. On the other hand, the stress Green's function has a second order singularity and the surface integral is not defined. Then, its principal value has to be used. The contribution of this second order singularity to the integral can be evaluated analytically. When the receiver and the source approach each other, the surface integral of the dynamic Green's function can be regularized using the static Green's function (Kupradze, 1963). The singularity integral of the dynamic Green's function is reduced to the integration of the static Green's function over a half elliptical surface around the source point. The limit as the axes of the elliptical surface goes to zero is the singular contribution.

Using the static Green's function, we first calculate the displacement and stress field for the vertical point force. We obtain

$$\begin{aligned} u_x &= -(c_{13}+c_{44})\frac{\partial^2\phi}{\partial x \partial z} \\ &= \frac{(c_{13}+c_{44})\mathrm{sgn}(z-z')}{4\pi c_{33}c_{44}(\nu_b^2-\nu_a^2)}\left\{\frac{x-x'}{R_b[R_b+\nu_b|z-z'|]}-\frac{x-x'}{R_a[R_a+\nu_a|z-z'|]}\right\} \quad (2.86) \\ u_y &= -(c_{13}+c_{44})\frac{\partial^2\phi}{\partial y \partial z} \\ &= \frac{(c_{13}+c_{44})\mathrm{sgn}(z-z')}{4\pi c_{33}c_{44}(\nu_b^2-\nu_a^2)}\left\{\frac{y-y'}{R_b[R_b+\nu_b|z-z'|]}-\frac{y-y'}{R_a[R_a+\nu_a|z-z'|]}\right\} \quad (2.87) \\ u_z &= L_z\phi. \quad (2.88) \end{aligned}$$

Notice that the displacements have a first order singularity only when $\mathbf{x} \to \mathbf{x}'$. The stress along the $\hat{z}$ direction on the surface whose normal is $\hat{x}$, τ_{xz} , is

$$\begin{aligned} \tau_{xz} &= c_{44}\left[\frac{\partial u_z}{\partial x}+\frac{\partial u_x}{\partial z}\right] \\ &= \frac{-1}{4\pi c_{33}(\nu_b^2-\nu_a^2)}\left\{\frac{c_{11}+c_{13}\nu_a^2}{\nu_a}\frac{x-x'}{R_a^3}-\frac{c_{11}+c_{13}\nu_b^2}{\nu_b}\frac{x-x'}{R_b^3}\right\}. \quad (2.89) \end{aligned}$$

The stress has a second order singularity when the receiver point coincides with the source point ($R_a = 0$ and $R_b = 0$). If this stress is integrated over a surface that includes the source, a finite value results. This value can be obtained by integrating τ_{xz} over all possible $dydz$ surrounding the source. This integration can be replaced by integration over a half ellipsoidal surface around the source point. The ellipsoidal surface is defined by

$$x - x' = R\sin\theta\cos\varphi, \quad y - y' = R\sin\theta\sin\varphi, \quad z - z' = \frac{1}{\nu}R\cos\theta. \tag{2.90}$$

Using $s = \nu z$, the ellipsoidal surface can be transformed into a spherical surface in the (x, y, s) system. Then, surface mapping between $dydz$ and a differential ellipsoidal surfaces is

$$dydz\sin\theta\cos\varphi = \frac{1}{\nu}dyds\sin\theta\cos\varphi = \frac{1}{\nu}R^2\sin\theta d\theta d\varphi, \tag{2.91}$$

as shown in Figure 2-9, where, $dz = \frac{1}{\nu}ds$, $ds = Rd\theta/\sin\theta$ and $dy = R\sin\theta d\varphi/\cos\varphi$. Then,

$$\begin{aligned}\int \tau_{xz}dydz &= \frac{-1}{4\pi c_{33}(\nu_b^2 - \nu_a^2)}\left(\frac{c_{11} + c_{13}\nu_a^2}{\nu_a^2} - \frac{c_{11} + c_{13}\nu_b^2}{\nu_b^2}\right)\int_{-\pi/2}^{\pi/2} d\varphi \int_0^{\pi}\sin\theta d\theta \\ &= \frac{-c_{11}}{2c_{33}\nu_a^2\nu_b^2} = -\frac{1}{2}.\end{aligned} \tag{2.92}$$

For a point force in the $\hat{x}$ direction, we have

$$\begin{aligned}u_x &= g + \frac{\partial^2}{\partial x^2}\frac{1}{\nabla_t^2}(L_t\phi - g) \qquad (2.93)\\ &= \frac{S_a}{\nu_a}\left(\frac{1}{D_a} - \frac{(x-x')^2}{D_a^2R_a}\right) - \frac{S_b}{\nu_b}\left(\frac{1}{D_b} - \frac{(x-x')^2}{D_b^2R_b}\right) + \frac{\nu_g}{4\pi c_{66}}\left(\frac{1}{D_g} - \frac{(y-y')^2}{D_g^2R_g}\right)\\ u_y &= \frac{\partial^2}{\partial x\partial y}\frac{1}{\nabla_t^2}(L_t\phi - g),\\ &= \frac{S_b}{\nu_b}\frac{(x-x')(y-y')}{D_b^2R_b} - \frac{S_a}{\nu_a}\frac{(x-x')(y-y')}{D_a^2R_a} + \frac{\nu_g}{4\pi c_{66}}\frac{(x-x')(y-y')}{D_g^2R_g} \qquad (2.94)\\ u_z &= -(c_{13} + c_{44})\frac{\partial^2\phi}{\partial x\partial z},\\ &= -S_c\left(\frac{x-x'}{D_bR_b} - \frac{x-x'}{D_aR_a}\right)\mathrm{sgn}(z-z'). \qquad (2.95)\end{aligned}$$

In the above equations, $D_a = R_a + \nu_a|z - z'|$ and $D_b = R_b + \nu_b|z - z'|$. The scalars S_a, S_b and S_c are

$$S_a = \frac{c_{44} - c_{33}\nu_a^2}{4\pi c_{33}c_{44}(\nu_b^2 - \nu_a^2)}, \quad S_b = \frac{c_{44} - c_{33}\nu_b^2}{4\pi c_{33}c_{44}(\nu_b^2 - \nu_a^2)}, \quad S_c = \frac{c_{13} + c_{44}}{4\pi c_{33}c_{44}(\nu_b^2 - \nu_a^2)}. \tag{2.96}$$

Then, the normal stress, τ_{xx}, is

$$\begin{aligned}
\tau_{xx} &= c_{11}\left(\frac{\partial u_x}{\partial x} + \frac{\partial u_y}{\partial y}\right) - 2c_{66}\frac{\partial u_y}{\partial y} + c_{13}\frac{\partial u_z}{\partial z} \\
&= -\frac{c_{11}S_a}{\nu_a}\frac{x - x'}{R_a^3} + \frac{2c_{66}S_a}{\nu_a}\left(\frac{x - x'}{R_a D_a^2} - \frac{(x - x')(y - y')^2}{D_a^2 R_a^3} - \frac{2(x - x')(y - y')^2}{R_a^2 D_a^3}\right) \\
&\quad + \frac{c_{11}S_b}{\nu_b}\frac{x - x'}{R_b^3} - \frac{2c_{66}S_b}{\nu_b}\left(\frac{x - x'}{R_b D_b^2} - \frac{(x - x')(y - y')^2}{D_b^2 R_b^3} - \frac{2(x - x')(y - y')^2}{R_b^2 D_b^3}\right) \\
&\quad - \frac{\nu_g}{2\pi}\left(\frac{x - x'}{R_g D_g^2} - \frac{(x - x')(y - y')^2}{D_g^2 R_g^3} - \frac{2(x - x')(y - y')^2}{R_g^2 D_g^3}\right) \\
&\quad + c_{13}S_c\left(\frac{\nu_b(x - x')}{R_b^3} - \frac{\nu_a(x - x')}{R_a^3}\right).
\end{aligned} \tag{2.97}$$

Similarly, integrating τ_{xx} over a small half ellipsoidal surface results in $-1/2$. This is so because integration of the second, the fourth, the fifth and the last term is zero, as shown in Appendix A, while integration of the first and third term is the same as in τ_{xz} for the vertical force.

2.7 Conclusions

The dynamic and static Green's functions have been obtained by solving the wave and equilibrium equations with general sources in a transversely isotropic elastic medium. The two Green's functions are shown to have a single dyadic form expressed through three scalars: g for the SH wave, ϕ for the $P - SV$ waves, and ψ for $P - SV - SH$ waves. In deriving these functions, the 2-D inverse Laplacian operator is removed to obtain a simplified and numerically feasible expression for the Green's functions. The final result is valid for arbitrary sources at arbitrary locations. This is particularly important to the BEM implementation of wave propagation and scattering problems.

The dynamic Green's function is applied to obtain a simple analytical expression for the displacements produced by three point sources. Evaluations of these displacements show agreement with previous numerical studies. The singular contribution, when integrating stresses over a half elliptical surface at the limit of the receiver coinciding with the source, is shown to be negative one-half of the applied force. The results of this chapter are directly applicable to the later BEM implementation.

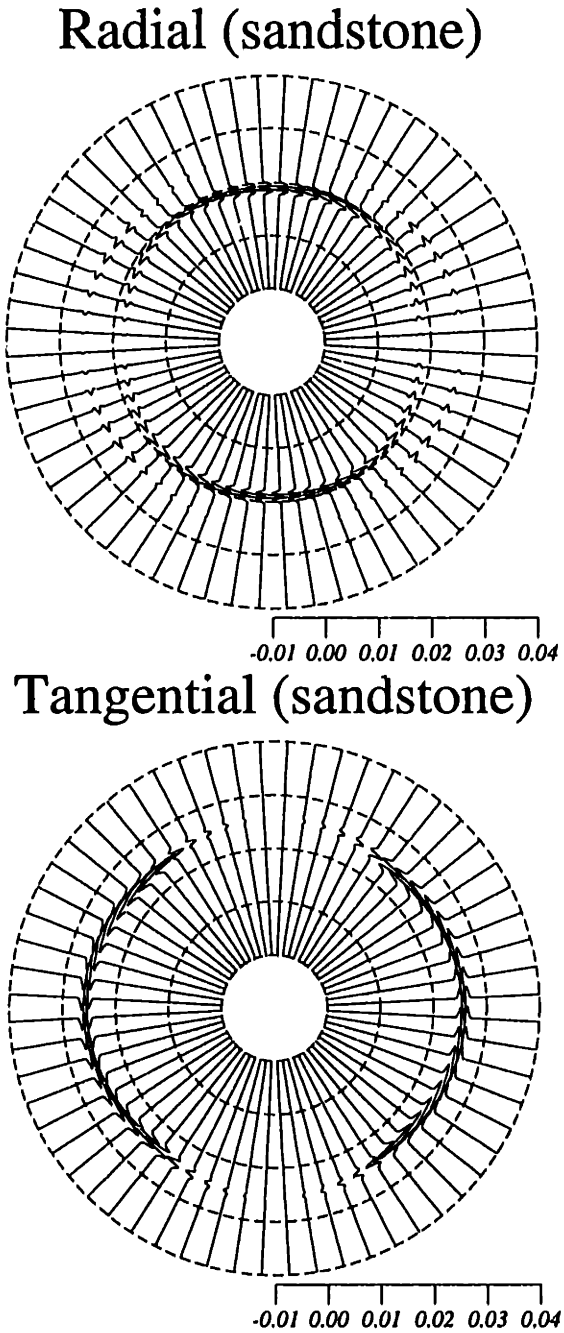

Figure 2-1: Radial and tangential components of the displacement produced by a point force along symmetry axis (vertical) in a slightly anisotropic medium: Mesaverde Sandstone. Wave amplitudes are normalized to the same scale. Receivers are 75 m away and time is in seconds.

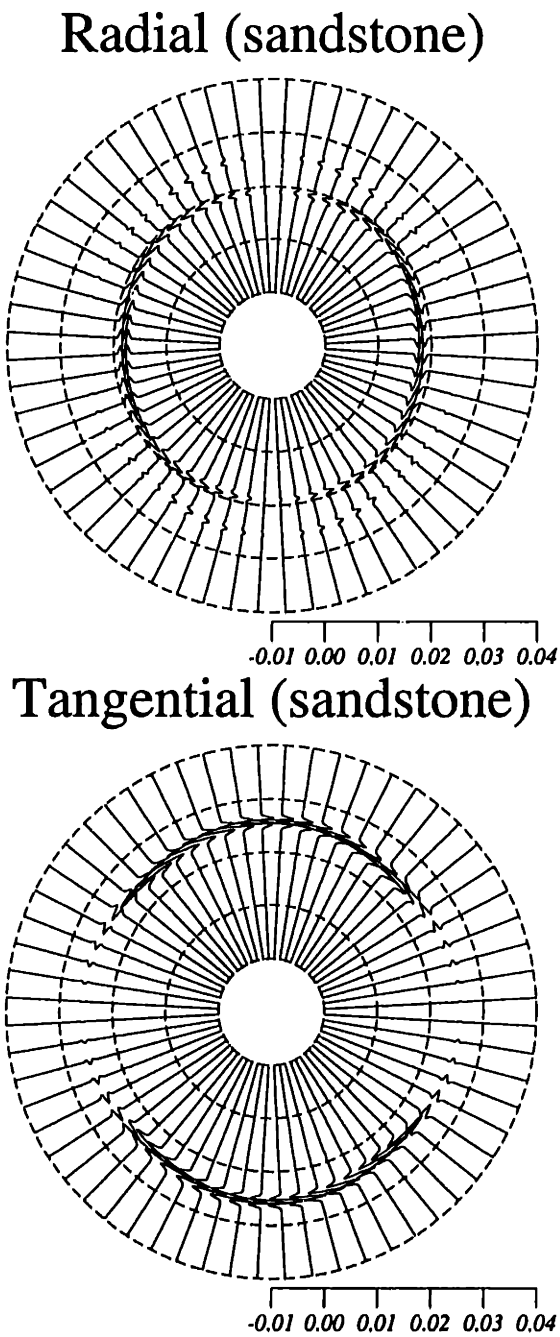

Figure 2-2: The radial and tangential components of the displacement produced by a point force along the isotropic plane (horizontal) in Mesaverde Sandstone. Receivers are 75 m away at 45° azimuth angle from the force direction.

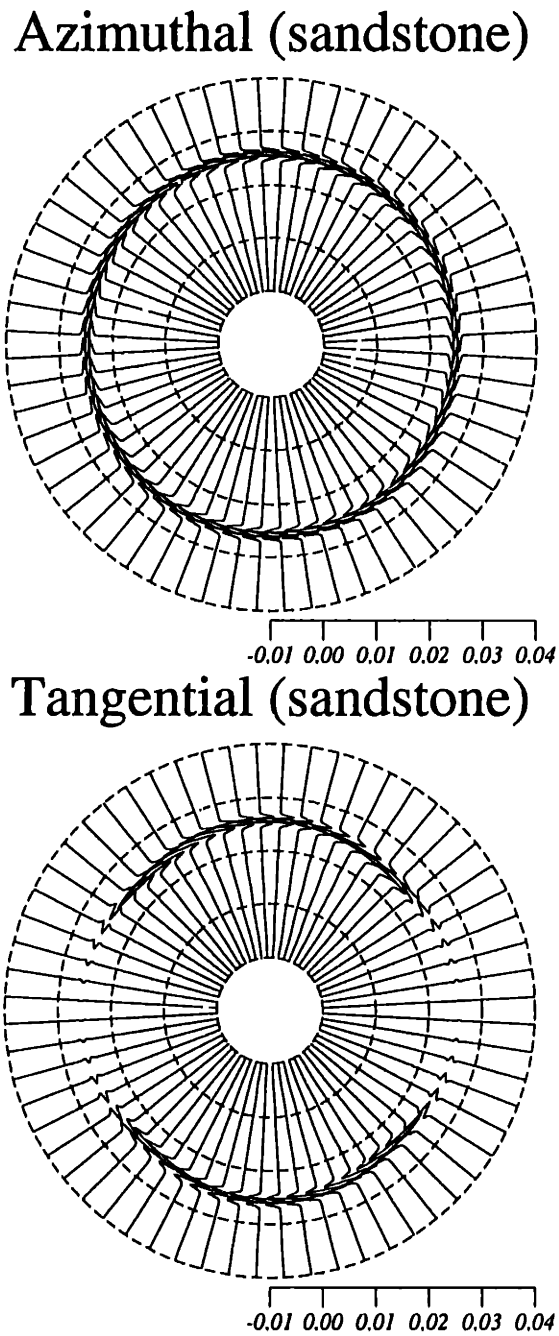

Figure 2-3: The azimuthal (SH wave) and tangential components of the displacement produced by a point force along the isotropic plane (horizontal) in Mesaverde Sandstone. Same receiver position as Figure 2-2.

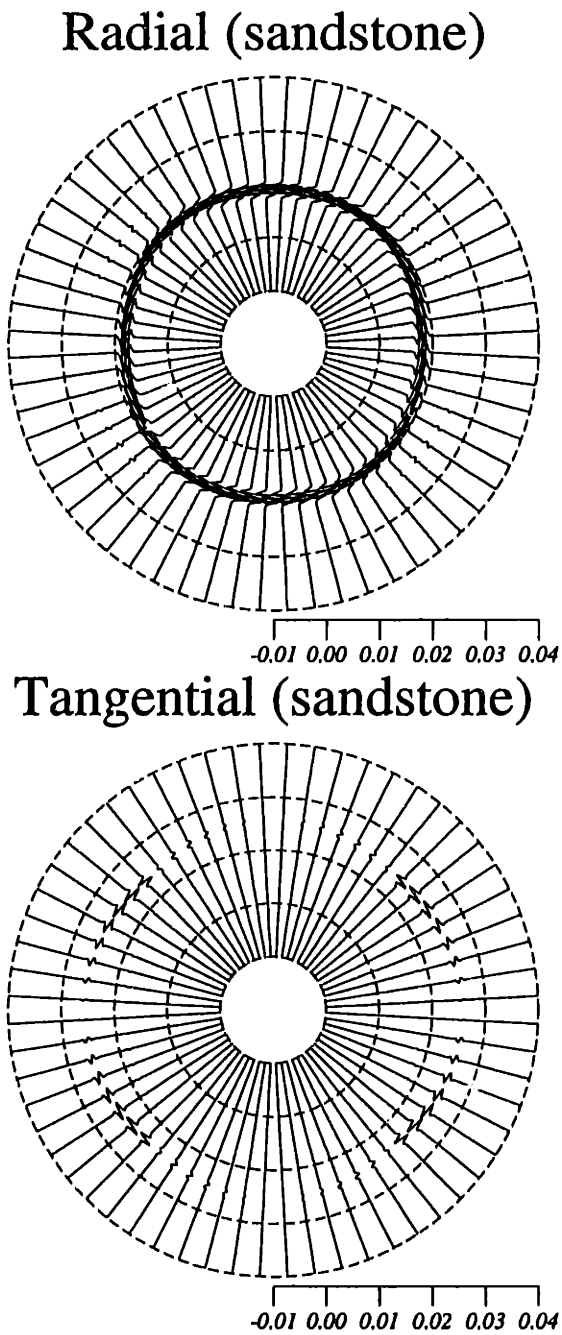

Figure 2-4: The radial and tangential components of the displacement produced by an explosion in Mesaverde Sandstone.

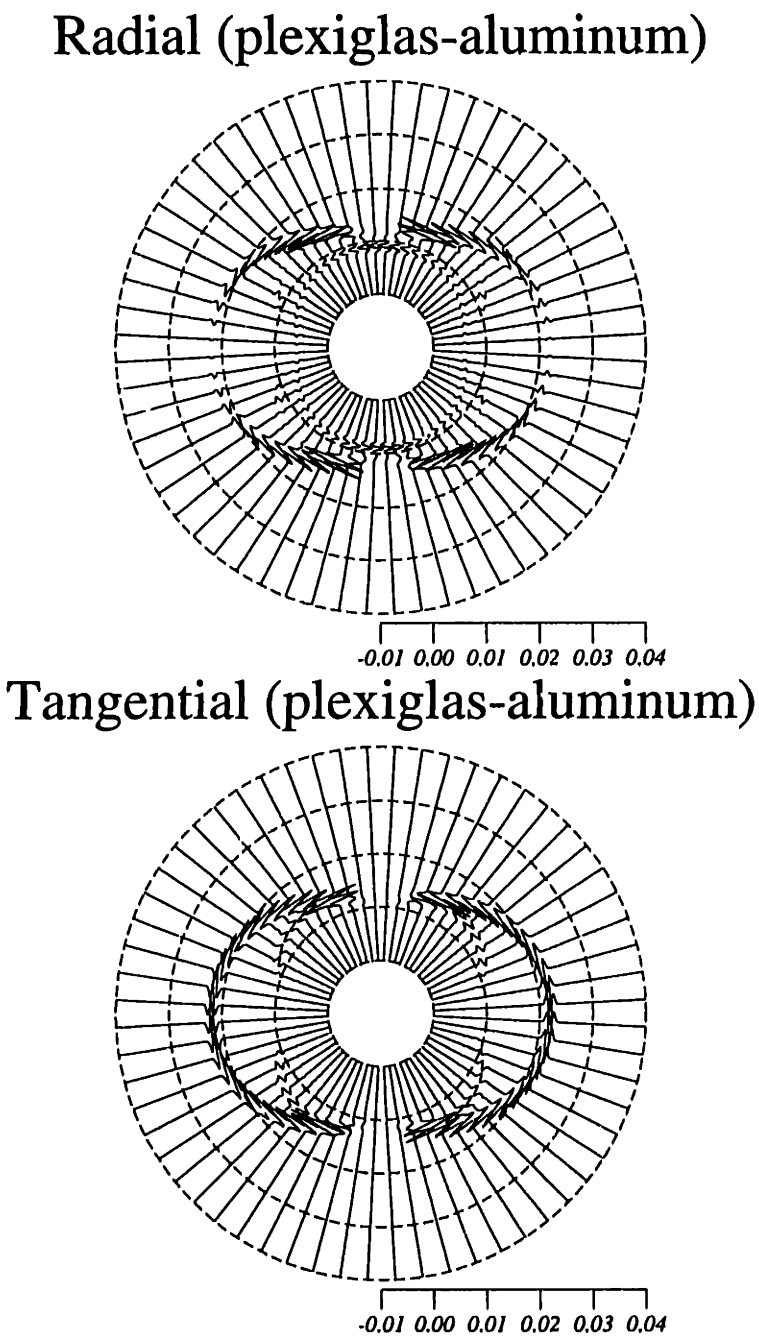

Figure 2-5: The radial and tangential components of the displacement produced by a point force along the symmetry axis (vertical) in a highly anisotropic medium: Plexiglas-aluminum. Receivers are 30 m away from the source.

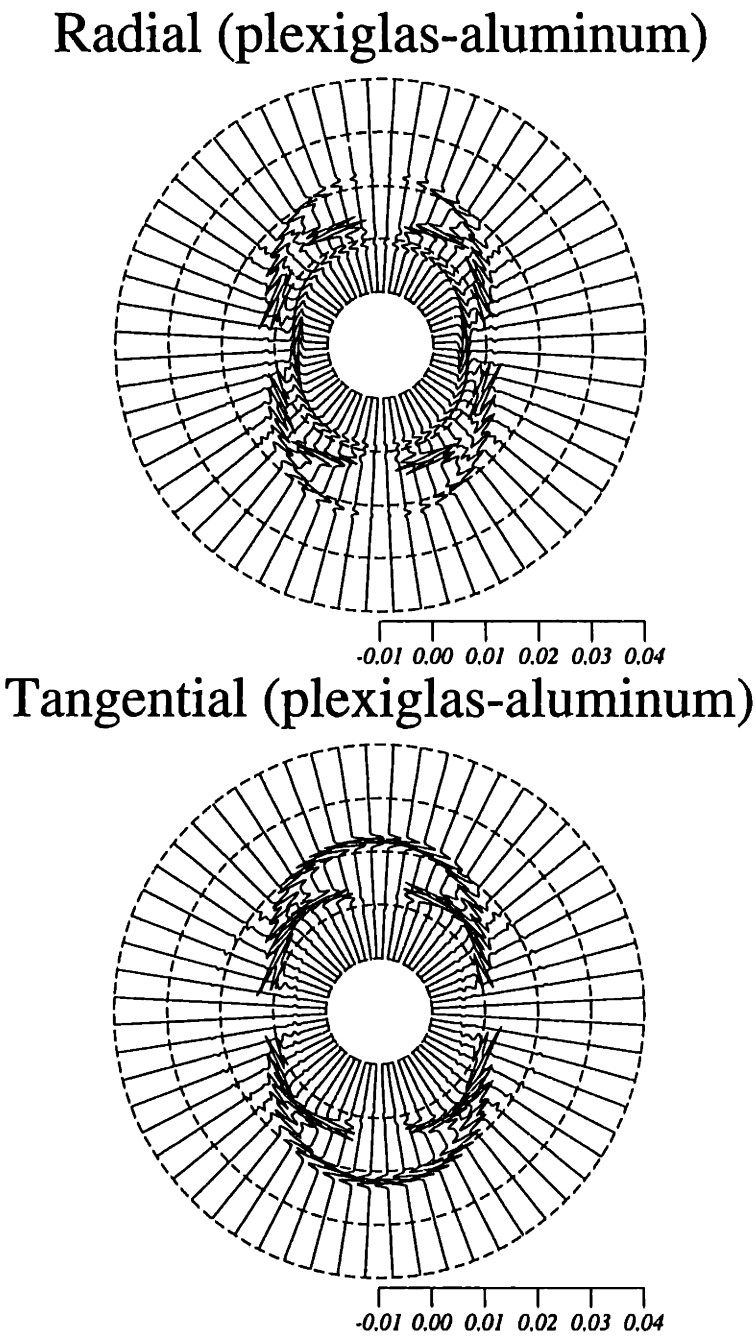

Figure 2-6: The radial and tangential components of the displacement produced by a point force along the isotropic plane (horizontal) in plexiglas-aluminum. Receivers are 30 m away at 45^o azimuth angle from the force direction.

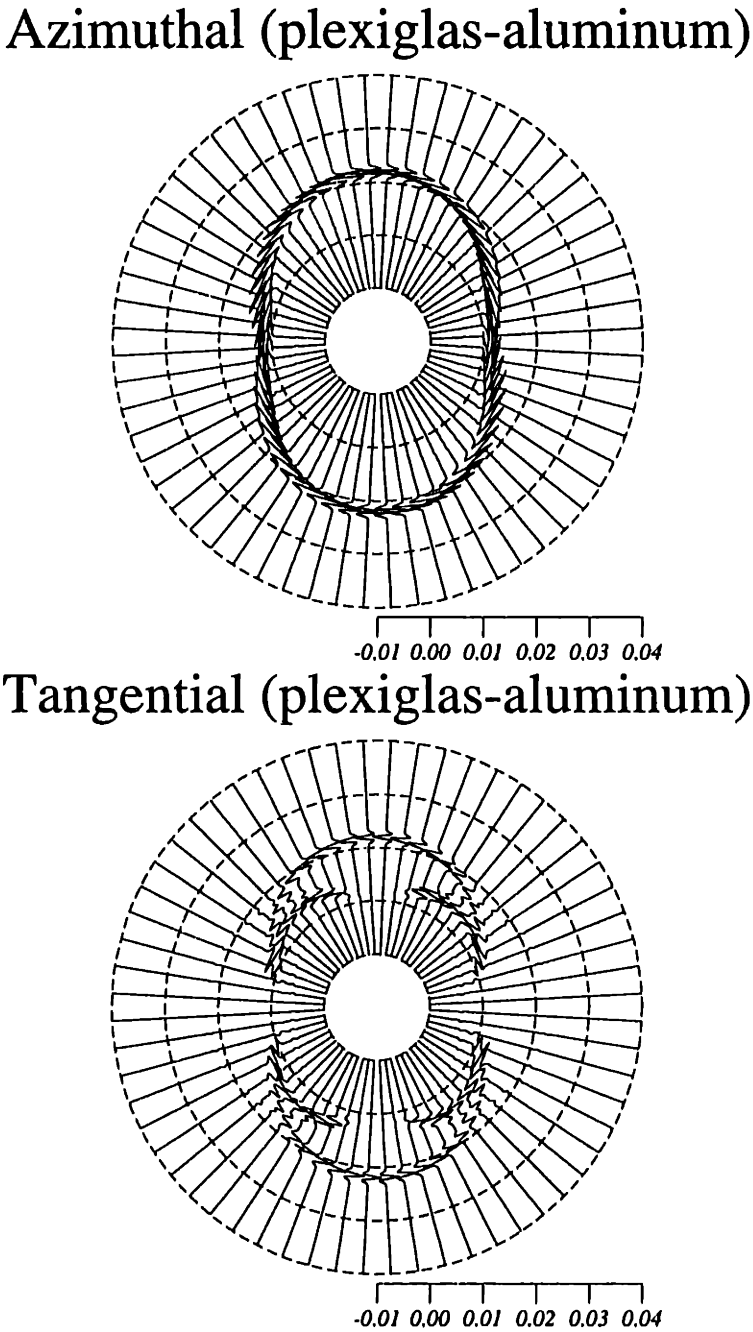

Figure 2-7: The azimuthal (SH wave) and tangential components of the displacement produced by a point force along the isotropic plane (horizontal) in plexiglas-aluminum. Same receiver position as Figure 2-6.

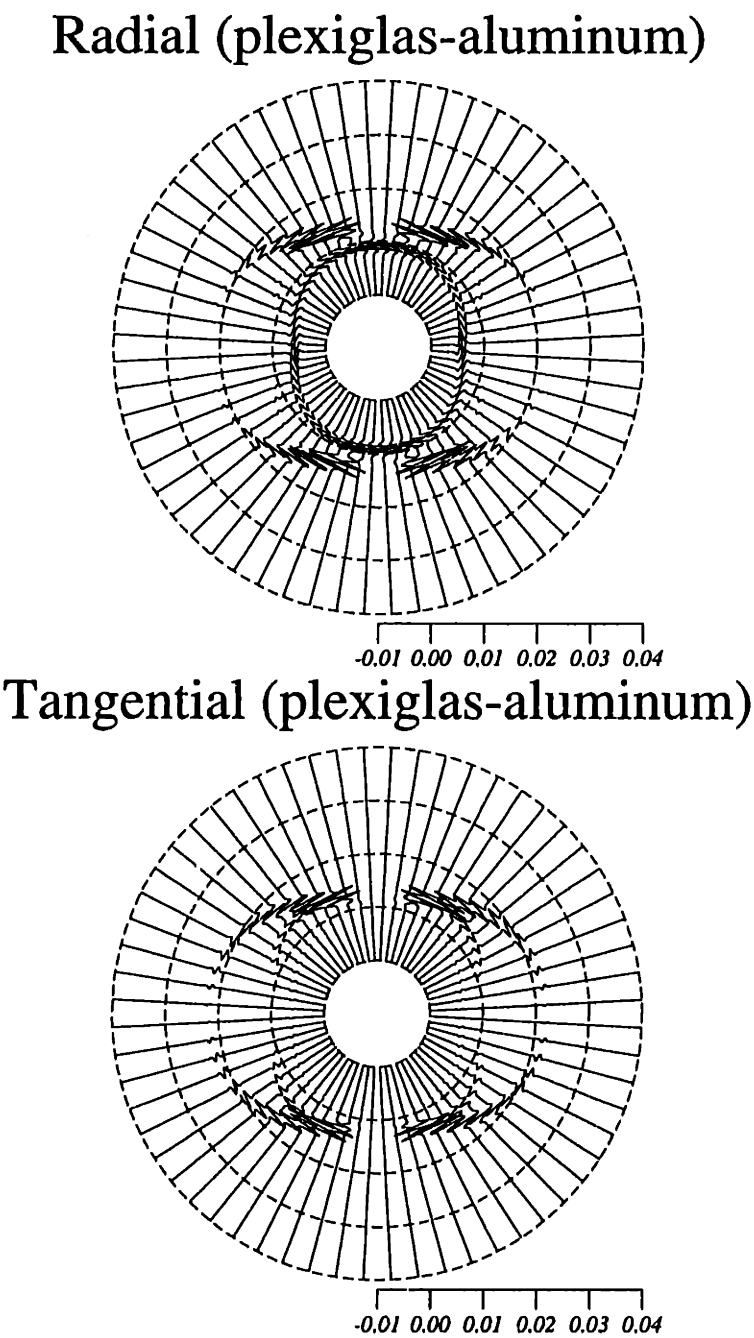

Figure 2-8: The radial and tangential components of the displacement produced by an explosion in Plexiglas-aluminum.

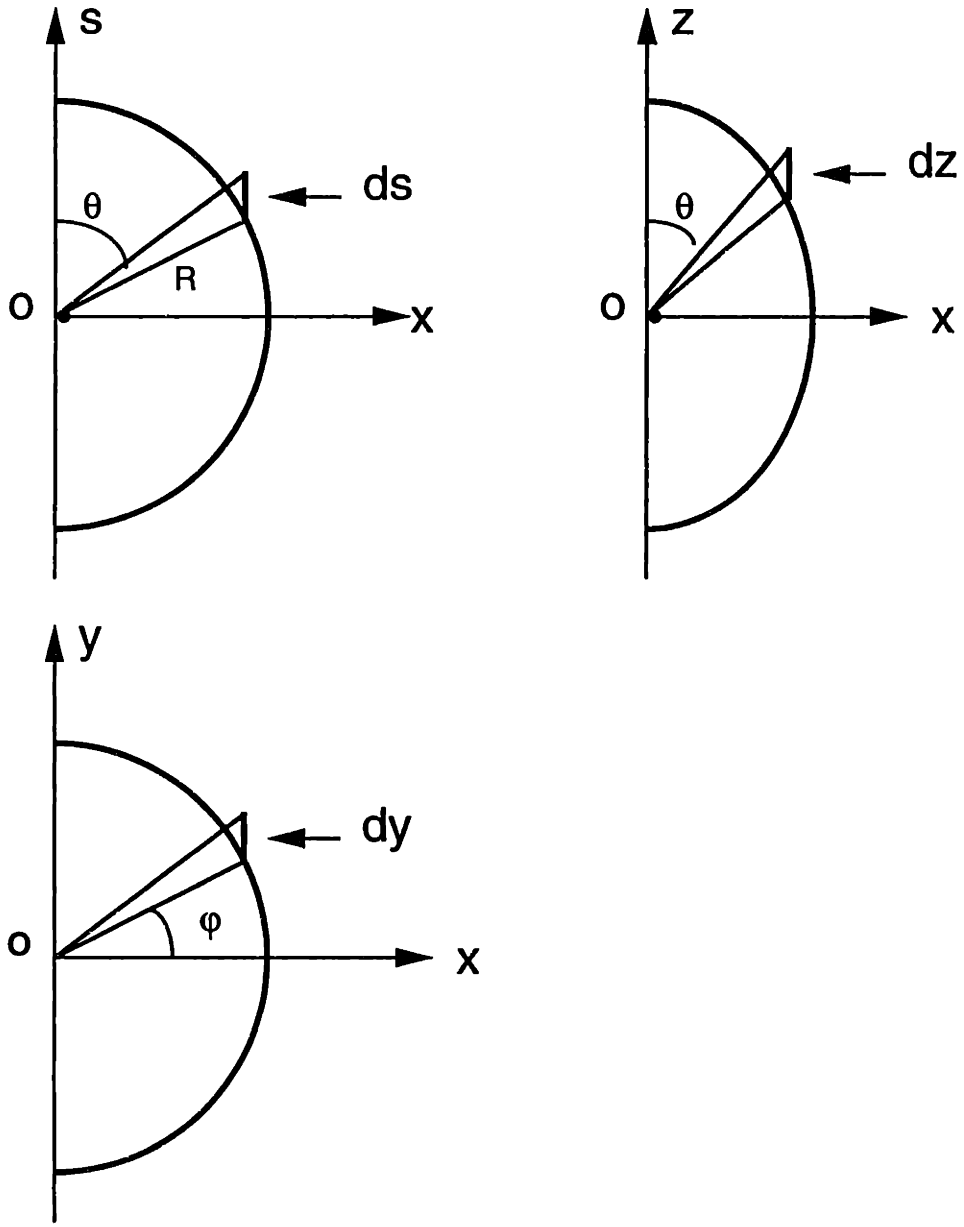

Figure 2-9: The geometry of the differential surfaces used in evaluating the singular contribution of surface integration of Green's functions.

Chapter 3

Borehole Seismic Source Radiation Pattern in Transversely Isotropic Media

3.1 Introduction

Elastic anisotropy in sedimentary rocks has long been observed and studied by many researchers. The causes for this anisotropy have generally been classified into three categories: fine layering, oriented minerals, and oriented micro- and macro-cracks due to regional stress. The anisotropic effect of periodic or fine lamination of isotropic layers has been thoroughly studied (e.g., Backus, 1962). Fine layering results in an overall transversely isotropic (TI) medium. Oriented vertical cracks in the rock produce azimuthal anisotropy or vertical transverse-isotropy (VTI) (e.g., Crampin, 1984). Regional stress acting on isotropic rocks causes anisotropy because of the closing of cracks (Nur and Simmons, 1969; Lo *et al.*, 1986; Gibson and Toksöz, 1990). The analysis and application of anisotropy in exploration seismology have been described by Crampin (1985), Thomsen (1986), Winterstein (1986), Larner (1993), Larner and Cohen (1993), Robertson and Corrigan (1983), White and Tongtaow (1981), and

Schmitt (1989), among others. Theoretical studies of wave propagation and radiation from seismic sources can be found in Buchwald (1959), Fedorov (1968), Takeuchi and Saito (1972), Ben-Menahem and Sena (1990).

Recently, anisotropy (either TI or VTI) has been included in the traveltime and wave equation based crosshole tomography techniques (e.g., Pratt and Chapman, 1992). In order to pick accurate traveltimes for the P and S waves, a good understanding of the source radiation patterns is required. This is especially true for the wave equation based tomography technique, since full wave effects are involved in the process. Through the work of Heelan (1953), White and Sengbush (1963), Lee and Balch (1982), Meredith (1990), Winbow (1991), and Gibson (1993), researchers have become aware that when seismic sources are placed inside an empty, fluid-filled, open, or cased borehole, their radiation patterns are dramatically affected by the borehole. These studies refer to the borehole in isotropic media only. To the best of our knowledge, no studies on borehole source radiation patterns in anisotropic media have been published as yet.

Therefore, it is the purpose of this chapter to consider the anisotropy effect on borehole source radiation patterns. Analytical radiation patterns are obtained for three typical downhole sources (Figure 3-1-a): an *explosion* or *volume* source to simulate an air gun or dynamite, a *vertical* source to resemble a wall-clamped vertical vibrator, and a *radial* source to model a bender source or a cavity resonator. These radiation patterns result from the asymptotic evaluation of the displacement integrals for the three sources. The displacement integrals are the results of matching boundary conditions between the borehole fluid and the TI formation.

3.2 Displacement Potentials in TI Media

Displacement potentials for an isotropic solid, as given by many authors, are the general solutions of homogeneous scalar wave equations satisfied by the P and S

potentials. Obviously, these potentials will not satisfy the wave equation in a TI medium. However, similar potentials in the TI medium are desirable because they can be used to determine the reflection and transmission coefficients at a cylindrical interface. These coefficients in turn can be used to study analytically the radiation from borehole sources. Without explaining in detail, White and Tongtaow (1981) gave the potentials as (translated to the notation of this thesis)

$$\phi = \frac{1}{2\pi}\int_{-\infty}^{\infty}[A_o K_0(\xi_a r) + b' B_o K_0(\xi_b r)]e^{ik_z(z-z')}dk_z, \tag{3.1}$$

$$\psi = \frac{1}{2\pi}\int_{-\infty}^{\infty}[a' A_o K_1(\xi_a r) + B_o K_1(\xi_b r)]e^{ik_z(z-z')}dk_z, \tag{3.2}$$

where, ϕ is the P-wave potential and ψ the S-wave potential. K_0 and K_1 are modified Bessel functions; r and z are the radial and vertical coordinates and k_z is the vertical wave number. The amplitudes of the outgoing P and S waves are A_o and B_o. Coefficients a' and b' are given as

$$a' = \frac{-\xi_a}{ik_z}\left(\frac{(c_{13}+2c_{44})k_z^2 - c_{11}\xi_a^2 - \rho\omega^2}{c_{44}k_z^2 - (c_{11}-c_{13}-c_{44})\xi_a^2 - \rho\omega^2}\right) \tag{3.3}$$

$$b' = \frac{-ik_z}{\xi_b}\left(\frac{c_{44}k_z^2 - (c_{11}-c_{13}-c_{44})\xi_b^2 - \rho\omega^2}{(c_{13}+2c_{44})k_z^2 - c_{11}\xi_b^2 - \rho\omega^2}\right). \tag{3.4}$$

In all the above, c_{ij} are the elastic constants, and ξ_a and ξ_b are the horizontal wave numbers corresponding to the *quasi-P* and *quasi-S* waves, respectively. They are the two solutions of the equation (see Equation 2.18)

$$\begin{aligned} c_{11}c_{44}\xi^4 &- [(c_{11}c_{33} - c_{13}^2 - 2c_{13}c_{44})k_z^2 - (c_{11}+c_{44})\rho\omega^2]\xi^2 \\ &+ (c_{44}k_z^2 - \rho\omega^2)(c_{33}k_z^2 - \rho\omega^2) = 0. \end{aligned} \tag{3.5}$$

In the isotropic limit, $a' = 0$ and $b' = 0$. The potentials reduce to those of an isotropic medium. Since the derivation of the coefficients a' and b' are of significant importance in understanding the coupling between the longitudinal particle motion and the transverse particle motion, two different solution methods are presented in the following. Tongtaow's approach is described first. Then an approach based on the Green's function results is presented. The latter is physically more meaningful.

3.2.1 Tongtaow's approach

There are in general three potentials for an isotropic medium (Morse and Feshbach, 1953). The potentials in a TI medium is at first assumed to have the same form as the three potentials satisfying the scalar wave equations in an isotropic solid. When these potentials are substituted into the wave equation for the TI medium, three equations for three unknown potential amplitudes yield. To have non-zero potential amplitudes, the determinant of the coefficient matrix is set to zero. This in turn yields three characteristic wave numbers for *quasi-P*, *quasi-SV*, and SH waves (see Chapter 1). Since the SH wave is decoupled from the rest, only the $P-SV$ part is needed to determine the coupling coefficient. The most general solutions for the potentials are the combination of waves with the *quasi-P* and *quasi-SV* wavenumbers. The combination factors are then obtained by substituting these general expressions back into the wave equation. Therefore, a formidable amount of algebra is involved in this approach. For detail, consult Tongtaow (1980) or Ellefsen (1990), or Schmitt (1989) for a TI poroelastic medium.

3.2.2 A Green's function approach

The coupling coefficients can also be obtained by using the previous results of Green's functions. To comply with the notation used above, we first need to express the dynamic Green's function using the modified Bessel functions. The dyadic form of the Green's function remains unchanged, while the three scalars have different form. Using the Bessel function relationships, we obtain

$$g = \frac{-1}{4\pi^2 c_{44}} \int_0^\infty K_0(\xi_c D) e^{ik_z(z-z')} dk_z \tag{3.6}$$

$$\phi = \frac{-1}{4\pi^2 c_{11} c_{44}} \int_0^\infty \frac{K_0(\xi_b D) - K_0(\xi_a D)}{\xi_b^2 - \xi_a^2} e^{ik_z(z-z')} dk_z \tag{3.7}$$

$$\psi = \frac{-1}{4\pi^2} \int_0^\infty \left[T_b' K_0(\xi_b D) - T_a' K_0(\xi_a D) - T_c' K_0(\xi_c D)\right] e^{ik_z(z-z')} dk_z \tag{3.8}$$

where,

$$T'_a = \frac{(c_{13}+c_{44})^2 k_z^2}{c_{11}c_{44}(c_{11}\xi_a^2 - c_{44}k_z^2 - \rho\omega^2)(\xi_b^2 - \xi_a^2)} \tag{3.9}$$

$$T'_b = \frac{(c_{13}+c_{44})^2 k_z^2}{c_{11}c_{44}(c_{11}\xi_b^2 - c_{44}k_z^2 - \rho\omega^2)(\xi_b^2 - \xi_a^2)} \tag{3.10}$$

$$T'_c = \frac{c_{11}-c_{66}}{c_{44}(\xi_z^2 - \xi_c^2)} = \frac{-c_{11}c_{66}}{c_{44}(\rho\omega^2 - c_{44}k_z^2)}. \tag{3.11}$$

In the above, $\xi_z^2 = (\rho\omega^2 - c_{44}k_z^2)/c_{11}$ and $\xi_c^2 = (\rho\omega^2 - c_{44}k_z^2)/c_{66}$.

From the above definition and the dyadic form of the Green's function, the displacement field due to a vertical point force in TI medium is

$$U_r = \frac{c_{13}+c_{44}}{4\pi^2 c_{11}c_{44}} \int_{-\infty}^{+\infty} \frac{ik_z}{\xi_b^2 - \xi_a^2} \left[\xi_a K_1(\xi_a r) - \xi_b K_1(\xi_b r)\right] e^{ik_z(z-z')} dk_z \tag{3.12}$$

$$U_z = \int_{-\infty}^{\infty} \left[\frac{c_{11}\xi_a^2 - c_{44}k_z^2 + \rho\omega^2}{4\pi^2 c_{11}c_{44}(\xi_b^2 - \xi_a^2)} K_0(\xi_a r) - \frac{c_{11}\xi_b^2 - c_{44}k_z^2 + \rho\omega^2}{4\pi^2 c_{11}c_{44}(\xi_b^2 - \xi_a^2)} K_0(\xi_b r)\right] e^{ik_z(z-z')} dk_z \tag{3.13}$$

The divergence and curl of the displacement field are

$$\begin{aligned}\nabla \cdot \mathbf{U} = & \int_{-\infty}^{\infty} \frac{c_{44}k_z^2 - (c_{11}-c_{13}-c_{44})\xi_b^2 - \rho\omega^2}{4\pi^2 c_{11}c_{44}(\xi_b^2 - \xi_a^2)} ik_z K_0(\xi_b r) e^{ik_z(z-z')} dk_z \\ & - \int_{-\infty}^{\infty} \frac{c_{44}k_z^2 - (c_{11}-c_{13}-c_{44})\xi_a^2 - \rho\omega^2}{4\pi^2 c_{11}c_{44}(\xi_b^2 - \xi_a^2)} ik_z K_0(\xi_a r) e^{ik_z(z-z')} dk_z \end{aligned} \tag{3.14}$$

$$\begin{aligned}-\nabla \times \mathbf{U} = & -\int_{-\infty}^{\infty} \frac{(c_{13}+2c_{44})k_z^2 - c_{11}\xi_b^2 - \rho\omega^2}{4\pi^2 c_{11}c_{44}(\xi_b^2 - \xi_a^2)} \xi_b K_0(\xi_b r) e^{ik_z(z-z')} dk_z \\ & + \int_{-\infty}^{\infty} \frac{(c_{13}+2c_{44})k_z^2 - c_{11}\xi_a^2 - \rho\omega^2}{4\pi^2 c_{11}c_{44}(\xi_b^2 - \xi_a^2)} \xi_a K_0(\xi_a r) e^{ik_z(z-z')} dk_z \end{aligned} \tag{3.15}$$

Since divergence and curl (minus sign to account for the direction of the vector potential) of the displacement are proportional to the dilatational and rotational potentials, the above results display the contribution of *quasi-P* and *quasi-S* to each of these potentials. If the *quasi-P* part of the dilational potential is measured to be A_o, its contribution to the rotational potential is A_o multiplied by the ratio between the *quasi-S* part of the rotational potential and the *quasi-P* part of the dilational potential. This ratio is exactly the coupling coefficient a', as defined in Equation 3.3. Similarly, if the the *quasi-S* part of the rotational potential is B_o, its contribution

to the dilational potential is just $b'B_o$. b' is exactly the ratio between the S part (subscript b) in $\nabla \cdot \mathbf{U}$ and the P part in $-\nabla \times \mathbf{U}$. It is defined in Equation 3.4.

In comparison, the Green's function approach reveals the physical meaning of these coupling coefficients better. Moreover, not much algebra is involved in getting the final results. Though the above analysis is based on the vertical point force (the simplest!) results, the conclusion stays the same for other sources. The dilational and rotational potentials given in (3.1) and (3.2) only contain the outgoing part. The coupling coefficients for the incoming potentials remain the same. Therefore, the most general displacement potentials in a TI medium are

$$\phi = \frac{1}{2\pi}\int_{-\infty}^{\infty}[A_s I_0(\xi_a r) + A_o K_0(\xi_a r) + b' B_s I_0(\xi_b r) + b' B_o K_0(\xi_b r)]e^{ik_z(z-z')}dk_z \quad (3.16)$$

$$\psi = \frac{1}{2\pi}\int_{-\infty}^{\infty}[a' A_s I_1(\xi_a r) + a' A_o K_1(\xi_a r) + B_s I_1(\xi_b r) + B_o K_1(\xi_b r)]e^{ik_z(z-z')}dk_z \quad (3.17)$$

The convention here is that A_s, A_o, ξ_a are for *quasi-P* waves and B_s, B_o, ξ_b for *quasi-SV* waves. ξ_a and ξ_b are defined through ξ_a^2 and ξ_b^2, which are the two roots of Equation 3.5.

3.3 Displacement Integrals

A borehole with a radius r_0, filled with fluid of density ρ_f and of sound speed c_f, penetrates along the symmetry axis a transversely isotropic (TI) elastic formation specified by its density and five elastic constants: ρ, c_{11}, c_{33}, c_{13}, c_{44}, and c_{66} (Figure 3-1-b). The displacements of radiated waves in the formation can be obtained by considering the displacement potentials of the fluid and the TI formation. In cylindrical coordinates and in the frequency domain, the displacement potential for the fluid has the following well-known form

$$\phi_f = \frac{1}{2\pi}\int_{-\infty}^{\infty}[C_s I_0(\xi_f r) + C_o K_0(\xi_f r)]e^{ik_z(z-z')}dk_z, \quad (3.18)$$

where, k_z is the vertical wave number and $\xi_f = \sqrt{k_z^2 - \omega^2/c_f^2}$. The depth of a source is at z'. I_0 and K_0 are the modified Bessel functions of the first and the second kind

and of order 0. The coefficients C_s and C_o are the potential amplitude of the standing (incoming) and outgoing waves, respectively.

From the displacement potentials in Equations (3.16) and (3.17), the displacement-stress vectors (k_z integral is omitted at the moment) in the TI solid and the fluid are

$$(u_r, u_z, \tau_{rr}, \tau_{rz})^T = S(r)(A_s, B_s, A_o, B_o)^T, \quad (u_r, u_z, \tau_{rr}, \tau_{rz})^T = F(r)(C_s, C_o)^T. \tag{3.19}$$

The elements of the $S(r)$ matrix in a TI medium are

$$\begin{aligned}
S_{11} &= (\xi_a - ik_z a')I_1(\xi_a r) \\
S_{12} &= (\xi_b b' - ik_z)I_1(\xi_b r) \\
S_{13} &= -(\xi_a + ik_z a')K_1(\xi_a r) \\
S_{14} &= -(\xi_b b' + ik_z)K_1(\xi_b r) \\
S_{21} &= (\xi_a a' + ik_z)I_0(\xi_a r) \\
S_{22} &= (\xi_b + ik_z b')I_0(\xi_b r) \\
S_{23} &= -(\xi_a a' - ik_z)K_0(\xi_a r) \\
S_{24} &= -(\xi_b - ik_z b')K_0(\xi_b r) \\
S_{31} &= [(c_{11}\xi_a^2 - c_{13}k_z^2) - (c_{11} - c_{13})ik_z\xi_a a']I_0(\xi_a r) - 2c_{66}(\xi_a - ik_z a')I_1(\xi_a r)/r \\
S_{32} &= [(c_{11}\xi_b^2 - c_{13}k_z^2)b' - (c_{11} - c_{13})ik_z\xi_b]I_0(\xi_b r) - 2c_{66}(\xi_b b' - ik_z)I_1(\xi_b r)/r \\
S_{33} &= [(c_{11}\xi_a^2 - c_{13}k_z^2) + (c_{11} - c_{13})ik_z\xi_a a']K_0(\xi_a r) + 2c_{66}(\xi_a + ik_z a')K_1(\xi_a r)/r \\
S_{34} &= [(c_{11}\xi_b^2 - c_{13}k_z^2)b' + (c_{11} - c_{13})ik_z\xi_b]K_0(\xi_b r) + 2c_{66}(\xi_b b' + ik_z)K_1(\xi_b r)/r \\
S_{41} &= c_{44}[(\xi_a^2 + k_z^2)a' + 2ik_z\xi_a]I_1(\xi_a r) \\
S_{42} &= c_{44}[(\xi_b^2 + k_z^2) + 2ik_z\xi_b b']I_1(\xi_b r) \\
S_{43} &= c_{44}[(\xi_a^2 + k_z^2)a' - 2ik_z\xi_a]K_1(\xi_a r) \\
S_{44} &= c_{44}[(\xi_b^2 + k_z^2) - 2ik_z\xi_b b']K_1(\xi_b r).
\end{aligned} \tag{3.20}$$

The elements of matrix $F(r)$ for the fluid are

$$\begin{aligned} F_{11} &= \xi_f I_1(\xi_f r) & F_{12} &= -\xi_f K_1(\xi_f r) & F_{21} &= ik_z I_0(\xi_f r) & F_{22} &= ik_z K_0(\xi_f r) \\ F_{31} &= -\rho_f \omega^2 I_0(\xi_f r) & F_{32} &= -\rho_f \omega^2 K_0(\xi_f r) & F_{41} &= 0 & F_{42} &= 0. \end{aligned} \tag{3.21}$$

For an interface at $r = r_0$ between a fluid column ($r < r_0$) and an elastic formation ($r > r_0$), the following equations hold (See Figure 3-1-c)

$$\begin{bmatrix} A_s \\ B_s \\ A_o \\ B_o \end{bmatrix} = \begin{bmatrix} 1 & 0 & 0 \\ 0 & 1 & 0 \\ R^i_{pp} & R^i_{sp} & T^o_{pp} \\ R^i_{ps} & R^i_{ss} & T^o_{ps} \end{bmatrix} \begin{bmatrix} A_s \\ B_s \\ C_o \end{bmatrix}, \tag{3.22}$$

$$\begin{bmatrix} C_s \\ C_o \end{bmatrix} = \begin{bmatrix} T^i_{pp} & T^i_{sp} & R^o_{pp} \\ 0 & 0 & 1 \end{bmatrix} \begin{bmatrix} A_s \\ B_s \\ C_o \end{bmatrix}. \tag{3.23}$$

The above equations simply state that outgoing P and S waves in the formation result from the reflection of incoming P and S waves in the formation, plus the transmission of an outgoing P wave in the fluid. An incoming P wave in the fluid is the consequence of an outgoing P wave reflection and an incoming P and S wave transmission. Substituting Equations (3.22) and (3.23) into Equation 3.19 and applying the three boundary conditions for a fluid and elastic medium interface, we obtain the transmission coefficients at the borehole wall for a volume point source in the fluid:

$$T^o_{pp} = \frac{S_{44}\rho_f\omega^2/r_0}{DET}, \quad T^o_{ps} = \frac{-S_{43}\rho_f\omega^2/r_0}{DET}, \tag{3.24}$$

where, DET stands for the common denominator

$$DET = F_{11}(S_{43}S_{34} - S_{33}S_{44}) + F_{31}(S_{13}S_{44} - S_{14}S_{43}).$$

For axial and radial sources of length $2l$, the potential amplitudes in the TI formation are

$$A^v_o = \frac{F_{11}S_{34} - F_{31}S_{14}}{DET}F(k_z), \quad B^v_o = \frac{F_{31}S_{13} - F_{11}S_{33}}{DET}F(k_z); \tag{3.25}$$

$$A_o^r = \frac{-F_{11}S_{44}F(k_z)}{DET}, \quad B_o^r = \frac{F_{11}S_{43}F(k_z)}{DET}, \tag{3.26}$$

where, $F(k_z) = 2l\,\mathrm{sinc}(k_z l)$. Coefficients in Equation 3.25 and Equation 3.26 are similar to those of Lee and Balch (1982) and Meredith (1990). Thus, written in compact forms, the outgoing wave displacements produced by these sources at position (r, z) in the formation are

$$\begin{matrix} U_r^e \\ U_r^v \\ U_r^r \end{matrix} = \frac{-1}{2\pi}\int_{-\infty}^{\infty} \left[(\xi_a + ik_z a') \begin{matrix} T_{pp}^o \\ A_o^v \\ A_o^r \end{matrix} K_1(\xi_a r) + (\xi_b b' + ik_z) \begin{matrix} T_{ps}^o \\ B_o^v \\ B_o^r \end{matrix} K_1(\xi_b r)\right] e^{ik_z(z-z_s)} dk_z \tag{3.27}$$

$$\begin{matrix} U_z^e \\ U_z^v \\ U_z^r \end{matrix} = \frac{-1}{2\pi}\int_{-\infty}^{\infty} \left[(\xi_a a' - ik_z) \begin{matrix} T_{pp}^o \\ A_o^v \\ A_o^r \end{matrix} K_0(\xi_a r) + (\xi_b - ik_z b') \begin{matrix} T_{ps}^o \\ B_o^v \\ B_o^r \end{matrix} K_0(\xi_b r)\right] e^{ik_z(z-z_s)} dk_z \tag{3.28}$$

Superscripts e, v, and r represent the explosive, vertical, and radial sources, respectively. In the following, these displacement integrals are evaluated asymptotically and numerically to obtain the radiation patterns of the three sources.

3.4 Small and Large Argument Approximation

Before proceeding with the calculation, two assumptions that allow the asymptotic evaluation of the above integrals have to be in place. The first assumption is that the borehole radius is very small and the frequency concerned is relatively low such that small argument approximation for the modified Bessel functions is justified. This small argument approximation renders much simplified integrands so that the physics of the problem are revealed without an explicit evaluation of these functions. The second assumption is that the observation point is far from the source so that the method of steepest descent (e.g. Bleistein, 1984) is employed to evaluate the k_z integral asymptotically.

If the arguments of the Bessel functions are small, i.e., if $\xi_a r_0$, $\xi_b r_0$, and $\xi_f r_0$ are

small, the Bessel functions can be approximated as follows:

$$I_0(z) \sim 1, \quad I_1(z) \sim \frac{z}{2}, \quad K_0(z) \sim -\ln z, \quad K_1(z) \sim \frac{1}{z}, \quad z \to 0. \tag{3.29}$$

Since $K_1(z)$ has a higher order singularity than $K_0(z)$ as $z \to 0$, $K_0(z)$ in S_{33} and S_{34} is much smaller when compared to $K_1(z)$ and can, therefore, be discarded. Then, the following simplification occurs for the denominator DET,

$$DET \sim \frac{c_{44}c_{66}}{\xi_a \xi_b r_0^2}\left(\xi_f^2 - \frac{\rho_f \omega^2}{c_{66}}\right)[\xi_a(k_z^2 - \xi_b^2) - ik_z\xi_b a'(\xi_b - ik_z b') + a'\xi_a^2(\xi_b b' + ik_z)]. \tag{3.30}$$

In the isotropic limit, $a' = b' = 0$, the above reduces to

$$DET \sim \left(\xi_f^2 - \frac{\rho_f \omega^2}{\mu}\right)\frac{\mu \rho \omega^2}{\xi_b r_0^2},$$

which is the same as in Lee and Balch (1982) and Meredith (1990), except for a factor of $\frac{-4}{\pi^2}$ resulting from the use of modified Bessel functions rather than Hankel functions.

In the isotropic case, it is obvious that $DET \sim 0$ when

$$\xi_f^2 - \frac{\rho_f \omega^2}{\mu} = 0 \Longleftrightarrow C_T = c_f\sqrt{\frac{\mu}{\mu + \rho_f c_f^2}}.$$

$C_T = \frac{\omega}{k_z}$ denotes the velocity of the tube wave propagating along the borehole; c_f is the speed of sound in the borehole fluid. Therefore, in the isotropic case, it is the shear modulus of the formation that determines the tube wave speed (the fluid sound speed does not change much). In the transversely isotropic case, the tube wave velocity is determined by

$$\xi_f^2 - \frac{\rho_f \omega^2}{c_{66}} = 0 \Longleftrightarrow C_T = c_f\sqrt{\frac{c_{66}}{c_{66} + \rho_f c_f^2}}.$$

That is, the speed of the tube wave is dictated by the elastic constant c_{66}. This observation is also given in White and Tongtaow (1981). Thus, the study of tube waves in a borehole penetrating a TI medium can provide a good estimate of the c_{66} constant. The sensitivity of the tube wave to this constant and others is studied in Ellefsen (1990) and Schmitt (1989).

Our concern here is not the study of the tube wave in detail. Rather, we are more interested in the mathematical property of the denominator DET, because the zeros of the denominator mean poles for the integrand of the k_z integrals. The locations of these poles are crucial to the correct evaluation of these integrals. As noted above, a tube wave arises from a pole of the integrand. One may ask if there is another zero for DET determined by the expressions in the square bracket. The answer can be reached by a further factorization of the inside expression using the definitions of a' and b'. Denoted by [], the inside expression is reduced to

$$[] = \frac{c_{11}(c_{13}+c_{44})\xi_a(k_z^2-\xi_b^2)(\xi_b^2-\xi_a^2)(k_z^2-\xi_a^2)}{[c_{44}k_z^2-(c_{11}-c_{13}-c_{44})\xi_a^2-\rho\omega^2][(c_{13}+2c_{44})k_z^2-c_{11}\xi_b^2-\rho\omega^2]}.$$

It is clear that the numerator of [] never vanishes. Therefore, the only possible pole for the integrands comes from the tube wave pole.

After calculating the numerator of A_o^v and B_o^v using the approximation in Equation 3.29, we find

$$F_{11}S_{34}-F_{31}S_{14} = \frac{c_{66}(\xi_b b'+ik_z)}{\xi_b r_0}\left(\xi_f^2-\frac{\rho_f\omega^2}{c_{66}}\right) \tag{3.31}$$

$$F_{31}S_{13}-F_{11}S_{33} = \frac{-c_{66}(\xi_a+ik_z a')}{\xi_a r_0}\left(\xi_f^2-\frac{\rho_f\omega^2}{c_{66}}\right). \tag{3.32}$$

As we have anticipated from the results of Winbow (1989) and Meredith (1990), the numerators for A_o^v and B_o^v for the vertical source contain the same tube wave factor as their denominators. As they cancel out, they leave no pole for the vertical source.

The far-field assumption (i.e., $\xi r \gg 1$) is used to approximate the Bessel functions of arguments $\xi_a r$ and $\xi_b r$ in the k_z integral. When z is large, both $K_0(z)$ and $K_1(z)$ have the following leading order approximation

$$K_0(z),\ \ K_1(z) \sim \sqrt{\frac{\pi}{2z}}e^{-z},\ \ \text{for } z \gg 1. \tag{3.33}$$

Using spherical coordinates (R,φ,θ), $r = R\sin\theta$, and $z - z_s = R\cos\theta$, where θ is measured from upright (positive z) vertical.

Putting all analysis together, the k_z integrals in Equation 3.27 and Equation 3.28 are

$$\begin{array}{lcl} U_r^e & & f_a^e(k_z) \\ U_r^v & = & \int_{-\infty}^{\infty} f_a^v(k_z)\ e^{R[ik_z\cos\theta-\xi_a\sin\theta]}dk_z + \int_{-\infty}^{\infty} f_b^v(k_z)\ e^{R[ik_z\cos\theta-\xi_b\sin\theta]}dk_z \\ U_r^r & & f_a^r(k_z) \end{array} \quad \begin{array}{l} f_b^e(k_z) \\ \\ f_b^r(k_z) \end{array} \tag{3.34}$$

$$\begin{array}{lcl} U_z^e & & g_a^e(k_z) \\ U_z^v & = & \int_{-\infty}^{\infty} g_a^v(k_z)\ e^{R[ik_z\cos\theta-\xi_a\sin\theta]}dk_z + \int_{-\infty}^{\infty} g_b^v(k_z)\ e^{R[ik_z\cos\theta-\xi_b\sin\theta]}dk_z \\ U_z^r & & g_a^r(k_z) \end{array} \quad \begin{array}{l} g_b^e(k_z) \\ \\ g_b^r(k_z) \end{array} \tag{3.35}$$

where the integrands are

$$\begin{aligned} f_a^e(k_z) &= \frac{\rho_f\omega^2\xi_a(c_{13}k_z^2+c_{11}\xi_b^2+\rho\omega^2)}{2c_{11}c_{66}(\xi_f^2-\rho_f\omega^2/c_{66})(\xi_b^2-\xi_a^2)\sqrt{2\pi\xi_a r}}, \\ f_b^e(k_z) &= \frac{-\rho_f\omega^2\xi_b(c_{13}k_z^2+c_{11}\xi_a^2+\rho\omega^2)}{2c_{11}c_{66}(\xi_f^2-\rho_f\omega^2/c_{66})(\xi_b^2-\xi_a^2)\sqrt{2\pi\xi_b r}}, \\ f_a^v(k_z) &= \frac{ik_z(c_{13}+c_{44})\xi_a r_0 F(k_z)}{2c_{11}c_{44}(\xi_b^2-\xi_a^2)\sqrt{2\pi\xi_a r}}, \\ f_b^v(k_z) &= \frac{-ik_z(c_{13}+c_{44})\xi_b r_0 F(k_z)}{2c_{11}c_{44}(\xi_b^2-\xi_a^2)\sqrt{2\pi\xi_b r}}, \\ f_a^r(k_z) &= -\frac{\xi_f^2 r_0^2 F(k_z)}{2\rho_f\omega^2} f_a^e(k_z), \\ f_b^r(k_z) &= -\frac{\xi_f^2 r_0^2 F(k_z)}{2\rho_f\omega^2} f_b^e(k_z), \\ g_a^e(k_z) &= \frac{-\rho_f\omega^2(c_{13}k_z^2+c_{11}\xi_b^2+\rho\omega^2)(c_{44}k_z^2-c_{11}\xi_a^2-\rho\omega^2)}{2ik_z c_{11}c_{66}(c_{13}+c_{44})(\xi_f^2-\rho_f\omega^2/c_{66})(\xi_b^2-\xi_a^2)\sqrt{2\pi\xi_a r}}, \\ g_b^e(k_z) &= \frac{\rho_f\omega^2(c_{13}k_z^2+c_{11}\xi_a^2+\rho\omega^2)(c_{44}k_z^2-c_{11}\xi_b^2-\rho\omega^2)}{2ik_z c_{11}c_{66}(c_{13}+c_{44})(\xi_f^2-\rho_f\omega^2/c_{66})(\xi_b^2-\xi_a^2)\sqrt{2\pi\xi_b r}}, \\ g_a^v(k_z) &= -\frac{(c_{44}k_z^2-c_{11}\xi_a^2-\rho\omega^2)r_0 F(k_z)}{2c_{11}c_{44}(\xi_b^2-\xi_a^2)\sqrt{2\pi\xi_a r}}, \\ g_b^v(k_z) &= \frac{(c_{44}k_z^2-c_{11}\xi_b^2-\rho\omega^2)r_0 F(k_z)}{2c_{11}c_{44}(\xi_b^2-\xi_a^2)\sqrt{2\pi\xi_b r}}, \\ g_a^r(k_z) &= -\frac{\xi_f^2 r_0^2 F(k_z)}{2\rho_f\omega^2} g_a^e(k_z), \\ g_b^r(k_z) &= -\frac{\xi_f^2 r_0^2 F(k_z)}{2\rho_f\omega^2} g_b^e(k_z). \end{aligned}$$

With these results, we proceed with their evaluation using the asymptotic expansion of integrals.

3.5 Asymptotic Evaluation of the Displacement Integrals

The above integrals have forms suitable for asymptotic evaluation by the *Method of Steepest Descent.* The essence of the method is that for large parameters (R in Eqs. 3.34 and 3.35), the contour of integration can be deformed into the steepest descent paths passing through the saddle points. When this is done, the integral becomes a Laplace type along the steepest descent path, and the dominant contribution comes from the saddle point only. Rigorous and detailed description of the method can be found in two excellent text books by Bleistein and Handelsman (1975) and Bleistein (1984).

We now apply the method of steepest descent to evaluate the *quasi-P* integral for the explosive source. Other integrals can be approximated following exactly the same analysis. Let $\mathrm{w}(k_z)$ stand for the complex exponents in the *quasi-P* wave integral (Eq. 3.35), i.e.,

$$\mathrm{w}(k_z) = ik_z \cos\theta - \xi_a \sin\theta, \tag{3.36}$$

the saddle point, k_{zs}, is determined by

$$\mathrm{w}'(k_{zs}) = 0 \Longrightarrow \left.\frac{d\xi_a}{dk_z}\right|_{k_z=k_{zs}} = i\cot\theta. \tag{3.37}$$

From the definition of ξ_a, the saddle point can be determined from the following implicit condition

$$i\cot\theta = \frac{k_z}{\xi_a}\epsilon(k_z) = \frac{k_z}{\xi_a}\frac{2c_{33}c_{44}k_z^2 - [(c_{11}c_{33} - c_{13}(c_{13}+2c_{44})]\xi_a^2 - (c_{33}+c_{44})\rho\omega^2}{-2c_{11}c_{44}\xi_a^2 + [(c_{11}c_{33} - c_{13}(c_{13}+2c_{44})]k_z^2 - (c_{11}+c_{44})\rho\omega^2}. \tag{3.38}$$

The second derivative of w is

$$\mathrm{w}''(k_z) = -\sin\theta \frac{d^2\xi_a}{d^2k_z} = -\frac{\sin\theta}{\xi_a}\left[\left(1 - \frac{k_z^2}{\xi_a^2}\epsilon(k_z)\right)\epsilon(k_z) + k_z\frac{d\epsilon(k_z)}{dk_z}\right]. \tag{3.39}$$

In the isotropic limit, $\epsilon(k_z) = 1$, and the following explicit expressions are obtained

$$k_{zs} = \frac{\omega}{\alpha}\cos\theta, \quad \mathrm{w}(k_{zs}) = i\frac{\omega}{\alpha}, \quad \mathrm{w}''(k_{zs}) = -i\frac{\alpha}{\omega\sin^2\theta}.$$

In arriving at the above, we used the Riemann surface corresponding to

$$\xi_a = \sqrt{k_z^2 - \omega^2/\alpha^2} = -i\sqrt{\omega^2/\alpha^2 - k_z^2} = -i\frac{\omega}{\alpha}\sin\theta.$$

On this surface, the Sommerfeld radiation condition is satisfied for ω with a positive imaginary part. This choice remains the same for the anisotropic case.

It should be remarked that while only one saddle point exists for the isotropic case, it is possible for the anisotropic case to have more than one. This depends on the shape of the slowness surface of the anisotropic medium, because the saddle point condition is related to the tangent of the slowness surface, as will be shown later. For an isotropic and moderately anisotropic medium, the slowness surfaces for both P and SV waves are concave and only one saddle point exists for each wave. For a highly anisotropic medium, such as Plexiglas-aluminum (White, 1982), the slowness surface for the SV wave is no longer concave and the wave surface is multi-valued (often referred as *triplication*). That is, for a single direction θ, there would be more than one tangent for the slowness surface satisfying the saddle point condition. The result of asymptotic analysis with multiple saddle points will yield multiple arrivals for a single direction.

Analysis of the steepest descent path according to Bleistein and Handelsman (1975) reveals that for the isotropic case, branch cuts in the integrand and in the exponent of the k_z integral are never crossed by the steepest descent path. Contributions to the integral come from the saddle point and possible poles of the integrand. For the anisotropic case, simple determination of the steepest descent path is impossible due to the implicit nature of the saddle point condition. However, it can be

said that for moderately anisotropic media, the above conclusion remains the same. Applying the asymptotic formula (e.g., Bleistein, 1984), the saddle point contribution is

$$\int_{-\infty}^{\infty} f_a^e(k_z) e^{Rw(k_z)} dk_z = f_a^e(k_{zs}) \sqrt{\frac{\pi}{2R|w''(k_{zs})|}} e^{Rw(k_{zs}) - i\pi/4}, \tag{3.40}$$

where, k_{zs} stands for the saddle point. $w(k_{zs})$ and $w''(k_{zs})$ are the exponent and its second derivative evaluated at the saddle point. We see that an extra $1/\sqrt{R}$ comes out of the saddle point evaluation. This combines with $1/\sqrt{r}$ in $f_a^e(k_{zs})$ and yields $1/R$ decay, which is a typical geometric spreading factor for body waves.

Anticipating that the saddle point is given as slowness components, the previous expressions of f's and g's need to be changed to functions of slowness components. Let s_z be the vertical component of the slowness vector, and s_a and s_b be the horizontal components of the vector for P and SV waves. Remembering the definition of ξ_a and ξ_b, we define these slowness components as the following,

$$s_z = \frac{k_z}{\omega}, \quad s_a = i\frac{\xi_a}{\omega}, \quad s_b = i\frac{\xi_b}{\omega}.$$

Then, according to Equations (3.34) and (3.35), the displacements in the frequency domain are

$$\begin{matrix} U_r^e \\ U_r^v \\ U_r^r \\ U_z^e \\ U_z^v \\ U_z^r \end{matrix} = \begin{matrix} p_a^e(s_z)\frac{i\omega e^{i\omega R(s_z\cos\theta + s_a\sin\theta)}}{2R} \\ p_a^v(s_z)\frac{e^{i\omega R(s_z\cos\theta + s_a\sin\theta)}}{2R} \\ p_a^r(s_z)\frac{i\omega e^{i\omega R(s_z\cos\theta + s_a\sin\theta)}}{2R} \\ q_a^e(s_z)\frac{i\omega e^{i\omega R(s_z\cos\theta + s_b\sin\theta)}}{2R} \\ q_a^v(s_z)\frac{e^{i\omega R(s_z\cos\theta + s_b\sin\theta)}}{2R} \\ q_a^r(s_z)\frac{i\omega e^{i\omega R(s_z\cos\theta + s_b\sin\theta)}}{2R} \end{matrix} + \begin{matrix} p_b^e(s_z)\frac{i\omega e^{i\omega R(s_z\cos\theta + s_a\sin\theta)}}{2R} \\ p_b^v(s_z)\frac{e^{i\omega R(s_z\cos\theta + s_a\sin\theta)}}{2R} \\ p_b^r(s_z)\frac{i\omega e^{i\omega R(s_z\cos\theta + s_a\sin\theta)}}{2R} \\ q_b^e(s_z)\frac{i\omega e^{i\omega R(s_z\cos\theta + s_b\sin\theta)}}{2R} \\ q_b^v(s_z)\frac{e^{i\omega R(s_z\cos\theta + s_b\sin\theta)}}{2R} \\ q_b^r(s_z)\frac{i\omega e^{i\omega R(s_z\cos\theta + s_b\sin\theta)}}{2R} \end{matrix}, \tag{3.41}$$

where p's are the amplitude of the horizontal components for *quasi-P* and *quasi-SV* waves, and q's are the amplitude of their vertical components. They are

$$\begin{aligned} p_a^e(s_z) &= \frac{\rho_f s_a(c_{13}s_z^2 - c_{11}s_b^2 + \rho)}{2c_{11}c_{66}(s_z^2 - 1/c_f^2 - \rho_f/c_{66})(s_b^2 - s_a^2)}\,\chi(\epsilon_a, \theta), \\ p_b^e(s_z) &= \frac{-\rho_f s_b(c_{13}s_z^2 - c_{11}s_a^2 + \rho)}{2c_{11}c_{66}(s_z^2 - 1/c_f^2 - \rho_f/c_{66})(s_b^2 - s_a^2)}\,\chi(\epsilon_b, \theta), \end{aligned}$$

$$
\begin{aligned}
p_a^v(s_z) &= \frac{-s_z(c_{13}+c_{44})s_a r_0 F(s_z)}{2c_{11}c_{44}(s_b^2-s_a^2)}\,\chi(\epsilon_a,\theta)\\
p_b^v(s_z) &= \frac{s_z(c_{13}+c_{44})s_b r_0 F(s_z)}{2c_{11}c_{44}(s_b^2-s_a^2)}\,\chi(\epsilon_b,\theta),\\
p_a^r(s_z) &= \frac{-(s_z^2-1/c_f^2)r_0^2 F(s_z)}{2\rho_f}\,p_a^e(s_z),\\
p_b^r(s_z) &= \frac{-(s_z^2-1/c_f^2)r_0^2 F(s_z)}{2\rho_f}\,p_b^e(s_z),\\
q_a^e(s_z) &= \frac{-\rho_f(c_{13}s_z^2-c_{11}s_b^2+\rho)(c_{44}s_z^2+c_{11}s_a^2-\rho)}{2s_z c_{11}c_{66}(c_{13}+c_{44})(s_z^2-1/c_f^2-\rho_f/c_{66})(s_b^2-s_a^2)}\,\chi(\epsilon_a,\theta),\\
q_b^e(s_z) &= \frac{\rho_f(c_{13}s_z^2-c_{11}s_a^2+\rho)(c_{44}s_z^2+c_{11}s_b^2-\rho)}{2s_z c_{11}c_{66}(c_{13}+c_{44})(s_z^2-1/c_f^2-\rho_f/c_{66})(s_b^2-s_a^2)}\,\chi(\epsilon_b,\theta),\\
q_a^v(s_z) &= \frac{(c_{44}s_z^2+c_{11}s_a^2-\rho)r_0 F(s_z)}{2c_{11}c_{44}(s_b^2-s_a^2)}\,\chi(\epsilon_a,\theta),\\
q_b^v(s_z) &= \frac{-(c_{44}s_z^2+c_{11}s_b^2-\rho)r_0 F(s_z)}{2c_{11}c_{44}(s_b^2-s_a^2)}\,\chi(\epsilon_b,\theta),\\
q_a^r(s_z) &= \frac{-(s_z^2-1/c_f^2)r_0^2 F(s_z)}{2\rho_f}\,g_a^e(s_z),\\
q_b^r(s_z) &= \frac{-(s_z^2-1/c_f^2)r_0^2 F(s_z)}{2\rho_f}\,g_b^e(s_z).
\end{aligned}
\tag{3.42}
$$

In the above, θ is the observation angle measured from upright vertical, and

$$
\chi(\epsilon_{a,b},\theta)=\left(\cos^2\theta+(\epsilon_{a,b}+s_z\epsilon'_{a,b})\sin^2\theta\right)^{-1/2},
$$

where,

$$
\epsilon_{a,b}(s_z)=\frac{2c_{33}c_{44}s_z^2+[(c_{11}c_{33}-c_{13}(c_{13}+2c_{44})]s_{a,b}^2-(c_{33}+c_{44})\rho}{2c_{11}c_{44}s_{a,b}^2+[(c_{11}c_{33}-c_{13}(c_{13}+2c_{44})]s_z^2-(c_{11}+c_{44})\rho}.
$$

Their derivatives with respect to s_z are denoted by ϵ'_a and ϵ'_b.

The amplitude factors for the explosion source are independent of the frequency of the source. While the amplitude for the other two sources depends on the frequency only through the term $F(s_z)=2l\ \mathrm{sinc}(\omega s_z l)$. If sources are at their low frequency regime $(0-1\ kHz)$ or the size of the source l is small compared to the wave length, $F(s_z)\sim 2l$, the amplitude factor is independent of frequency. Under this assumption for the radial and vertical source, we have the following displacements in the time

domain for all three sources:

$$\begin{array}{lll} u_r^e & p_a^e(s_z)\frac{\delta'(t-R(s_z\cos\theta+s_a\sin\theta))}{4\pi R} & p_b^e(s_z)\frac{\delta'(t-R(s_z\cos\theta+s_a\sin\theta))}{4\pi R} \\ u_r^v & p_a^v(s_z)\frac{\delta(t-R(s_z\cos\theta+s_a\sin\theta))}{4\pi R} & p_b^v(s_z)\frac{\delta(t-R(s_z\cos\theta+s_a\sin\theta))}{4\pi R} \\ u_r^r & p_a^r(s_z)\frac{\delta'(t-R(s_z\cos\theta+s_a\sin\theta))}{4\pi R} & p_b^r(s_z)\frac{\delta'(t-R(s_z\cos\theta+s_a\sin\theta))}{4\pi R} \\ u_z^e & q_a^e(s_z)\frac{\delta'(t-R(s_z\cos\theta+s_b\sin\theta))}{4\pi R} & q_b^e(s_z)\frac{\delta'(t-R(s_z\cos\theta+s_b\sin\theta))}{4\pi R} \\ u_z^v & q_a^v(s_z)\frac{\delta(t-R(s_z\cos\theta+s_b\sin\theta))}{4\pi R} & q_b^v(s_z)\frac{\delta(t-R(s_z\cos\theta+s_b\sin\theta))}{4\pi R} \\ u_z^r & q_a^r(s_z)\frac{\delta'(t-R(s_z\cos\theta+s_b\sin\theta))}{4\pi R} & q_b^r(s_z)\frac{\delta'(t-R(s_z\cos\theta+s_b\sin\theta))}{4\pi R} \end{array} \quad (3.43)$$

Thus, the recorded waveform at a distance from the radiating volume and radial sources is the derivative of the source waveform, while for the axial source the recorded waves bear the same waveform as the source. The arrival time of these waves depends on the direction of observation.

In the isotropic limit, $\epsilon_{a,b} = 1$, $\epsilon'_{a,b} = 0$, and $\chi(\epsilon_{a,b}, \theta) = 1$. Furthermore, $s_a^2 = 1/\alpha^2 - s_z^2$, $s_b^2 = 1/\beta^2 - s_z^2$, we obtain

$$\begin{array}{ll} p_a^e = \frac{\frac{\rho_f}{\rho}\sin\theta(1-\frac{2\beta^2}{\alpha^2}\cos^2\theta)}{2\alpha(\frac{\rho_f}{\rho}+\frac{\beta^2}{c_f^2}-\frac{\beta^2}{\alpha^2}\cos^2\theta)} & p_b^e = \frac{-\frac{\rho_f}{\rho}\cos\theta\sin 2\theta}{2\beta(\cos^2\theta-\frac{\rho_f}{\rho}-\frac{\beta^2}{c_f^2})} \\ p_a^v = -\frac{lr_0\sin\theta\cos\theta}{\rho\alpha^2} & p_b^v = \frac{lr_0\sin\theta\cos\theta}{\rho\beta^2} \\ p_a^r = \frac{lr_0^2(1-\frac{c_f^2}{\alpha^2}\cos^2\theta)}{\rho_f c_f^2}p_a^e & p_b^r = \frac{lr_0^2(1-\frac{c_f^2}{\beta^2}\cos^2\theta)}{\rho_f c_f^2}p_b^e \\ q_a^e = \frac{\frac{\rho_f}{\rho}\cos\theta(1-\frac{2\beta^2}{\alpha^2}\cos^2\theta)}{2\alpha(\frac{\rho_f}{\rho}+\frac{\beta^2}{c_f^2}-\frac{\beta^2}{\alpha^2}\cos^2\theta)} & q_b^e = \frac{\frac{\rho_f}{\rho}\sin\theta\sin 2\theta}{2\beta(\cos^2\theta-\frac{\rho_f}{\rho}-\frac{\beta^2}{c_f^2})} \\ q_a^v = -\frac{lr_0\cos^2\theta}{\rho\alpha^2} & q_b^v = -\frac{lr_0\sin^2\theta}{\rho\beta^2} \\ q_a^r = \frac{lr_0^2(1-\frac{c_f^2}{\alpha^2}\cos^2\theta)}{\rho_f c_f^2}q_a^e & q_b^r = \frac{lr_0^2(1-\frac{c_f^2}{\beta^2}\cos^2\theta)}{\rho_f c_f^2}q_b^e. \end{array} \quad (3.44)$$

These radiation patterns can be found in Lee and Balch (1982) and Meredith (1990). The reduction of our anisotropic results to the isotropic case provides a necessary check to the previous derivation.

3.6 Mach Wave in Anisotropic Media

Borehole-related Mach waves, or conical waves, were noticed in de Bruin and Huizer (1989). Meredith (1990) presented a detailed numerical and analytical description of the physics and mathematics of the Mach wave. Physically, the borehole Mach wave is caused by a fast-moving tube wave in a borehole embedded in a formation whose shear wave velocity is lower than the tube wave speed. Such formation is often referred to as soft and can be encountered in practice (Rutledge *et al.*, 1992). The boundary conditions between the fluid (with casing borehole is cased) and such a soft formation dictate the existence of the Mach wave.

Mathematically, the Mach wave arises from the tube wave pole when evaluating the SV part of the k_z integrals. For a borehole in a soft formation, the tube wave pole is situated between the saddle point and the crossing point between the steepest descent path with the real k_z axis. Contour integration along the steepest descent path will pick up the tube wave pole. The contribution of this pole can be evaluated using the residue theorem.

For the anisotropic case, the physics and mathematics of the Mach wave are basically similar to that of the isotropic case. However, for transverse isotropy, the existence of the Mach wave depends on the comparison of the tube wave velocity with the shear wave velocity, determined by $\sqrt{c_{66}/\rho}$. Due to anisotropy, the speed of Mach wave propagation now depends on the Mach angle. In other words, for two different TI formations with the same c_{66}, Mach wave velocity and propagation direction will be different. Since the tube wave arises from a pole, its asymptotic behavior will be different from that of waves due to saddle points. In fact, the Mach wave decays as $1/\sqrt{R}$ instead of $1/R$ (body waves) and thus becomes prominent at large distances.

3.7 Radiation Patterns of Three Downhole Sources

As the previous sections show, borehole source radiation patterns in an isotropic formation have much simpler forms than in a TI formation. The complexity associated with the TI case is mainly due to the implicit nature of the saddle point condition. The determination of the saddle point k_{zs} from Equation 3.38 is analytically impossible. It is also numerically difficult in terms of finding the correct root(s) with accuracy. To avoid this, a method based on the slowness and wave surfaces geometry of the TI medium is applied.

The *slowness surface* of a TI medium is defined by

$$c_{11}c_{44}s^4 + [(c_{11}c_{33} - c_{13}^2 - 2c_{13}c_{44})s_z^2 - (c_{11} + c_{44})\rho]s^2 + (c_{44}s_z^2 - \rho)(c_{33}s_z^2 - \rho) = 0,$$

where s and s_z are the horizontal and vertical slowness components. Each point on this surface with (s, s_z) corresponds to a wave traveling with phase velocity $(1/s, 1/s_z)$. The saddle point condition is just the statement that the dominant contribution comes from the point on the slowness surface where its tangent is normal to the observation direction. In other words, the saddle point is a point on the slowness surface at which the normal direction is parallel to the direction of observation. This normal direction is also the group velocity direction along which energy propagates. This can be easily seen using the concept of *wave surface*. Buchwald (1959) defines it as the envelope at time $t = 1$ of waves originating from a source at the origin at time $t = 0$. Thus, the wave surface is also the group velocity surface. The components of a group velocity vector (a point on the wave surface) are

$$\begin{aligned} g_x &= s\,\frac{2c_{11}c_{44}s^2 + [(c_{11}c_{33} - c_{13}(c_{13} + 2c_{44})]s_z^2 - (c_{11} + c_{44})\rho}{\rho[(c_{11} + c_{44})s^2 + (c_{33} + c_{44})s_z^2 - 2\rho]}, \\ g_z &= s_z\,\frac{2c_{33}c_{44}s_z^2 + [(c_{11}c_{33} - c_{13}(c_{13} + 2c_{44})]s^2 - (c_{33} + c_{44})\rho}{\rho[(c_{11} + c_{44})s^2 + (c_{33} + c_{44})s_z^2 - 2\rho]}. \end{aligned}$$

Comparing the above with the saddle point condition, the right-hand side of Equation 3.38 is the ratio of g_z to g_x. This implies that the saddle point is the point on the slowness surface whose corresponding point(s) on the wave surface is the intersection

point of the wave surface with a line along the observation direction. This property of the saddle point greatly simplifies the calculation of radiation patterns for various downhole sources. We determine the saddle point by the numerical algorithm that follows.

Given a transversely isotropic formation, the slowness surface and the wave surface (group velocity surface) are thus uniquely obtained. Points on the slowness surface and the corresponding points on the wave surface are tabulated. Thus, given an observation angle (θ), the point(s) on the wave surface associated with this angle is readily determined. The corresponding point(s) on the slowness surface is obtained by checking with the tabulated results. Once the saddle point is known, the radiation patterns of the three sources can be calculated easily by using the results of the previous sections (Equation 3.42). The procedure is illustrated in Figure 3-2 through the slowness and wave surfaces of the slightly anisotropic Mesaverde Sandstone (Thomsen, 1986; Ben-Menahem and Sena, 1990). This rock has a density of 2870 kg/m^3 and the following elastic constants (in $10^9 Pa$): $c_{11} = 50$, $c_{33} = 45$, $c_{13} = -8.6$, $c_{44} = 24.6$, and $c_{66} = 26.6$.

To plot radiation patterns, the conventional usage of radial (U_R) and tangential (U_θ) is followed. The transformation from U_r and U_z to U_R and U_θ is

$$U_R = U_r \sin\theta + U_z \cos\theta, \quad U_\theta = U_r \cos\theta - U_z \sin\theta.$$

With this, Figure 3-3 shows the radiation patterns of an explosion on the axis of a fluid-filled borehole in Mesaverde sandstone. The radiation patterns for vertical and radial sources are shown in Figure 3-4. In both figures, bold lines are for *quasi-P* waves and thin lines for *quasi-SV* waves. The radiation patterns are very different from those of an isotropic medium. In an anisotropic medium, particle motions of *quasi-P* and *quasi-SV* waves are no longer pure compression and torsion. Thus, a graph of radial displacement (U_R), which excludes shear waves in the isotropic case, now includes *quasi-SV* wave contribution for an anisotropic medium. Similarly, the *quasi-P* wave also appears on the tangential components (U_θ). However, the *quasi-*

P part of U_θ is a few magnitudes smaller than the *quasi-SV* part of U_R, and it is numerically contaminated, as shown by both figures.

Quasi-SV waves from explosive and radial sources form a narrow beam directed toward 45° in the U_θ graphs, while its U_R component forms two beams. The explosion and radial sources have similar radiation patterns because the radiation pattern of the radial source contains the radiation factor of the explosion source, as can be seen in Equation 3.42. The existence of a nodal point (zero radiation) for the *quasi-P* wave in the U_R pattern is due to the negative value of the c_{13} constant, which is only possible for very hard rock. The U_θ pattern for a vertical source shows a fan-shaped radiation pattern for the *quasi-SV* wave, which is quite different from the pattern for an isotropic medium.

To verify the analytical prediction from the asymptotic analysis, the discrete wavenumber method is used to numerically evaluate the displacement integrals for the three sources. The observation points are circularly distributed and are 100 m from the source. A Ricker wavelet with a center frequency of 600 Hz is used as the source waveform. The results for the explosion, vertical, and radial sources, are shown in Figure 3-5-Figure 3-7, respectively. As predicted by previous analyses, waveforms for P and SV waves due to explosion and radial sources experience either a 90° or 270° phase shift, while wave pulses from a vertical source have either a 0° or 180° phase shift. The nodal points on the U_R pattern for the P and SV waves radiated from explosion and radial sources are clearly visible. So is the nodal point on U_R for the SV wave from the vertical source. On the two sides of these nodal points, waveforms have a 180° phase difference. The narrow SV-wave beams associated with explosion and radial sources are clearly shown by the amplitudes of the corresponding waveforms. So is the fan-shaped SV beam from the vertical source.

3.8 Anisotropy Effect on P and S Wave Radiation

To obtain better insight into the effect of anisotropy on the amplitude and direction of radiated *quasi-P* and *quasi-S* waves, radiation patterns of a test isotropic rock are studied as the rock is made anisotropic at different degrees. This rock has a density of 2 g/cm^3, a P-wave velocity of 3162 m/s, and a S-wave velocity of 1732 m/s. Thus, the five elastic constants (c_{11},c_{33},c_{13},c_{44},c_{66}) are 20, 20, 8, 6, 6, in GPa. In the first case, c_{33} is decreased by 5, 10, 15, 20, and 25 percent while all other constants remain unchanged, representing P-wave anisotropy as it is usually referred to. In terms of the anisotropy measures defined by Thomsen (1986), $\epsilon = \frac{c_{11}-c_{33}}{2c_{33}} = (2.6, 5.6, 8.8, 12.5, 16.7)\%$, and $\delta^* = \frac{2(c_{13}+c_{44})^2-(c_{33}-c_{44})(c_{11}+c_{33}-2c_{44})}{2c_{33}^2} = (5.7, 12, 20, 30, 41)\%$. In the second case, we decrease c_{44} from its isotropic value in the same manner, which results in the following Thomsen's measures: $\gamma = \frac{c_{66}-c_{44}}{2c_{44}} = (2.6, 5.6, 8.8, 12.5, 16.7)\%$, and $\delta^* = -(4.2, 8.4, 12.6, 16.8, 21)\%$.

These two cases are shown in Figure 3-8 and Figure 3-10, respectively. For clarity, P and S contributions to U_R and U_θ are plotted on separate graphs. The thick dark line corresponds to the radiation patterns at the isotropic limit, and the others correspond to the five anisotropic stages. The thinner and lighter the line, the higher the degree of anisotropy. Both figures show that the amplitude of the S-wave is much stronger than that of the P-wave, as observed in the isotropic case. In the isotropic case, there is no U_R component from the S-wave and no U_θ component from the P-wave. As the rock becomes more anisotropic, the P-wave U_R amplitude in Figure 3-8 increases moderately in the range of 30-75 degrees from the vertical, while in Figure 3-10 it increases at both extremes. On the other hand, the S-wave amplitude ($U_\theta - qSV$) change with the degree of anisotropy is more dramatic as the pattern rotates towards or away from the vertical in Figure 3-8 and Figure 3-10. Figure 3-8 shows that when c_{33} decreases away from the isotropic value, significant shear waves should be expected at low and high angles. Contrarily, when c_{44} decreases, most shear wave energy is in the direction around 45°. Since the S-wave amplitude

is much greater than the P-wave's, its contribution to U_R is on the same order as the P-wave. In contrast, the P-wave contribution to U_θ is two orders of magnitude smaller that the S-wave contribution. In fact, its noisy appearance reminisces the numerical inaccuracy resulting from such small amplitudes.

When c_{33} and c_{44} decrease over 20% from their isotropic value, triplications for the SV wave surface come into existence in the vertical direction for the first case, and in a 45^o direction for the second. At the two turning points of these triplications, the second order derivative of $\mathrm{w}(k_z)$ at the saddle point is also zero, resulting in a higher order saddle point (2nd order). To correctly predict the radiation amplitude, a formula for a second order saddle point (see Bleistein and Handlesman (1975) for details), rather than Equation 3.40, has to be used. Evaluation of the second order saddle point contribution yields a geometrical spreading factor $R^{-5/6}$, instead of $1/R$. Thus, wave amplitudes near the triplication edge are larger. Since this special case is not included in the final formula, and because the cusp is very small, unusually large amplitudes appear near the vertical direction in Figure 3-8, and at 45^o in Figure 3-10. If the triplication is severe (e.g., Plexiglas-aluminum), the previous radiation formula will accurately predict wave amplitudes corresponding to points between triplication edges on the wave surface.

Figure 3-9 and Figure 3-11 provide independent checks to the analytical results in Figure 3-8 and Figure 3-10, respectively. Plotted in these figures are the actual wave displacements recorded by a circular array of receivers 25 m away from the borehole explosion source. They are obtained from numerical evaluation of the exact displacement integrals. The parameters used are those for the most anisotropic cases in Figure 3-8 and Figure 3-10. The nodal directions in $U_R - qSV$ graphs are clearly shown as polarity changes in Figure 3-9 and Figure 3-11. Near the vertical direction, the large amplitudes of $U_R - qSV$ and $U_\theta - qSV$ of Figure 3-8 are manifested in Figure 3-9. The large amplitudes of Figure 3-10 are also apparent in Figure 3-11. The huge amplitudes appearing later than the shear waves are the tube wave expression

E.C.	c_{11}		c_{33}		c_{13}		c_{44}		c_{66}	
change	↑	↓	↑	↓	↑	↓	↑	↓	↑	↓
ϵ	+	−	−	+	0	0	0	0	0	0
γ	0	0	0	0	0	0	−	+	+	−
δ^*	−	+	−	+	+	−	+	−	0	0
δ^*_{max}	−.09	+.09	−.19	+.41	+.15	−.13	+.21	−.21	0	0
S-pattern	*F*	*D*	*F*	*D*	*D*	*F*	*D*	*F*	*N*	*N*

Table 3.1: The sign of Thomsen's measures as the elastic constant is changed from their isotropic value for the test rock. δ^*_{max} is measured at 25% change. Letter F is for focusing, D for diverging, and N for no change.

in the elastic medium. Tube waves decay exponentially into the formation, thus only the two receivers closest to the borehole can detect them.

Tests with other parameters show that the effect of c_{66}, shown in Figure 3-12, scales uniformly up or down the amplitude of radiated waves and does not change the shape of the radiation patterns. Increasing c_{13} (Figure 3-13) and decreasing c_{11} have similar effects as decreasing c_{33}, but not as much as the latter. Increasing c_{33} and c_{11}, and decreasing c_{13} (Figure 3-14), result in similar patterns as decreasing c_{44}, but not as dramatically as the latter. Thus, the effects of c_{13} and c_{44} on the radiation patterns are similar when the two are changed in the same way. However, the effects of c_{13} and c_{44} are opposite to those of c_{11} and c_{33} when they are perturbed in a similar fashion.

Table 3.1 summarizes the correspondence of the S-pattern variation with respect to the signs of the three Thomsen measures. It clearly shows that TI formations with positive δ^* diverge S-wave radiation to cover all angles, and those with negative δ^* focus the S-wave radiation to the 45° direction. The Mesaverde sandstone has a negative δ^* and its focusing S-pattern is predicted. Thus, the sign of δ^* is a direct indicator of the S-wave radiation pattern for explosion sources in borehole.

3.9 Source Radiation From a Cased Borehole

When downhole sources are placed inside a cased and cemented borehole, their radiation characteristics are affected by the casing and cement. In this section, we investigate the effect of casing and cement. A cased and cemented borehole embedded in a general TI medium is considered. From this general consideration the isotropic limit is easily obtained.

To simplify the algebra, let r_0, r_m and r_c, respectively represent the inner radius of the TI formation, cement, and casing. And also let S_f, S_m and S_c be the matrices connecting the displacement-stress vector to the potential amplitude vector, for the TI formation, cement and casing, respectively. Definition of these matrices is similar to Equation 3.20. Then, the following relationship between potential amplitudes in borehole fluid and in TI formation exists because of the boundary conditions. i.e.,

$$F_{3\times 2}(r_c)\begin{pmatrix} C_s \\ C_o \end{pmatrix} = S_c(r_c)S_c^{-1}(r_m)S_m(r_m)S_m^{-1}(r_0)S_f(r_0)\begin{pmatrix} A_s \\ B_s \\ A_o \\ B_o \end{pmatrix}. \tag{3.45}$$

Matrix F is as given in Equation 3.21. Its subscript 3×2 reminds us that only three boundary conditions are necessary at the fluid/casing interface. The arguments of the matrices in the above indicate at which interface the matrices should be evaluated. Immediately one sees that if $r_m = r_0$ and $r_c = r_0$ the open borehole case is encountered. Thus, for $r_m \sim r_0$ and $r_c \sim r_0$, the casing effects are negligible. In reality, compared to the borehole radius r_0, the thicknesses of casing and cement are not small enough to be neglected.

3.9.1 Low frequency sources

The effect of casing and cement is entirely determined by the matrix product

$$I(r_c, r_m, r_0) = S_c(r_c)S_c^{-1}(r_m)S_m(r_m)S_m^{-1}(r_0). \tag{3.46}$$

For the open borehole case, $I(r_c, r_m, r_0)$ is an identity matrix. Applying small argument approximation to the Bessel functions involved in the matrices in I, we obtain I in the low frequency regime.

$$I \sim \begin{bmatrix} a_1 & 0 & 0 & 0 \\ 0 & 1 & 0 & 0 \\ 0 & 0 & a_3 & 0 \\ 0 & 0 & 0 & a_4 \end{bmatrix}, \tag{3.47}$$

where,

$$\begin{aligned} a_1 &= \left(\frac{r_m}{r_c} - [\frac{r_m}{r_c} - \frac{r_c}{r_m}]\frac{\beta_c^2}{\alpha_c^2}\right)\left(\frac{r_0}{r_m} - [\frac{r_0}{r_m} - \frac{r_m}{r_0}]\frac{\beta_m^2}{\alpha_m^2}\right) \\ a_3 &= \left(1 + [\frac{r_m^2}{r_c^2} - 1]\frac{\beta_c^2}{\alpha_c^2}\right)\left(1 + [\frac{r_0^2}{r_m^2} - 1]\frac{\beta_m^2}{\alpha_m^2}\right) \\ a4 &= \frac{r_0}{r_c}. \end{aligned}$$

$\alpha_{c,m}$ and $\beta_{c,m}$ are the P and S wave velocities of the casing (c) and cement (m). From equation 3.45 and the reflection and transmission coefficients in the previous chapter, the P-P and P-S transmission coefficients for an explosion source are

$$T_{pp}^o = \frac{S_{44}\rho_f\omega^2/r_0}{a_3\ DET}, \quad T_{ps}^o = \frac{-S_{43}\rho_f\omega^2/r_0}{a_3\ DET}, \tag{3.48}$$

where, DET stands for the common denominator

$$DET = F_{11}(S_{43}S_{34} - S_{33}S_{44}) + \frac{a_1}{a_3}F_{31}(S_{13}S_{44} - S_{14}S_{43}). \tag{3.49}$$

For axial and radial sources, the potential amplitudes in the TI formation are

$$A_o^v = \frac{F_{11}S_{34} - \frac{a_1}{a_3}F_{31}S_{14}}{a_4\ DET}F(k_z), \quad B_o^v = \frac{F_{31}S_{13} - \frac{a_1}{a_3}F_{11}S_{33}}{a_4\ DET}F(k_z); \tag{3.50}$$

$$A_o^r = \frac{-F_{11}S_{44}F(k_z)}{a_3\ DET}, \quad B_o^r = \frac{F_{11}S_{43}F(k_z)}{a_3\ DET}. \tag{3.51}$$

The above differ from the open borehole results (Equation 3.25 to Equation 3.26) only by an amplitude scaling factor, a_3 for volume and radial sources and a_4 for a vertical source, and an equivalent scaling factor $\frac{a_1}{a_3}$ for F_{31}. The former introduces

amplitude reduction due to the casing and cement since $a_3 > 1$ and $a_4 > 1$. The latter introduces a different tube wave factor in the denominator and numerator. i.e.,

$$\left.\begin{array}{l} DET \\ F_{11}S_{34} - \frac{a_1}{a_3}F_{31}S_{14} \\ F_{31}S_{13} - \frac{a_1}{a_3}F_{11}S_{33} \end{array}\right\} \propto \left(\xi_f^2 - \frac{a_1\rho_f\omega^2}{a_3 c_{66}}\right). \tag{3.52}$$

This corresponds to a tube wave traveling along the cased borehole at a speed

$$C_T = c_f\sqrt{\frac{c_{66}}{c_{66} + \rho_f c_f^2 a_1/a_3}}. \tag{3.53}$$

It is easy to show that a_3 is always greater than a_1. Thus, Tube wave speed in a cased borehole is larger than that of an open borehole. The casing, cement, the formation is equivalent to a transversely isotropic medium with $c'_{66} = \frac{a_3}{a_1}c_{66}$.

3.9.2 High frequency sources

For high frequency sources, the above small argument approximation is less justified and the conclusions may no longer apply. Thus, explicit evaluation of matrix I is required. In the far field, the steepest descent approximation for the open borehole case stays the same for the cased borehole. That is, major contribution for source radiation from an open or a cased borehole comes from the same saddle point. This is because the displacements for cased borehole radiation have similar integral form as Equations (3.27) and (3.28). The only difference lies in the transmission coefficients (T^o_{pp} and T^o_{ps}) and the potential amplitude (A^o_r, A^o_v, B^o_r, and B^o_v). If we let

$$S = S_c(r_c)S_c^{-1}(r_m)S_m(r_m)S_m^{-1}(r_0)S_f(r_0),$$

then, these quantities have the same expression as previous results for an open borehole. Evaluation of the integrands at the saddle point yields the desired radiation patterns.

3.9.3 Effect of casing and cement on wave radiation

To understand what effects casing and cement may have on the radiation pattern and amplitude of three typical downhole sources, we compare amplitudes of P and S waves radiated from cased and open boreholes. Five different frequencies (10, 100, 500, 1000, 2000 Hz) are considered and will be represented by dark to light lines in the following figures, respectively. For the cased borehole, the outer radius for fluid, casing, and cement, is respectively 0.1, 0.12, and 0.16 meters, while 0.16 is used for the radius of the open borehole.

hard formation

Figure 3-15 shows the amplitude ratio in Mesaverde sandstone, which is essentially a hard rock. P-wave amplitude from the explosion source in a cased borehole is roughly 60% of the amplitude from an open borehole in the horizontal direction. The amplitude reduction due to casing and cement is more severe near the vertical. With a constant amplitude reduction of 40% for all angles, the P radiation pattern for the vertical source is hardly affected by casing and cement. However, they apparently have a much stronger effect on the radial source as the P amplitude from a cased hole is only 25% of the amplitude from an open hole.

For lower frequencies, the S-wave pattern for sources in cased or open borehole remains unchanged. The amplitude reduction factor is about 25% for the explosion source, 40% for the vertical source, and 70% for the radial source. As frequency gets higher (2 kHz in this example), the effect of casing and cement is more dramatic. This is not surprising because in the higher frequency limit, the S wave treats casing and cement more like a layered medium than an uniform medium, as is the case for lower frequencies.

intermediate formation

The amplitude ratios in an intermediate formation (the isotropic test model used before) are shown in Figure 3-16. The figure shows that for vertical sources in a cased borehole, if the surrounding formation is relatively soft, the radiation pattern and amplitude from a cased borehole is quite different from that of an open borehole. P and S wave radiation is significantly reduced near the vertical axis, especially for higher frequencies. Unlike the vertical source, the radiation pattern of a radial source is marginally affected, for both P and S waves. For explosion sources, the P wave pattern for different frequencies stays roughly the same, while the S pattern changes significantly. These results illustrate the importance of considering radiation pattern and casing-cement influence in high frequency cross-well data acquisition, especially in regions of soft to intermediate-hard rock layers.

3.10 Discussion and Conclusion

Radiation patterns for three typical downhole sources are obtained in terms of the slowness components of the saddle point of the displacement integrals. From a geometrical argument using the slowness and wave surface of the TI medium, the saddle point is readily determined. Since the saddle point condition dictates that major energy radiates along the group velocity direction, i.e., along the ray direction, the radiation patterns presented in this paper can be readily adapted to a ray tracing-based modeling and inversion (tomography) program to account for the source borehole effect. Given a ray direction (ray parameters), the P and S wave radiation amplitudes are computed based on the geometric determination of the saddle point(s) on the slowness surfaces.

Examples show that the anisotropy effect on S-wave radiation is dramatic, even for a medium with a small degree of anisotropy. The results indicate that the S-wave radiation pattern in a TI medium can be predicted using the sign of the Thomsen

measure, δ^*. Media with positive δ^* tend to broaden the radiation angle of the S-wave, as is the case in Figure 3-8 and Figure 3-13. In contrast, media with negative δ^* tend to beam together S-wave radiation, as is the case in Figure 3-10 and Figure 3-14.

For hard formation surrounding a cased borehole, the effect of casing and cement on wave radiation is more or less frequency independent, if the source frequency is not very high. The amplitude reduction factor for a radial source is much larger than for explosion and vertical sources. If the formation is relatively soft, casing and cement introduce frequency dependence to the radiation pattern, even if the source frequency is relatively low.

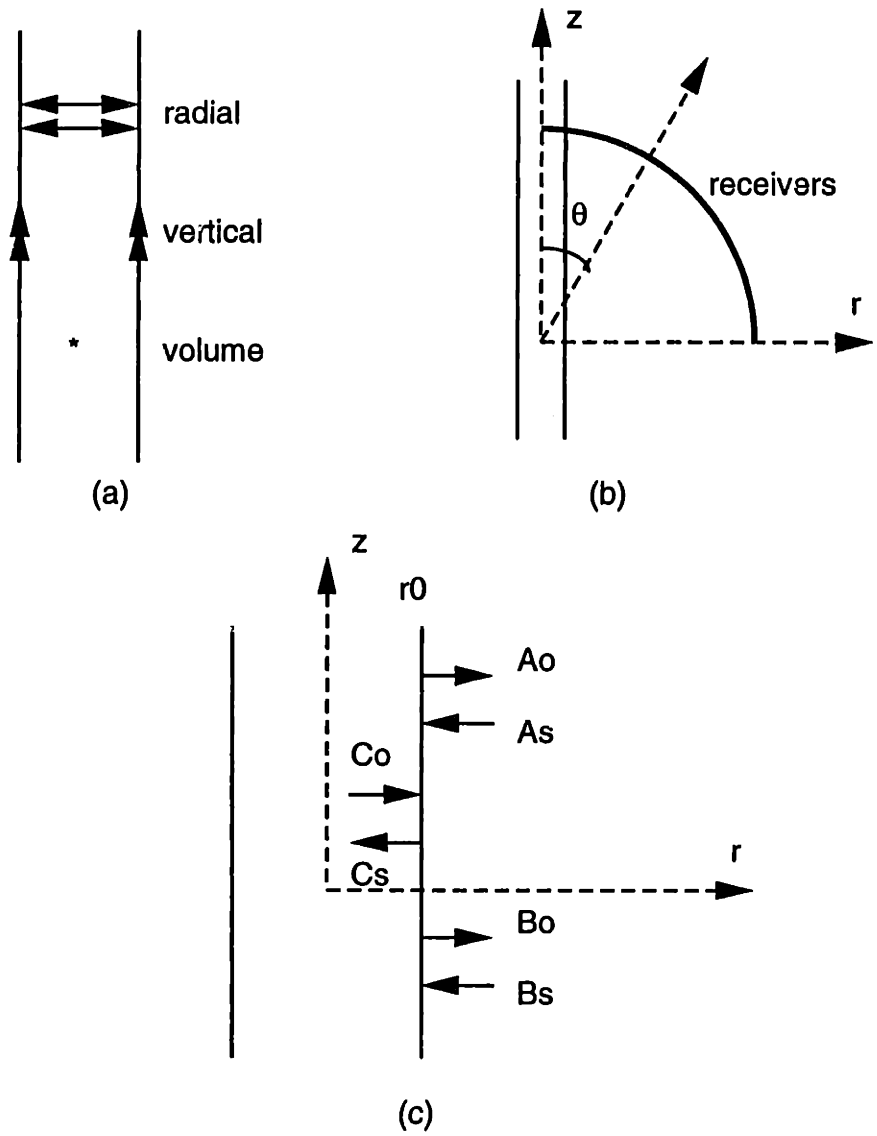

Figure 3-1: Sources (a), geometry (b), and waves at borehole wall (c).

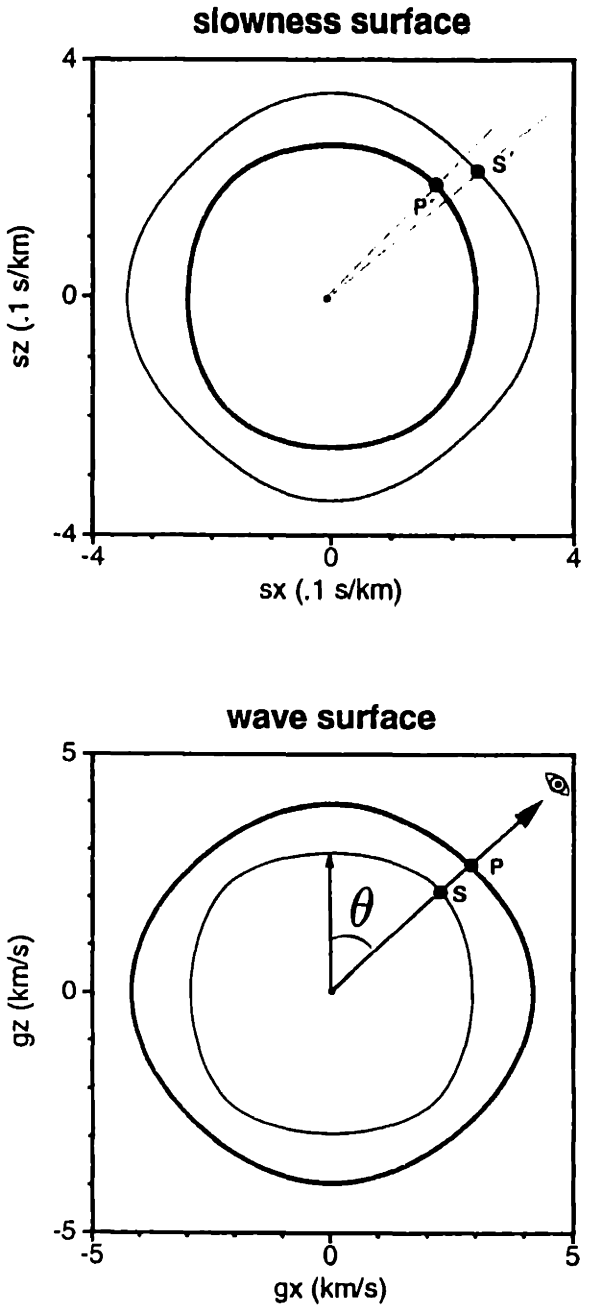

Figure 3-2: Slowness (top) and wave (bottom) surfaces for Mesaverde Sandstone, and the geometrical determination of the saddle points of P- and S-wave integrals.

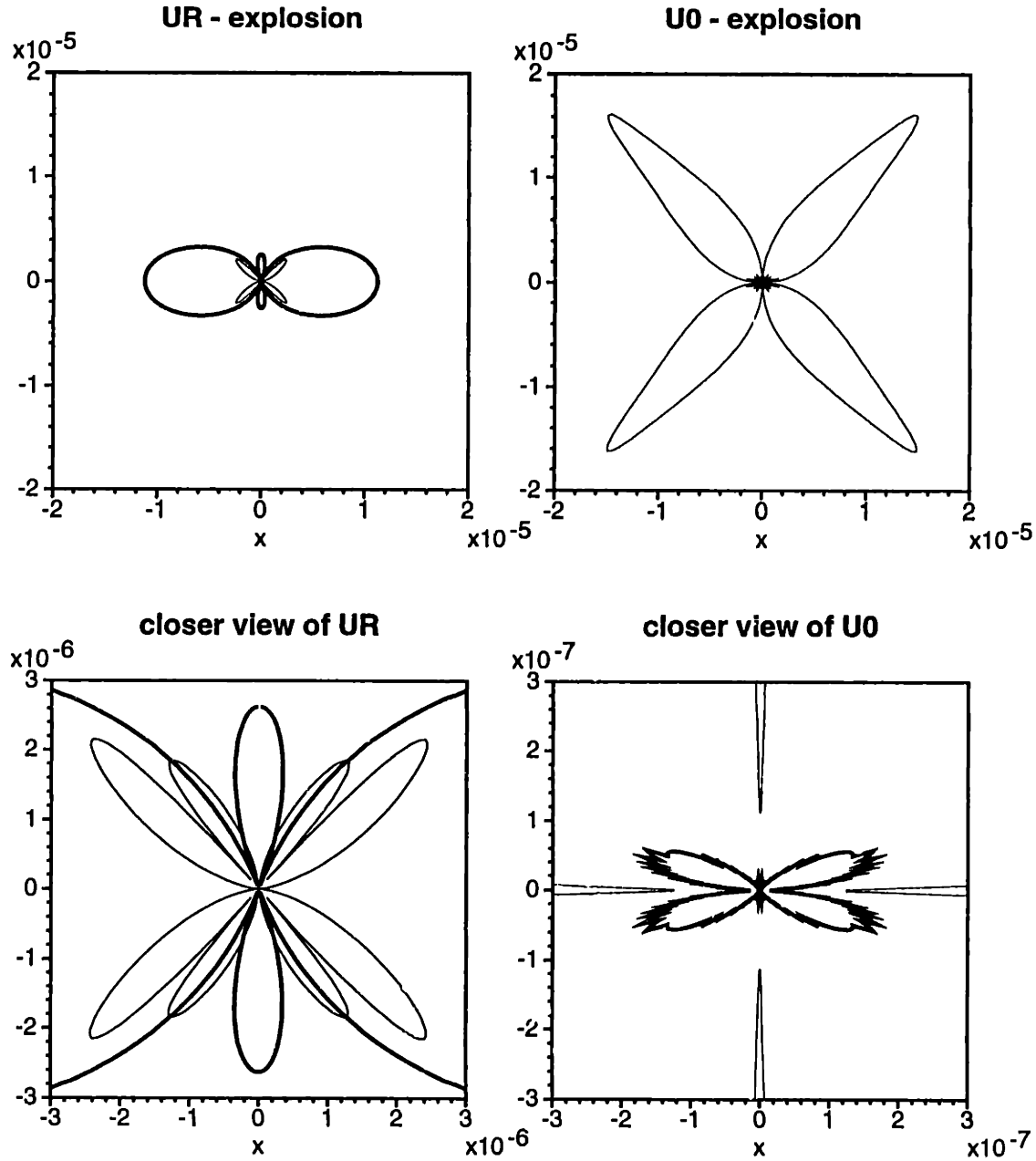

Figure 3-3: Radial (U_R) and tangential (U_θ) patterns for an explosion source in a water-filled borehole of radius .1 m penetrating Mesaverde Sandstone along symmetry axis. Dark lines are for the *quasi-P* wave and light lines for the *quasi-SV* wave. Due to the much smaller amplitude of the *quasi-P* wave on the tangential component (U_θ), it is contaminated by numerical noise during computation.

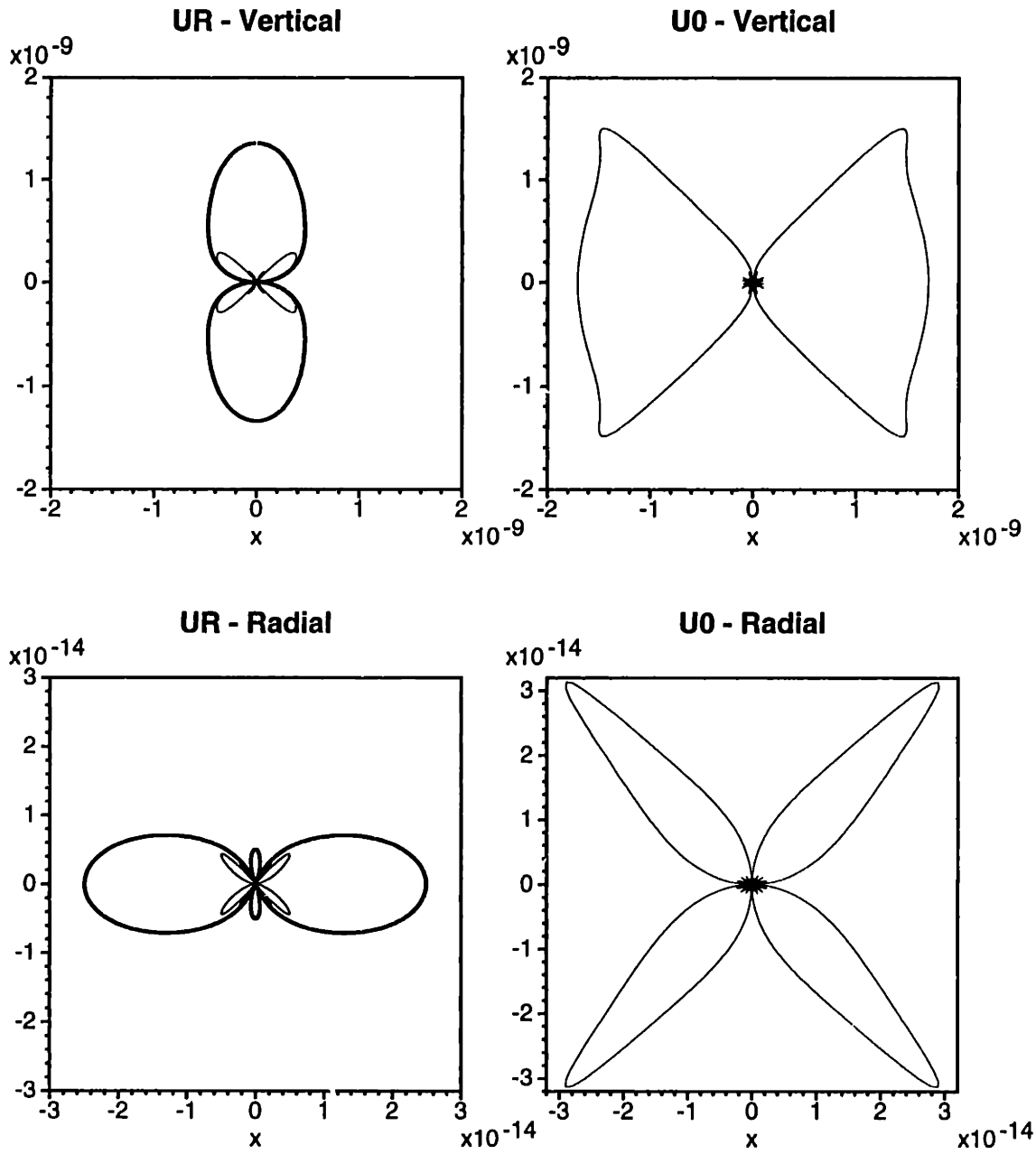

Figure 3-4: Radial (U_R) and tangential (U_θ) patterns for vertical and radial sources (size .2 m) in a water-filled borehole of radius .1 m penetrating Mesaverde Sandstone.

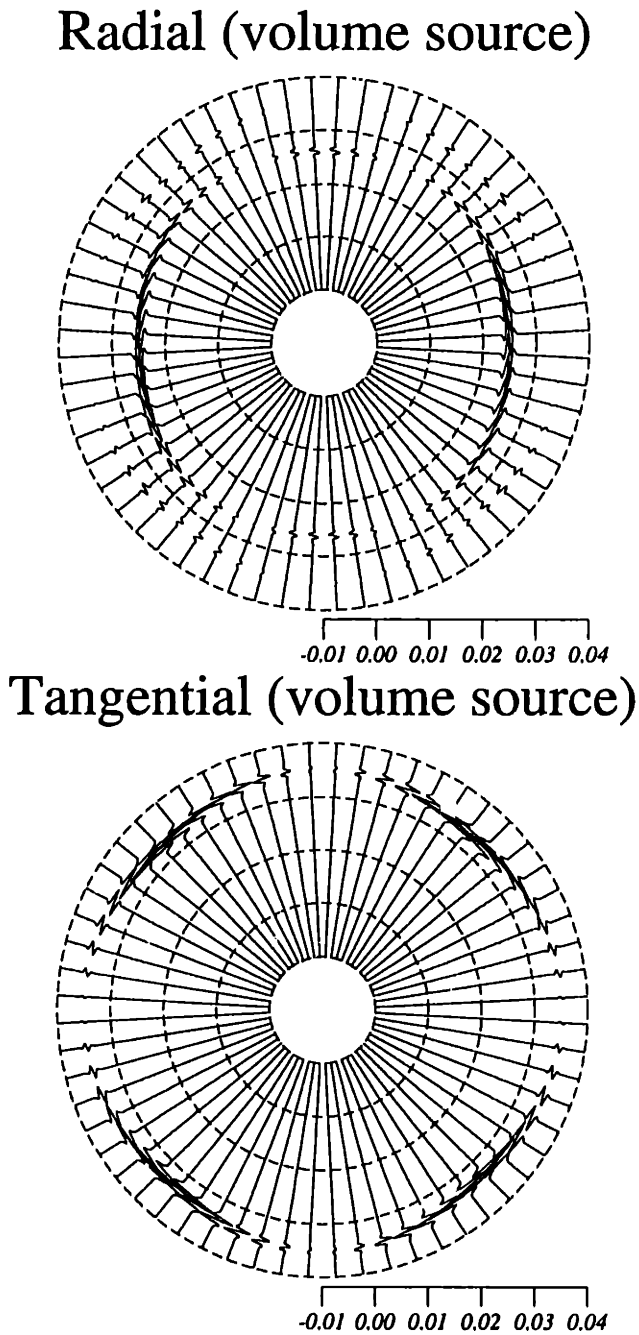

Figure 3-5: The radial and tangential displacements recorded by a circular receiver array 100 m away from an explosion source in a water-filled borehole in Mesaverde Sandstone.

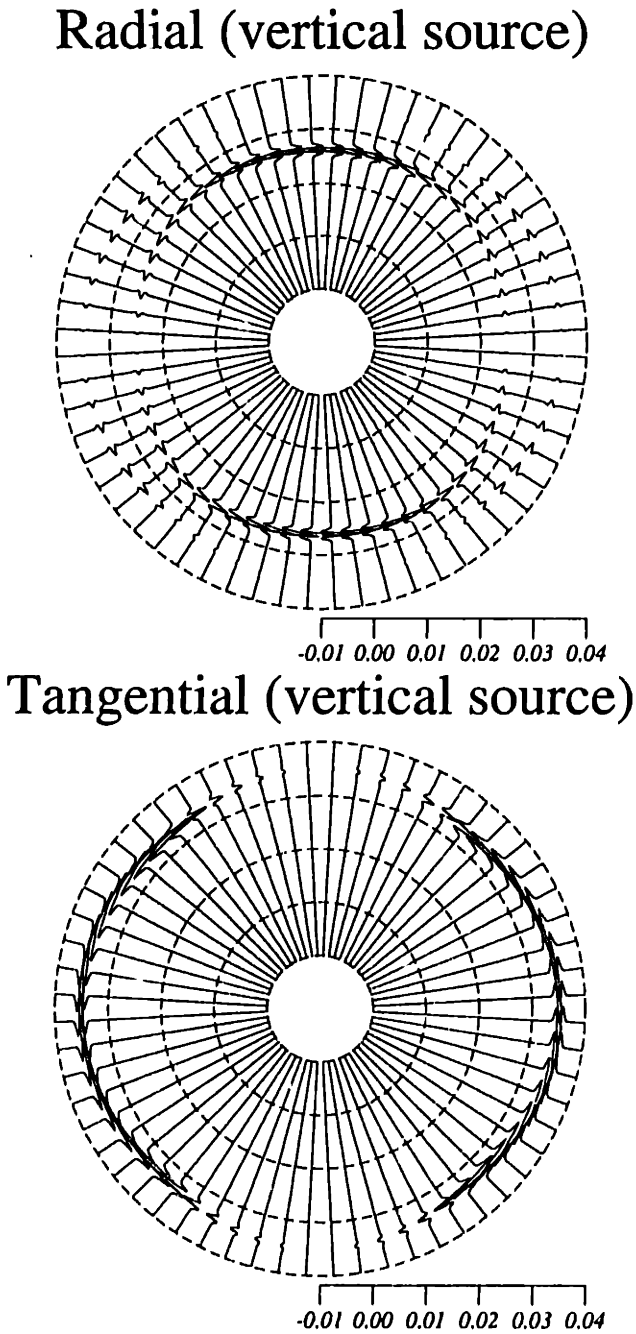

Figure 3-6: The radial and tangential displacements recorded by a circular receiver array 100 m away from a vertical source (l = .2 m) in a water-filled borehole in Mesaverde Sandstone.

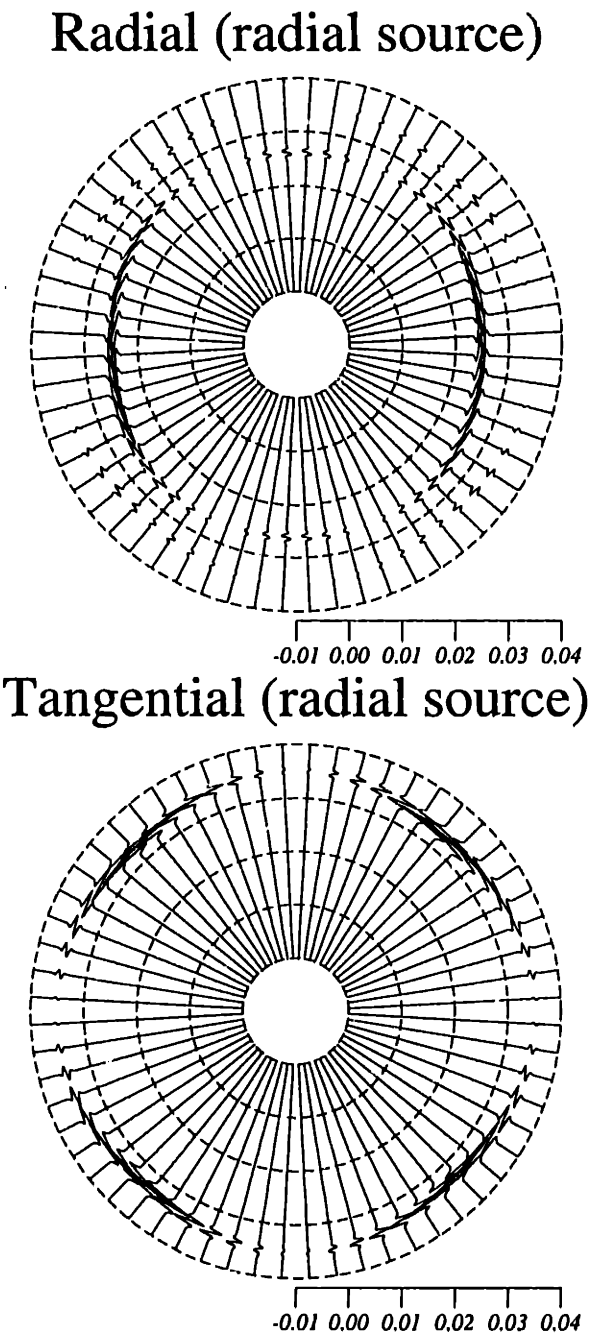

Figure 3-7: The radial and tangential displacements recorded by a circular receiver array 100 m away from a radial source ($l = .2\ m$) in a water-filled borehole in Mesaverde Sandstone.

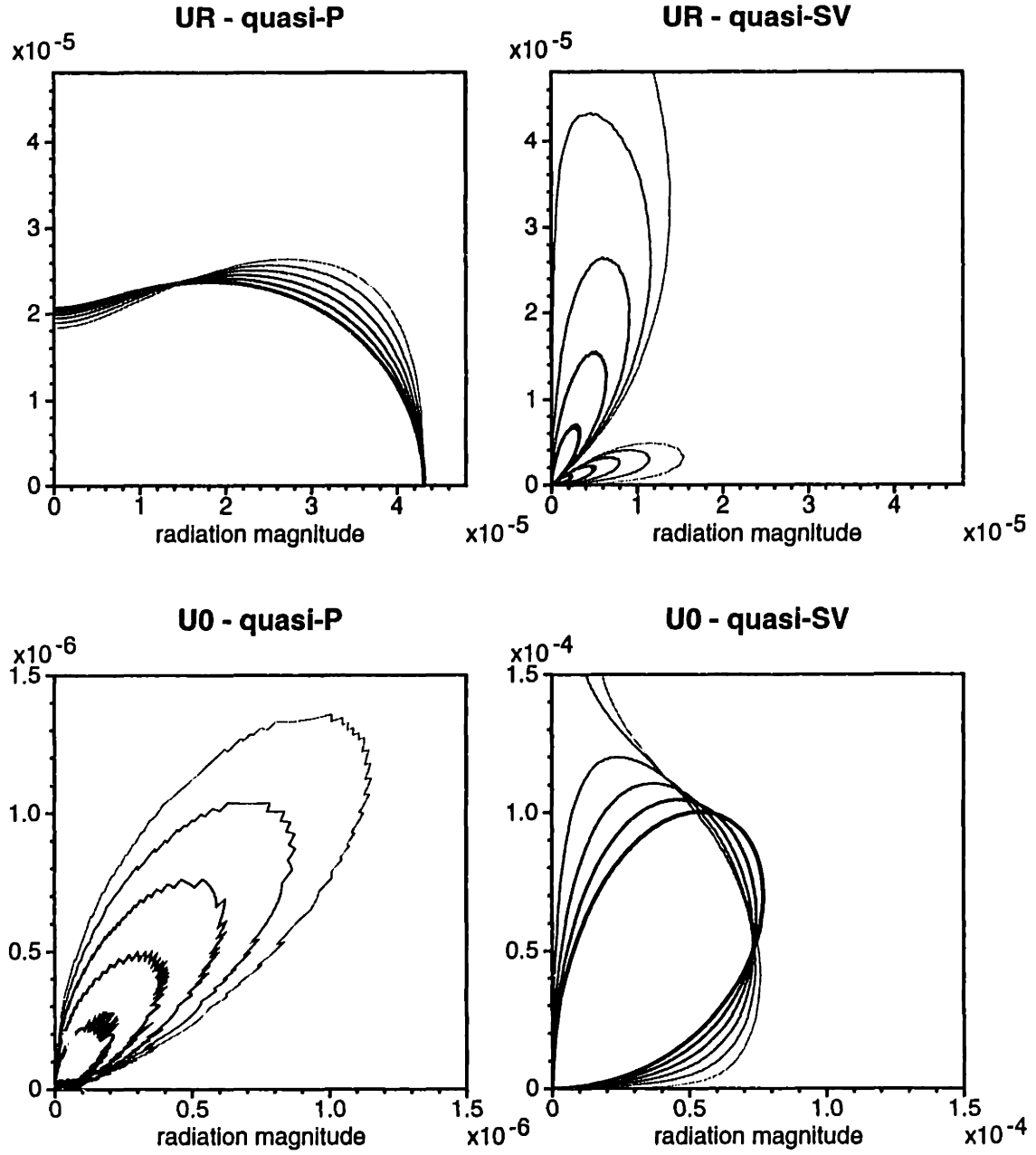

Figure 3-8: Radial and tangential patterns for an explosion source in a borehole ($r_0 = .1\ m$) penetrating six test models. Models result from decreasing c_{33} of an isotropic solid (bold line) ($c_{11} = c_{33} = 20$, $c_{13} = 8$, $c_{44} = c_{66} = 6$ (in GPa), and $\rho = 2\ g/cm^3$) from its original value 5% each time up to 25%. The thinner and lighter the line, the stronger the anisotropy.

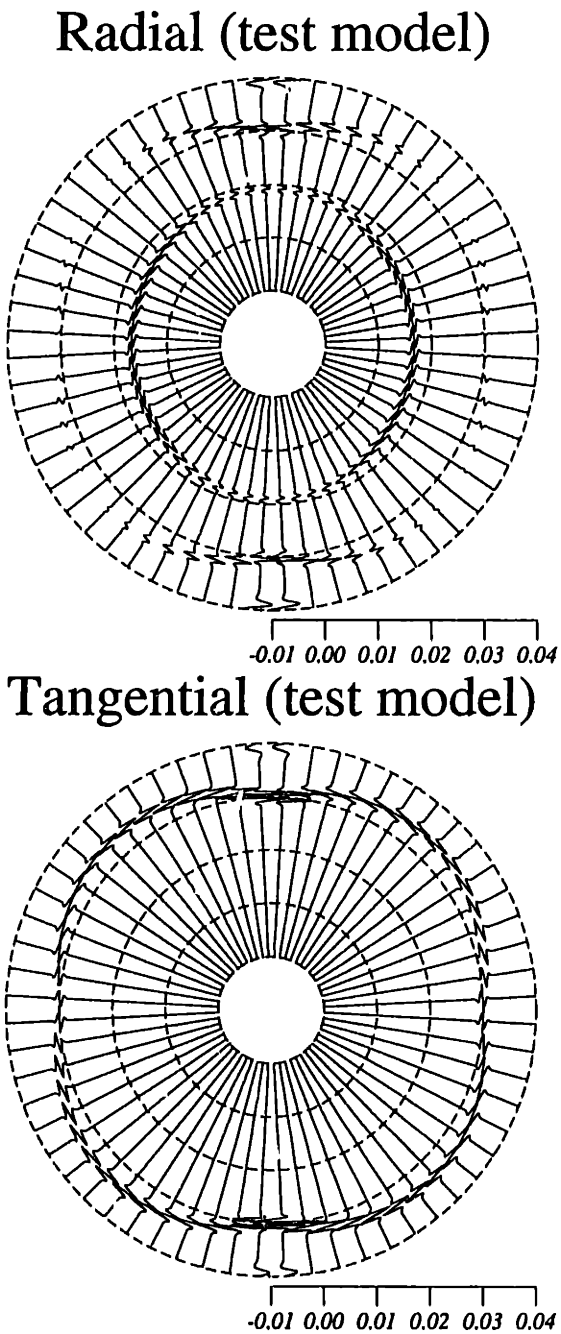

Figure 3-9: Displacements recorded by a circular receiver array 50 m away from the explosion source in a water-filled borehole penetrating the most anisotropic medium in Figure 3-8.

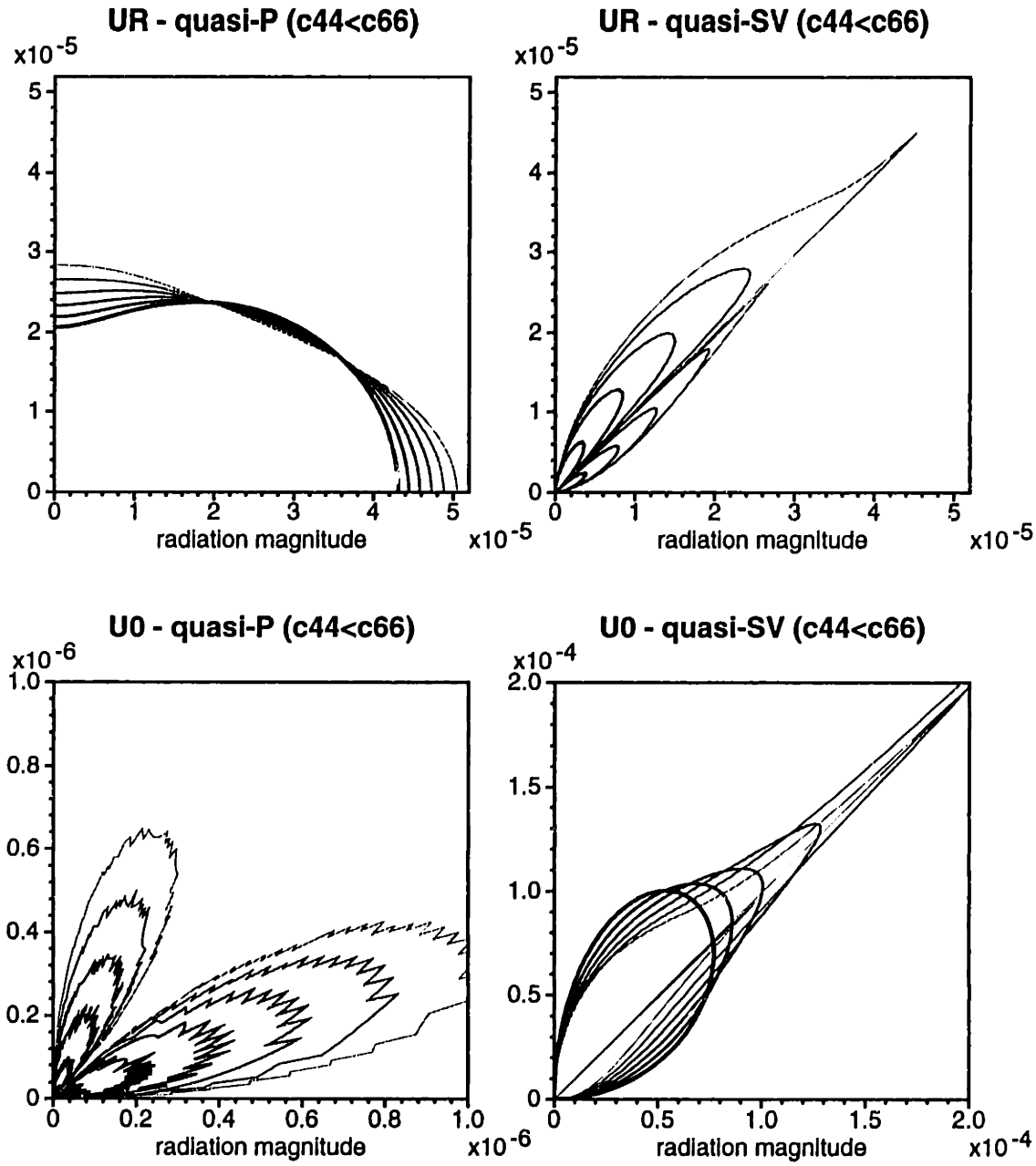

Figure 3-10: Same as Figure 3-8, except that the six test models result from decreasing c_{44} of the isotropic model in Figure 3-8, 5% each time up to 25%.

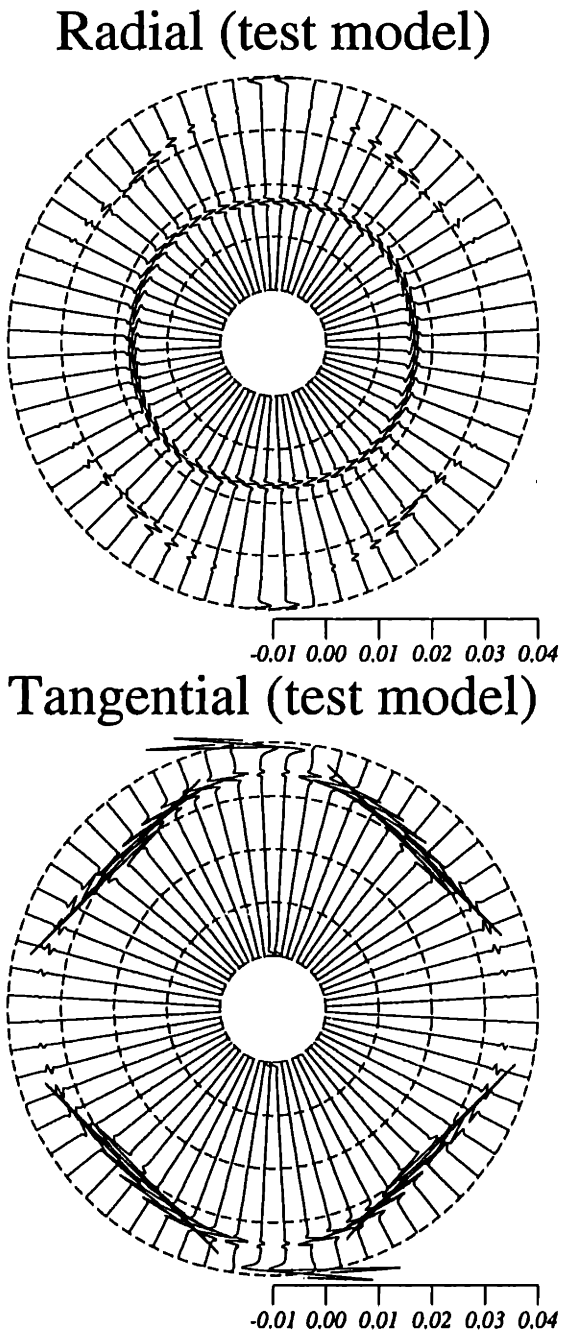

Figure 3-11: Displacements recorded by a circular receiver array 50 m away from the explosion source in a water-filled borehole penetrating the most anisotropic medium in Figure 3-10.

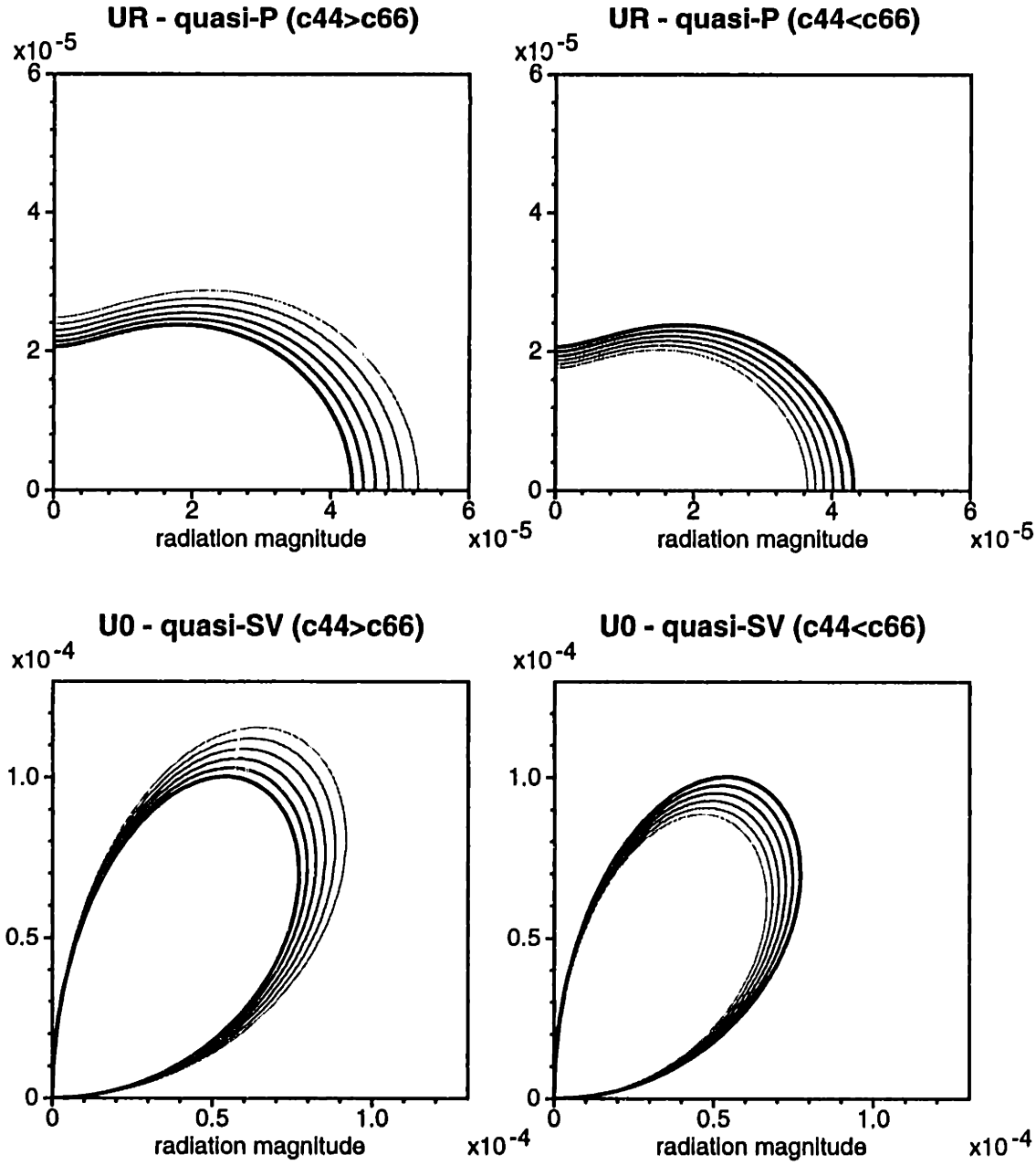

Figure 3-12: Radial and tangential patterns for an explosion source in a borehole ($r_0 = .1\ m$) penetrating six test models. Models result from increasing and decreasing c_{66} of an isotropic solid (bold line) ($c_{11} = c_{33} = 20$, $c_{13} = 8$, $c_{44} = c_{66} = 6$ (in GPa), and $\rho = 2\ g/cm^3$) from its original value 5% each time up to 25%. The thinner and lighter the line, the stronger the anisotropy.

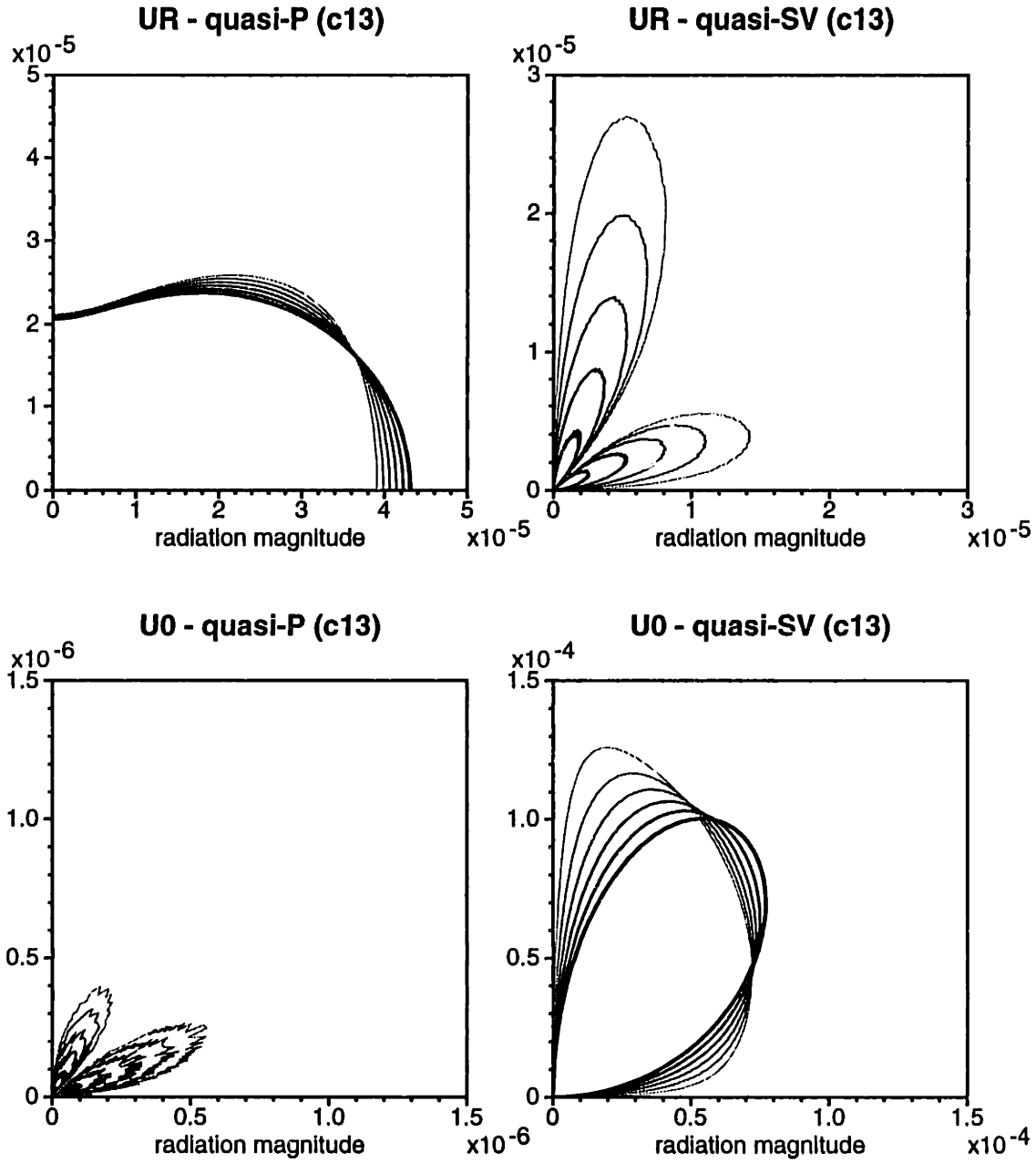

Figure 3-13: Same as Figure 3-12, except that the six test models result from increasing c_{13} of the isotropic model in Figure 3-12, 5% each time up to 25%.

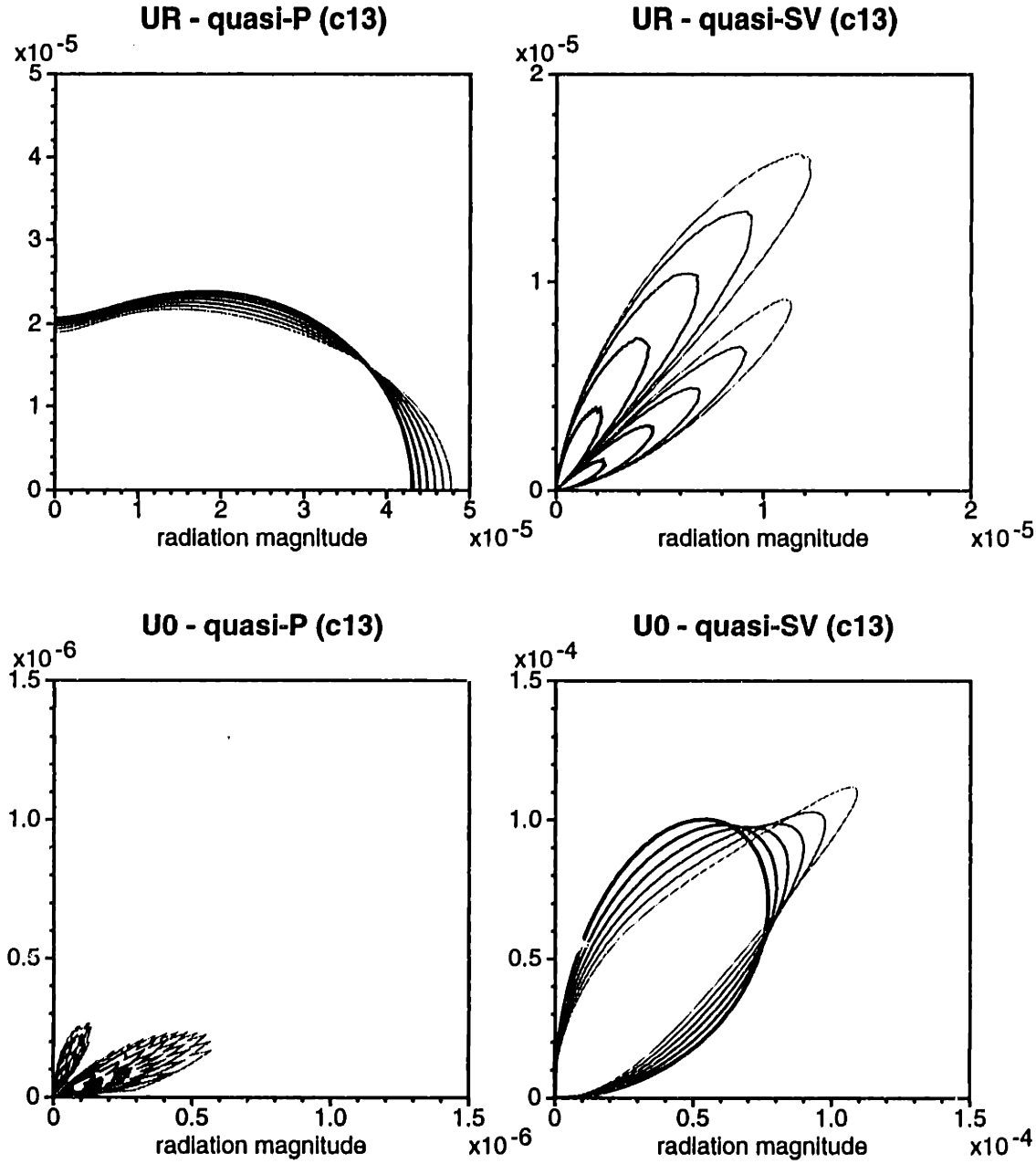

Figure 3-14: Same as Figure 3-12, except that the six test models result from decreasing c_{13} of the isotropic model in Figure 3-12, 5% each time up to 25%.

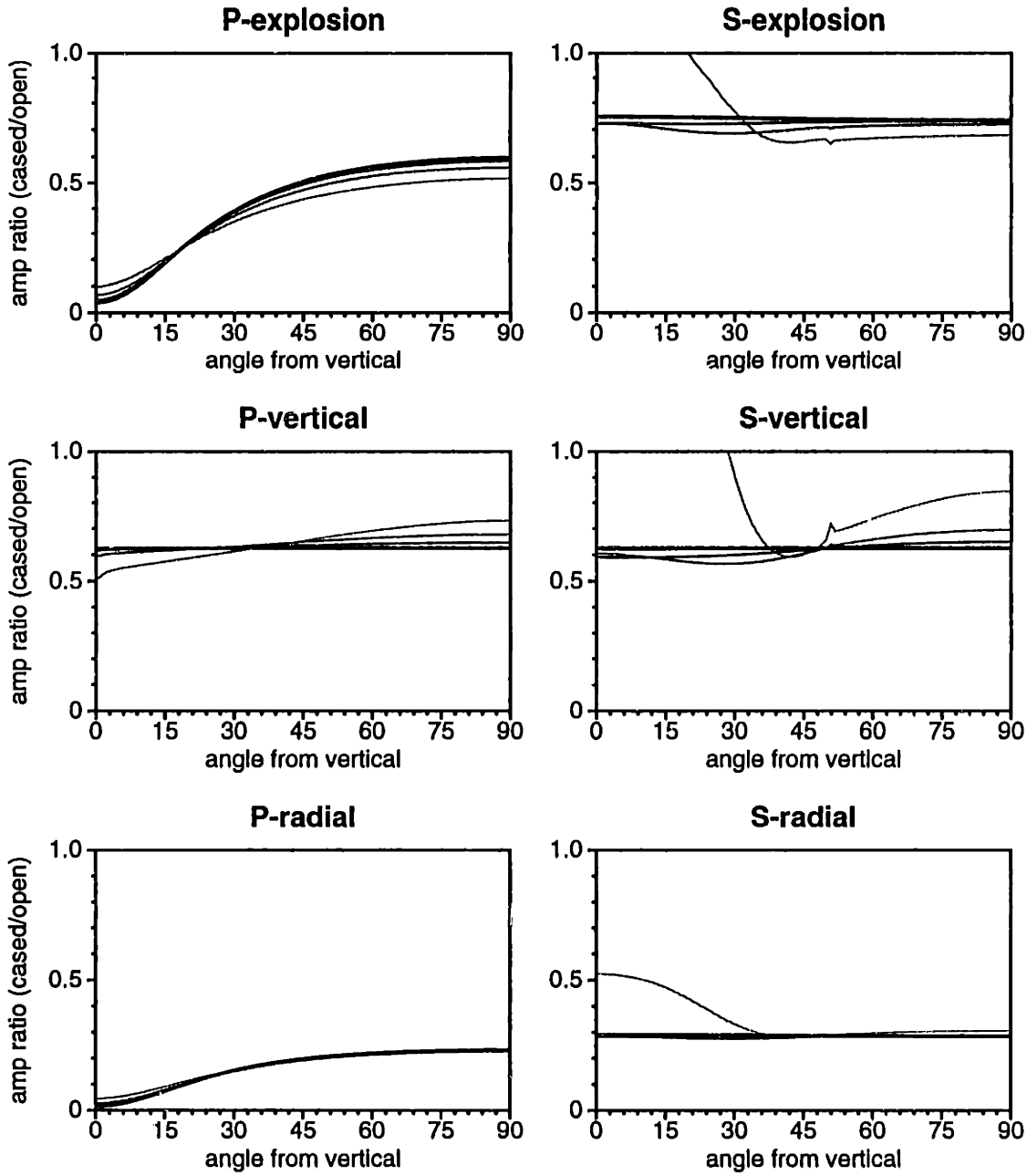

Figure 3-15: Effect of casing and cement on P and S wave radiation at different frequencies in a hard formation: Mesaverde Sandstone. Five frequencies, corresponding to dark to light lines, are: 10, 100, 500, 1000, 2000 Hz.

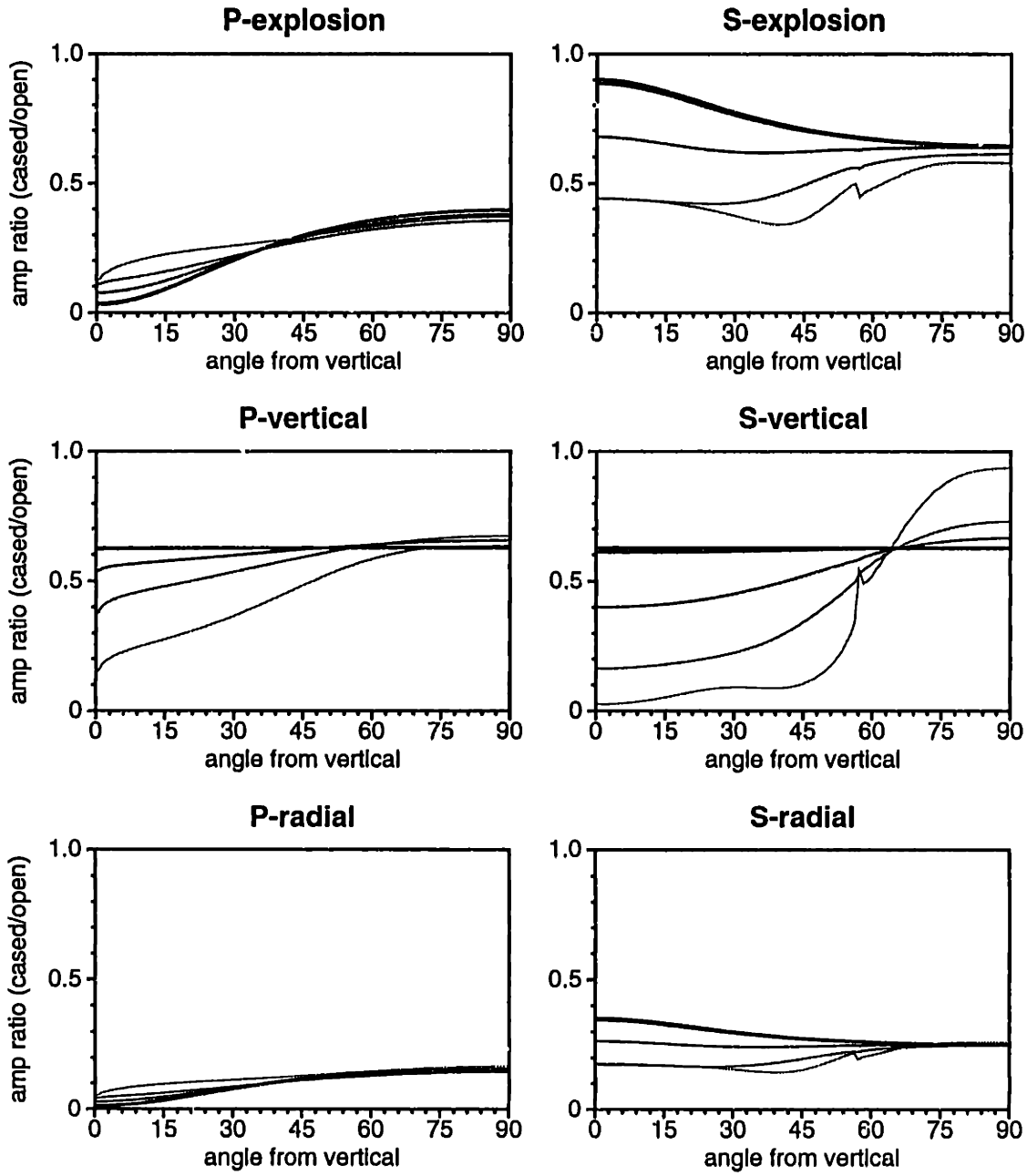

Figure 3-16: Effect of casing and cement on P and S wave radiation at different frequencies in a intermediate formation: isotropic test model used in previous figures. Five frequencies, corresponding to dark to light lines, are: 10, 100, 500, 1000, 2000 Hz.

Chapter 4

Boundary Element Modeling of Downhole Source Radiation in Layered Anisotropic Media

4.1 Introduction

Wave propagation along a fluid-filled borehole embedded in an isotropic or transversely isotropic half space has been studied by matching boundary conditions on the borehole wall and evaluating wave number integrals (e.g. Tsang and Rader, 1979; Cheng and Toksöz, 1981; Schoenberg *et al.*, 1981; White and Tongtaow, 1981; Schmitt and Bouchon, 1985). Tubman *et al.* (1984) applied the same method for waves in a cased borehole embedded in a homogeneous isotropic half space. If the formation becomes inhomogeneous, this method no longer applies and other numerical techniques have to be utilized. The finite difference and finite element methods have been extensively used by many researchers to investigate the acoustic logging problems (Stephen *et al.*, 1985; Randall *et al.*, 1991; Ellefsen, 1990). Difficulties arise when these two methods are used to model far-field radiation, because of the large scale difference between borehole diameter and formation extent. The ability to calculate the far-field

is severely restricted by memory space needed for both methods. Accuracy of these methods is also hampered by grid dispersion and inaccurate handling of fluid and formation interface.

A boundary element-based modeling technique proposed by Bouchon (1993) overcomes these problems. The boundary element method (BEM) is perfectly suited to the borehole geometry and the scale problem is easily dealt with. Bouchon (1993) used the method in an infinite open borehole in layered isotropic media. Prior to this implementation, BEM was used by Kawase (1988) in studying seismic wave scattering by surface topographies. Bouchon and Schmitt (1989) applied a boundary integral and discrete wavenumber formulation to model an irregular borehole in a homogeneous formation.

This chapter presents two extensions to Bouchon's BEM modeling method. First, the formation is generalized to incorporate transversely isotropic layers. This is necessary because many sedimentary rocks exhibit transverse isotropy (e.g. Thomsen, 1986). Including anisotropy will lead to a better understanding of real data. The other extension is to include casing and cement in the formulation. The effect of casing and cement was shown to have significant influence on the logging waveform (Tubman *et al.*, 1984). As shown in Chapter 3, they also affect wave diffraction and radiation from a borehole. Figure 4-1 shows the configuration of the problem. In addition to the explosion source, other source types, such as the vertical and orbital vibrators and bender source, are also accommodated. Examples are given at the end to illustrate the implementation.

4.2 The Indirect BEM Method

Generally speaking, there are two types of BEM implementation. The one often used by engineers can be called the *direct formulation*, where both the field and its gradient are solved for (e.g., Banerjee and Rutterfield, 1981; Brebbia and Dominguez, 1989).

This approach is usually seen in the static problems of elasticity. The one commonly used in wave propagation is named *indirect formulation*, where the quantities to be solved at the boundary have no physical meanings. Within the framework of this thesis, rigorous descriptions of these two approaches are presented in Appendix C, where they are shown to be equivalent. In the following, the indirect formulation is used and its implementation is discussed.

4.2.1 Indirect boundary integral equations

If a volume point source is placed inside a fluid-filled borehole, the total displacement potential in the borehole fluid is the sum of a direct potential pertaining to the source and a reflected potential due to the boundary. In the case of steady state radiation (or in the frequency domain) the reflected field can be expressed as an integral of a fictitious source distribution over the borehole surface, with Green's function being the integrand. Therefore, the displacement potential in the fluid is

$$\phi_1(\mathbf{x}) = \phi_i + \int_B dS' g_1(\mathbf{x}, \mathbf{x}')\psi(\mathbf{x}') \quad \text{for } \mathbf{x} \in V_b + B \ , \tag{4.1}$$

where, the volume of borehole fluid and the borehole surface are denoted by V_b and B. Subscript 1 stands for the fluid region and ϕ_i is the incident potential. The fictitious source distribution over the borehole surface is denoted by $\psi(\mathbf{x}')$. Integral kernel, g_1, is the scalar Green's function in an infinite homogeneous medium. It is in the well-known form

$$g_1(\mathbf{x}, \mathbf{x}') = \frac{e^{ik_f|\mathbf{x}-\mathbf{x}'|}}{4\pi|\mathbf{x}-\mathbf{x}'|}, \tag{4.2}$$

where, $k_f = \omega/c_f$ is the wavenumber for the fluid.

The above representation is not only physically intuitive but also mathematically rigorous. In fact, this representation can be obtained from the mathematical formulation of Huygen's principle with the assistance of the uniqueness and equivalence principles (see Appendix C or Banerjee and Butterfield, 1981). That is, the influence of the elastic medium on the wavefield inside the borehole is equivalent to impressing

a sheet of fictitious sources on the boundary between the fluid and the elastic medium. The fictitious source distribution density is the unknown function to be determined. Figure 4-2 shows the equivalent problem for the borehole fluid.

For the source-free elastic medium outside the borehole, the displacement field can be expressed as

$$\mathbf{U}_2(\mathbf{x}) = \int_B dS' \overline{\mathbf{G}}(\mathbf{x}, \mathbf{x}') \cdot \Psi(\mathbf{x}') \quad \text{for } \mathbf{x} \in V_e + B, \tag{4.3}$$

where, $\Psi(\mathbf{x}')$ is a vector fictitious source distribution on the boundary. $\overline{\mathbf{G}}(\mathbf{x}, \mathbf{x}')$ is the dyadic Green's function for displacement and has the following form for an homogeneous isotropic formation

$$\overline{\mathbf{G}}(\mathbf{x}, \mathbf{x}') = \frac{1}{\rho\omega^2} \left\{ k_\beta^2 \overline{\mathbf{I}} g_\beta(\mathbf{x}, \mathbf{x}') + \nabla\nabla \left[g_\beta(\mathbf{x}, \mathbf{x}') - g_\alpha(\mathbf{x}, \mathbf{x}') \right] \right\}. \tag{4.4}$$

Here, g_α and g_β are scalar Green's functions of the same form as in Equation 4.2, except that k_f is changed to k_α for the dilatational wave and to k_β for the shear wave. Equation 4.3 says that the displacement in the outside region, (V_e), results from the vector fictitious source distributed along the boundary. For axially symmetrical problems in cylindrical coordinates, the vector fictitious source can be decomposed into source distributions in radial and vertical directions. Therefore, one has to determine the two unknown distribution functions before calculating the displacement field in the elastic medium. Uniqueness of the calculated displacement is guaranteed by the equivalence principle and more fundamentally by the uniqueness theorem. Figure 4-3 describes the equivalent problem for the surrounding formation.

4.2.2 BEM implementation

The essence of Indirect BEM implementation is to discretize the boundary between borehole fluid and the surrounding formation into a set of small sized surfaces called elements. Each element is a ring-shaped surface with height dz and borehole radius r_0. The density of the fictitious source is assumed to be constant on each element.

According to the previous boundary integrals, a fictitious volume source distribution for the fluid, and a fictitious source vector for the elastic medium are required in order to uniquely describe the borehole source radiation. A fictitious source vector in an axially symmetrical system consists of the vertical and radial components only. Therefore, on each element, i, three unknowns are to be determined: the fictitious fluid volume source, V_i^f; the vertical source for the elastic medium, F_i^v; and the radial source for the elastic medium, F_i^r. Our goal is to obtain these sources on each element so that one can calculate the displacement fields in the elastic medium and the pressure in the fluid.

The maximum number of elements is restricted by the power of current computers and the specified accuracy. In practice, three elements per shortest wavelength are used and the number of elements depends on the time window and the fastest wave speed. Thus, the element heights dz satisfy

$$dz \leq \frac{\min(c, \beta, \alpha)}{3f}, \tag{4.5}$$

and the number of elements, N_e, is given by

$$N_e = \frac{t_{max} \times \max(c, \beta, \alpha)}{dz} = \frac{3f \times t_{max} \times \max(c, \beta, \alpha)}{\min(c, \beta, \alpha)}. \tag{4.6}$$

The frequency and the maximum time window are denoted by f and t_{max}. With each element, the usual fluid/solid boundary conditions have to be satisfied: i.e., continuity of normal displacements, continuity of normal stresses, and vanishing tangential stress of the solid,

$$\begin{aligned} U_r|_{r=r_0^+} - U_r|_{r=r_0^-} &= 0, \\ \sigma_{rr}|_{r=r_0^+} - \sigma_{rr}|_{r=r_0^-} &= 0, \\ \sigma_{rz}|_{r=r_0^+} &= 0. \end{aligned} \tag{4.7}$$

These boundary conditions are satisfied at the center of each element. Displacements and stresses (or pressure) at the center of each element are contributed by all three

fictitious sources on all the elements. To calculate the displacement at the j-th element due to a source at the i-th element, we use the indirect formulations in Equations 4.1 and 4.3. At the j-th element, the boundary conditions become

$$\begin{aligned}
\sum_{i=1}^{N_e} A_{ji}^f V_i^f + \sum_{i=1}^{N_e} A_{ji}^v F_i^v + \sum_{i=1}^{N_e} A_{ji}^r F_i^r &= D_j^u, \\
\sum_{i=1}^{N_e} B_{ji}^f V_i^f + \sum_{i=1}^{N_e} B_{ji}^v F_i^v + \sum_{i=1}^{N_e} B_{ji}^r F_i^r &= D_j^{\sigma_{rr}}, \\
\sum_{i=1}^{N_e} C_{ji}^v F_i^v + \sum_{i=1}^{N_e} C_{ji}^r F_i^r &= D_j^{\sigma_{rz}}.
\end{aligned} \tag{4.8}$$

A_{ji}^f, A_{ji}^v and A_{ji}^r represent displacements at the j-th element due to the volume, vertical, and radial ring sources of unit strength at the i-th element, respectively. They are surface integrals of the Green's functions over the surfaces of the borehole (bottom + wall). The B's and C's are the radial and tangential stresses at the j-th element due to sources at the i-th element. They are the surface integrals of the stress Green's function. The D's are the exciting fields (indicated by their superscripts) at the j-th element. With j ranging from 1 to N_e, we obtain $3 \times N_e$ equations that can be easily solved for the $3 \times N_e$ unknowns. Once these fictitious source densities are available, fields inside and outside the borehole can be easily obtained using Equations 4.1 and 4.3.

4.2.3 Element surface integral

Surface integration of Green's functions is accomplished in two steps. The integrals are first transformed into wave number integrals by applying the Sommerfeld integral representation to the function e^{ikR}/R. The wavenumber integration is then evaluated by the discrete wavenumber method.

Expressed in a horizontal wavenumber integral, the scalar Green's function, g_1, is

$$g_1 = \frac{i}{4\pi} \int_0^\infty \frac{k}{\nu_f} J_0(kD) e^{i\nu_f |z-z'|} dk, \tag{4.9}$$

where $\nu_f = \sqrt{k_f^2 - k^2}$ and $D = \sqrt{r^2 + r_0^2 - 2rr_0\cos(\varphi - \varphi_0)}$. Physically, this equation represents the synthesis of a spherical wavefront by infinitely many cylindrical wavefronts. It is the use of the Sommerfeld integral representation that allows vertical layering to be incorporated. Using the addition theorem for the zeroth order Bessel function (Watson, 1944)

$$J_0(kD) = \sum_{m=0}^{\infty} \varepsilon_m J_m(kr) J_m(kr_0) \cos m(\varphi - \varphi_0), \tag{4.10}$$

one obtains

$$g_1 = \frac{i}{4\pi} \sum_{m=0}^{\infty} \varepsilon_m \cos m(\varphi - \varphi_0) \int_0^{\infty} \frac{k}{\nu_f} J_m(kr_0) J_m(kr) e^{i\nu_f |z - z'|} dk, \tag{4.11}$$

where, $\varepsilon_1 = 1$ and $\varepsilon_2 = 2$, and J_m is the m-th order Bessel function of the first kind. Given the above relations, the $r_0 d\varphi_0$ part of surface integration ($r_0 d\varphi_0 dz$) simplifies the integrand of the wavenumber integral significantly, thanks to the orthogonal cosine and sine functions over the range of 0 to 2π. *The result of this integration represents the response of a circular ring source.* The dz part of the surface integral can be analytically evaluated through integrating the ring source results over z'. Thus, the element surface integration of the Green's function basically reduces to a horizontal wavenumber integral. Essentially, this simplification results from the axial symmetry of the problem.

As discussed in the first chapter, when a source and a receiver coincide, the static contribution must be included in the integrals that calculate certain stresses. The static contribution is $-\frac{1}{2}$ of the force strength.

The coefficients in Equation 4.8 form a fully populated, non-symmetrical, and complex matrix. This is often regarded as the disadvantage of BEM as compared to FEM or FDM. In the latter two methods, tridiagonal matrices are obtained, and a special faster algorithm exists for this kind of matrix. Nevertheless, this matrix can still be easily manipulated as the number of elements is not exceedingly high and the system of equations is only solved once for each frequency.

4.3 Ring Source Results in Isotropic Media

As mentioned in the previous section, the major task for the BEM algorithm comes down to the frequent evaluation of the element surface integral of the Green's function. This often causes great numerical difficulty if the element surface is irregular. Thanks to the circularly cylindrical nature of our problem, the surface integrals can be computed analytically. Their values are equal to the line integral (dz) of the circular source Green's functions. In his paper, Bouchon (1993) started from point force potentials to derive the potentials for ring forces. In this section, the displacements and stresses of the ring sources are obtained by integrating the Green's function directly over the ring.

4.3.1 Vertical ring source

For a vertical source located at (r_0, z'), $\mathbf{F}(\mathbf{x}) = \hat{z}\delta(z - z')\delta(r - r_0)$. According to the orthogonality of the set $\{1, \cos\varphi, \cos 2\varphi, ...\}$, integration over φ_0 is nonzero only for $m = 0$. i.e.,

$$\int_0^{2\pi} \frac{e^{ik_0 R}}{R} \hat{z}\, r_0 d\varphi_0 = \hat{z}\, 2\pi i r_0 \int_0^{\infty} \frac{k}{\nu} J_0(kr_0) J_0(kr) e^{i\nu|z-z'|} dk. \tag{4.12}$$

Using this result and Equation 4.4 in Equation 4.3, we obtain the displacements at point (r, z) by a ring of unit vertical forces at $\mathbf{x}_0 = (r_0, z')$,

$$U_r = \frac{\mathrm{sgn}(z - z')}{2\rho\omega^2} \int_0^{\infty} k^2 r_0 J_0(kr_0) J_1(kr) \left[e^{i\nu_b|z-z'|} - e^{i\nu_a|z-z'|}\right] dk, \tag{4.13}$$

$$U_z = \frac{i}{2\rho\omega^2} \int_0^{\infty} k r_0 J_0(kr_0) J_0(kr) \left[\frac{k^2}{\nu_b} e^{i\nu_b|z-z'|} + \nu_a e^{i\nu_a|z-z'|}\right] dk. \tag{4.14}$$

Substituting U_r and U_z into the equations for strain and stresses in the cylindrical coordinates, and bearing in mind that static contribution has to be taken into account in σ_{rz} as the observation point is at the source point, we obtain the stresses at $\mathbf{x} = (r, z)$

$$\sigma_{rr} = \frac{1}{2\rho\omega^2} \int_0^{\infty} k r_0 J_0(kr_0) I_0 dk, \tag{4.15}$$

$$
\begin{aligned}
I_0 = & \left\{-\lambda k_a^2 J_0(kr) - 2\mu k\left[kJ_0(kr) - J_1(kr)/r\right]\right\}\mathrm{sgn}(z-z')e^{i\nu_a|z-z'|} \\
& +2\mu k\left[kJ_0(kr) - J_1(kr)/r\right]\mathrm{sgn}(z-z')e^{i\nu_b|z-z'|}, \\
\sigma_{rz} = & -\frac{1}{2}\delta(z-z') + \frac{i}{2\rho\omega^2}\int_0^\infty k^2 r_0 J_0(kr_0)J_1(kr)I_1 dk, \qquad (4.16) \\
I_1 = & -2\mu\nu_a e^{i\nu_a|z-z'|} + \mu\left(\nu_b - k^2/\nu_b\right)e^{i\nu_b|z-z'|}\ , \\
\sigma_{zz} = & \frac{1}{2\rho\omega^2}\int_0^\infty k r_0 J_0(kr_0)J_0(kr)I_2 dk, \qquad (4.17) \\
I_2 = & \left(-\lambda k_a^2 - 2\mu\nu_a^2\right)\mathrm{sgn}(z-z')e^{i\nu_a|z-z'|} - 2\mu k^2 \mathrm{sgn}(z-z')e^{i\nu_b|z-z'|}\ .
\end{aligned}
$$

4.3.2 Radial ring source

For a radial force, $\mathbf{F}(\mathbf{x}) = [\hat{r}\cos(\varphi-\varphi_0) - \hat{\varphi}\sin(\varphi-\varphi_0)]\delta(r-r_0)\delta(z-z')$. Using the orthogonal property in the integration over φ_0, we obtain the displacements at (r,z) by a ring of unit radial forces at $\mathbf{x}' = (r_0, z')$,

$$
\begin{aligned}
U_r = & \frac{i}{2\rho\omega^2}\int_0^\infty k r_0 J_1(kr_0)J_1(kr)\left[\frac{k^2}{\nu_a}e^{i\nu_a|z-z'|} + \nu_b e^{i\nu_b|z-z'|}\right]dk, \qquad (4.18) \\
U_z = & \frac{\mathrm{sgn}(z-z')}{2\rho\omega^2}\int_0^\infty k^2 r_0 J_1(kr_0)J_0(kr)\left[e^{i\nu_a|z-z'|} - e^{i\nu_b|z-z'|}\right]dk. \qquad (4.19)
\end{aligned}
$$

Substituting U_r and U_z into the strain and stress equations in cylindrical coordinates, and adding the static term on σ_{rr} as the field point approaches the source point, we obtain stresses at $\mathbf{x} = (r,z)$

$$
\begin{aligned}
\sigma_{rr} = & -\frac{1}{2}\delta(z-z') + \frac{i}{2\rho\omega^2}\int_0^\infty k r_0 J_1(kr_0)I_3 dk, \qquad (4.20) \\
I_3 = & \ k/\nu_a\left\{\lambda k_a^2 J_0(kr) + 2\mu k\left[kJ_0(kr) - J_1(kr)/r\right]\right\}e^{i\nu_a|z-z'|} \\
& +2\mu\nu_b\left[kJ_0(kr) - J_1(kr)/r\right]e^{i\nu_b|z-z'|}, \\
\sigma_{rz} = & \frac{1}{2\rho\omega^2}\int_0^\infty k r_0 J_1(kr_0)J_1(kr)I_4 dk, \qquad (4.21) \\
I_4 = & \ \mu\mathrm{sgn}(z-z')\left[(k^2-\nu_b^2)e^{i\nu_b|z-z'|} - 2k^2 e^{i\nu_a|z-z'|}\right]\ , \\
\sigma_{zz} = & \frac{i}{2\rho\omega^2}\int_0^\infty k r_0 J_1(kr_0)J_0(kr)I_5 dk, \qquad (4.22) \\
I_5 = & \ k/\nu_a\left(\lambda k_a^2 + 2\mu\nu_a^2\right)e^{i\nu_a|z-z'|} - 2\mu k\nu_b e^{i\nu_b|z-z'|}\ .
\end{aligned}
$$

4.3.3 Torsional ring source

A torsional ring source is composed of a ring of forces in the direction of $\hat{r}\sin(\varphi - \varphi_0) + \hat{\varphi}\cos(\varphi - \varphi_0)$. Using the orthogonality in the integration over φ_0, we obtain the displacements at (r, z) by a ring of unit torsional forces at (r_0, z'),

$$U_\varphi = \frac{i}{2\mu}\int_0^\infty \frac{kr_0}{\nu_b} J_1(kr_0)J_1(kr)e^{i\nu_b|z-z'|}dk. \tag{4.23}$$

Using the cylindrical coordinate expressions for strain and stress, and adding a static contribution to $\sigma_{r\varphi}$, we have

$$\sigma_{r\varphi} = -\frac{1}{2}\delta(z-z') + \frac{i}{2}\int_0^\infty \frac{kr_0}{\nu_b} J_1(kr_0)[kJ_0(kr) - 2J_1(kr)/r]e^{i\nu_b|z-z'|}dk, \tag{4.24}$$

$$\sigma_{\varphi z} = -\frac{\mathrm{sgn}(z-z')}{2}\int_0^\infty kr_0 J_1(kr_0)J_1(kr)e^{i\nu_b|z-z'|}dk. \tag{4.25}$$

All other displacement and stress components vanish.

4.3.4 Explosive ring source in fluid

For a ring of explosive point sources, the displacement potential is obtained by integrating Equation 4.2 with respect to angle φ_0,

$$\phi = -\frac{i}{2}\int_0^\infty \frac{kr_0}{\nu_f} J_0(kr_0)J_0(kr)e^{i\nu_f|z-z'|}dk. \tag{4.26}$$

Upon taking the derivative of this potential with respect to r and z, and according to the discussion on singularity of the scalar Green's function in Appendix B.1, we obtain

$$U_r = -\frac{1}{2}\delta(z-z') + \frac{i}{2}\int_0^\infty \frac{k^2r_0}{\nu_f} J_0(kr_0)J_1(kr)e^{i\nu_f|z-z'|}dk, \tag{4.27}$$

$$U_z = \frac{\mathrm{sgn}(z-z')}{2}\int_0^\infty kr_0 J_0(kr_0)J_0(kr)e^{i\nu_f|z-z'|}dk. \tag{4.28}$$

The stresses are the pressure inside the fluid, and they are

$$\sigma_{rr} = \frac{i}{2\rho\omega^2}\int_0^\infty \frac{kr_0}{\nu_f} J_0(kr_0)J_0(kr)e^{i\nu_f|z-z'|}dk, \tag{4.29}$$

$$\sigma_{zz} = \sigma_{rr}, \tag{4.30}$$

$$\sigma_{rz} = 0. \tag{4.31}$$

4.4 Ring Source Results in TI Media

If the surrounding formation is anisotropic with a low degree of symmetry, a simple Green's function like Equation 4.4 does not exist in general. However, for a transversely isotropic medium, Chapter 1 provided a simple and numerically feasible Green's function similar to the isotropic Green's function. The dynamic Green's function in a transversely isotropic medium is

$$\overline{\mathbf{G}} = g\bar{\mathbf{I}}_t + \hat{z}\hat{z}L_z\phi - (c_{13}+c_{44})(\nabla_t\hat{z}+\hat{z}\nabla_t)\frac{\partial\phi}{\partial z} + \nabla_t\nabla_t\psi. \tag{4.32}$$

The individual symbols are

$$L_z = c_{11}\nabla_t^2 + c_{44}\frac{\partial^2}{\partial z^2} + \rho\omega^2, \tag{4.33}$$

$$g(\mathbf{x},\mathbf{x}') = \frac{i}{4\pi c_{44}}\int_0^\infty \frac{e^{i\nu_c|z-z'|}}{\nu_c} kJ_0(kD)dk, \tag{4.34}$$

$$\phi(\mathbf{x},\mathbf{x}') = \frac{-i}{4\pi c_{33}c_{44}}\int_0^\infty \frac{1}{\nu_b^2-\nu_a^2}\left(\frac{e^{i\nu_b|z-z'|}}{\nu_b} - \frac{e^{i\nu_a|z-z'|}}{\nu_a}\right) kJ_0(kD)dk, \tag{4.35}$$

$$\psi(\mathbf{x},\mathbf{x}') = \frac{i}{4\pi}\int_0^\infty f(z,z')\, kJ_0(kD)dk, \tag{4.36}$$

$$\begin{aligned} f(z,z') = &-\frac{(c_{13}+c_{44})^2\nu_a}{c_{33}c_{44}^2(\nu_b^2-\nu_a^2)(\nu_z^2-\nu_a^2)}e^{i\nu_a|z-z'|} \\ &+\frac{(c_{13}+c_{44})^2\nu_b}{c_{33}c_{44}^2(\nu_b^2-\nu_a^2)(\nu_z^2-\nu_b^2)}e^{i\nu_b|z-z'|} - \frac{c_{11}-c_{66}}{c_{44}^2\nu_c(\nu_z^2-\nu_c^2)}e^{i\nu_c|z-z'|}. \end{aligned} \tag{4.37}$$

In these equations, k is the horizontal wave number, $D = \sqrt{r^2+r_0^2-2rr_0\cos(\varphi-\varphi_0)}$ is the source-receiver distance. The five elastic constants are c_{11}, c_{33}, c_{13}, c_{44}, and c_{66}. ν_a, ν_b, and ν_c are the vertical wave numbers for the *quasi-P*, *quasi-SV*, and *quasi-SH* waves in the medium, respectively. ν_a and ν_b are the solutions of the following equation

$$\begin{aligned} c_{33}c_{44}k_z^4 &+ [(c_{11}c_{33}-c_{13}^2-2c_{13}c_{44})k^2 - (c_{33}+c_{44})\rho\omega^2]k_z^2 \\ &+ (c_{44}k^2-\rho\omega^2)(c_{11}k^2-\rho\omega^2) = 0, \end{aligned} \tag{4.38}$$

and $\nu_c = \sqrt{(\rho\omega^2 - c_{66}k^2)/c_{44}}$ and $\nu_z = \sqrt{(\rho\omega^2-c_{11}k^2)/c_{44}}$.

4.4.1 Vertical ring forces

For a vertical ring source of unit strength, $\mathbf{F} = \hat{z}\delta(z-z')\delta(r-r_0)$. Integration over φ_0 is nonzero only for $m = 0$ according to the orthogonality of the set $\{1, \cos\varphi, \cos 2\varphi, ...\}$. The two displacement components are

$$U_r = \frac{\mathrm{sgn}(z-z')}{2} \int_0^\infty S_{ab} k^2 r_0 J_0(kr_0) J_1(kr) \left[e^{i\nu_b|z-z'|} - e^{i\nu_a|z-z'|} \right] dk, \quad (4.39)$$

$$U_z = \frac{i}{2} \int_0^\infty k r_0 J_0(kr_0) J_0(kr) \left[S_b e^{i\nu_b|z-z'|} - S_a e^{i\nu_a|z-z'|} \right] dk, \quad (4.40)$$

where,

$$S_{ab} = \frac{c_{13}+c_{44}}{c_{33}c_{44}(\nu_b^2-\nu_a^2)}, \quad S_a = \frac{\nu_a^2-\nu_z^2}{c_{33}(\nu_b^2-\nu_a^2)\nu_a}, \quad S_b = \frac{\nu_b^2-\nu_z^2}{c_{33}(\nu_b^2-\nu_a^2)\nu_b}. \quad (4.41)$$

Using U_r and U_z in the equations for strain and stresses in cylindrical coordinates, and bearing in mind that static contribution has to be taken into account in σ_{rz} as the observation point is at the source point, we obtain stresses at $\mathbf{x} = (r, z)$

$$\sigma_{rr} = \frac{\mathrm{sgn}(z-z')}{2} \int_0^\infty k r_0 J_0(kr_0) I_0 dk, \quad (4.42)$$

$$I_0 = \left[-(c_{11}S_{ab}k^2 - c_{13}S_a\nu_a) J_0(kr) + 2c_{66}kS_{ab}J_1(kr)/r \right] e^{i\nu_a|z-z'|} + \left[(c_{11}S_{ab}k^2 - c_{13}S_b\nu_b) J_0(kr) - 2c_{66}kS_{ab}J_1(kr)/r \right] e^{i\nu_b|z-z'|},$$

$$\sigma_{rz} = -\frac{1}{2}\delta(z-z') + \frac{i}{2} \int_0^\infty k^2 r_0 J_0(kr_0) J_1(kr) I_1 dk, \quad (4.43)$$

$$I_1 = -c_{44}(S_{ab}\nu_a - S_a) e^{i\nu_a|z-z'|} + c_{44}(S_{ab}\nu_b - S_b) e^{i\nu_b|z-z'|},$$

$$\sigma_{zz} = \frac{\mathrm{sgn}(z-z')}{2} \int_0^\infty k r_0 J_0(kr_0) J_0(kr) I_2 dk, \quad (4.44)$$

$$I_2 = (-c_{13}S_{ab}k^2 + c_{33}S_a\nu_a) e^{i\nu_a|z-z'|} + (c_{13}S_{ab}k^2 - c_{33}S_b\nu_b) e^{i\nu_b|z-z'|}.$$

4.4.2 Radial ring forces

For a radial ring source of unit strength, $\mathbf{F}(\mathbf{x}) = [\hat{r}\cos(\varphi-\varphi_0) - \hat{\varphi}\sin(\varphi-\varphi_0)]\delta(r-r_0)\delta(z-z')$. Using orthogonality in the integration over φ_0, we obtain displacements at (r, z) by a ring of radial forces at $\mathbf{x}' = (r_0, z')$ in a TI medium

$$U_r = \frac{i}{2} \int_0^\infty k r_0 J_1(kr_0) J_1(kr) \left[T_a e^{i\nu_a|z-z'|} - T_b e^{i\nu_b|z-z'|} \right] dk, \quad (4.45)$$

$$U_z = \frac{\mathrm{sgn}(z-z')}{2}\int_0^\infty S_{ab}k^2 r_0 J_1(kr_0)J_0(kr)\left[e^{i\nu_a|z-z'|}-e^{i\nu_b|z-z'|}\right]dk. \quad (4.46)$$

The stresses are

$$\sigma_{rr} = -\frac{1}{2}\delta(z-z') + \frac{i}{2}\int_0^\infty kr_0 J_1(kr_0)I_3 dk, \quad (4.47)$$

$$I_3 = [(c_{11}T_a + c_{13}S_{ab}\nu_a)kJ_0(kr) - 2c_{66}T_a J_1(kr)/r]\, e^{i\nu_a|z-z'|}$$
$$- [(c_{11}T_b + c_{13}S_{ab}\nu_b)kJ_0(kr) - 2c_{66}T_b J_1(kr)/r]\, e^{i\nu_b|z-z'|},$$

$$\sigma_{rz} = \frac{\mathrm{sgn}(z-z')}{2}\int_0^\infty kr_0 J_1(kr_0)J_1(kr)I_4 dk, \quad (4.48)$$

$$I_4 = c_{44}\left\{(T_b\nu_b + k^2 S_{ab})e^{i\nu_b|z-z'|} - (T_a\nu_a + k^2 S_{ab})e^{i\nu_a|z-z'|}\right\},$$

$$\sigma_{zz} = \frac{i}{2}\int_0^\infty kr_0 J_1(kr_0)J_0(kr)I_5 dk, \quad (4.49)$$

$$I_5 = k(c_{13}T_a + c_{33}S_{ab}\nu_a)e^{i\nu_a|z-z'|} - k(c_{13}T_b + c_{33}S_{ab}\nu_b)e^{i\nu_b|z-z'|}.$$

In the above equations,

$$T_a = \frac{(c_{13}+c_{44})^2\nu_a k^2}{c_{33}c_{44}^2(\nu_b^2-\nu_a^2)(\nu_z^2-\nu_a^2)}, \quad T_b = \frac{(c_{13}+c_{44})^2\nu_b k^2}{c_{33}c_{44}^2(\nu_b^2-\nu_a^2)(\nu_z^2-\nu_b^2)}. \quad (4.50)$$

4.4.3 Torsional ring forces

A torsional ring source is composed of a ring of forces in direction $\mathbf{F} = \hat{r}\sin(\varphi-\varphi_0) + \hat{\varphi}\cos(\varphi-\varphi_0)$. Using the orthogonality in the integration over φ_0, we obtain the only displacement component

$$U_\varphi = \frac{i}{2c_{44}}\int_0^\infty kr_0 J_1(kr_0)J_1(kr)\frac{e^{i\nu_c|z-z'|}}{\nu_c}dk. \quad (4.51)$$

The two related stresses are

$$\sigma_{r\theta} = -\frac{1}{2}\delta(z-z') + \frac{i}{2}\frac{c_{66}}{c_{44}}\int_0^\infty \frac{kr_0}{\nu_c}J_1(kr_0)[kJ_0(kr) - 2J_1(kr)/r]e^{i\nu_c|z-z'|}dk, \quad (4.52)$$

$$\sigma_{\theta z} = -\frac{1}{2}\mathrm{sgn}(z-z')\int_0^\infty kr_0 J_1(kr_0)J_1(kr)e^{i\nu_c|z-z'|}dk. \quad (4.53)$$

4.5 Waves in Horizontally Layered TI Media: Outside the Borehole

From the displacement and stress expressions for the circular sources, we may speculate that for a given k (plane wave), the recorded displacements and stresses at a receiver away from the circular source in a layered TI medium would have the following form

$$\begin{aligned}
U_r(r,z) &= \int_0^\infty u_r(k,z)\, kJ_1(kr)dk, \\
U_z(r,z) &= \int_0^\infty u_z(k,z)\, kJ_0(kr)dk, \\
\sigma_{zz}(r,z) &= \int_0^\infty \tau_{zz}(k,z)\, kJ_0(kr)dk, \\
\sigma_{rz}(r,z) &= \int_0^\infty \tau_{rz}(k,z)\, kJ_1(kr)dk, \\
U_\theta(r,z) &= \int_0^\infty u_\theta(k,z)\, kJ_1(kr)dk, \\
\sigma_{\theta z}(r,z) &= \int_0^\infty \tau_{\theta z}(k,z) k\, J_1(kr)dk.
\end{aligned} \tag{4.54}$$

These displacements and stresses satisfy the stress-strain relation and the wave equation in cylindrical coordinates with axial symmetry. These equations can be manipulated to yield (Takeuchi and Saito, 1972)

$$\begin{aligned}
\frac{\partial U_z}{\partial z} &= -\frac{c_{13}}{c_{33}}\left(\frac{\partial U_r}{\partial r}+\frac{U_r}{r}\right)+\frac{1}{c_{33}}\sigma_{zz}, \\
\frac{\partial U_r}{\partial z} &= -\frac{\partial U_z}{\partial r}+\frac{1}{c_{44}}\sigma_{rz}, \\
\frac{\partial \sigma_{zz}}{\partial z} &= -\rho\omega^2 U_z\left(\frac{\partial \sigma_{rz}}{\partial r}+\frac{\sigma_{rz}}{r}\right), \\
\frac{\partial \sigma_{rz}}{\partial z} &= \left(-c_{11}+\frac{c_{13}^2}{c_{33}}\right)\frac{\partial}{\partial r}\left(\frac{\partial U_r}{\partial r}+\frac{U_r}{r}\right)-\frac{c_{13}}{c_{33}}\frac{\partial \sigma_{zz}}{\partial r}-\rho\omega^2 U_r, \\
\frac{\partial U_\theta}{\partial z} &= \frac{1}{c_{44}}\sigma_{\theta z}, \\
\frac{\partial \sigma_{\theta z}}{\partial z} &= -\frac{\partial}{\partial r}\left(\frac{\partial U_\theta}{\partial r}+\frac{U_\theta}{r}\right)-\rho\omega^2 U_\theta.
\end{aligned} \tag{4.55}$$

These equations reduce to equations for the unknown integrands in Equation 4.54. Written in a matrix form, they are

$$\frac{\partial}{\partial z}\begin{bmatrix} u_r \\ u_z \\ \tau_{zz} \\ \tau_{rz} \end{bmatrix} = \begin{bmatrix} 0 & k & 0 & \frac{1}{c_{44}} \\ -k\frac{c_{13}}{c_{33}} & 0 & \frac{1}{c_{33}} & 0 \\ 0 & -\rho\omega^2 & 0 & -k \\ k^2\left(c_{11}-\frac{c_{13}^2}{c_{33}}\right)-\rho\omega^2 & 0 & k\frac{c_{13}}{c_{33}} & 0 \end{bmatrix}\begin{bmatrix} u_r \\ u_z \\ \tau_{zz} \\ \tau_{rz} \end{bmatrix}, \tag{4.56}$$

and,

$$\frac{\partial}{\partial z}\begin{bmatrix} u_\theta \\ \tau_{\theta z} \end{bmatrix} = \begin{bmatrix} 0 & \frac{1}{c_{44}} \\ k^2 c_{66}-\rho\omega^2 & 0 \end{bmatrix}\begin{bmatrix} u_\theta \\ \tau_{\theta z} \end{bmatrix}. \tag{4.57}$$

The solutions for the two differential equations are

$$(u_r, u_z, \tau_{zz}, \tau_{rz})^T = D_4 e^{\Lambda_4(z-z')} D_4^{-1}(u_r^0, u_z^0, \tau_{zz}^0, \tau_{rz}^0)^T, \tag{4.58}$$

$$(u_\theta, \tau_{\theta z})^T = D_2 e^{\Lambda_2(z-z')} D_2^{-1}(u_\theta, \tau_{\theta z})^T. \tag{4.59}$$

Λ_4 and D_4, and Λ_2 and D_2, are the eigenvalue and the eigenvector matrices of the coefficient matrices in Equation 4.56 and Equation 4.57. The six eigenvalues are

$$\nu_{1,2} = i\nu_{a,b}, \quad \nu_{3,4} = -i\nu_{a,b}, \quad \text{and } \nu_{5,6} = \pm i\nu_c. \tag{4.60}$$

The corresponding eigenvector (column vector) matrices and their inverses are

$$D_4 = \begin{bmatrix} 1 & 1 & 1 & 1 \\ -x_2^a & -x_2^b & x_2^a & x_2^b \\ x_3^a & x_3^b & x_3^a & x_3^b \\ -x_4^a & -x_4^b & x_4^a & x_4^b \end{bmatrix}, \quad D_2 = \begin{bmatrix} 1 & 1 \\ ic_{44}\nu_c & -ic_{44}\nu_c \end{bmatrix}, \tag{4.61}$$

and,

$$D_4^{-1} = \begin{bmatrix} px_3^b & qx_4^b & -p & -qx_2^b \\ -px_3^a & -qx_4^a & p & qx_2^a \\ px_3^b & -qx_4^b & -p & qx_2^b \\ -px_3^a & qx_4^a & p & -qx_2^a \end{bmatrix}, \quad D_2^{-1} = \begin{bmatrix} \frac{1}{2} & \frac{1}{2ic_{44}\nu_c} \\ \frac{1}{2} & \frac{-1}{2ic_{44}\nu_c} \end{bmatrix}, \tag{4.62}$$

where,

$$
\begin{aligned}
x_2^{a,b} &= \frac{-ik\nu_{a,b}(c_{13}+c_{44})}{\rho\omega^2 - k^2 c_{44} - c_{33}\nu_{a,b}^2}, \\
x_3^{a,b} &= kc_{13} + ic_{33}\nu_{a,b}x_2^{a,b}, \\
x_4^{a,b} &= c_{44}(i\nu_{a,b} - kx_2^{a,b}), \\
p &= \frac{0.5}{x_3^b - x_3^a}, \\
q &= \frac{0.5}{x_4^a x_2^b - x_4^b x_2^a}.
\end{aligned}
$$

If a positive z-coordinate is chosen to point downward, the first two columns of D_4 and the first two rows of D_4^{-1} correspond to the up-going P and S waves. The others are for the down-going waves.

The stress-displacement vectors, $(u_r, u_z, \tau_{zz}, \tau_{rz})^T$ and $(u_\theta, \tau_{\theta z})^T$, represent the z-dependent part of displacements and stresses at level z due to up and down-going $P-SV$ and SH waves. If the amplitudes of these waves are represented by wave vectors $\mathbf{v}_4$ and $\mathbf{v}_2$, with $\mathbf{v}_4 = (P_u, SV_u, P_d, SV_d)^T$ and $\mathbf{v}_2 = (SH_u, SH_d)^T$, the stress-displacement vectors can be written as

$$
(u_r, u_z, \tau_{zz}, \tau_{rz})^T = D_4(z)\mathbf{v}_4(z), \quad (u_\theta, \tau_{\theta z})^T = D_2(z)\mathbf{v}_2(z). \tag{4.63}
$$

That is, the contribution of each wave to the displacements and stresses is allocated according to the eigenvector or the direction of each wave. The relation between two wave vectors at different levels of the same medium is obtained by substituting Equation 4.63 into Equations 4.58 and 4.59, i.e.,

$$
\mathbf{v}_4(z) = e^{\Lambda_4(z-z')}\mathbf{v}_4(z'), \quad \mathbf{v}_2(z) = e^{\Lambda_2(z-z')}\mathbf{v}_2(z'). \tag{4.64}
$$

The relation between two wave vectors on two sides of an interface separating two different TI media follows from the boundary conditions of two media in welded contact: the continuous stress-displacement vector $(u_r, u_z, \tau_{zz}, \tau_{rz})^T$ and $(u_\theta, \tau_{\theta z})^T$. Thus, we have

$$
\mathbf{v}_4(z_i^+) = D_4^{-1}(z_i^+)D_4(z_i^-)\mathbf{v}_4(z_i^-), \quad \mathbf{v}_2(z_i^+) = D_2^{-1}(z_i^+)D_2(z_i^-)\mathbf{v}_2(z_i^-). \tag{4.65}
$$

where, z_i^+ denotes the side above the interface and z_i^- below the interface.

4.5.1 Reflection and transmission coefficients

The relations in Equation 4.65 can be used to obtain the reflection and transmission coefficients of down-going and up-going waves at an interface (e.g., Mandal, 1991). If these reflection and transmission coefficients are denoted by 2×2 matrices R_d, T_d, R_u and T_u for the $P-SV$ case, and r_d, t_d, r_u and t_u for the SH case, we have

$$\begin{bmatrix} P_u^+ \\ SV_u^+ \\ P_d^+ \\ SV_d^+ \end{bmatrix} = \begin{bmatrix} R_d & T_u \\ \mathbf{1} & \mathbf{0} \end{bmatrix} \begin{bmatrix} P_d^+ \\ SV_d^+ \\ P_u^- \\ SV_u^- \end{bmatrix}, \quad \begin{bmatrix} SH_u^+ \\ SH_d^+ \end{bmatrix} = \begin{bmatrix} r_d & t_u \\ 0 & 1 \end{bmatrix} \begin{bmatrix} SH_d^+ \\ SH_u^- \end{bmatrix}, \tag{4.66}$$

and,

$$\begin{bmatrix} P_u^- \\ SV_u^- \\ P_d^- \\ SV_d^- \end{bmatrix} = \begin{bmatrix} \mathbf{0} & \mathbf{1} \\ T_d & R_u \end{bmatrix} \begin{bmatrix} P_d^+ \\ SV_d^+ \\ P_u^- \\ SV_u^- \end{bmatrix}, \quad \begin{bmatrix} SH_u^- \\ SH_d^- \end{bmatrix} = \begin{bmatrix} 0 & 1 \\ t_d & r_u \end{bmatrix} \begin{bmatrix} SH_d^+ \\ SH_u^- \end{bmatrix}. \tag{4.67}$$

Substituting Equations 4.66 and 4.67 into Equation 4.65 and defining W (4×4) and w (2×2) as the resultant matrices of $D_4^{-1}(z_i^+)D_4(z_i^-)$ and $D_2^{-1}(z_i^+)D_2(z_i^-)$, we then have

$$\begin{bmatrix} R_d & T_u \\ \mathbf{1} & \mathbf{0} \end{bmatrix} = \begin{bmatrix} W_{11} & W_{12} \\ W_{21} & W_{22} \end{bmatrix} \begin{bmatrix} \mathbf{0} & \mathbf{1} \\ T_d & R_u \end{bmatrix}, \tag{4.68}$$

$$\begin{bmatrix} r_d & t_u \\ 1 & 0 \end{bmatrix} = \begin{bmatrix} w_{11} & w_{12} \\ w_{21} & w_{22} \end{bmatrix} \begin{bmatrix} 0 & 1 \\ t_d & r_u \end{bmatrix}. \tag{4.69}$$

In the above, the 2×2 zero and identity matrices are represented by $\mathbf{0}$ and $\mathbf{1}$. The 2×2 submatrices of the 4×4 matrix W are represented by W_{11}, W_{12}, W_{21} and W_{22}. Solving the above matrix equation, we obtain the expression of reflection and

transmission matrices in terms of W_{ij}

$$\begin{bmatrix} R_d & T_u \\ T_d & R_u \end{bmatrix} = \begin{bmatrix} W_{12}W_{22}^{-1} & W_{11} - W_{12}W_{22}^{-1}W_{21} \\ W_{22}^{-1} & -W_{22}^{-1}W_{21} \end{bmatrix}, \tag{4.70}$$

$$\begin{bmatrix} r_d & t_u \\ t_d & r_u \end{bmatrix} = \begin{bmatrix} w_{12}w_{22}^{-1} & w_{11} - w_{12}w_{22}^{-1}w_{21} \\ w_{22}^{-1} & -w_{22}^{-1}w_{21} \end{bmatrix}. \tag{4.71}$$

Equations 4.70 and 4.71 apply only to a single interface separating two half spaces. These are the simple reflection or transmission coefficients. To calculate the generalized reflection and transmission coefficient for a stack of layers, the reflectivity method (Kennet, 1983; Müller, 1985) can be followed.

Special treatment is needed when the interface in consideration is a free surface (earth surface) or a fluid/solid contact (ocean bottom). For the free surface, application of the two boundary conditions (zero stresses) to Equation 4.63 results in a relation between the up and down-going waves beneath the free surface

$$\begin{bmatrix} D_{31} & D_{32} \\ D_{41} & D_{42} \end{bmatrix} \begin{bmatrix} P_u^- \\ SV_u^- \end{bmatrix} + \begin{bmatrix} D_{33} & D_{34} \\ D_{43} & D_{44} \end{bmatrix} \begin{bmatrix} P_d^- \\ SV_d^- \end{bmatrix} = 0, \tag{4.72}$$

where, D_{ij} refers to the elements of the eigenvector matrix D. The reflection coefficient of the free surface, R_u^f, and defined through $[P_d^-, SV_d^-]^T = R_u^f [P_u^-, SV_u^-]^T$, is

$$R_u^f = -\begin{bmatrix} D_{33} & D_{34} \\ D_{43} & D_{44} \end{bmatrix}^{-1} \begin{bmatrix} D_{31} & D_{32} \\ D_{41} & D_{42} \end{bmatrix}. \tag{4.73}$$

For a fluid/solid contact, the reflection and transmission coefficients can be obtained by writing out the displacement-pressure vector and applying the three boundary conditions. The procedures are given in the next section, where fluid-solid interfaces are more pertinent.

4.5.2 Initial wave amplitudes for the reflectivity method

Given the reflection and transmission coefficients at a single interface, the reflectivity method (Kennett, 1983, Müller, 1985) can be used to calculate the generalized reflec-

tion and transmission coefficient within any layer. As a personal preference, Müller's notation is followed in this thesis. The only distinction is that in Müller's paper the reflection and transmission coefficients were the ratio of potentials. While in our case these coefficients are the ratio of wave amplitudes. Thus, the input to the reflectivity code has to be the direct wave amplitudes.

These wave amplitudes can be obtained by applying the inverse eigenvector operator to the stress-displacement vector of the direct waves, as indicated by Equation 4.63. According to Section 4.4, the direct up-going wave stress-displacement for a vertical ring force is,

$$\begin{bmatrix} u_r \\ u_z \\ \tau_{zz} \\ \tau_{rz} \end{bmatrix}_v = \begin{bmatrix} \mathrm{sgn}(z-z')kS_{ab} \\ iS_b \\ \mathrm{sgn}(z-z')(c_{13}S_{ab}k^2 - c_{33}S_b\nu_b) \\ ikc_{44}(S_{ab}\nu_b - S_b) \end{bmatrix} \frac{r_0 J_0(kr_0)}{2} e^{i\nu_b|z-z'|} + \begin{bmatrix} -\mathrm{sgn}(z-z')kS_{ab} \\ -iS_a \\ -\mathrm{sgn}(z-z')(c_{13}S_{ab}k^2 - c_{33}S_a\nu_a) \\ -ikc_{44}(S_{ab}\nu_a - S_a) \end{bmatrix} \frac{r_0 J_0(kr_0)}{2} e^{i\nu_a|z-z'|}. \quad (4.74)$$

And, for a radial ring force, the vector is

$$\begin{bmatrix} u_r \\ u_z \\ \tau_{zz} \\ \tau_{rz} \end{bmatrix}_r = \begin{bmatrix} -iT_b \\ -\mathrm{sgn}(z-z')kS_{ab} \\ -ik(c_{13}T_b + c_{33}S_{ab}\nu_b) \\ \mathrm{sgn}(z-z')c_{44}(T_b\nu_b + k^2S_{ab}) \end{bmatrix} \frac{r_0 J_1(kr_0)}{2} e^{i\nu_b|z-z'|} + \begin{bmatrix} iT_a \\ \mathrm{sgn}(z-z')kS_{ab} \\ ik(c_{13}T_a + c_{33}S_{ab}\nu_a) \\ -\mathrm{sgn}(z-z')c_{44}(T_a\nu_a + k^2S_{ab}) \end{bmatrix} \frac{r_0 J_1(kr_0)}{2} e^{i\nu_a|z-z'|}. \quad (4.75)$$

Before applying the inverse eigenvector operator to above stress-displacement vectors,

we rewrite the operator by noticing

$$q = \frac{\rho\omega^2 - k^2 c_{44}}{c_{44}\nu_a\nu_b} p = \frac{\nu_c^2}{\nu_a\nu_b} p, \quad \text{where, } \nu_c^2 = \frac{\rho\omega^2}{c_{44}} - k^2. \tag{4.76}$$

The eigenvector matrix becomes

$$D_4^{-1} = p \begin{bmatrix} x_3^b & \frac{\nu_c^2}{\nu_a\nu_b}x_4^b & -1 & -\frac{\nu_c^2}{\nu_a\nu_b}x_2^b \\ -x_3^a & -\frac{\nu_c^2}{\nu_a\nu_b}x_4^a & 1 & \frac{\nu_c^2}{\nu_a\nu_b}x_2^a \\ x_3^b & -\frac{\nu_c^2}{\nu_a\nu_b}x_4^b & -1 & \frac{\nu_c^2}{\nu_a\nu_b}x_2^b \\ -x_3^a & \frac{\nu_c^2}{\nu_a\nu_b}x_4^a & 1 & -\frac{\nu_c^2}{\nu_a\nu_b}x_2^a \end{bmatrix} = q \begin{bmatrix} \frac{\nu_a\nu_b}{\nu_c^2}x_3^b & x_4^b & -\frac{\nu_a\nu_b}{\nu_c^2} & -x_2^b \\ -\frac{\nu_a\nu_b}{\nu_c^2}x_3^a & -x_4^a & \frac{\nu_a\nu_b}{\nu_c^2} & x_2^a \\ \frac{\nu_a\nu_b}{\nu_c^2}x_3^b & -x_4^b & -\frac{\nu_a\nu_b}{\nu_c^2} & x_2^b \\ -\frac{\nu_a\nu_b}{\nu_c^2}x_3^a & x_4^a & \frac{\nu_a\nu_b}{\nu_c^2} & -x_2^a \end{bmatrix}. \tag{4.77}$$

Applying D_4^{-1} to the stress-displacement vectors, we obtain the following simple expressions for the up and down-going P and SV wave amplitudes

$$\begin{bmatrix} P_u \\ SV_u \\ P_d \\ SV_d \end{bmatrix}_v = D_4^{-1} \begin{bmatrix} u_r \\ u_z \\ \tau_{zz} \\ \tau_{rz} \end{bmatrix}_v = \begin{bmatrix} -pe^{-i\nu_a(z-z')} \\ pe^{-i\nu_b(z-z')} \\ pe^{i\nu_a(z-z')} \\ -pe^{i\nu_b(z-z')} \end{bmatrix} r_0 J_0(kr_0), \tag{4.78}$$

$$\begin{bmatrix} P_u \\ SV_u \\ P_d \\ SV_d \end{bmatrix}_r = D_4^{-1} \begin{bmatrix} u_r \\ u_z \\ \tau_{zz} \\ \tau_{rz} \end{bmatrix}_r = \begin{bmatrix} -qx_2^b e^{-i\nu_a(z-z')} \\ qx_2^a e^{-i\nu_b(z-z')} \\ -qx_2^b e^{i\nu_a(z-z')} \\ qx_2^a e^{i\nu_b(z-z')} \end{bmatrix} r_0 J_1(kr_0). \tag{4.79}$$

In arriving at the above results, the following identities were used.

$$k^2(c_{13} + c_{44})^2\nu_b^2 + (c_{44}\nu_b^2 - c_{11}\nu_e^2)(c_{44}\nu_c^2 - c_{33}\nu_b^2) = 0 \tag{4.80}$$

$$k^2(c_{13} + c_{44})^2\nu_a^2 + (c_{44}\nu_a^2 - c_{11}\nu_e^2)(c_{44}\nu_c^2 - c_{33}\nu_a^2) = 0 \tag{4.81}$$

where, $\nu_e^2 = \rho\omega^2/c_{11} - k^2$. These two results follow from the definition of ν_b^2 and ν_a^2 through some manipulations.

In the BEM implementation as outlined in Section 4.2, Equations 4.78 and 4.79 need to be integrated over the source position z' for the wall elements, and over r_0 for the bottom elements. The results of these integrations are the input to the reflectivity program.

4.6 Waves in Cylindrically Layered Isotropic Media: Inside the Borehole

When casing and cement are installed in a borehole, the original fluid column changes to a cylindrically layered isotropic medium. To apply the boundary element method, this radially layered medium needs to be treated as a separate system and the wave propagation in it has to be studied.

Similar to the case of a plane layered medium, wave propagation in the cylindrically layered medium can be studied by rewriting the wave equation into an ordinary differential equation for the displacement-stress vector. Nevertheless, it is most expedient to work with potentials because of the isotropic nature of each layer. Furthermore, for the plane layered medium displacements are expressed as horizontal wave number integrals so as to satisfy the phase-matching condition at the interfaces. For the cylindrically layered medium, the phase-matching condition is satisfied by expressing the potentials as integrals over the vertical wave number. Let A_s, B_s, A_o, and B_o represent the amplitudes of the incoming (standing) and outgoing P and S wave potentials in any solid layer, C_s and C_o be the correspondent potential amplitudes for the P wave in any fluid layer, then the potentials assume the following form

$$\phi = \frac{1}{2\pi}\int_{-\infty}^{\infty}[A_s I_0(\xi_a r) + A_o K_0(\xi_a r)]e^{ik_z(z-z')}dk_z, \tag{4.82}$$

$$\psi = \frac{1}{2\pi}\int_{-\infty}^{\infty}[B_s I_1(\xi_b r) + B_o K_1(\xi_b r)]e^{ik_z(z-z')}dk_z, \tag{4.83}$$

$$\phi_f = \frac{1}{2\pi}\int_{-\infty}^{\infty}[C_s I_0(\xi_f r) + C_o K_0(\xi_f r)]e^{ik_z(z-z')}dk_z. \tag{4.84}$$

where,

$$\xi_a = i\sqrt{k_a^2 - k_z^2}, \quad \xi_b = i\sqrt{k_b^2 - k_z^2}, \quad \xi_f = i\sqrt{k_f^2 - k_z^2}, \tag{4.85}$$

and k_a, k_b, and k_f are the total P and S wavenumbers in the solid and P wave number in the fluid.

With the above defined potentials, the displacement-stress vectors in the solid and fluid are

$$(u_r, u_z, \tau_{rr}, \tau_{rz})^T = S(r)\mathbf{v}_4, \quad (u_r, u_z, \tau_{rr}, \tau_{rz})^T = F(r)\mathbf{v}_2, \tag{4.86}$$

where, $\mathbf{v}_4 = (A_s, B_s, A_o, B_o)^T$ and $\mathbf{v}_2 = (C_s, C_o)^T$ are the amplitude vectors. The elements of matrix $S(r)$ for the solid are

$$\begin{aligned}
S_{11} &= \xi_a I_1(\xi_a r), \\
S_{12} &= -ik_z I_1(\xi_b r), \\
S_{13} &= -\xi_a K_1(\xi_a r), \\
S_{14} &= -ik_z K_1(\xi_b r), \\
S_{21} &= ik_z I_0(\xi_a r), \\
S_{22} &= \xi_b I_0(\xi_b r), \\
S_{23} &= ik_z K_0(\xi_a r), \\
S_{24} &= -\xi_b K_0(\xi_b r), \\
S_{31} &= (2\mu k_z^2 - \rho\omega^2) I_0(\xi_a r) - 2\mu\xi_a I_1(\xi_a r)/r, \\
S_{32} &= -2i\mu k_z [\xi_b I_0(\xi_b r) - I_1(\xi_b r)/r], \\
S_{33} &= (2\mu k_z^2 - \rho\omega^2) K_0(\xi_a r) + 2\mu\xi_a K_1(\xi_a r)/r, \\
S_{34} &= 2i\mu k_z [\xi_b K_0(\xi_b r) + K_1(\xi_b r)/r], \\
S_{41} &= 2i\mu k_z \xi_a I_1(\xi_a r), \\
S_{42} &= (2\mu k_z^2 - \rho\omega^2) I_1(\xi_b r), \\
S_{43} &= -2i\mu k_z \xi_a K_1(\xi_a r), \\
S_{44} &= (2\mu k_z^2 - \rho\omega^2) K_1(\xi_b r).
\end{aligned}$$

Elements of matrix $F(r)$ for the fluid are

$$\begin{aligned}
F_{11} &= \xi_f I_1(\xi_f r), \\
F_{12} &= -\xi_f K_1(\xi_f r), \\
F_{21} &= ik_z I_0(\xi_f r),
\end{aligned}$$

$$
\begin{aligned}
F_{22} &= ik_z K_0(\xi_f r), \\
F_{31} &= -\rho_f \omega^2 I_0(\xi_f r), \\
F_{32} &= -\rho_f \omega^2 K_0(\xi_f r), \\
F_{41} &= 0, \\
F_{42} &= 0.
\end{aligned}
$$

From these matrices, the reflection and transmission coefficients of P and S waves at the solid-solid and solid-fluid interfaces can be readily obtained. The procedure for the solid-solid contact is the same as in the previous section. The solid-fluid contact case is illustrated in the following subsection.

4.6.1 Reflection and transmission coefficients

For an interface at $r = r_0$ between a fluid column ($r < r_0$) and an elastic formation ($r > r_0$), the following equations hold

$$
\begin{bmatrix} A_s \\ B_s \\ A_o \\ B_o \end{bmatrix} = \begin{bmatrix} 1 & 0 & 0 \\ 0 & 1 & 0 \\ R^i_{pp} & R^i_{sp} & T^o_{pp} \\ R^i_{ps} & R^i_{ss} & T^o_{ps} \end{bmatrix} \begin{bmatrix} A_s \\ B_s \\ C_o \end{bmatrix}, \tag{4.87}
$$

$$
\begin{bmatrix} C_s \\ C_o \end{bmatrix} = \begin{bmatrix} T^i_{pp} & T^i_{sp} & R^o_{pp} \\ 0 & 0 & 1 \end{bmatrix} \begin{bmatrix} A_s \\ B_s \\ C_o \end{bmatrix}. \tag{4.88}
$$

The above equations simply state that the outgoing P and S waves in the formation result from the reflection of incoming P and S waves in the formation, plus the transmission of an outgoing P wave in the fluid. An incoming P wave in the fluid is the consequence of an outgoing P wave reflection and an incoming P and S wave transmission. Substituting equations (4.87) and (4.88) into Equation 4.86 and

applying the three boundary conditions, we obtain

$$\begin{bmatrix} S_{11} & S_{12} & S_{13} & S_{14} \\ S_{31} & S_{32} & S_{33} & S_{34} \\ S_{41} & S_{42} & S_{43} & S_{44} \end{bmatrix} \begin{bmatrix} 1 & 0 & 0 \\ 0 & 1 & 0 \\ R^i_{pp} & R^i_{sp} & T^o_{pp} \\ R^i_{ps} & R^i_{ss} & T^o_{ps} \end{bmatrix} = \begin{bmatrix} F_{11} & F_{12} \\ F_{31} & F_{32} \\ F_{41} & F_{42} \end{bmatrix} \begin{bmatrix} T^i_{pp} & T^i_{sp} & R^o_{pp} \\ 0 & 0 & 1 \end{bmatrix}. \tag{4.89}$$

The nine unknown coefficients are solved from the nine equations implied by Equation 4.89. We have

$$\begin{aligned}
R^o_{pp} &= -\frac{F_{12}(S_{43}S_{34} - S_{33}S_{44}) + F_{32}(S_{13}S_{44} - S_{14}S_{43})}{F_{11}(S_{43}S_{34} - S_{33}S_{44}) + F_{31}(S_{13}S_{44} - S_{14}S_{43})}, \\
T^o_{pp} &= \frac{S_{44}(F_{12}F_{31} - F_{11}F_{32})}{F_{11}(S_{43}S_{34} - S_{33}S_{44}) + F_{31}(S_{13}S_{44} - S_{14}S_{43})}, \\
T^o_{ps} &= \frac{-S_{43}(F_{12}F_{31} - F_{11}F_{32})}{F_{11}(S_{43}S_{34} - S_{33}S_{44}) + F_{31}(S_{13}S_{44} - S_{14}S_{43})}, \\
T^i_{pp} &= \frac{S_{44}(S_{13}S_{31} - S_{11}S_{33}) + S_{14}(S_{33}S_{41} - S_{31}S_{43})}{F_{11}(S_{43}S_{34} - S_{33}S_{44}) + F_{31}(S_{13}S_{44} - S_{14}S_{43})}, \\
T^i_{sp} &= \frac{S_{43}(S_{12}S_{34} - S_{14}S_{32}) + S_{13}(S_{32}S_{44} - S_{34}S_{42})}{F_{11}(S_{43}S_{34} - S_{33}S_{44}) + F_{31}(S_{13}S_{44} - S_{14}S_{43})}, \\
R^i_{pp} &= \frac{F_{11}(S_{44}S_{31} - S_{34}S_{41}) - F_{31}(S_{11}S_{44} - S_{14}S_{41})}{F_{11}(S_{43}S_{34} - S_{33}S_{44}) + F_{31}(S_{13}S_{44} - S_{14}S_{43})}, \\
R^i_{ps} &= \frac{F_{11}(S_{33}S_{41} - S_{31}S_{43})}{F_{11}(S_{43}S_{34} - S_{33}S_{44}) + F_{31}(S_{13}S_{44} - S_{14}S_{43})}, \\
R^i_{sp} &= \frac{F_{11}(S_{32}S_{44} - S_{34}S_{42})}{F_{11}(S_{43}S_{34} - S_{33}S_{44}) + F_{31}(S_{13}S_{44} - S_{14}S_{43})}, \\
R^i_{ss} &= \frac{F_{11}(S_{42}S_{33} - S_{32}S_{43}) - F_{31}(S_{13}S_{42} - S_{12}S_{43})}{F_{11}(S_{43}S_{34} - S_{33}S_{44}) + F_{31}(S_{13}S_{44} - S_{14}S_{43})}.
\end{aligned} \tag{4.90}$$

If $r > r_0$ is the fluid region and $r < r_0$ the solid region, the resulting equation for the coefficients is

$$\begin{bmatrix} S_{11} & S_{12} & S_{13} & S_{14} \\ S_{31} & S_{32} & S_{33} & S_{34} \\ S_{41} & S_{42} & S_{43} & S_{44} \end{bmatrix} \begin{bmatrix} R^o_{pp} & R^o_{sp} & T^i_{pp} \\ R^o_{ps} & R^o_{ss} & T^i_{ps} \\ 1 & 0 & 0 \\ 0 & 1 & 0 \end{bmatrix} = \begin{bmatrix} F_{11} & F_{12} \\ F_{31} & F_{32} \\ F_{41} & F_{42} \end{bmatrix} \begin{bmatrix} 0 & 0 & 1 \\ T^o_{pp} & T^o_{sp} & R^i_{pp} \end{bmatrix}. \tag{4.91}$$

As this equation differs from Equation 4.89 only in the column position of the S and F matrices, the individual coefficients can be readily obtained by corresponding element substitution.

4.6.2 Initial potential of element sources

Before proceeding with the derivation of the P and SV wave potentials for circular sources, one detail needs to be pointed out. i.e., the relation between potential and displacements used in this section is

$$u_r = \frac{\partial \phi}{\partial r} - \frac{\partial \psi}{\partial z}, \quad u_z = \frac{\partial \phi}{\partial z} + \frac{\partial (r\psi)}{r \partial r}. \tag{4.92}$$

While in Bouchon (1993) and Müller (1985) the used relation is

$$u_r = \frac{\partial \phi}{\partial r} + \frac{\partial^2 \psi}{\partial r \partial z}, \quad u_z = \frac{\partial \phi}{\partial z} - \frac{\partial \left(r \frac{\partial \psi}{\partial r}\right)}{r \partial r}. \tag{4.93}$$

With this difference in mind, the initial potentials can be obtained from manipulations of Müller's or Bouchon's results by transfering J_0 and J_1 into the modified functions. An easier way is to express the scalar Green's function in Equation 4.4 as

$$\frac{e^{ik_a R}}{R} = \frac{1}{\pi} \int_{-\infty}^{\infty} K_0(\xi_a D) e^{ik_z(z-z')} dk_z \tag{4.94}$$

$$= \sum_{m=0}^{\infty} \epsilon_m \cos m(\varphi - \varphi_0) \frac{1}{\pi} \int_{-\infty}^{\infty} K_m(\xi_a r_0) I_m(\xi_a r) e^{ik_z(z-z')} dk_z. \tag{4.95}$$

In the above, the addition theorem for the modified Bessel function is used for the $r < r_0$ case, which is pertinent to our problem where all cylindrical layers are inside the radius of the borehole (r_0). Then, integrating the Green's tensor in Equation 4.4 over the source ring yields the displacements expressed by the modified Bessel functions.

For a vertical ring force, the radial displacement is

$$U_r = \frac{\partial}{\partial r} \left(2ir_0 \int_{-\infty}^{\infty} k_z [K_0(\xi_b r_0) I_0(\xi_b r) - K_0(\xi_a r_0) I_0(\xi_a r)] e^{ik_z(z-z')} dk_z \right). \tag{4.96}$$

A comparison of this result with Equation 4.92 yields immediately the P and SV wave potentials due to a vertical force circle. They are

$$\phi_v^c = \frac{-ir_0}{2\pi\rho\omega^2} \int_{-\infty}^{\infty} k_z K_0(\xi_a r_0) I_0(\xi_a r) e^{ik_z(z-z')} dk_z, \tag{4.97}$$

$$\psi_v^c = \frac{-r_0}{2\pi\rho\omega^2}\int_{-\infty}^{\infty}\xi_b K_0(\xi_b r_0)I_1(\xi_b r)e^{ik_z(z-z')}dk_z. \quad (4.98)$$

For a radial ring force, the vertical displacement is

$$U_z = \frac{\partial}{\partial z}\left(\frac{-r_0}{2\pi\rho\omega^2}\int_{-\infty}^{\infty}\xi_a K_1(\xi_a r_0)I_0(\xi_a r)e^{ik_z(z-z')}dk_z\right) + \frac{1}{r}\frac{\partial}{\partial r}\left(\frac{ir_0}{2\pi\rho\omega^2}\int_{-\infty}^{\infty}k_z K_1(\xi_b r_0)I_0(\xi_b r)e^{ik_z(z-z')}dk_z\right). \quad (4.99)$$

Thus, a comparison with Equation 4.92 gives the P and SV wave potentials produced by a radial ring source

$$\phi_r^c = \frac{-r_0}{2\pi\rho\omega^2}\int_{-\infty}^{\infty}\xi_a K_1(\xi_a r_0)I_0(\xi_a r)e^{ik_z(z-z')}dk_z, \quad (4.100)$$

$$\psi_r^c = \frac{ir_0}{2\pi\rho\omega^2}\int_{-\infty}^{\infty}k_z K_1(\xi_b r_0)I_1(\xi_b r)e^{ik_z(z-z')}dk_z. \quad (4.101)$$

When compared with Equations (4.82) and (4.83), these expressions provide the incident potential amplitude at the outer cylindrical interface. The products (matrix multiplication) of these incident potentials with the reflection and transmission coefficient matrices yield the reflected potentials in the solid layer and transmitted potentials in the fluid. The total potentials then yield the total displacements and stresses used for matching boundary conditions and for program output.

4.7 The Initial Data at the Elements

To solve the system of equations in Equation 4.8 for the fictitious sources on each element, the initial displacements and stresses due directly to the physical source are required. They appear on the right hand side of the system of equations. These data depend on the type of sources used and whether or not the borehole is cased. We consider three conventional sources here: the explosive volume source, the axial source, and the radial source. In practice, they correspond to an air gun or dynamite, wall-clamped vibrators, and a bender source or cavity resonator, respectively.

4.7.1 Sources in an open borehole

For sources in an open borehole, empty or fluid-filled, either the source or its direct wavefield is in direct contact with the formation. With the axial and radial sources, the vibrating forces are applied directly at the boundary of interest. Thus, the initial data for these two sources are just the driving forces applied to the elements. The initial data for the displacements are set to zero. For an explosive source at the center of a fluid-filled borehole, the initial data at the boundary are

$$\begin{aligned} U_r &= \frac{V_s}{4\pi} i \int_0^\infty \frac{k^2}{\nu_f} J_1(kr_0) e^{i\nu_f|z-z_s|} dk, \\ \sigma_{rr} &= \frac{V_s}{4\pi\rho_f\omega^2} i \int_0^\infty \frac{k}{\nu_f} J_0(kr_0) e^{i\nu_f|z-z_s|} dk, \\ \sigma_{rz} &= 0. \end{aligned} \tag{4.102}$$

The vertical position of the source and the element is z_s and z. The strength of the volume source is denoted by V_s, whose unit is in m^3. The usual value for V_s is 1600 cm^3.

4.7.2 Sources in a cased borehole

In a cased borehole, the sources and their direct fields are not in direct contact with the boundary elements. The initial data is influenced by the casing and the cement. Since the boundary of the cement and formation is in weld contact, four boundary conditions have to be satisfied. Consequently, four data are needed on an element. In what follows, we only present the P and S potentials that can be used to derive the displacements and stresses by applying matrix $S(r_0)$ to their amplitudes, as indicated by Equation 4.86.

The two potentials due to a volume source of strength V_s are

$$\phi = \frac{1}{4\pi^2} \int_{-\infty}^{\infty} V_s \, \overline{T}^o_{pp} \, K_0(\xi_a r_0) e^{ik_z(z-z')} dk_z, \tag{4.103}$$

$$\psi = -\frac{1}{4\pi^2} \int_{-\infty}^{\infty} V_s \, \overline{T}^o_{ps} \, K_1(\xi_b r_0) e^{ik_z(z-z')} dk_z, \tag{4.104}$$

where, $\overline{T}^o_{pp}$ and $\overline{T}^o_{ps}$ are the *overall* $P-P$ and $P-S$ transmission coefficients from the fluid to the elements.

To obtain data for the other two sources, let's first define a 4×4 matrix, E,

$$E = S(r_1)S^{-1}(r_2^-)S(r_2^+), \tag{4.105}$$

where, S is the matrix defined in Equation 4.86, and r_1 and r_2 are the inner (-) and outer (+) radius of the casing. Then, the potentials at the boundary element and in the fluid, due to an axial force applied on the casing over a range of $2l$ and centered at z_s, are

$$\phi = \frac{1}{2\pi}\int_{-\infty}^{\infty} \frac{F_{11}E_{34} - F_{31}E_{14}}{DET} F(k_z)K_0(\xi_a r_0)e^{ik_z(z-z_s)}dk_z, \tag{4.106}$$

$$\psi = \frac{1}{2\pi}\int_{-\infty}^{\infty} \frac{F_{11}E_{33} - F_{31}E_{13}}{DET} F(k_z)K_1(\xi_b r_0)e^{ik_z(z-z_s)}dk_z, \tag{4.107}$$

$$\phi_f = \frac{1}{2\pi}\int_{-\infty}^{\infty} \frac{E_{13}E_{34} - E_{14}E_{33}}{DET} F(k_z)I_0(\xi_f r)e^{ik_z(z-z_s)}dk_z. \tag{4.108}$$

E_{ij} in the above is the corresponding (i,j) element of the E matrix. DET is the denominator in terms of elements of the E-matrix and it has a form similar to the denominator in the reflection and transmission coefficients in Section (4.6). $F(k_z)$ is the source spectrum and has the following form

$$F(k_z) = \frac{2\sin(k_z l)}{k_z}. \tag{4.109}$$

The potentials for the radial source are

$$\phi = \frac{1}{2\pi}\int_{-\infty}^{\infty} \frac{-F_{11}E_{44}}{DET} F(k_z)K_0(\xi_a r_0)e^{ik_z(z-z_s)}dk_z, \tag{4.110}$$

$$\psi = \frac{1}{2\pi}\int_{-\infty}^{\infty} \frac{F_{11}E_{31}}{DET} F(k_z)K_1(\xi_b r_0)e^{ik_z(z-z_s)}dk_z, \tag{4.111}$$

$$\phi_f = \frac{1}{2\pi}\int_{-\infty}^{\infty} \frac{E_{14}E_{43} - E_{13}E_{44}}{DET} F(k_z)I_0(\xi_f r)e^{ik_z(z-z_s)}dk_z. \tag{4.112}$$

It should be pointed out that when pressure in the fluid is calculated from the fictitious sources on the boundary, the resulting pressure is only part of the solution. The total pressure in the fluid should include the casing reflection from the direct

wavefield in the case of the volume source. In the case of the axial and the radial source, direct contributions from the source to the pressure should be taken into account, because this part of the wavefield did not contribute to the BEM calculation of the fictitious sources on the boundary.

4.8 More on BEM Implementation

After the circular source results are incorporated into the reflectivity scheme, the end products are two wavenumber integrals, a horizontal wavenumber integral for the plane layered isotropic or anisotropic formation, and a vertical wavenumber integral for the cylindrically layered isotropic medium. Since integral over element height depends on wavenumbers, its evaluation must precede the wavenumber integration. The integration over the source element coordinate, z', for plane layers is of two types: integral of a complex exponential, and integral of a sign function multiplied by the exponential function. Either can be easily integrated to yield

$$\int_{z_l}^{z_h} e^{i\nu|z-z'|}dz' = \begin{cases} \frac{e^{i\nu(z-z_h)}-e^{i\nu(z-z_l)}}{-i\nu} & \text{for } z > z_h; \\ \frac{e^{i\nu(z_h-z)}-e^{i\nu(z_l-z)}}{i\nu} & \text{for } z < z_l; \\ \frac{e^{i\nu(z_h-z)}+e^{i\nu(z-z_l)}-2}{i\nu} & \text{for } z_l < z < z_h, \end{cases} \tag{4.113}$$

and,

$$\int_{z_l}^{z_h} \mathrm{sgn}(z-z')e^{i\nu|z-z'|}dz' = \begin{cases} \frac{e^{i\nu(z-z_h)}-e^{i\nu(z-z_l)}}{-i\nu} & \text{for } z > z_h; \\ \frac{e^{i\nu(z_h-z)}-e^{i\nu(z_l-z)}}{-i\nu} & \text{for } z < z_l; \\ \frac{e^{i\nu(z_h-z)}-e^{i\nu(z-z_l)}}{i\nu} & \text{for } z_l < z < z_h. \end{cases} \tag{4.114}$$

The z' integral for the cylindrical layers is

$$\int_{z_l}^{z_h} e^{ik_z(z-z')}dz' = \begin{cases} z_h - z_l & \text{if } k_z = 0; \\ 2\frac{\sin\frac{1}{2}k_z(z_h-z_l)}{k_z}e^{ik_z[z-\frac{1}{2}(z_h+z_l)]} & \text{others.} \end{cases} \tag{4.115}$$

Now, all that is left to be done is the computation of the wavenumber integrals. The k_z integrals seem to present a computational problem because both k_z and $-k_z$

calculations are required. Actually, the integrals can be folded according to the oddness or evenness of the integrands. From the results in Section (4.6), one can show that the $P-P$ and $S-S$ wave reflection and transmission coefficients at a single interface are even functions of k_z, while their $P-S$ and $S-P$ counterparts are odd functions of k_z. The same can be said about the generalized or overall reflection and transmission coefficients. Using these properties along with the signs of the initial potentials and the operator S, one finds that the exponentials are replaced by sine and cosine functions, and only positive k_z calculations are needed. This reduces the computation by a factor of 2. Explosive and radial sources have a similar replacement, which is different from that of an axial source.

An exact analytical evaluation of the wavenumber integrals (both k and k_z) is impossible, and a numerical method is necessary. Bessel functions J_0 and J_1 in the k integrals suggest the use of fast Hankel transform algorithms. Unfortunately, one can not employ these fast algorithms because the upper bound of the wavenumber is not known for a certain accuracy specification. That is, given an accuracy requirement for the integrated results, one cannot predict up to which wavenumber the inputs to these algorithms should be prepared. Thus, the only alternative is to evaluate these integrals by discrete summation for many wavenumbers. This is the so-called *Discrete Wavenumber Method* (Bouchon and Aki, 1977).

The discretization of wavenumbers k and k_z in cylindrical coordinates introduces periodicity into the source distribution. Instead of a single source for the original problem, periodic concentric sources for the k case, and vertically periodic ring sources for the k_z case, result from discretization. Taking the k case as an example, the periodicity of these sources or the distance between two adjacent circular sources, L, is related to the discretization interval of the wavenumber, Δk, by the well-known sampling relation

$$L = \frac{2\pi}{\Delta k}. \tag{4.116}$$

We determine L (therefore Δk) by considering a receiver located at $\mathbf{x}_r = (R_0, Z_0)$

and a real source at $\mathbf{x}_s = (0, Z_s)$ inside the borehole. Given the time window to record radiated waves from zero to t_{max}, we should not allow any *pseudo* wave due to periodic sources to enter this time window. This requirement is

$$L > R_0 + \sqrt{\alpha^2 t_{max}^2 - (Z_0 - Z_s)^2}. \tag{4.117}$$

With this equation and the sampling equation, we have

$$\Delta k < \frac{2\pi}{R_0 + \sqrt{\alpha^2 t_{max}^2 - (Z_0 - Z_s)^2}}. \tag{4.118}$$

This equation is the criterion for choosing the sampling rate for discrete wavenumber summation. Similar considerations for the k_z case are required.

To perform the summation, the singularities of the integrands must be removed from the real k-axis. The singularities include poles and branch points. As discussed by Chew (1990), branch points exist only for the upper and lower half space of the plane layered formation. The branch points correspond physically to the radiation modes in the two half spaces. The poles of the integrands correspond to the guided modes within the layers. Near these singularities, especially near the poles, the wavenumber summation converges incredibly slowly or it may not converge at all. A robust way to overcome these problems is to introduce a small imaginary part into the frequency, i.e., $\omega = \omega_R + i\omega_I$ with $\omega_I > 0$. If $e^{-i\omega t}$ was used, there would be a minus sign for the imaginary part of the frequency. The singularities of the integrands are then offset to the first and third quadrants of the complex k-plane. This is equivalent to shifting the integration path of the contour integral on the complex k plane. The use of the complex frequency has the effect of smoothing the spectrum and enhancing the first motions relative to the later arrivals. The resulting attenuation is used to minimize the influence of the neighboring fictitious sources introduced by discretizing k. The effect of the imaginary part of the frequency can be removed from the final time-domain solution by inverse Fourier transform of the frequency-domain solution with a complex frequency of the same imaginary part. This is to magnify the later

arrivals that were attenuated. The magnitude of the imaginary part is usually chosen to be

$$\omega_I = \pi / t_{max}. \tag{4.119}$$

Large ω_I results in better attenuation for the later arrivals, but it also magnifies the random noise for the later part. If ω_I is too small, attenuation may be not large enough for the later fictitious arrivals. The above chosen number is one half of the frequency sampling interval.

In wavenumber summation, the convergence of the partial sums are tested using asymptotic approximations. This is because the integrands are alternating functions of the wavenumber. Instead of the actual N-th term, the modulus of its asymptotic expression is used to compare with the partial sum. If the ratio of the N-th term to the partial sum is smaller than the specified accuracy, summation is stopped.

4.9 Bench-Mark Examples:

This section contains examples chosen to test the computer implementation of the technique outlined in the previous sections. BEM results for a borehole in homogeneous isotropic and TI media are first compared against those from a discrete wavenumber (DWN) calculation. Then, the technique is used to illustrate the effect of a borehole, either open or cased, in a three-layer medium.

4.9.1 BEM vs. DWN: waveform comparison

The parameters of this example are obtained from Figure 3 in Bouchon and Schmitt (1989). A water-filled borehole of radius 0.12 m penetrating an elastic medium with a P velocity of 3600 m/s, a S velocity of 2100 m/s (actual used value in Bouchon's Fig. 3), and a density of 2.5 g/cm^3. Radial and tangential displacements in the formation are recorded by 30 receivers circularly and evenly distributed around, and 2 m away, from an explosion source in the fluid-filled borehole (see Figure 3-1-b).

Fluid pressure is obtained from 30 hydrophone receivers located along the borehole axis at distances ranging from 10 cm to 3 m from the source. The source emits a Ricker pressure pulse at a center frequency of 5 kHz. Calculation is done from 0 to 15 kHz. The periodicity length L (Equation 4.116) is 9 m. The DWN and BEM results and fictitious boundary sources are shown in Figures 4-4, 4-5, and 4-6, respectively. Displacements and pressures in Figures 4-4 and 4-5 are on the same scale.

The displacements and pressure from two very different methods agree very well in appearance, as well as in actual amplitude. The ringing appearance of these quantities are due to the high source center frequency. At 5 kHz, the wavelength in water (0.3 m) is comparable to the diameter of the borehole (0.24 m), the tunnel effect of the borehole dominates the wave radiation. For the pressure in the borehole, the Stoneley wave and the early arriving S-wave are quite clear. Auxiliary information from the BEM method comes from the fictitious sources on the boundary between the borehole fluid and the formation. As mentioned in Section 4.2 and in Appendix C, the fictitious sources for the formation should reflect the influence of the borehole fluid on the radiated waves. At 5 kHz, multiple reflections inside borehole affect the radiation characteristics. This influence is well expressed by the ringing nature of both the vertical and radial fictitious ring sources on the boundary. On the other hand, fictitious volume sources for the fluid are not ringing, and the tube (or Stoneley) wave and the faster shear wave are evident, which reflects the nature of the problem.

As another example, displacements from the BEM are compared with those from a DWN for a transversely isotropic medium. They are shown in Figure 4-7. The elastic parameters for the medium are: $c_{11} = 50.78$, $c_{33} = 36.85$, $c_{13} = 21.49$, $c_{44} = 11.01$, $c_{66} = 14.87$, $\rho = 2.56$. The circular receiver array is 40 m from the explosion source placed in a water-filled open borehole of radius $r_0 = 0.1$ m. The strong P-wave anisotropy is clearly shown in Figure 4-7. The large contribution of a *quasi-SV* wave on the U_R section, and the negligible *quasi-P* energy on the U_θ section, agree with what has been discussed in Chapter 3. More importantly, the BEM and DWN results

agree with each other very well.

4.9.2 Borehole in three-layer media

When a fluid-filled borehole is inside a layered isotropic or anisotropic medium, the tube waves, excited by the borehole source and propagating along the borehole, will interact with the vertical inhomogeneities. This interaction results in wave scattering and conversion along the path of the tube wave. The phenomena is illustrated here through several examples.

Figures 4-8, 4-10, and 4-12 show the solid displacements and the fluid pressure for volume, radial, and vertical sources in a water-filled borehole in a three-layer medium. The parameters of the medium are: $\alpha_1 = \alpha_3 = 3000\ m/s$, $\beta_1 = \beta_3 = 1700\ m/s$, $\rho_1 = \rho_3 = 2.7\ g/cm^3$, $\alpha_2 = 2000\ m/s$, $\beta_2 = 850\ m/s$, $\rho_2 = 2.4\ m/s$. The borehole radius is 0.1 m and the vertical geophone array in the formation is 4 m away from the borehole axis. The hydrophones are on the borehole axis and the offset between the source and the first hydrophone is 1 m. The center frequency of the wavelet is 2.5 kHz. These parameters are taken from the second example of Bouchon (1993) for comparison purposes. The fluid pressure in the case of a volume source (Figure 4-8), agrees with Bouchon's result very well (though his plot was scaled with velocity). The reflected tube waves at the top and the bottom interfaces are well defined. The first arrivals in far-offset traces are the tube-to-P scattered (or converted) waves. The later events in the pressure seismogram are due to periodic sources related to k_z sampling, thus they should not be confused with the real events. In addition to the primary P and S waves in the displacement seismograms, which are normally observable if the borehole is absent, strong events appear at a later time and with energy concentrated in the second and third layer. They are of tube wave origin and trapped in the second layer as guided modes. The trapped waves for the volume and radial sources are very similar, confirming once again that these two sources have similar characteristics in terms of wave radiation from a borehole. Since a vertical source does not generate

significant tube waves, the trapped energy for the vertical source is much smaller (see Figure 4-12).

Figures 4-9, 4-11, and 4-13 show the fictitious sources on the borehole boundary for the volume, radial, and vertical sources in the three-layer medium. These sources specify uniquely how a borehole source should be equivalently approximated. The reflection of a tube wave at the upper and lower interfaces is clearly indicated in these figures. The reflections from the top and bottom of each figure result from the finite borehole length used in the calculation. The reverberations inside the second layer are the expressions of trapped energy as sources. The trapped energy also results from the stronger vertical fictitious sources within the second layer which have a similar slope to that of the sources in the lower medium. In studying these figures, one needs to be aware that the vertical coordinates are numbers of elements. Since the element height in the different layers is different, one cannot simply measure the velocity from these figures.

In the next three cases, while the parameters of the first and third layers remain unchanged, the parameters of the second layer vary in each case. Figure 4-14 shows the displacements when the second layer is a TI medium with parameters: $c_{11} = 11.5$, $c_{33} = 10$, $c_{13} = 4.8$, $c_{44} = c_{66} = 2.6$, in Gpa and $\rho_2 = 2\ g/cm^3$. Since the tube wave speed (1100 m/s) is smaller than the shear wave velocity (1140 m/s), the tube-to-Mach wave conversion will not be observed. On the other hand, the displacement sections show that significant later arriving energy exists in the second and third layers. Thus, there is another mechanism that is responsible for the arising of trapped energy. It'll be discussed in the next Chapter. When the velocities of the second layer are increased, the trapped energy decreases (Figure 4-15), and it disappears when the velocities are very high (Figure 4-16). This illustrates that tube wave conversion is mainly associated with low velocity channels.

The displacements for a volume source in a cased borehole are shown in Figure 4-17. The medium parameters of Figure 4-14 are used for the modeling. Comparison

with Figure 4-14 shows that the amplitude of the trapped energy is relatively larger in Figure 4-17. This illustrates the fact that casing and cement reduce the amplitude of primary body waves (see 3.9), while they only subtly affect the tube wave and its conversions.

4.10 Conclusions

Bouchon's BEM modeling method is extended to include transverse isotropy and cased boreholes. The method overcomes the problem of scale associated with other numerical methods in the borehole environment. It is especially suitable for modeling wave radiation and propagation from or in a fluid-filled borehole, open or cased. The method is semi-analytical in the sense that the only discretization occurs on the borehole wall and, wave propagation is realized through the analytical Green's function of the layered TI medium outside the borehole, and through the isotropic Green's function for cylindrical layers inside the borehole. Comparison of the BEM results with their discrete wavenumber counterparts validates the implementation. Tests on several three-layer media show the importance of low velocity layers in the tube wave interaction with the surrounding formation. The by-product of the method - fictitious boundary sources - can be used to test approximations for actual borehole sources.

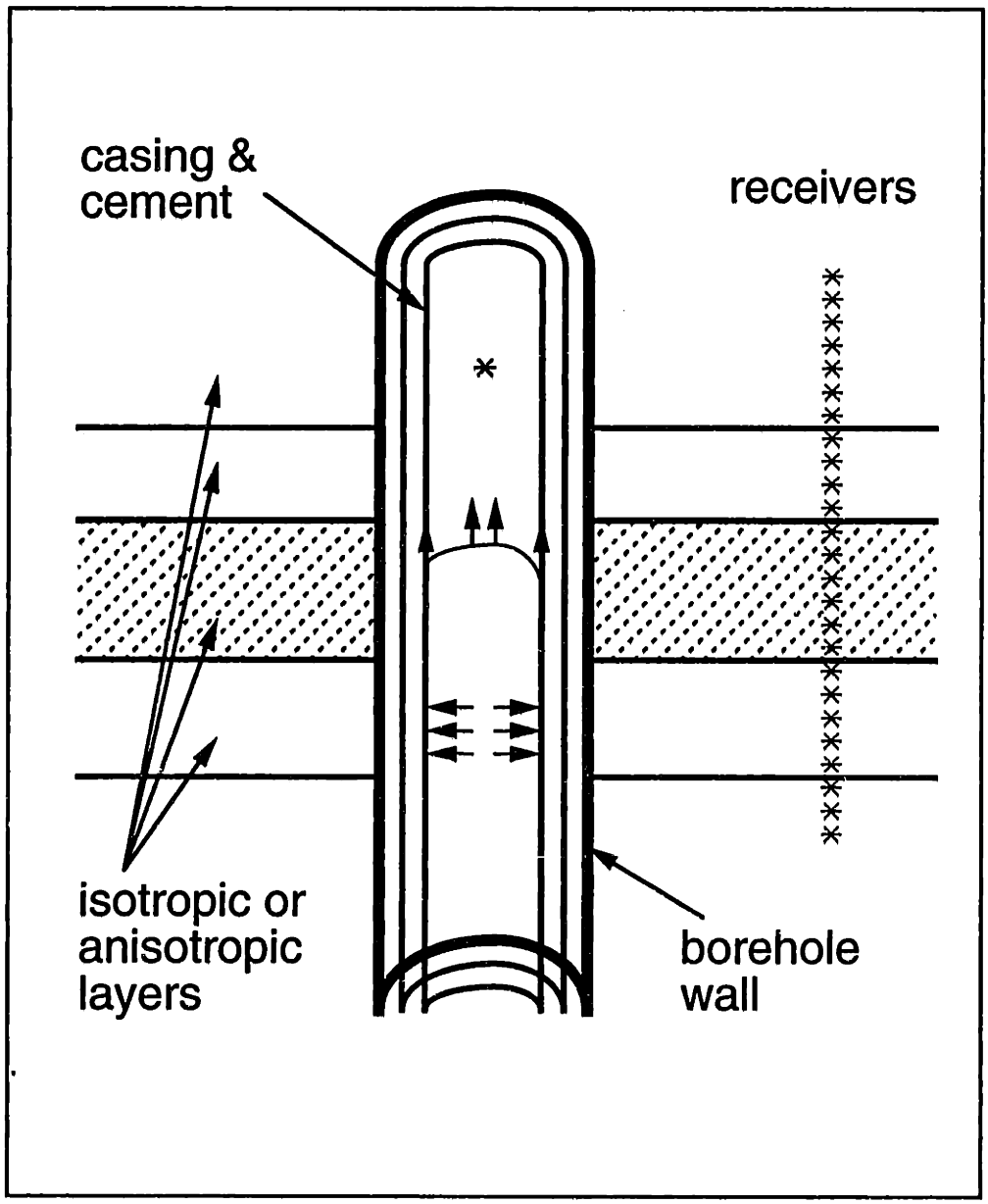

Figure 4-1: Problem configuration for a cased borehole in a layered transversely isotropic medium. Given a downhole source (explosion; vibrator; bender), the problem is to determine the fluid pressure inside the borehole and the displacements in the solid formation.

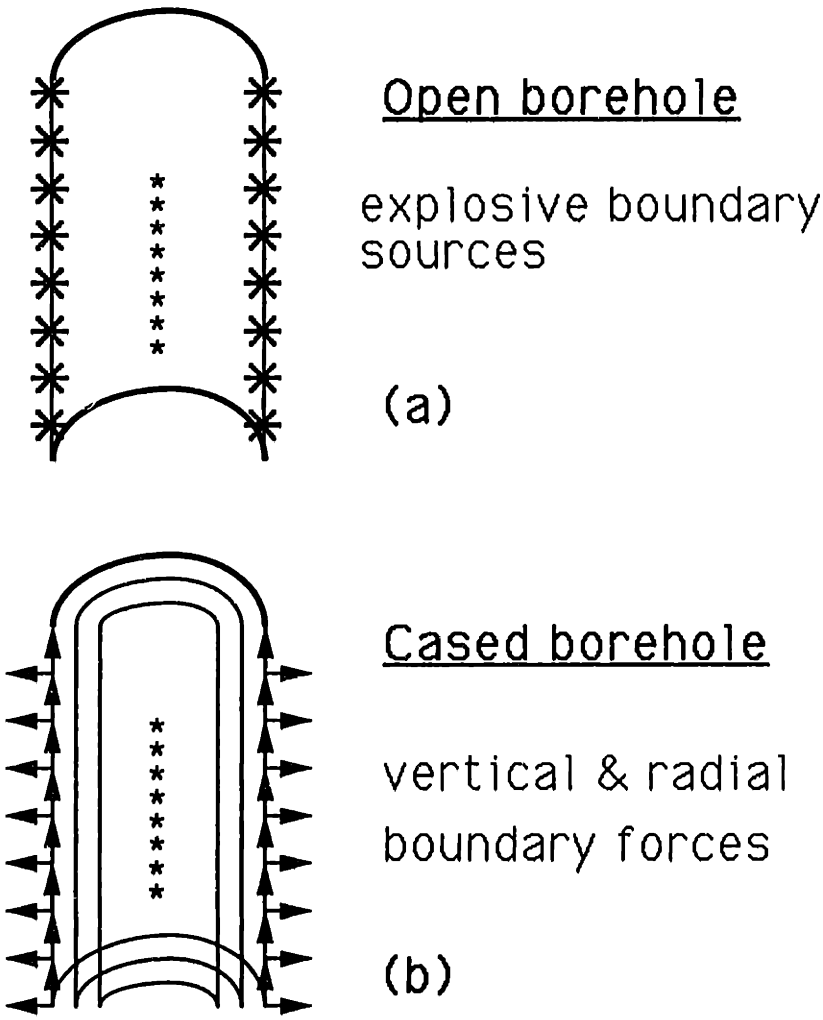

Figure 4-2: Equivalent problem for borehole fluid in an open borehole (a), and in a cased borehole (b). The effect of a solid formation on the wavefield is equivalent to a sheet of explosion sources at the borehole wall for case (a), and a sheet of vertical and radial forces at the wall for case (b). Once these assumed source sheets are known, pressure in the borehole fluid is readily computed.

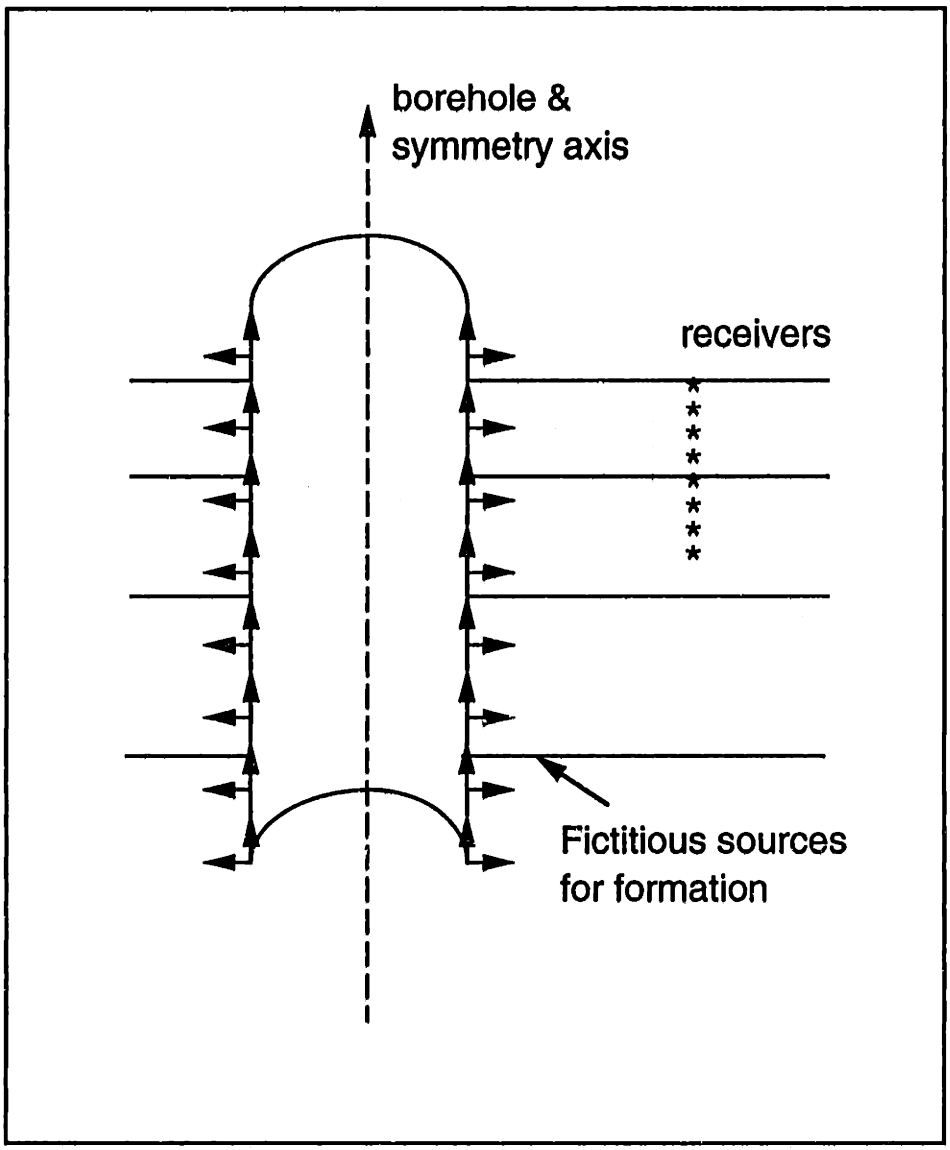

Figure 4-3: Equivalent problem for the layered formation in the cases of open and cased boreholes. The effect of the borehole fluid, casing, and cement on the out-going wavefield is equivalent to a sheet of vertical and radial forces at the wall. Once these assumed source sheets are known, displacements in the surrounding formation are readily obtained.

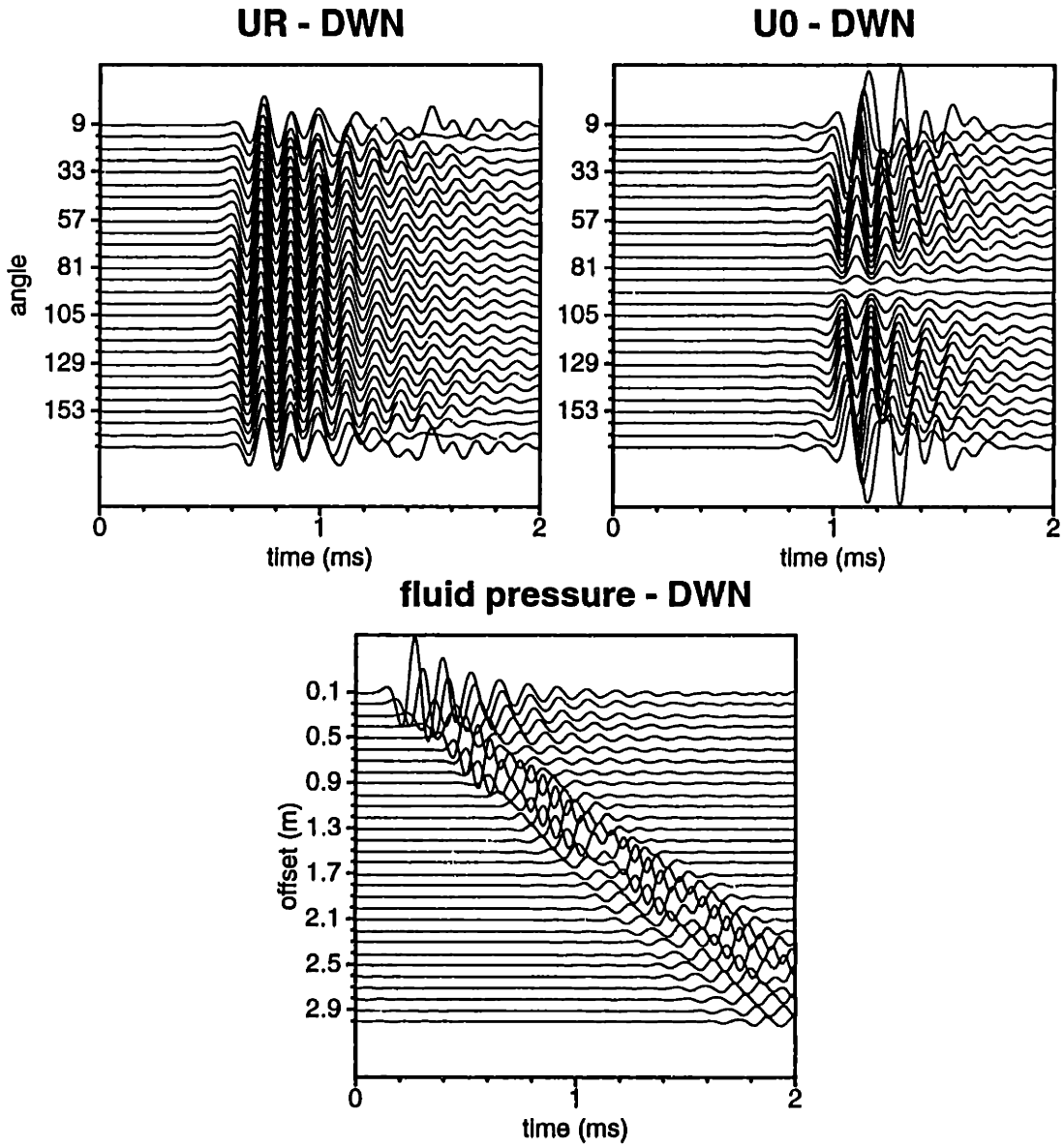

Figure 4-4: Displacements in the formation and pressure in the fluid, calculated by the discrete wavenumber method (DWN) for a volume source in a fluid-filled borehole embedded in a homogeneous isotropic formation. Parameters: $r_0 = 12\ cm$, $c_f = 1500\ m/s$, $\rho_f = 1.\ g/cm^3$, $V_p = 3600\ m/s$, $V_s = 2100\ m/s$, $\rho = 2.5\ g/cm^3$, $f_0 = 5\ kHz$, receiver array radius $R = 2\ m$.

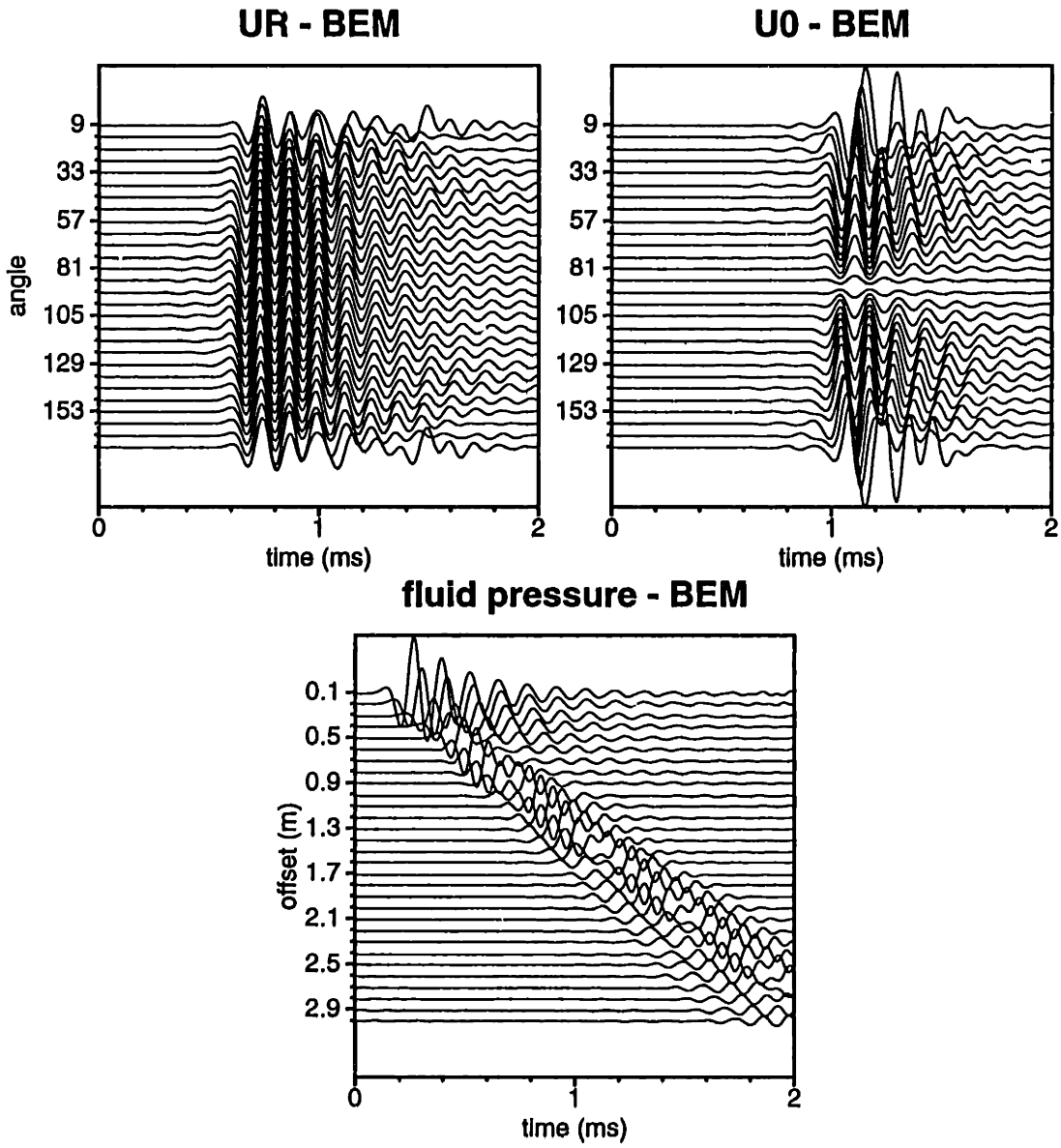

Figure 4-5: Displacements in the formation and pressure in the fluid, calculated by the boundary element method (BEM) for a volume source in a fluid-filled borehole embedded in a homogeneous isotropic formation. Parameters: $r_0 = 12\ cm$, $c_f = 1500\ m/s$, $\rho_f = 1.\ g/cm^3$, $V_p = 3600\ m/s$, $V_s = 2100\ m/s$, $\rho = 2.5\ g/cm^3$, $f_0 = 5\ kHz$, $R = 2\ m$.

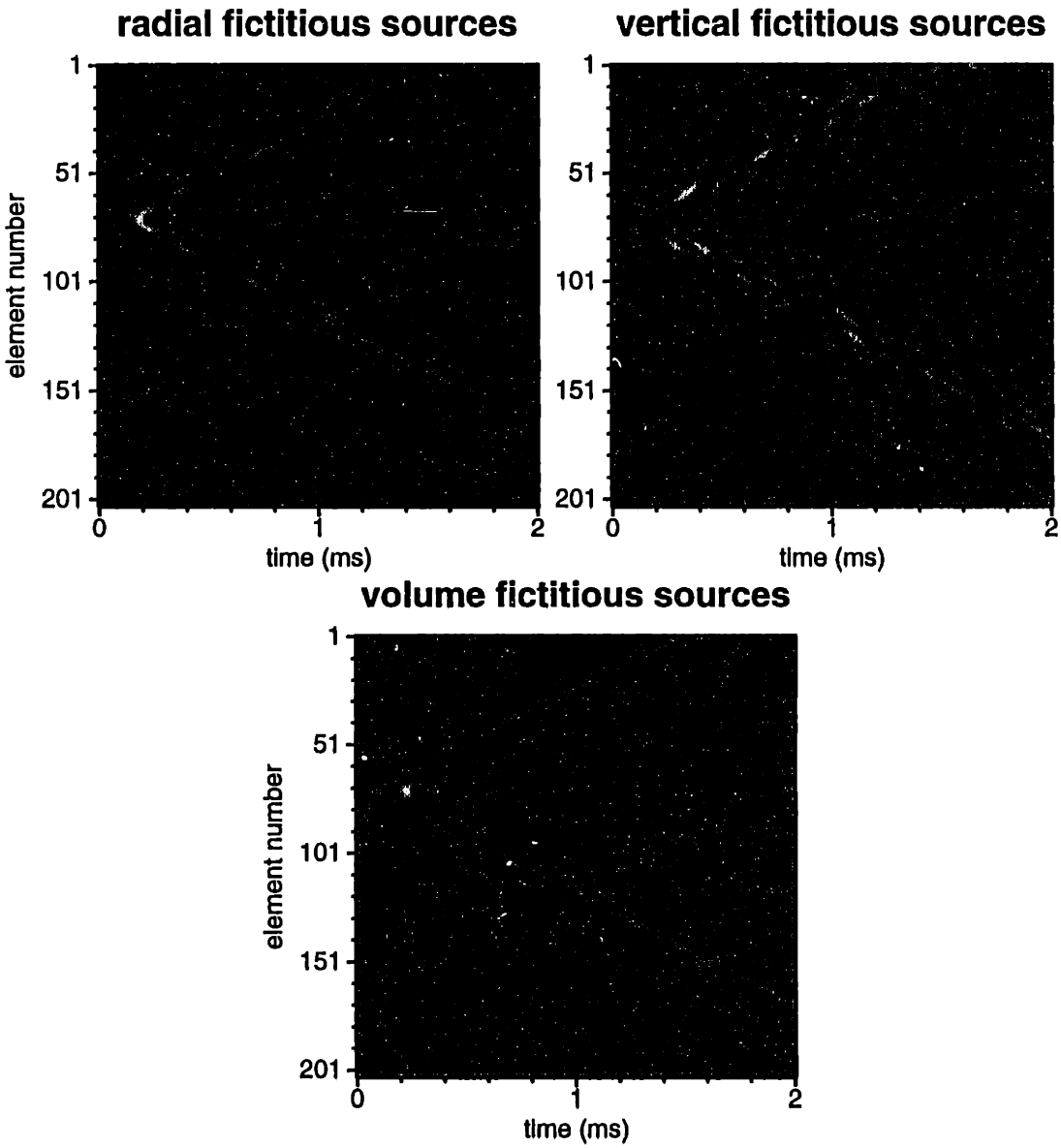

Figure 4-6: Fictitious boundary sources obtained from the boundary element method (BEM) for a volume source in a fluid-filled borehole embedded in a homogeneous isotropic formation. Parameters: $r_0 = 12\ cm$, $c_f = 1500\ m/s$, $\rho_f = 1.\ g/cm^3$, $V_p = 3600\ m/s$, $V_s = 2100\ m/s$, $\rho = 2.5\ g/cm^3$, $f_0 = 5\ kHz$.

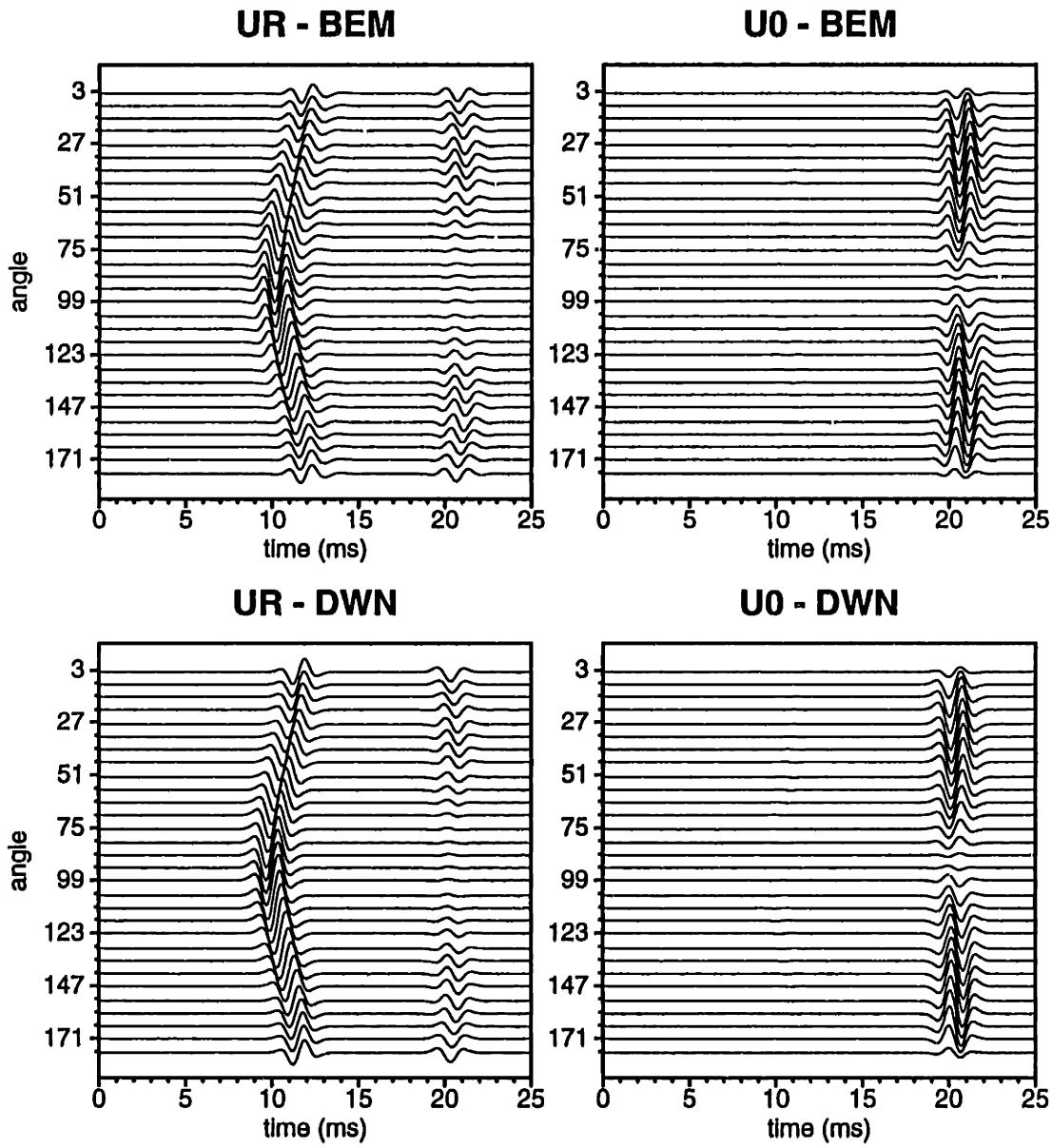

Figure 4-7: Comparison of BEM and DWN results for a volume source in a fluid-filled borehole embedded in a transversely isotropic medium. Parameters: $r_0 = 0.1$, $f_0 = 500\ Hz$, $R = 40\ m$, $c_{11} = 50.78$, $c_{33} = 36.85$, $c_{13} = 21.49$, $c_{44} = 11.01$, $c_{66} = 14.87$, $\rho = 2.56$, receiver array radius $R = 30\ m$.

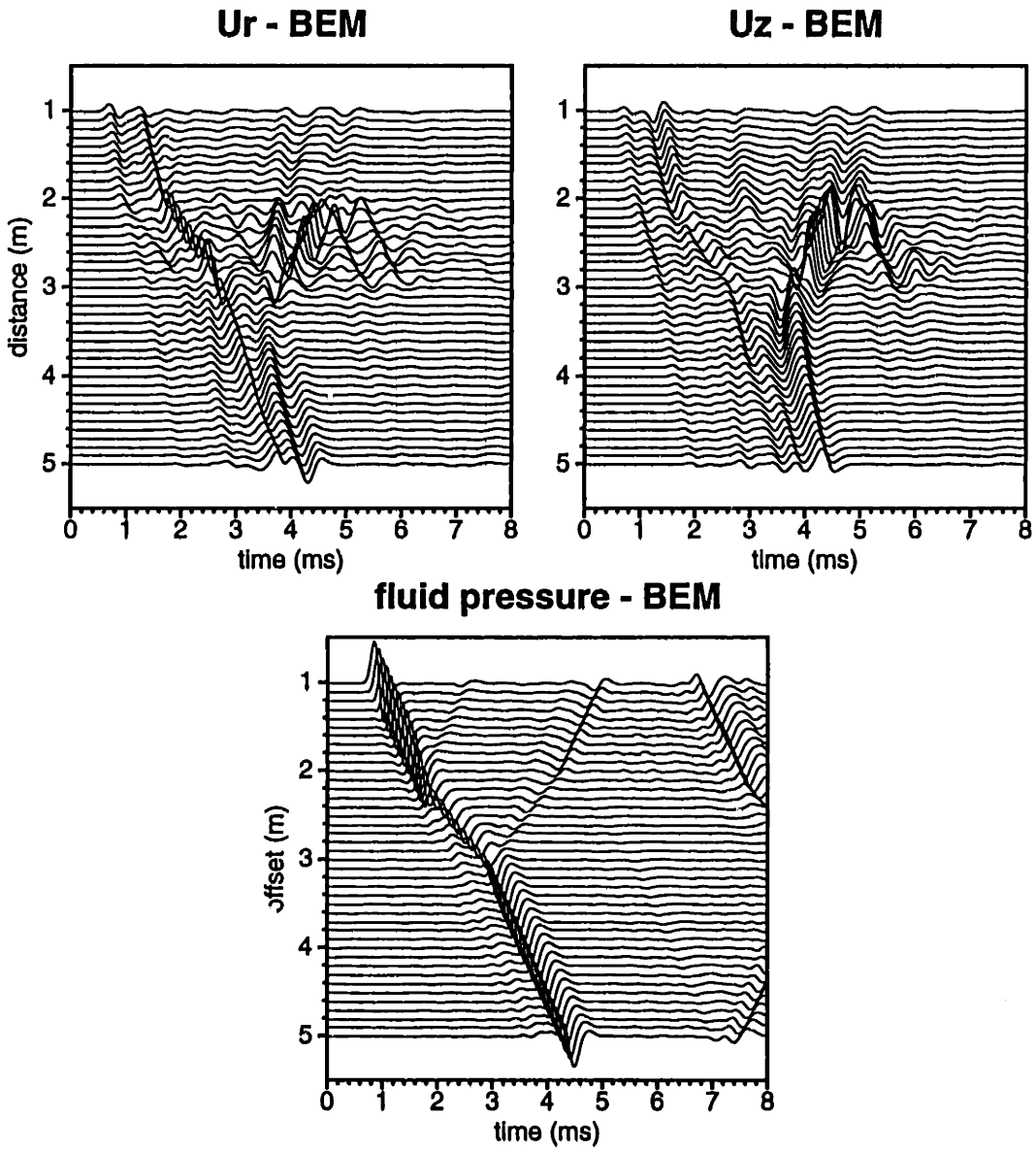

Figure 4-8: Displacements in the formation and pressure in the fluid for a volume source (air-gun or dynamite) in a fluid-filled borehole penetrating a three-layer isotropic medium. Vertical geophone array is 4 m from the borehole axis. Parameters: $\alpha_1 = \alpha_3 = 3000\ m/s$, $\beta_1 = \beta_3 = 1700\ m/s$, $\rho_1 = \rho_3 = 2.7\ g/cm^3$; $\alpha_2 = 2000\ m/s$, $\beta_2 = 850\ m/s$, $\rho_2 = 2.4\ m/s$.

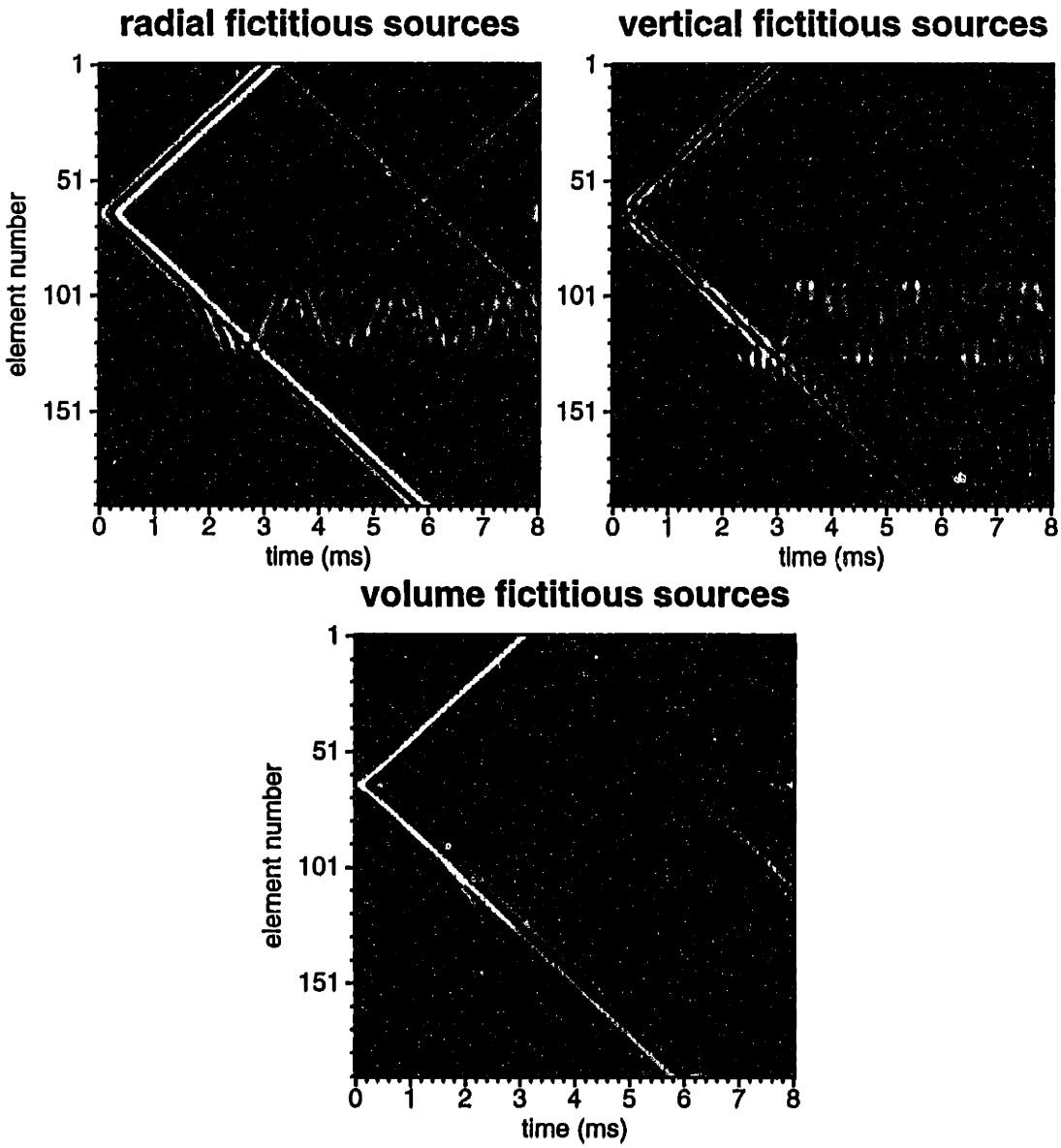

Figure 4-9: Fictitious boundary sources for the volume source in a fluid-filled borehole penetrating the three-layer isotropic medium in Figure 4-8.

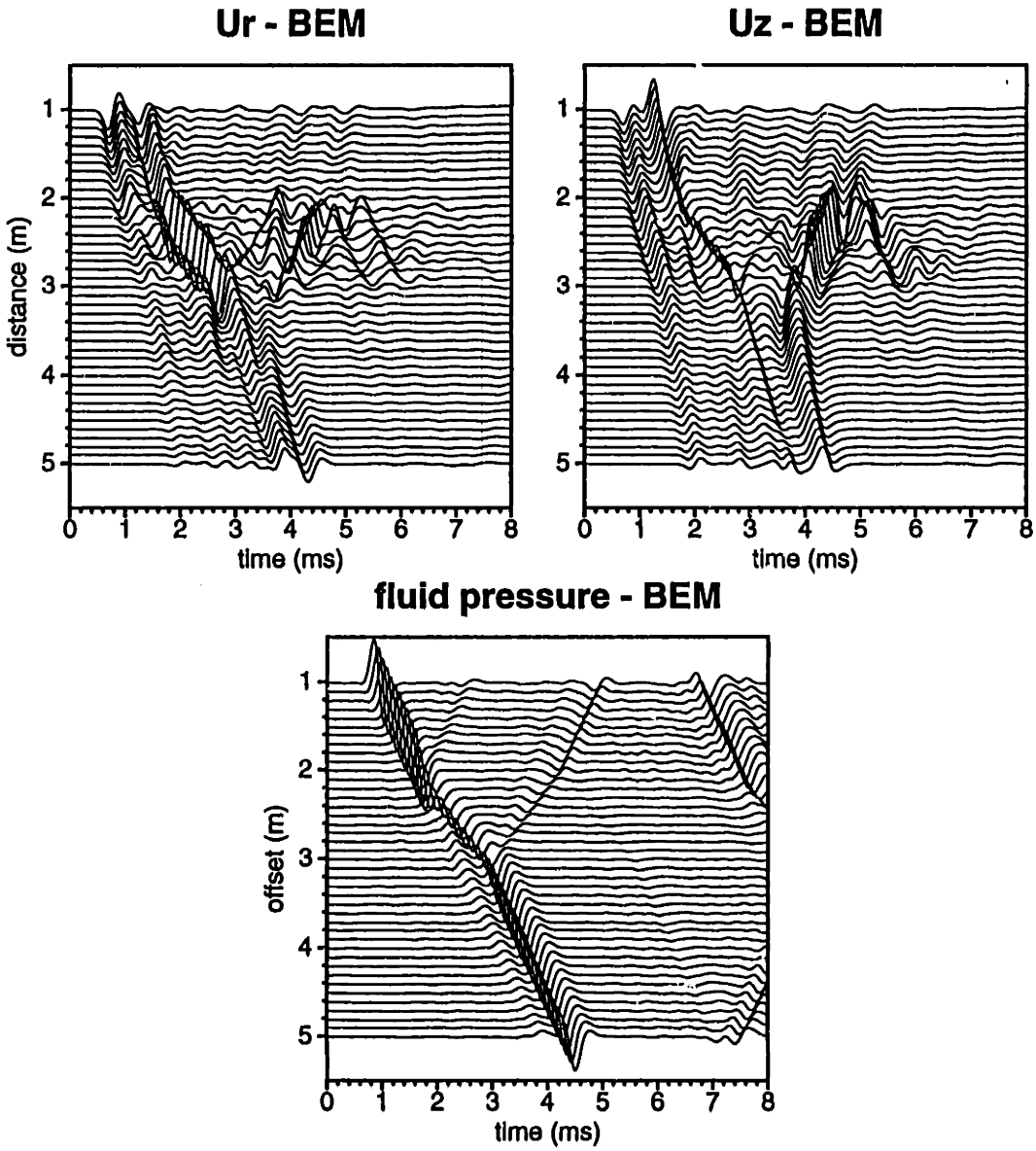

Figure 4-10: Displacements in the formation and pressure in the fluid for a radial source (radially applied pressure over a range) in a fluid-filled borehole penetrating a three-layer isotropic medium. Parameters: $\alpha_1 = \alpha_3 = 3000\ m/s$, $\beta_1 = \beta_3 = 1700\ m/s$, $\rho_1 = \rho_3 = 2.7\ g/cm^3$; $\alpha_2 = 2000\ m/s$, $\beta_2 = 850\ m/s$, $\rho_2 = 2.4\ m/s$.

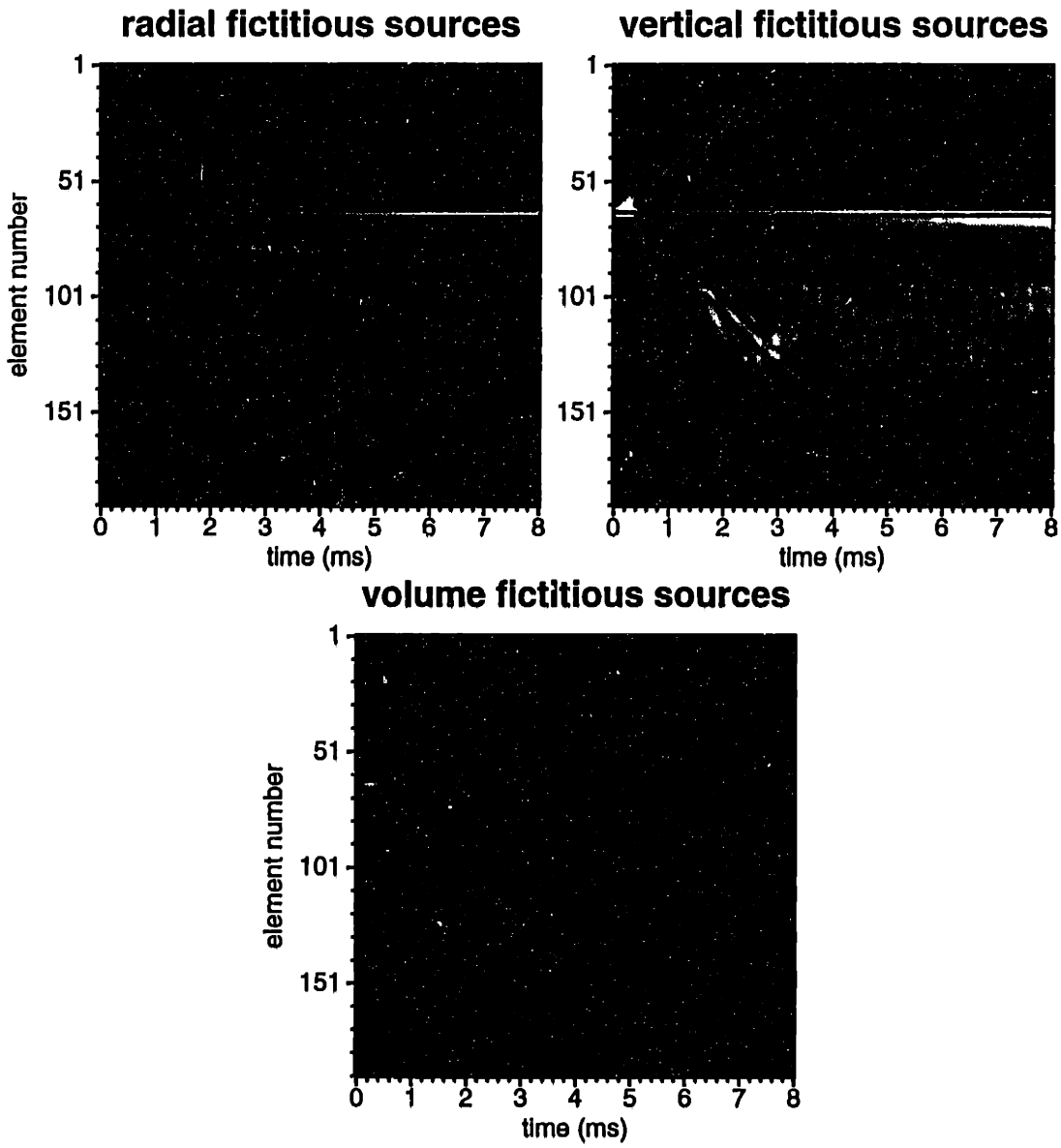

Figure 4-11: Fictitious boundary sources for the radial source in the fluid-filled borehole penetrating the three-layer isotropic medium in Figure 4-10.

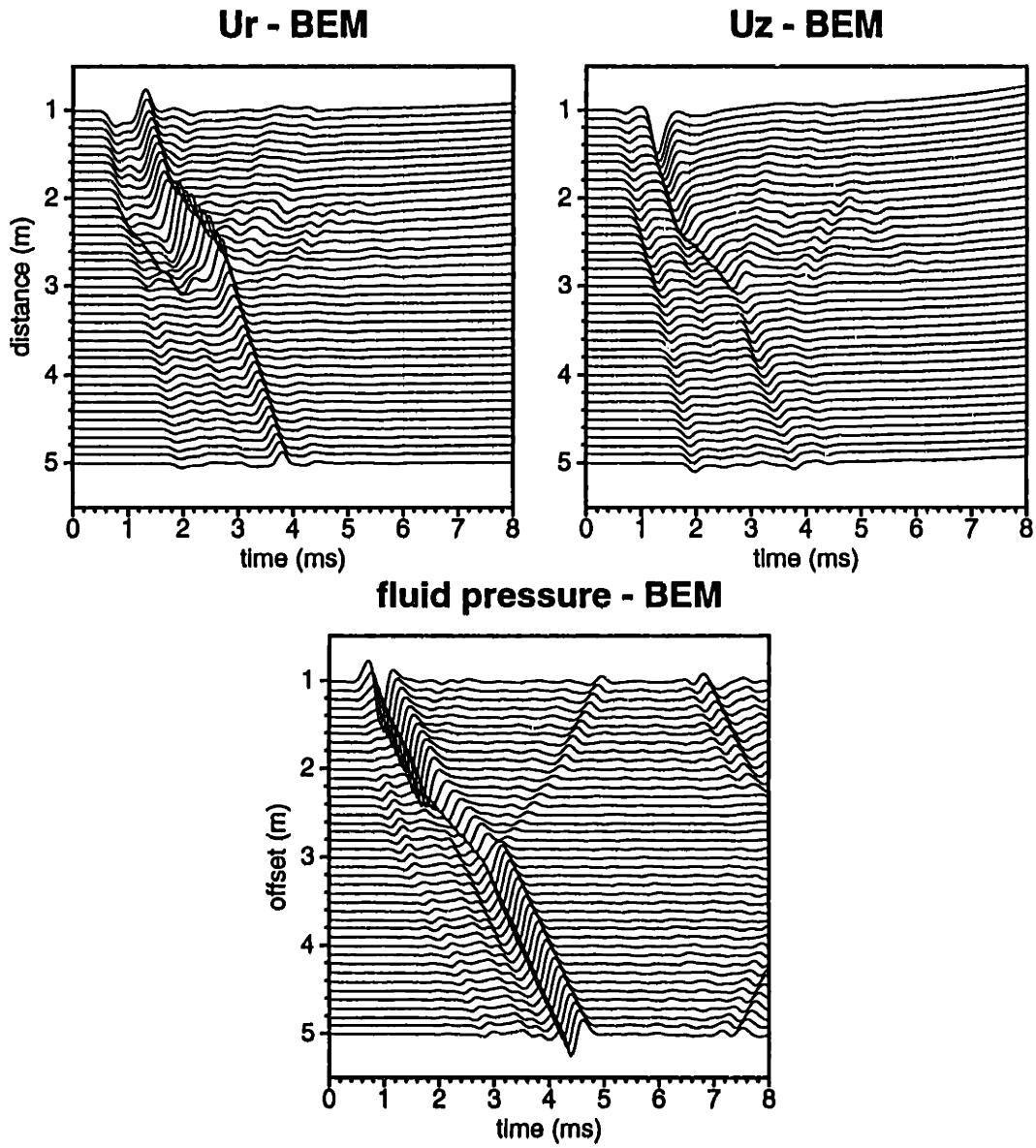

Figure 4-12: Displacements in the formation and pressure in the fluid for a vertical source (wall-clamped vertical vibrator) in a fluid-filled borehole penetrating a three-layer isotropic medium. Parameters: $\alpha_1 = \alpha_3 = 3000\ m/s$, $\beta_1 = \beta_3 = 1700\ m/s$, $\rho_1 = \rho_3 = 2.7\ g/cm^3$; $\alpha_2 = 2000\ m/s$, $\beta_2 = 850\ m/s$, $\rho_2 = 2.4\ m/s$.

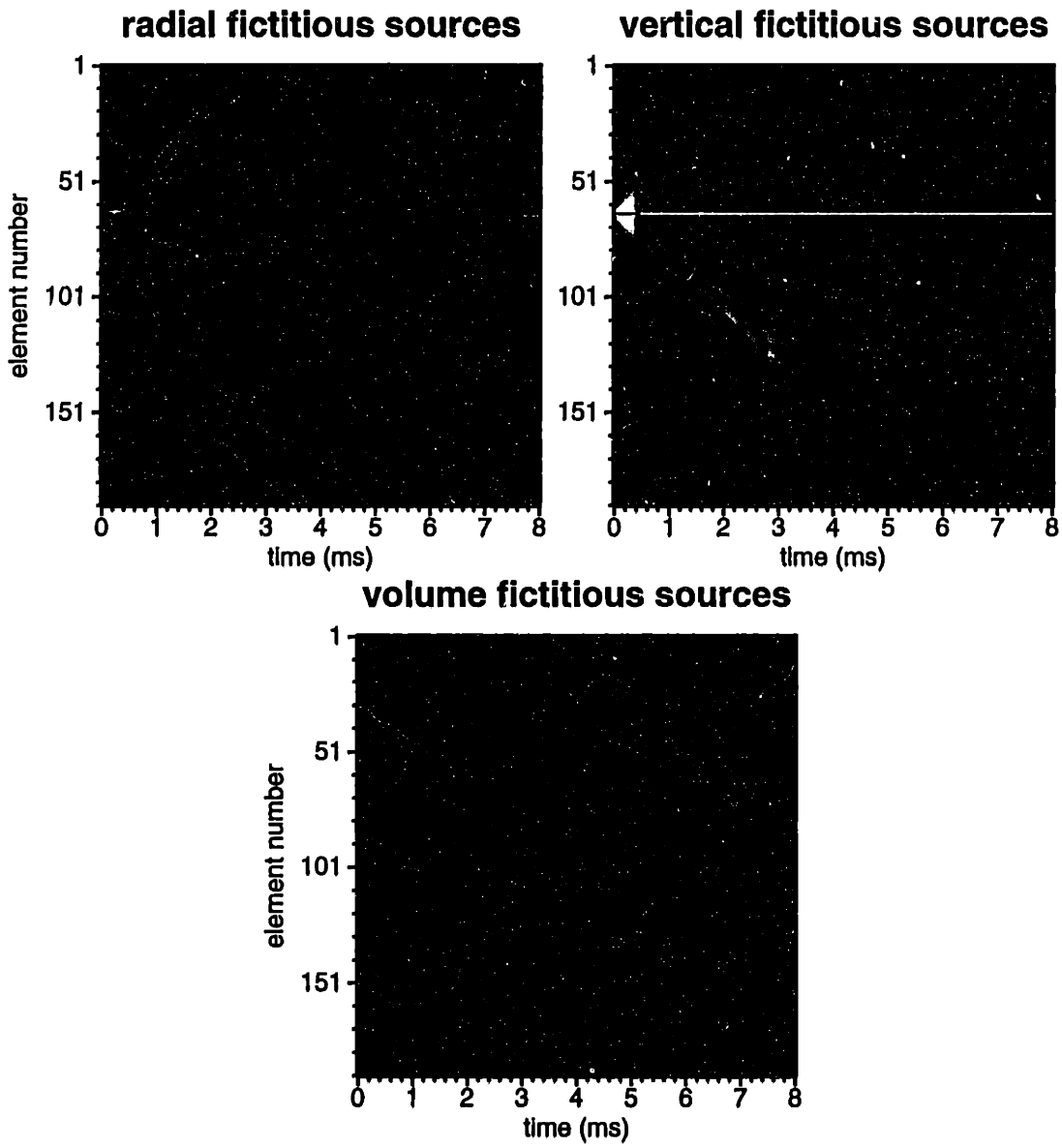

Figure 4-13: Fictitious boundary sources for the vertical source in the fluid-filled borehole penetrating the three-layer isotropic medium in Figure 4-12.

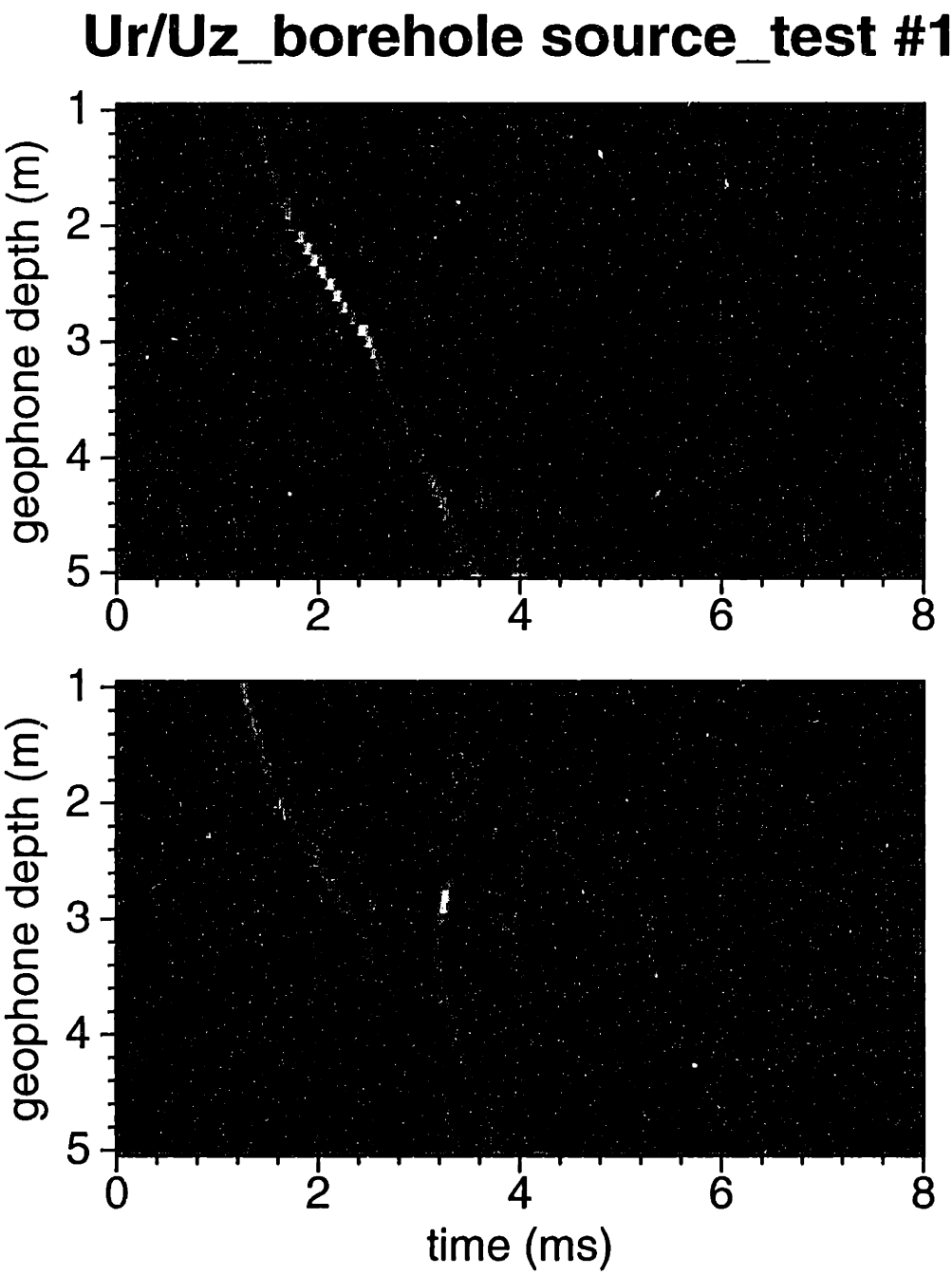

Figure 4-14: Displacements for a three-layer medium with the same first and third layer parameters as in Figure 4-8. The second layer now is anisotropic with parameters: $c_{11} = 11.5$, $c_{33} = 10$, $c_{13} = 4.8$, $c_{44} = c_{56} = 2.6$, in Gpa and $\rho_2 = 2\ g/cm^3$.

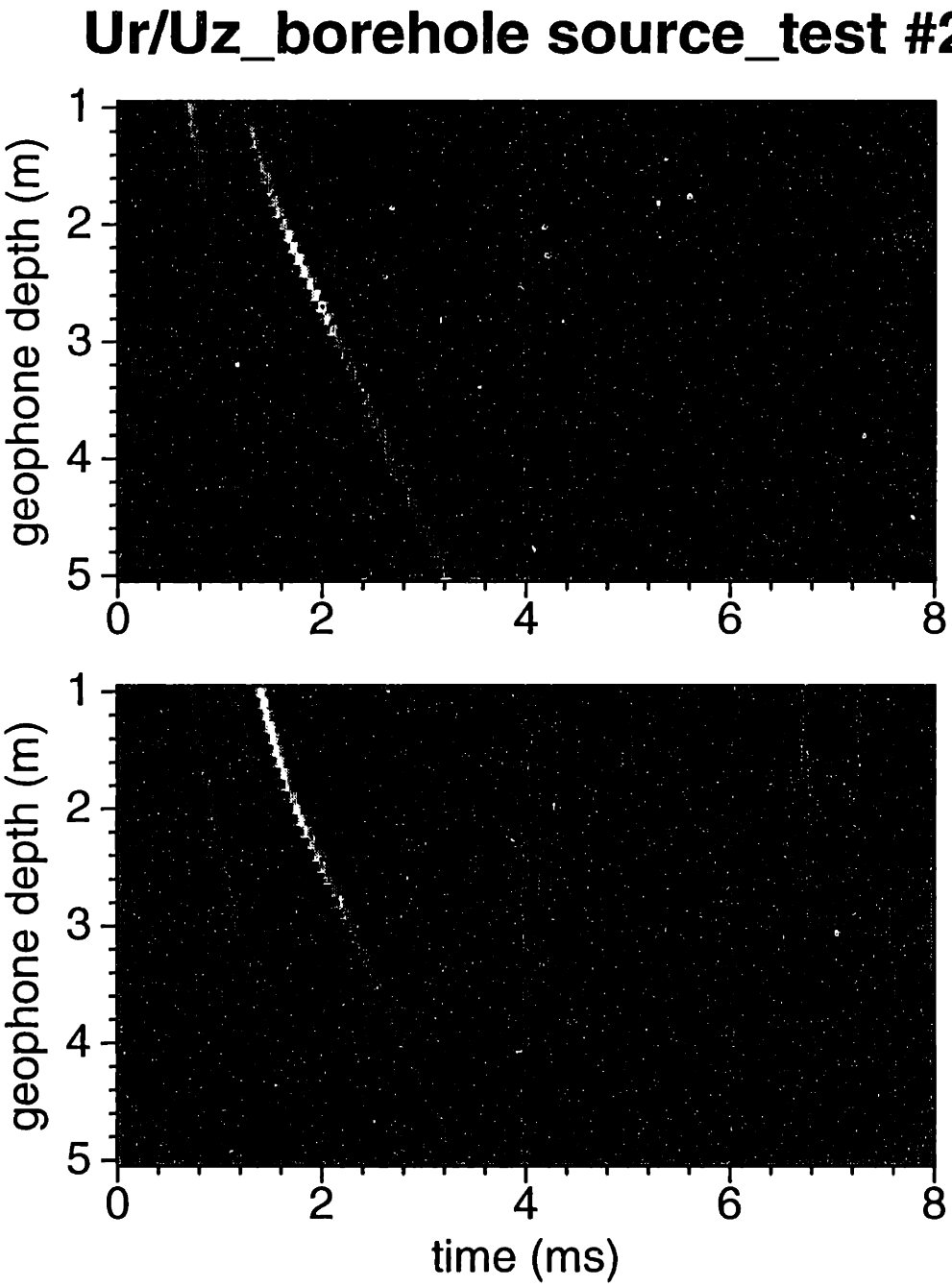

Figure 4-15: Displacements for a three-layer medium with the same first and third layer parameters as in Figure 4-8. The second layer now is isotropic with $\alpha_2 = 3000\ m/s$, $\beta_2 = 1500\ m/s$, $\rho_2 = 2$.

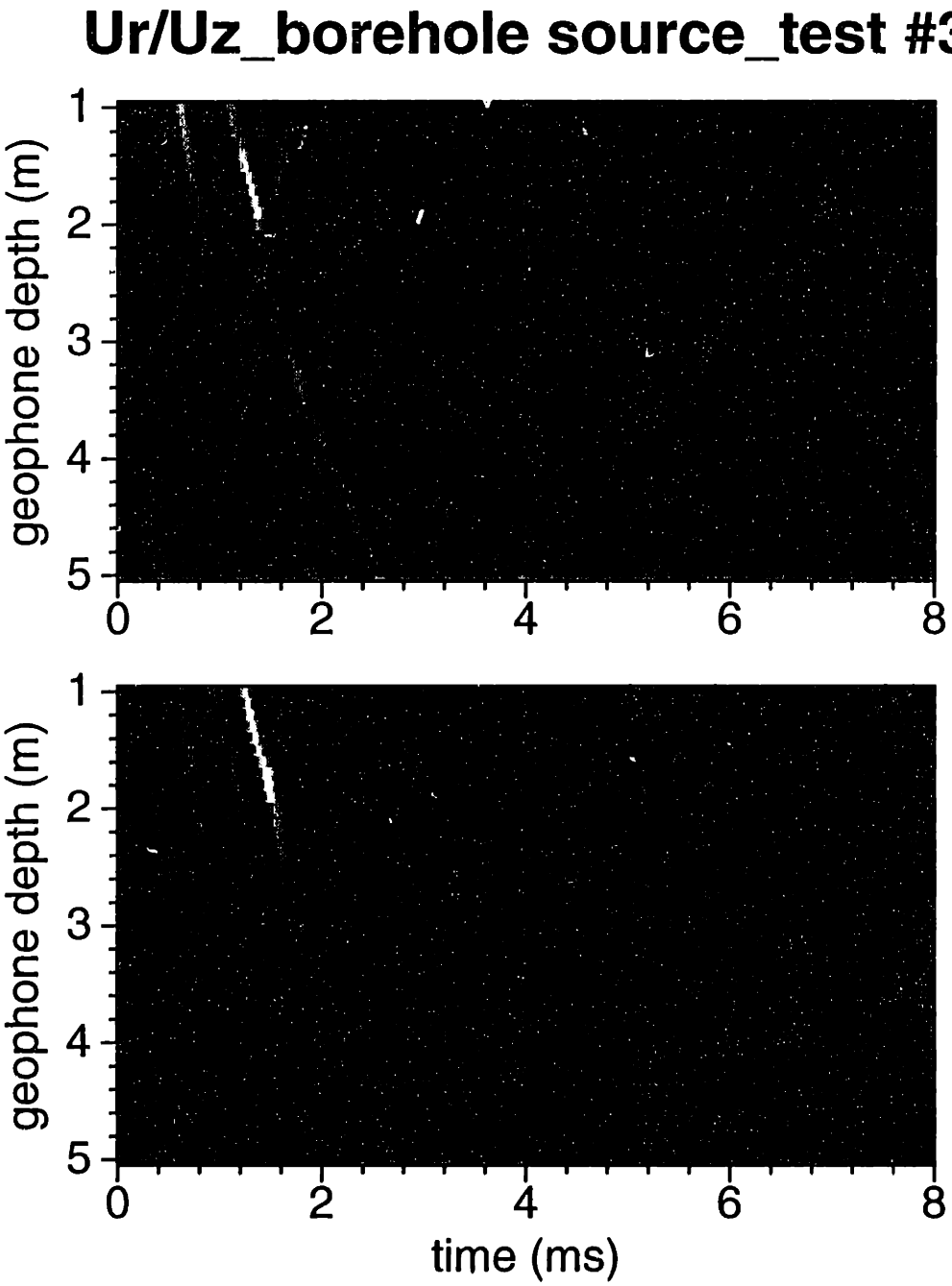

Figure 4-16: Displacements for a three-layer medium with the same first and third layer parameters as in Figure 4-8. The second layer now is isotropic with $\alpha_2 = 5000\ m/s$, $\beta_2 = 3000\ m/s$, $\rho_2 = 2.3$.

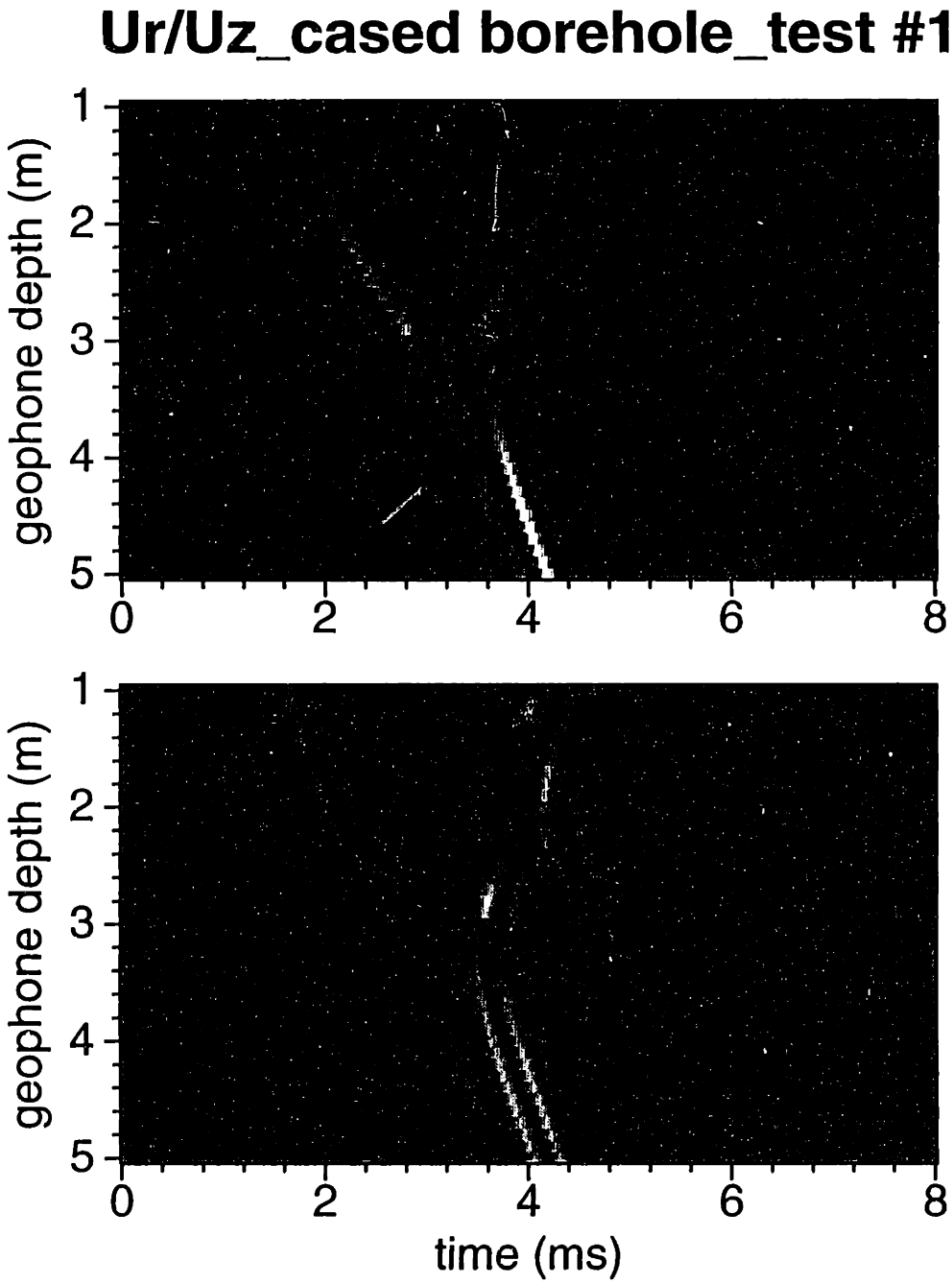

Figure 4-17: Displacements for an explosion in a cased borehole in the three-layer medium of Figure 4-14. Borehole radius, casing thickness, and cement thickness are 12, 2, 2 in *cm*.

Chapter 5

Real Data Modeling and Analysis: the Buckhorn Crosshole Experiment, Illinois

5.1 Introduction

Cross-well data, with its rich information contents, have been used in traveltime tomography as means of picking first arrival time (e.g., McMechan, 1983), in diffraction or reflection tomography where scattered waves are utilized to obtain high-resolution images (e.g., Pratt and Goulty, 1991). Recent studies in cross-well continuity logging, full waveform inversion of cross-well data, and wave equation-based tomography, have prompted interested geophysicists to look into the various possible waves in the data (Harris, 1988; Krohn, 1990; Lines *et al.*, 1992, among others).

In the previous chapter, we developed a BEM based algorithm to model the radiated waves from borehole sources in layered anisotropic media. This algorithm is utilized in this chapter to analyze a real cross-well hydrophone data set from Buckhorn, Illinois. The site geology and experiment setup are presented first. Previous tomography work on the data set and conclusions are reviewed to set up our model.

Then, three types of modeling are carried out to fully understand the data: one without including the source and receiver boreholes, one with the receiver borehole only, and one with the source borehole only. Results from the one including the source borehole show remarkable agreement with the data, the others do not.

5.2 The Site and the Experiment

A crosshole tomography experiment was conducted in 1990 by OYO Corporation at its Buckhorn test facility in Illinois to determine the details of an oil producing limestone formation (Takahashi *et al.*, 1991; Saito *et al.*, 1991). The oil field and the crosshole data set are owned by Western Kentucky Petroleum Company. The reason for carrying out the experiment is shown in Figure 5-1. The letters represent the names of each borehole in chronologic order of drilling and, their economic values are indicated by words inside the parentheses. After encountering a dry hole (B) only 45 meters away from the producing hole (A), a decision was made to drill the other three. Holes C and E are dry, while hole D is wet. It was obvious that a change in the geology or the reservoir condition between borehole B and borehole D would be found. This justified the crosshole experiment between these two boreholes (see Takahashi *et al.* (1991) for detail).

The stratigraphy of the test site is shown in Figure 5-2. According to the exploration and production histories of the field, the oil reservoir is the porous zone of the Silurian *Kankakee* limestone formation, which is sandwiched between layers of shale and is horizontally distributed at a depth of about 200 m with less than 10 m thickness. The five boreholes were drilled to a depth of 270 m, inside the Trenton limestone. In Figure 5-3 and Figure 5-4, the resistivity and acoustic logs conducted at hole B and D show the stratigraphic layering. The acoustic log indicates that the P and S wave velocities for the oil reservoir are about 5500 m/s and 3000 m/s. The velocities of the shale formations are 2300 to 2600 m/s for P-wave and 1000 to

1300 m/s for S-wave. The logs for borehole D show a low velocity zone inside the Kankakee limestone which probably represents the porous zone of the formation. On the other hand, this low velocity zone is not visible from the well-logs in borehole B, indicating the termination of the porous zone before it reaches well B.

The setup of the crosshole experiment, which uses hydrophones as receivers, is shown in Figure 5-5. In this experiment, 48 traces ranging from 18.5 m to 253.5 m at a 5 m spacing are recorded for 19 shots with 10 m spacing at a depth of 80 m to 260 m. The source used in borehole D is an explosion source - a small amount of dynamite, strong enough to destroy the inside of a typical graduate student's office, but gentle enough to not damage the borehole. Both B and D are fluid-filled open boreholes (only the near surface parts are cased with PVC casing). with a diameter of 6 in (15.25 cm). In Figure 5-5, only the major interfaces between shale and limestone are shown although other shale/shale interfaces prove to be very important, as discussed in later sections.

5.3 Preliminary Data Analysis

Hydrophone data for six shot points are shown from Figure 5-6 to Figure 5-11. A low pass filter of trapezoid shape in frequency domain, with corner frequencies at 0-100-600-800 Hz, is applied to all sections to remove high frequency noise. In the following pages, we describe the present understanding of these data.

5.3.1 Shale anisotropy

The first arrival times from the hydrophone data set were used by Saito *et al.* (1991) in their tomographic traveltime inversion for the test area. They assumed that the shale and limestone layers were isotropic. Although the tomogram clearly showed the Kankakee limestone and its low velocity zone near the D borehole, the shale layers appeared very inhomogeneous and were corrupted by seemingly high velocity

artifacts extending horizontally in the shale formation. Saito (1991) concluded that these artifacts were due to the anisotropy of the shales. He went on to determine the anisotropy of these shales from the data and used the information in a "stretched" isotropic tomography to incorporate the anisotropy. The artifacts in the tomogram were largely suppressed.

Saito (1991) assumed the shales had elliptical velocity dependency such that

$$V^2(\phi) = \frac{V_v^2 V_h^2}{V_v^2 \sin^2\phi + V_h^2 \cos^2\phi}, \tag{5.1}$$

where, $V(\phi)$ is the shale P-wave velocity in the ray direction ϕ from vertical. V_v and V_h are the velocities in the vertical and horizontal directions. The anisotropy measure is then given by V_h/V_v. Its value is determined by fitting an ellipse to the plotted points of the direct wave velocities as a function of ray angles. Saito (1991) also used some head wave information to improve the estimation by increasing angular coverage. The reliability of the head wave data is questionable because of shorter time separation between head wave and the direct wave, because of the small well spacing (25 m). Nevertheless, Saito (1991) concluded that the V_h/V_v ratios for the shales range from 1.026 to 1.149. This P-wave anisotropy information will be incorporated in the later modeling. From the hydrophone data one sees that the formation shear wave induced fluid pressure in borehole B is not clear. This makes it very difficult, if not impossible, to estimate the shear wave anisotropy of these formations. Thus, shear wave isotropy is assumed in later modeling.

5.3.2 Receiver borehole tube waves and their implications

Most of the later arrivals in the hydrophone data are induced tube waves in the receiver borehole. There are several ways that wave energy in the formation can convert to borehole tube waves. The easiest and most efficient conversion is through rock fractures. A passing seismic wave squeezes fluid inside the fractures and into the borehole and creates disturbances that can propagate up and down along the

borehole. For real data examples of this type, one can consult Lee (1990) and Cicerone (1991), where Kent Cliffs VSP data present an excellent illustration of this conversion mechanism. Body wave to tube wave conversion through borehole irregularities, such as wash-outs and radius changes, has a similar mechanism. Another efficient tube wave excitation is provided by guided waves in formation, especially for low velocity waveguide. When the effect of the source borehole is considered, thin low velocity layers sandwiched by high velocity layers will always be good waveguides, no matter where the actual source may be. This phenomena has been discussed in the previous chapter. Finally, formation interfaces may generate tube waves due to different elastic responses of the media to body waves squeeze strain on the borehole wall. This mechanism has been studied by White (1953; 1983) using his borehole coupling theory, which is briefly described in the following subsection.

5.3.3 A review of borehole coupling theory

Borehole fluid pressure and tube waves due to formation interfaces intersecting with a fluid-filled borehole are governed by the low frequency borehole coupling theory proposed by White (White, 1953; 1983). This theory states that the borehole fluid pressure at any point in the fluid column is due to a collective contribution of secondary sources distributed along the borehole wall. Physically, these sources are created by the squeeze effect of seismic waves propagating in the formation. A quantity that express this effect is termed *squeeze strain*, which is the fractional change in the cross-sectional area of the borehole. Mathematically, the pressure in fluid is

$$P(t,z) = -\frac{\rho_f c_T}{2}\int_{z_1}^{z_2} \frac{\partial \epsilon(t-|z-z'|/c_T),z')}{\partial t} dz' + P_d(t,z) + P_u(t,z), \qquad (5.2)$$

where, z_1 and z_2 are boundaries of the borehole section of interest. This pressure, $P(t,z)$, satisfies the well-known 1-D acoustic wave equation, but with the tube wave velocity. P_u and P_d are up- and down-going waves dictated by the boundary conditions

for the fluid at z_1 and z_2. The borehole squeeze strain, $\epsilon(t,z)$ is

$$\epsilon(t,z) = \frac{\delta A}{A} = \frac{2(\tau_{xx} + \tau_{yy} - \nu\tau_{zz})}{E}, \tag{5.3}$$

where, τ_{xx}, τ_{yy}, and τ_{zz} are the normal stresses measured at the borehole wall as if the borehole were absent. E and ν are Young's modulus (here, a measure of the borehole deformation) and Poisson's ratio. The squeeze strain can also be written as

$$\epsilon(t,z) = \frac{\overline{u}_r(t,z,r_0)}{2r_0}, \tag{5.4}$$

where, $\overline{u}_r(t,z,r_0)$ is the average horizontal displacement at the borehole wall. At low frequency, it is close to the actual horizontal displacement when borehole is absent.

White's coupling theory has been verified by Schoenberg (1986) by taking the low frequency limit to the complete solution. Marzetta (1992) applied the theory to remove tube waves in VSP hydrophone data. He termed his technique the inverse borehole coupling. Subsequent modeling of VSP hydrophone data using White's theory is implemented by Peng *et al.* (1993) for layered medium by assuming an explosion source in the formation.

Keeping in mind the results of previous subsections, we proceed to analyze the hydrophone data by three kinds of modeling. First, we model the data with no borehole effect included in the wave field. Second, the receiver borehole effect is isolated to show how the receiver borehole affects the data. Third, only the source borehole effect is considered to see what events in the data are actually caused by the source borehole.

5.4 Model I: No Boreholes

The computer code used for this modeling is implemented according to the discussions in Section 4.5. Source and receiver boreholes are not included so that the wave effects due to direct propagation, reflection, transmission, and conversion may be isolated. For the source, a radial ring force of .2 m length is used to simulate the effect of a

rocks	*depth (m)*	*properties (in GPa and g/cm^3)*					
		c_{11}	c_{33}	c_{13}	c_{44}	c_{66}	ρ
shale	71	10	10	4.8	2.6	2.6	2.0
limestone	137	50	50	16.4	16.8	16.8	2.3
shale 1	166	11.5	10	4.8	2.6	2.6	2.0
shale 2	195	13.5	12.5	7.1	2.7	2.7	2.0
limestone	202	58	58	16	21	21	2.3
shale	220	10	10	6.0	2.0	2.0	2.0
shale	226	19	19	10.2	4.4	4.4	2.2
shale	257	17	15	7.9	3.55	3.55	2.1
limestone	N/A	58	58	16	21	21	2.3

Table 5.1: Model and parameters used for Buckhorn crosshole data modeling.

source borehole on the radiation pattern of the P and SV waves. Though this is not exact, it is a reasonable approximation. For the receiver, 3-component geophones are assumed. However, we only show the horizontal component of the displacement in subsequent discussions.

Table 5.1 lists the model parameters. The conclusions from Saito (1991) about shale anisotropy are incorporated in the model. The number of layers does not correspond exactly to the one specified in Figure 5-5. Rather, the layering in Table 5.1 is based on the resistivity and acoustic logs in Figure 5-3 and Figure 5-4. Figure 5-12 to Figure 5-17 show the horizontal displacements for the source at 110, 150, 180, 200, 210, and 240 m, respectively. A Ricker wavelet, with center frequency 600 Hz, is used for these figures.

Comparing Figure 5-12 and Figure 5-6, one immediately sees that the shear wave is the dominant feature in both the real data section and the synthetic section. The well-behaved and early arriving strong wave, extending from 137 m to 202.5 m, is identified as the transmitted shear wave through the limestone/shale interface at 137 m. It has an apparent velocity of 1220 m/s, with almost constant move-out, due to the sharp shear wave contrast between the two media. The critical angle for shear-

shear transmission at this interface is about 20 degrees. The reflections of the direct shear wave from interfaces at 71 and 137 meters are visible in both the data and the synthetics. So is the reflection of the strong shear wave from the interface at 193 meters (I believe the data have a shift of two traces downward). The less developed waveform in the limestone region is probably caused by the borehole irregularities in this section, as indicated by the logs. One should note that the other strong event in the data is not modeled by this synthetic. Thus, we deduce that it has no body wave origin. The reason will be explained later.

For Figure 5-13, the source is in the shale layer. In the limestone section, though the P-P transmitted wave is not visible, the P-S converted wave and S-S transmitted shear wave are recognizable. Their expressions as fluid pressure are immediately identified in the real data. The primary P and S waves in the shale section from 137 to 193 meters are much stronger due to the softness of shale relative to limestone. This shear wave is reflected, transmitted at the 193 meter interface. The up-going primary S wave S-S reflection from the 137 meter interface causes the other strong shear wave in the synthetic. It can be correlated with the real data only to a certain extent, because the data at these traces have a more complicated waveform. Other events that are not modeled by the synthetic include those propagating upward and crossing the 137 meter interface without much move-out alternations, and the disturbance arriving after 80 ms at a depth of 208 m.

For a source at 180 meters, the synthetic (Figure 5-14) and the data (Figure 5-8) look quite different. This is mainly due to the strong events extending across the whole section and the event arriving at 60 ms at depth 208 meters. Despite all these, the primary P and S waves and their reflection and transmission at major interfaces are clearly shown on the synthetic, and the corresponding waves are identifiable on the data section.

For Figure 5-9 and Figure 5-15, the dynamite source is at 200 meters, which is within the limestone section. The high velocity and hardness of the limestone make it

impossible to trap energy within the layer, and most of it leaks into the softer shales above and below. This is clearly shown by the symmetrical appearance of the P and S waves. When the source is moved to the shale section at 210 meters (Figure 5-10 and Figure 5-16), most energy is blocked by the limestone layer. The reflected wave interferes with reflections from the 220 meter interface and forms complicated waveforms. This is especially true for the real data. The seemingly constant move-out for the transmitted shear wave results from the extraordinary refraction effect of the limestone layer. Similar features exist in Figure 5-17 for shot point at 240 meters.

In summary, modeling crosshole seismic data using radial forces in the absence of both the source and the receiver borehole can predict, at least kinematically, the direct, reflected, and transmitted P and S waves. Thus, one can obtain a feeling about the nature of the waves contained in the data. This modeling, however, cannot explain three major events in the data set: the later arriving wave in Figure 5-6, later events in Figure 5-7 to Figure 5-11, and events crossing major interfaces without significant move-out change. In the next two sections, where receiver and source boreholes are subsequently included in the modeling, these three features are identified as being related to both boreholes.

5.5 Model II: Receiver Borehole Only

In this section, pressure at the axis of the fluid-filled receiver borehole is calculated in order to identify events in data that result from the receiver borehole. An implementation of White's coupling theory for explosion sources within layered isotropic formation is given by Peng *et al.* (1993). Though it is straight forward to code up White's theory (see subsection 5.3.3) for more complicated sources in layered anisotropic media, the implementation by Peng *et al.* suits to our purpose well, thus, is used to illustrate the receiver borehole effect.

Figure 5-18 shows the pressure in the receiver hole due to an explosion source at

110 meters inside the limestone formation. Since there is no direct S wave excited by the source, only the P wave-created pressure is recorded in this limestone section. One can also exclude events related to direct shear wave reflection and transmission. Thus, above and below the limestone layer, the first arrivals are pressures due to transmitted P waves, while the second arrivals are pressures caused by P to S converted waves at both interfaces. The third arrivals, that are parallel to the second arrivals are the P to S reflected, then transmitted S waves. Events with opposite move-out in the upper part of the figure are reflected P and S waves due to an assumed free surface at a depth of 0 m. The down-going P wave is reflected and transmitted into P and S waves at the 195 meter interface. Also generated at this interface is a tube wave propagating up and down along the borehole, manifested by two separate waveforms for the transmitted waves. The tube wave and the shear wave cluster together because of their similar propagating velocity and direction. In studying this figure, one should not be concerned with the later time numerical noise (after 80 $msec$) at the source location.

The pressure due to the source at 150 meters is shown in Figure 5-19. Its comparison to Figure 5-13 immediately shows the presence of tube waves. Significant tube waves are generated at the 137 meter and 195 meter interfaces. They have the characteristically slower velocity than the sound speed in water (1500 m/s), and they cross major interfaces (such as the one at 71 meters) without significant move-out variation. The measured tube wave velocity in the limestone section is 1390 m/s. Tube waves in the shale section have roughly the same velocity as the shear wave apparent velocity. They interfere with each other and form complicated waveforms, which are evident from the hydrophone synthetic and the real data in Figure 5-7. Similar observations can be made about Figure 5-20, where the explosion source is at a depth of 180 meters. When comparing Figure 5-20 with the real data in Figure 5-8, one notices that the tube waves induced by a shear wave are much stronger than those excited by a compressional wave. This is because the shear wave amplitude

is usually much larger than that of the compressional wave, and the deformation of borehole in the shear wave case is more severe.

For sources at 200 meters (Figure 5-21) and 210 meters (Figure 5-22), the P to S converted waves above and below the source position dominate the section. The up-going shear wave generates a strong tube wave at the 137 m interface. Interfering with this up-going shear wave is a tube wave, generated at the 195 m interface, and propagating with a slower velocity than the apparent velocity of the up-going shear wave. This is evident from the separated waveform of the tube wave in the limestone section in later time. It is also evident from these sections that the down-going converted shear wave also produces tube waves at deeper interfaces. For an explosion source at 240 meters (Figure 5-23), one observes that tube waves are generated at all interfaces above the source.

In summary, when P and S waves pass by a fluid-filled borehole, squeeze strain is created at every point along the borehole. If the borehole is in a homogeneous formation, no tube wave will be generated because of the continuity of the squeeze strain along the hole. However, if the borehole penetrates a layered formation, tube waves will be excited at these interfaces due to the discontinuity of the squeeze strain. Since the shear wave amplitude in an elastic formation (no attenuation) is usually stronger than that of a P wave, tube waves associated with a shear wave normally dominate a hydrophone section. Although tube waves propagating up and down from an interface come from the same origin (same squeeze strain discontinuity), fluid pressure, due to these waves (thus their amplitudes) on both sides of the interface, may be very different. The direction of incident wave affects the tube waves going up or down. They add more constructively in one direction because of phase velocity is closer to tube wave velocity. The pressure difference is also attributed to the different confinement to the tube waves by the elastic formation. Pressure is usually higher in a borehole section surrounded by a hard formation than by a soft formation. Comparison of synthetic to real data identifies the existence of tube waves, and shows

the adequacy of White's coupling theory in predicting borehole tube waves generated by passing body waves.

5.6 Model III: Source Borehole Only

In this section, the algorithm developed in Chapter 4 is utilized to determine the effect of the source borehole on the Buckhorn crosshole data. Same model parameters, as listed in Table 5.1 are used. However, to simplify the computation, different portions of the model are used for different source positions. The actual borehole radius of well D, 0.762 cm, is incorporated in the modeling.

5.6.1 Source at 110 meters

Figure 5-24 shows the horizontal displacement recorded by 28 geophones ranging from 69 m to 203 m for the explosion source inside Well D, at a depth of 110 meters. Comparing this result with the real data in Figure 5-6 and the no-borehole synthetic in Figure 5-12, we immediately recognize that the later arrival in the data is real, and it is due to the presence of the source borehole.

What is the nature of this event? Is it a Mach wave? The existence condition for a Mach wave is that the tube wave velocity must exceed the shear wave velocity of the formation. At the low frequency limit, the tube wave velocities in isotropic and anisotropic media are

$$C_T = \begin{cases} c_f \sqrt{\frac{\mu}{\mu+\rho_f c_f^2}}, & \text{for isotropic media,} \\ c_f \sqrt{\frac{c_{66}}{c_{66}+\rho_f c_f^2}}, & \text{for anisotropic media.} \end{cases} \tag{5.5}$$

According to this and the shear wave parameters used in the model, the tube wave should have a velocity of 1100 m/s, which is slightly less than the shear wave velocity, which is 1140 m/s. Thus, the extra event is not of Mach wave origin. Measurement of the arriving time for this event from the trace at 193 m, and from different source positions, shows a nearly constant time delay of 7.1 ms. This is understandable only

if the wave travels as a tube wave in the limestone formation, which can support a tube wave velocity of 1400 m/s. With this velocity and the source spacing of 10 m, the proper time delay is achieved. Figure 5-25 shows the traces of interest from the real data for shot points from 80 to 120 meters.

Most of the energy from a dynamite explosion is trapped by the fluid-filled source borehole due to the extraordinary stiffness of the limestone formation. The trapped energy propagates along the borehole as tube waves. Once a tube wave encounters the interface between the limestone and the much softer shale, the energy is quickly released into the shale, because a borehole in the shale section traps less tube wave energy. The sudden transition of formation, and the quick release of energy, create a strong secondary source at the limestone/shale interface, resembling a radial force. This induced source radiates shear wave energy efficiently into the shale formation. This postulate for the mechanism of this wave phenomenon is supported by the synthetic simulation, where a hyperbolic time move-out with apex at the level of limestone/shale interface is obvious in the vertical displacement section (Figure 5-24). Also clearly shown is the shear wave radiation pattern associated with this secondary source: larger shear wave amplitudes at a greater observation angle from the direction of the force. This hyperbolic time curve and radiation characteristic is observable in the real data (see Figure 5-6).

Another test with different rock overlaid by the same limestone proves the above postulate and rules out the possibility of a Mach wave. Figure 5-26 shows the radial and vertical displacements for limestone over a rock having 3600 m/s and 1700 m/s as its P and S wave velocities and 2.1 g/cm^3 as its density. One notices the existence of a tube wave converted shear wave, and the conversion occurs at the interface. Though the kinematics of this wave is similar to that in the limestone/shale case, its amplitude is significantly smaller. This amplitude reduction confirms the previous postulate, and demonstrates that the magnitude of the secondary source depends on the contrast between the two formations. The sharper the contrast, the stronger the

converted wave.

Another important condition for the clear visibility of this wave conversion phenomena, is the relative amplitude of the wave with respect to the primary waves. Since the dynamite source is in the limestone section, little energy is radiated out and the amplitudes of the primary waves are thus relatively small. Winbow (1991) concludes that for point volume source, 99% of its energy is trapped as a tube wave. Thus, the secondary source is on the same order as the effective borehole source that radiates the primary waves.

5.6.2 Source at other positions

A common feature among the real data for shot points at 150, 180, 200, 210, and 240 meters is the later arriving events following the shear waves. These waves have very complicated waveforms, with up-going and down-going branches. When examined carefully, they have a linear move-out in each layer, and the move-out changes slightly from layer to layer. Their speeds are less than the sound speed of the borehole fluid (water), both in hard (limestone) and in soft (shale) formations. All this suggests and supports that these waves are tube waves. They are characteristically similar to the tube waves in the source borehole, but different in origin. In Section 5.3.2, several possible causes for receiver borehole tube waves have been listed. However, the possibilities of fracture, borehole irregularity, and interface conversion at the receiver borehole, can be ruled out. This is due to the following reasons:

- tube wave arrival time would be much earlier than the one observed in the data, if a fracture, irregularity, or interface conversion was the cause for the tube waves.

- these waves would be observed in Section 5.5 if interface conversion at the receiver borehole was the cause.

- the excitation time of the tube waves would be a hyperbolic function of the shot position.
- the measured time at the apex of the late arriving tube waves in the data is basically a linear function of the shot point position. This is shown in Figure 5-27.

Thus, these tube waves are of a guided wave origin. On the other hand, this guided wave is not the type of guided waves commonly observed in seismology and ocean acoustics. It specifically pertains to the acquisition geometry of cross-borehole seismics. More accurately, it is due to the presence of the source borehole.

With the source borehole included in the modeling, the displacements resulting from the five sources, are shown in Figures 5-28 to 5-32 respectively. In all the synthetic seismic sections, the P wave amplitude is much smaller than the S wave because, as stated before, attenuations for both waves are not included. S wave attenuation is usually more severe than that of a P wave, thus, more balanced P and S waves appear in the real data. Nonetheless, in these synthetics, strong waves appear near the apex position of the tube waves in the real data. These are the waves responsible for the tube waves in the hydrophone data. According to White's coupling theory and the wave equation governing the propagation of tube waves in a borehole, these waves in the displacement synthetic sections serve as the excitation (source) for receiver borehole tube waves.

The traveling path of these waves can then be inferred from Figure 5-27 and the fact that they appear only when a source borehole is included in the modeling. In the source borehole, the explosion source excites a very strong tube wave (99% of the source energy). This tube wave travels up and down the source borehole with little loss of energy. When passing through a soft formation, such as the shale layer ($V_s = 1000\ m/s$) beneath the oil-producing limestone, the tube wave converts to shear waves. And these shear waves are guided by the low velocity channel. The stronger vertical displacement components of these waves in Figure 5-28 to Figure 5-

32 verify this mechanism. Then, these shear waves excite tube wave propagating up and down in the receiver borehole. It is due to this path that the arrival time of tube waves in the data is much longer than that of the primary shear waves. This wave phenomenon and the one associated with the source at 110 m are schematically shown in Figure 5-33.

5.7 The Interface Wave Possibility

One may question whether interface waves at the limestone/shale boundary do exist and whether they cause disturbances in the receiver borehole. According to Gilbert *et al.* (1962), two pulse-like phenomena, denoted by $\bar{P}$ and $\bar{S}$, exist near the boundary of an elastic solid in addition to the P and S pulses. The $\bar{P}$ pulse is distinguishable only if the Poisson's ratio of the material is greater than 0.4, which is close to liquid. It is the classic Stoneley wave in the fluid/solid contact problem, such as the fluid-filled borehole problem. The $\bar{S}$ pulse is the classic Rayleigh pulse in Lamb's problem, and the classic Stoneley pulse in Cagniard's problem.

For the limestone/shale interface we are considering, the existence of $\bar{P}$ can be ruled out, because neither medium has a Poisson's ratio of 0.4 or greater. For a propagating loseless $\bar{S}$ wave to exist, the Stoneley wave existence condition has to be met. Checking with the condition diagram provided in Gilbert *et al.* (1962), we found the rigidity ratio of the limestone and shale to be about 0.1, while their density ratio is probably close to one (although we don't know the exact density of each rock) and, the existence condition of the Stoneley wave is violated. Thus, one should not expect a Stoneley wave to propagate along a limestone/shale interface.

When the Stoneley wave existence conditions are violated, the $\bar{S}$ pulse still exists for many solid pairs. But, as it travels along the interface, it loses energy to the surrounding media. This is the leaky wave. Since its energy is weak over large distance, this wave is usually invisible in cross-well seismic sections.

According to the above analysis, we rule out the possibility of interface waves causing the later arriving tube waves in the receiver borehole.

5.8 Observation of Reciprocity

The next logical step in the analysis of cross-well data is to incorporate both the source and the receiver boreholes in the model. Unfortunately, this step is limited by the available computing power, thus is not carried out in this thesis. However, the effects of the receiver borehole and the source borehole have been discussed separately in Section 5.5 and Section 5.6. The results of the two sections can be combined to achieve a qualitative understanding of the source and receiver borehole influence. The combination can be facilitated by the general principle of acoustic reciprocity.

Dynamite source and hydrophone receiver in the borehole fluid, which were used in the Buckhorn experiment, form good reciprocal source and receiver pair for the acoustic wavefield. That is, if the source and receiver positions are interchanged, the recorded wavefield remains unchanged. Unfortunately, the Buckhorn data were collected by hydrophones in one borehole with dynamite sources in another borehole. Thus, one does not have the luxury to interchange source and receiver to verify the reciprocity principle. However, if the medium between the two boreholes is horizontally layered, and if the conditions for both boreholes are the same, reciprocity can still be observed from the data. In other words, if the above conditions are met, a receiver at d_s^s (depth of a source in the source borehole) in the receiver borehole with a source at d_r^r (depth of a receiver in the receiver borehole) will record the same wavefield as the receiver at d_r^r with a source at d_s^s.

For the Buckhorn data set, the medium property and the borehole conditions (see Figures 5-3 and 5-4) are not far from those assumed in the above. Thus, when the original common-shot gathers are sorted into common-receiver gathers (with the receiver at the source position), similar wave phenomena should be expected on both

gathers. This speculation is confirmed by Figure 5-34 and Figure 5-35, where the common-shot and common-receiver gathers at or near 110 m and 180 m are shown. As discussed before, the strong later arrival in the common-shot section of Figure 5-34 is due to the source borehole and results from tube-to-shear wave conversion at the 137 m limestone/shale interface. On the other hand, the similar event in the common-receiver section of Figure 5-34 is due to the presence of the receiver borehole and is the result of shear-to-tube wave conversion at the same interface. In the common-shot section of Figure 5-35, the up-going tube wave within the limestone layer is due to the shear-to-tube wave conversion at the 137 m interface. The later arrivals are tube-to-shear-to-tube converted waves from source borehole to receiver borehole. In the common-receiver section of Figure 5-35, the "up-going" tube wave within the limestone layer results from the same wave phenomena as that in the common-shot section of Figure 5-34. The mechanism for the later arrival in the common-receiver section of Figure 5-35 is the same as its common-shot section.

Therefore, the source and the receiver boreholes are equally important in explaining the hydrophone cross-well data due to explosive sources. Both figures illustrate the fact that the effects of source and receiver boreholes on the Buckhorn cross-well data are equivalent and, that wave conversions at an interface intersecting a fluid-filled borehole are reciprocal.

5.9 Discussion and Conclusion

Using a real cross-well data set from Buckhorn, Illinois, we've demonstrated in this chapter the importance of a source borehole in the understanding of the data. The complicated wave phenomena in the data is shown to be caused by the presence of a fluid-filled borehole for the dynamite sources. Tube waves in the source borehole, the presence of a soft formation (low velocity layers), and a highly contrasted local stratigraphy, are the important factors responsible for these waves. In the presence

of interfaces between hard and soft formations, if the source is in the hard formation, 99% of the source energy propagates as tube waves. When the tube wave propagates through the interface, it not only looses speed, but also leaks energy to the formation because a soft formation confines energy less efficiently. This sudden drop of speed and loss of energy create a secondary shear wave source, strong enough to generate a shear wave that dominates the recorded primary waves. We have shown that this new shear wave is not of Mach wave origin.

Later arriving tube waves in the receiver well hydrophone data have been identified as due to a tube wave-converted shear wave, guided by a soft shale layer right beneath the oil-producing Kankakee limestone. Their energetic characteristic is caused by the fact that most of the dynamite explosion energy is trapped by the source borehole. A low percent conversion from source borehole tube wave to shear wave in a soft formation will result in significant shear-to-tube wave conversion at the receiver borehole. Since the shale layer has a $V_s = 1000\ m/s$ and a $C_T = 1200\ m/s$, a Mach wave may be responsible for the tube-to-shear wave conversion. Though the later arrivals are due to the source borehole, one needs both boreholes (source and receiver) to explain the observation. And, according to the theorem of reciprocity, the receiver borehole and the source borehole are equally important for explaining the waves in hydrophone data due to volume sources. Comparison between common-source and common-receiver gathers illustrates that the effects of the source and the receiver boreholes on the Buckhorn cross-well data are equivalent or reciprocal.

The analysis in this chapter illustrates the complexity associated with the wave phenomena in cross-well experiments. In order to fully understand and utilize the information carried by the data, we feel that detailed analysis of any cross-well recording should be a necessary step, *prior* to any kind of processing.

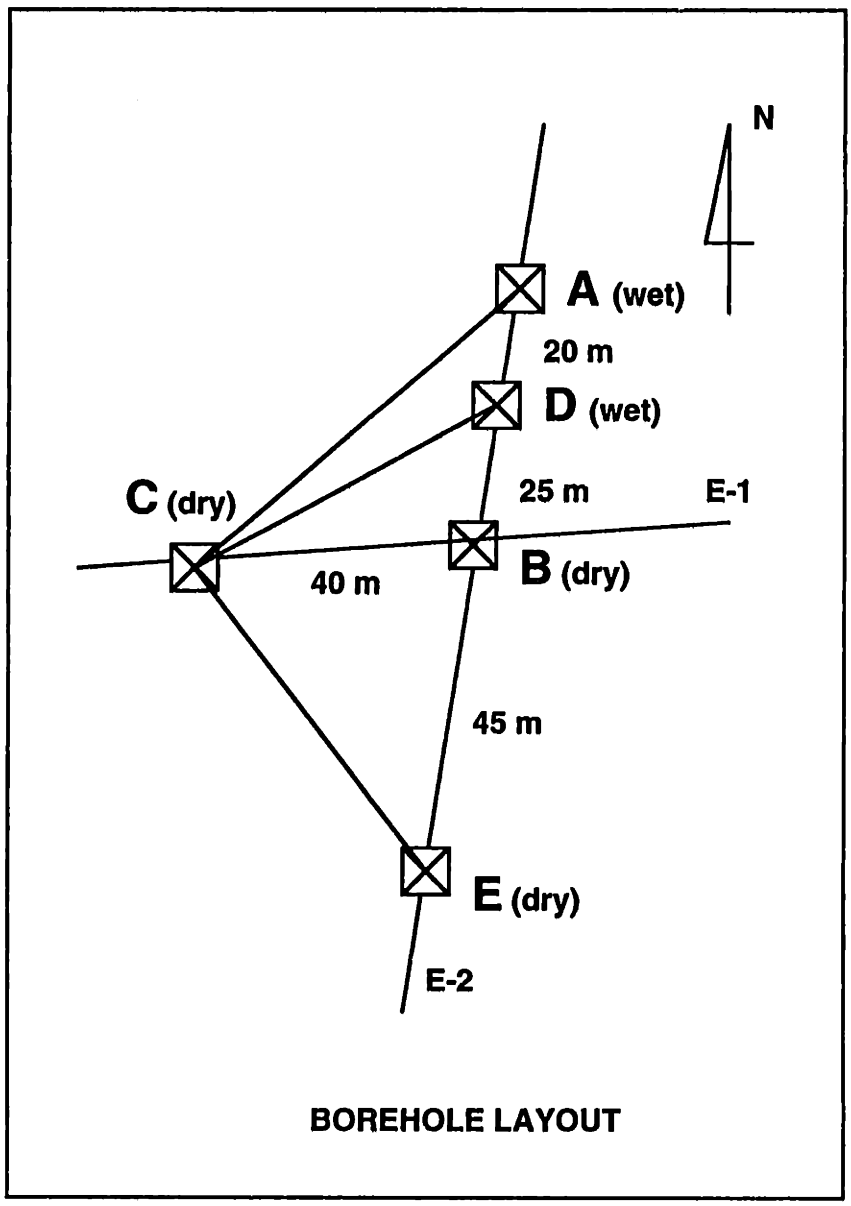

Figure 5-1: Borehole layout at the Buckhorn test site in Illinois (from Takahashi *et al.*, 1991). Cross-well seismic experiments were carried out in Well D (source borehole) and Well B (receiver borehole).

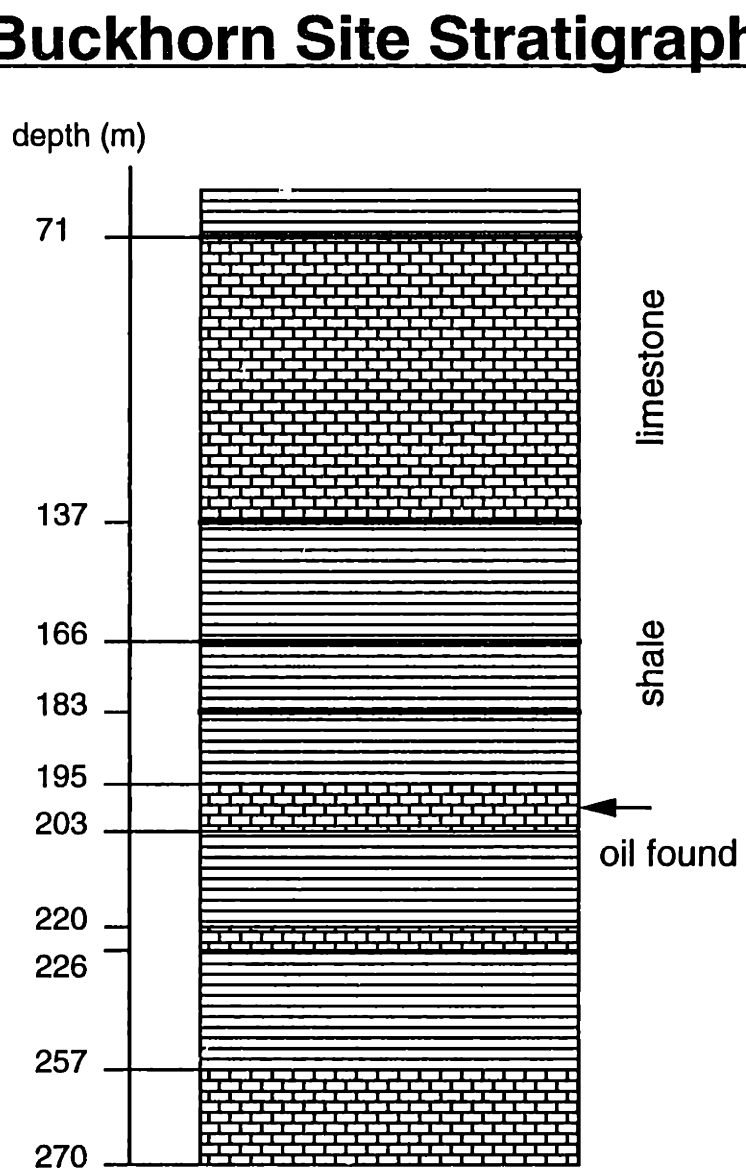

Figure 5-2: Buckhorn test site stratigraphy generated from the well-logs. The oil-producing Kankakee limestone formation is roughly 8 m thick. The depth of the boreholes is 270 m.

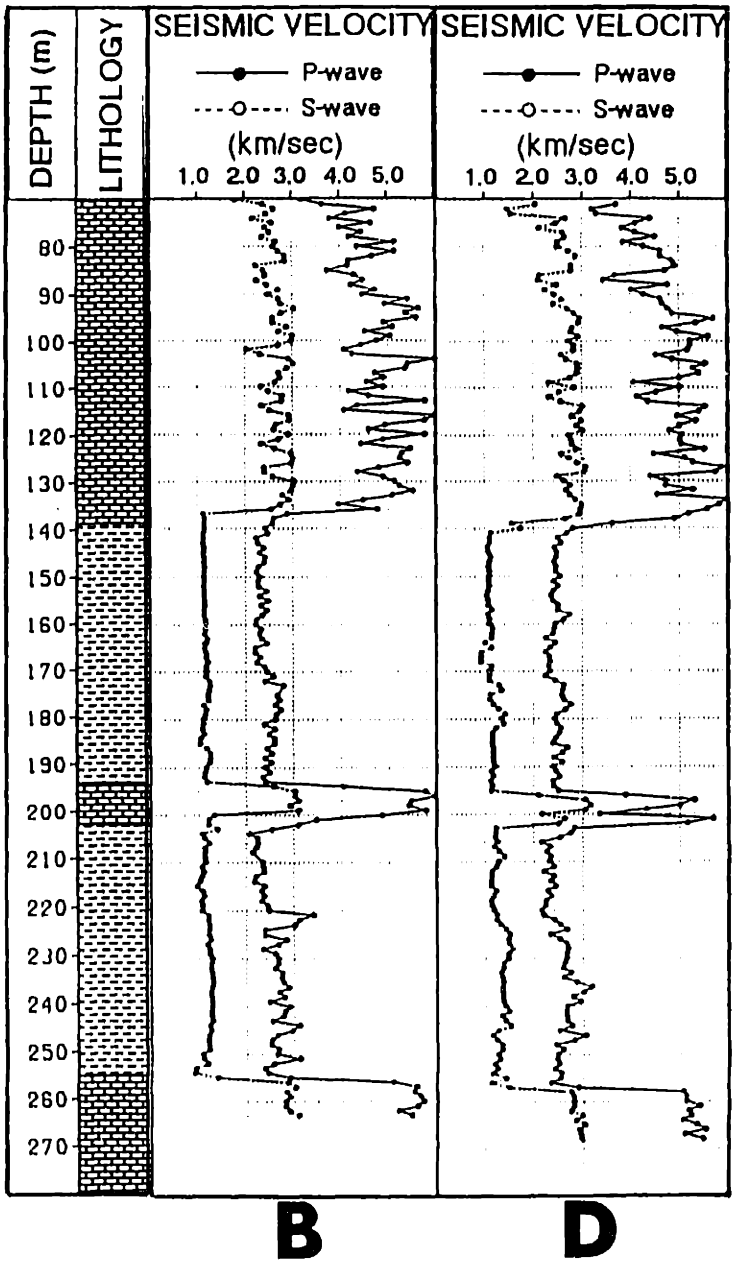

Figure 5-3: Acoustic logs of Well B and Well D at the Buckhorn site (from Takahashi *et al.*, 1991). Low velocity zone is detected in Well D, not in Well B, for the Kankakee formation, indicating lateral reservoir heterogeneity. Also indicated is a high velocity streak below the Kankakee limestone.

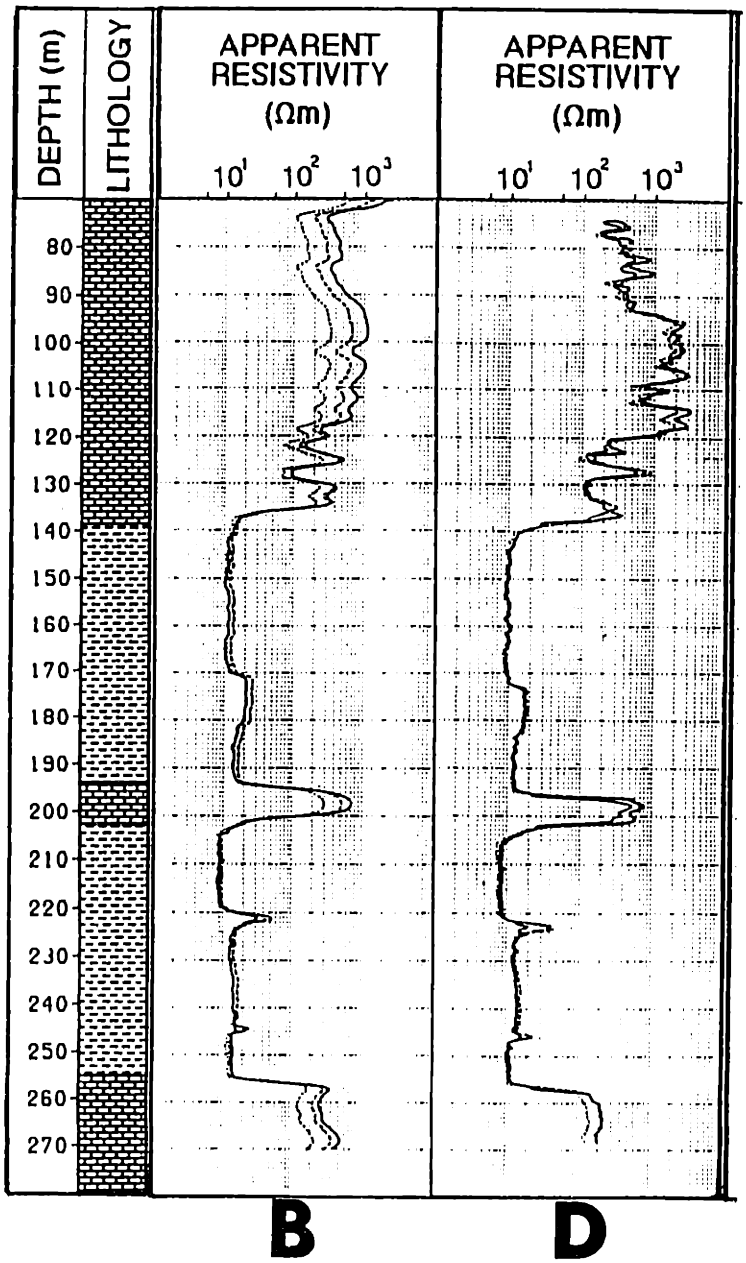

Figure 5-4: Resistivity logs of Well *B* and Well *D* at the Buckhorn site (from Takahashi *et al.*, 1991). Low velocity zone in Kankakee formation is not very clear on these logs. The shale layer right beneath the Kankakee limestone is more conductive than other shales, indicating a soft layer. The high velocity kink of Figure 5-3 is also shown. The three curves represent different current penetrations.

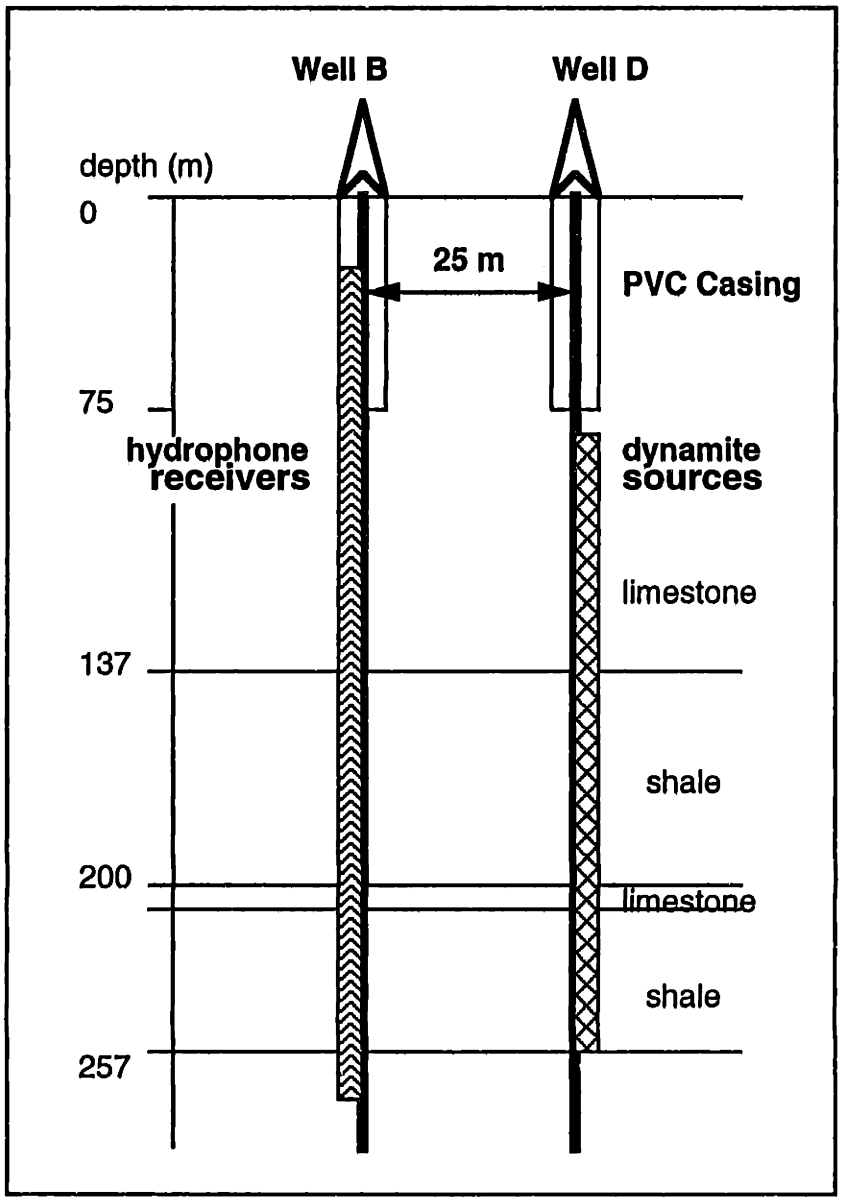

Figure 5-5: Setup for hydrophone cross-well experiment (Takahashi, 1993; personal communication). Small amount of dynamite was used as sources. Both B and D are fluid-filled open boreholes with a diameter of 15.24 cm (6 in). Only the major interfaces are shown here.

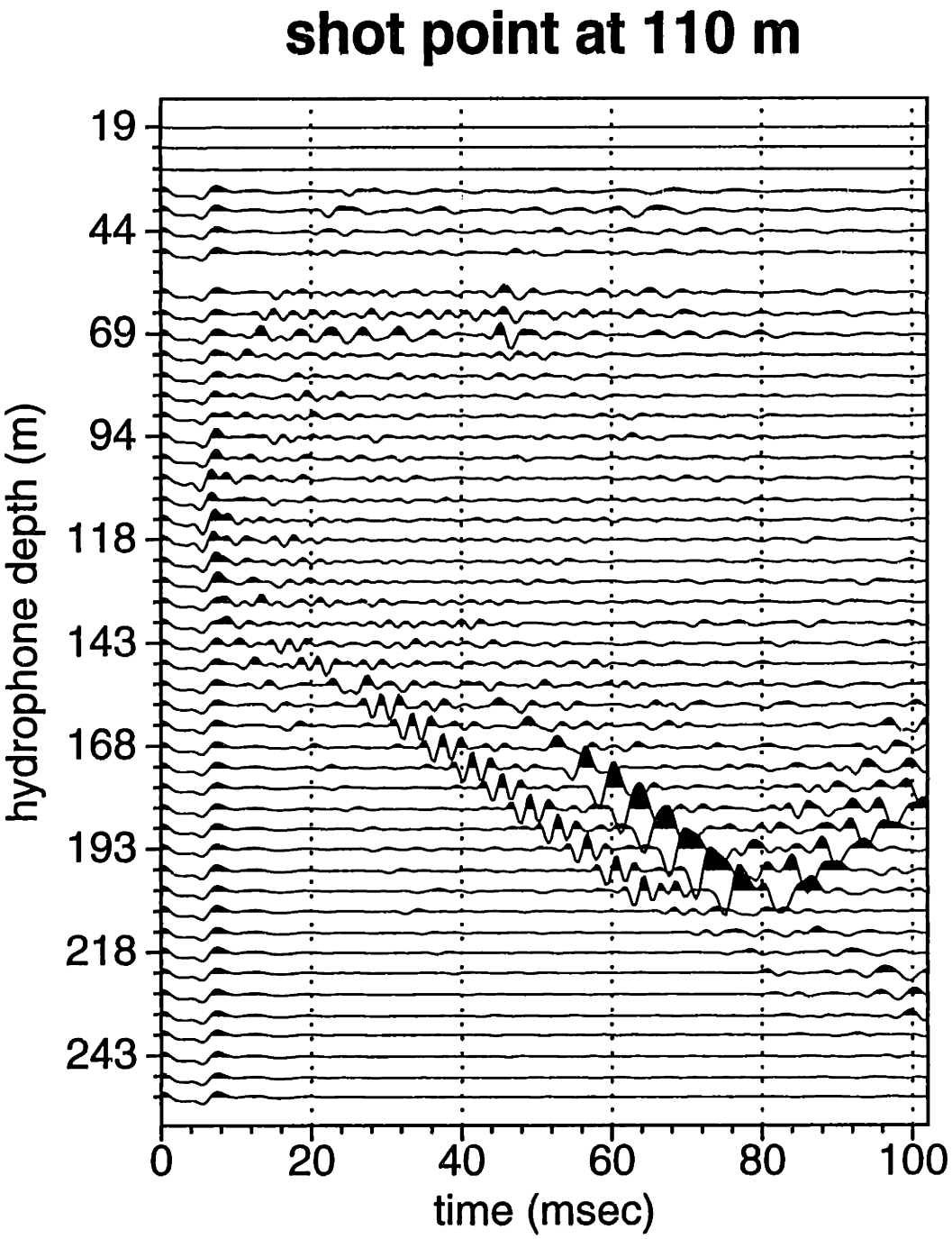

Figure 5-6: Real hydrophone data (common shot, 48 receivers) for a dynamite source in borehole fluid at a depth of 110 meters. The data shown are the filtered version of the original recording with a trapezoidal band-pass filter. Four corner frequencies are 0-100-600-800 Hz.

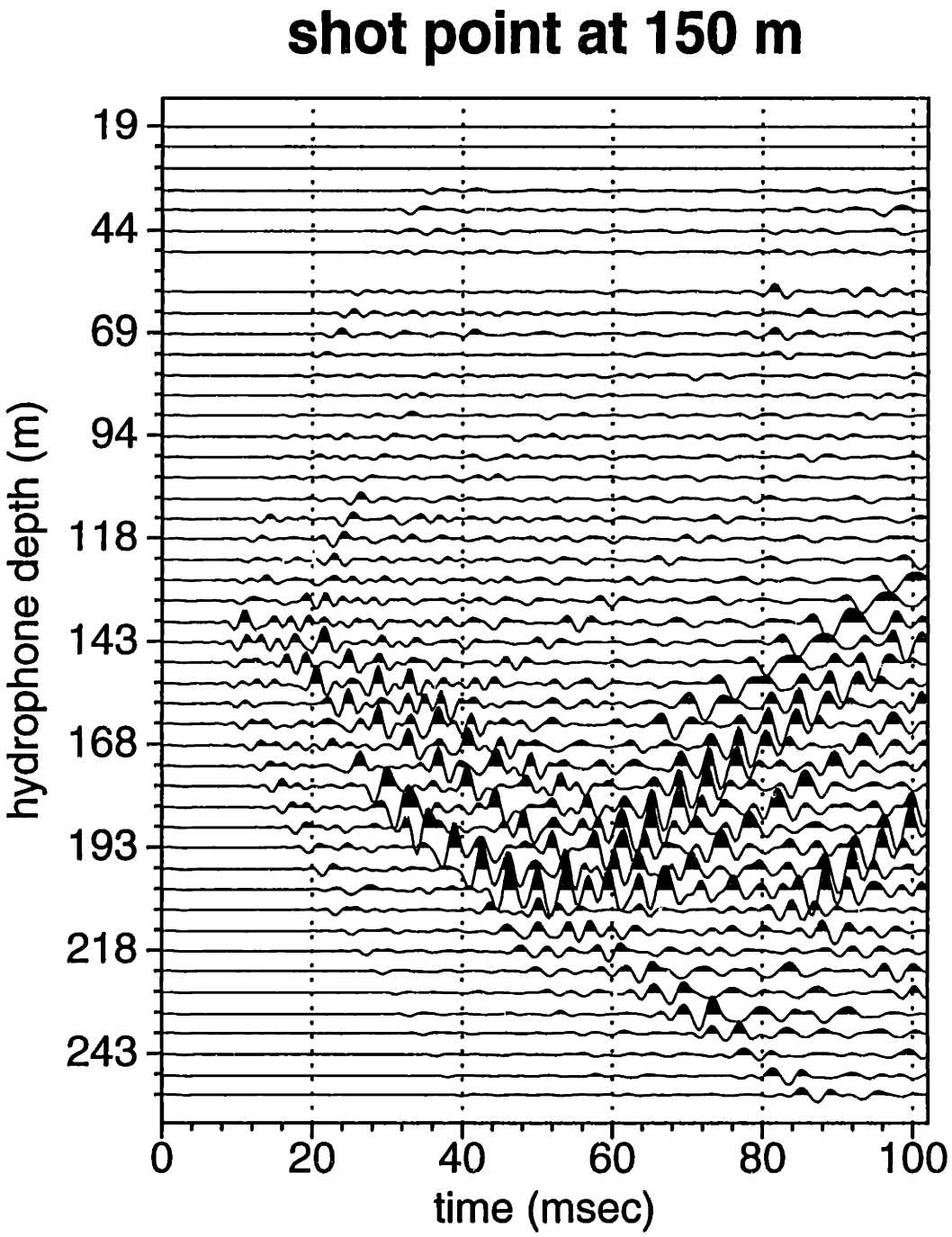

Figure 5-7: Real hydrophone data (common shot, 48 receivers) for a dynamite source in borehole fluid at a depth of 150 meters. The data shown are the filtered version of the original recording with a trapezoidal band-pass filter. Four corner frequencies are 0-100-600-800 Hz.

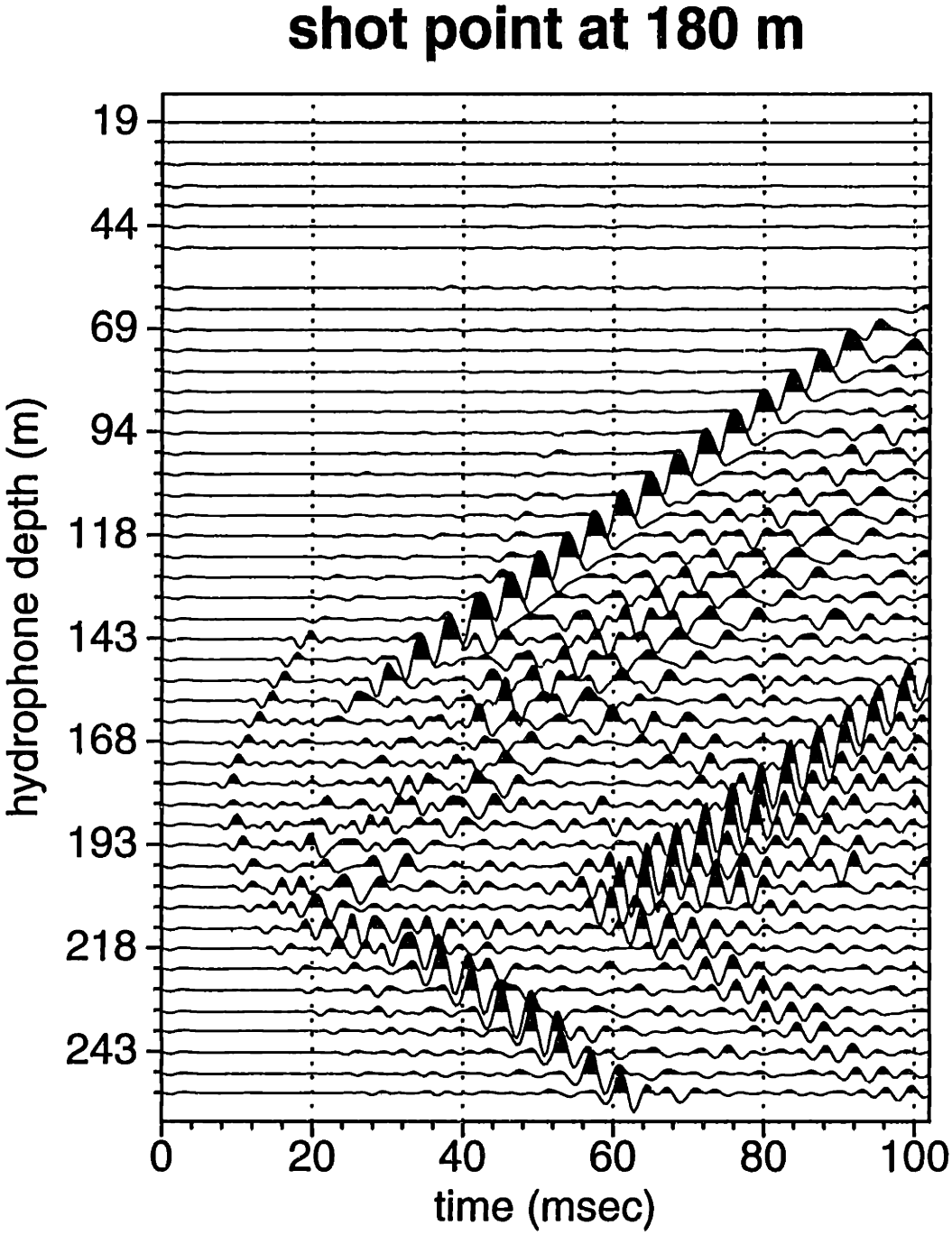

Figure 5-8: Real hydrophone data (common shot, 48 receivers) for a dynamite source in borehole fluid at a depth of 180 meters. The data shown are the filtered version of the original recording with a trapezoidal band-pass filter. Four corner frequencies are 0-100-600-800 Hz.

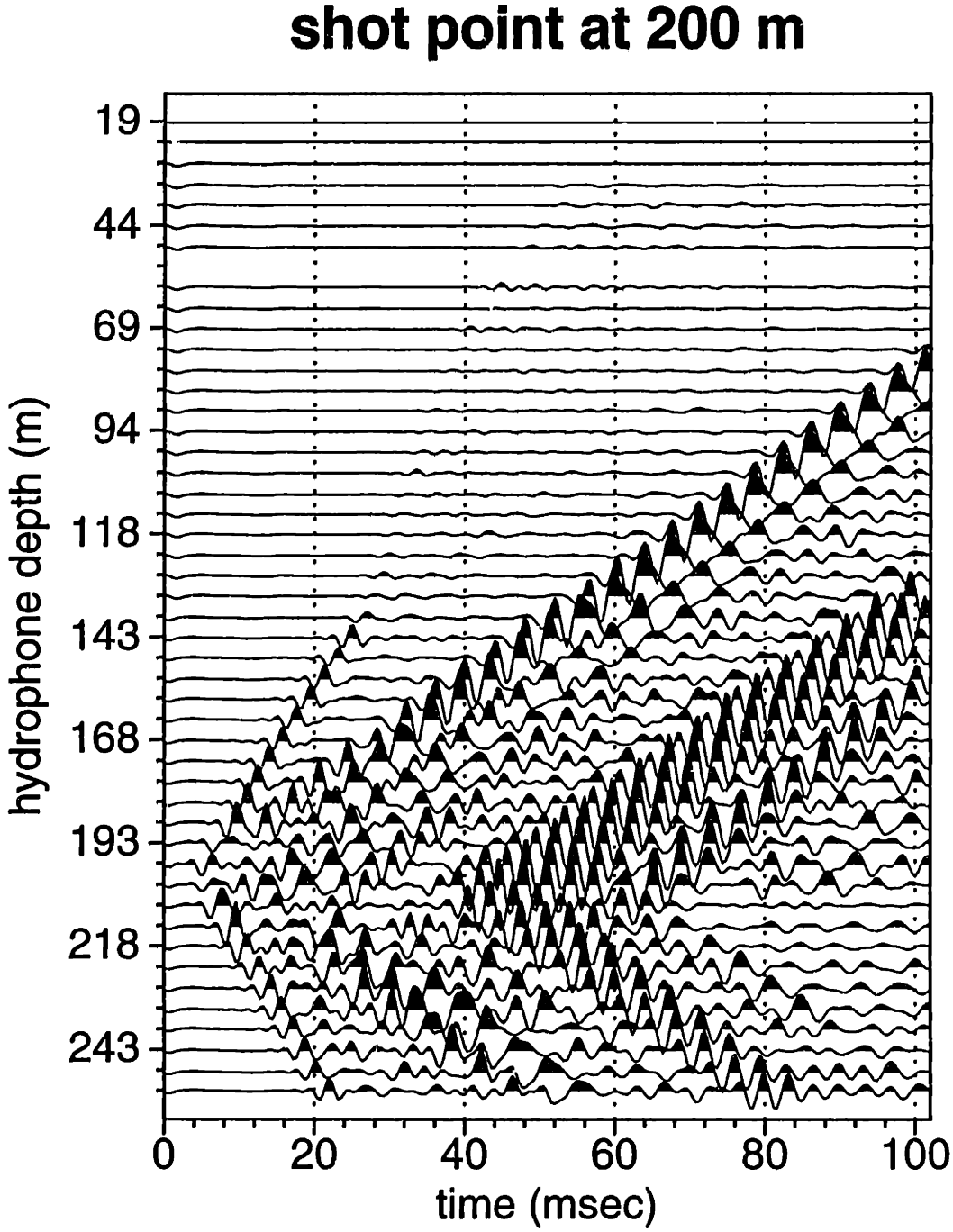

Figure 5-9: Real hydrophone data (common shot, 48 receivers) for a dynamite source in borehole fluid at a depth of 200 meters. The data shown are the filtered version of the original recording with a trapezoidal band-pass filter. Four corner frequencies are 0-100-600-800 Hz.

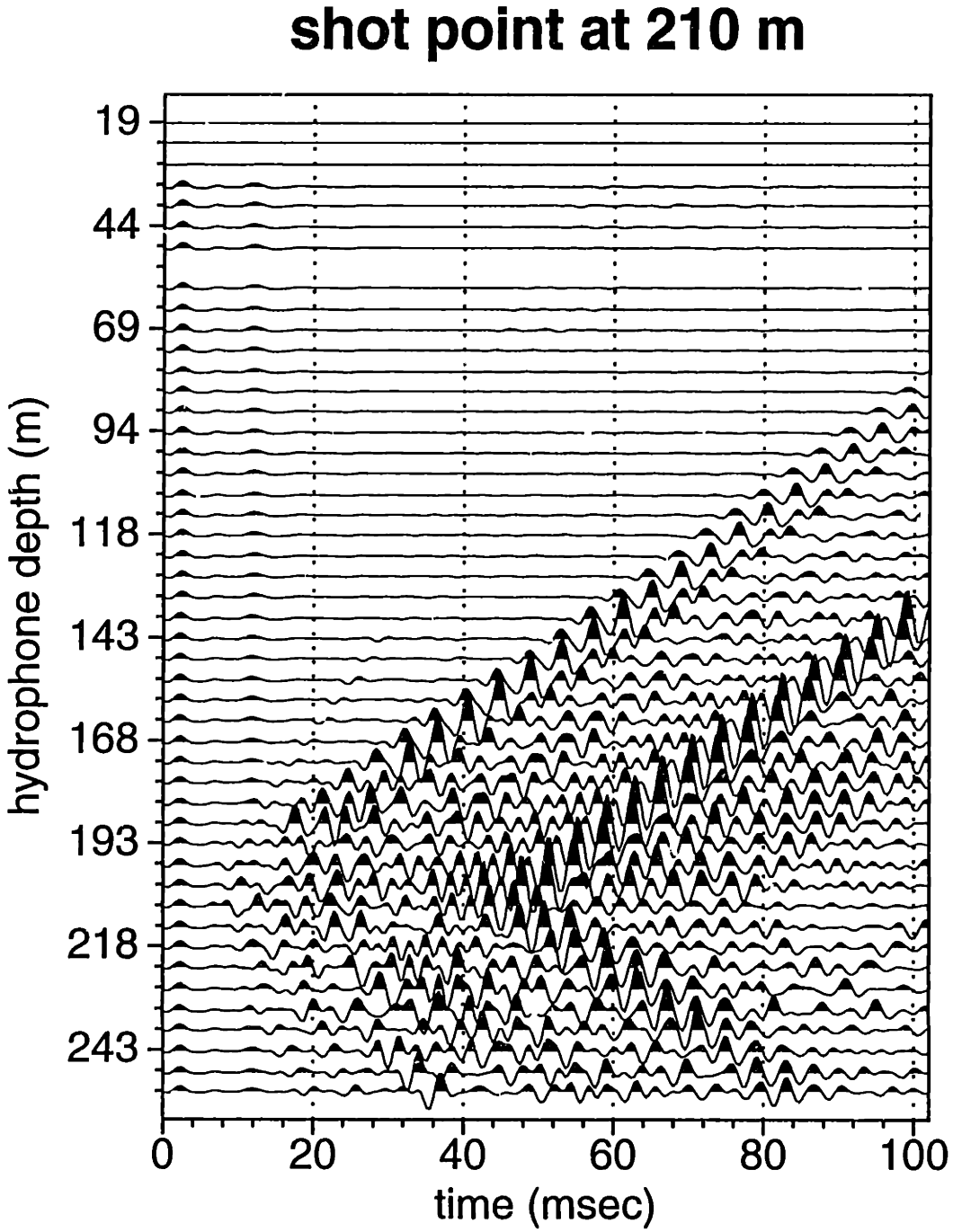

Figure 5-10: Real hydrophone data (common shot, 48 receivers) for a dynamite source in borehole fluid at a depth of 210 meters. The data shown are the filtered version of the original recording with a trapezoidal band-pass filter. Four corner frequencies are 0-100-600-800 Hz.

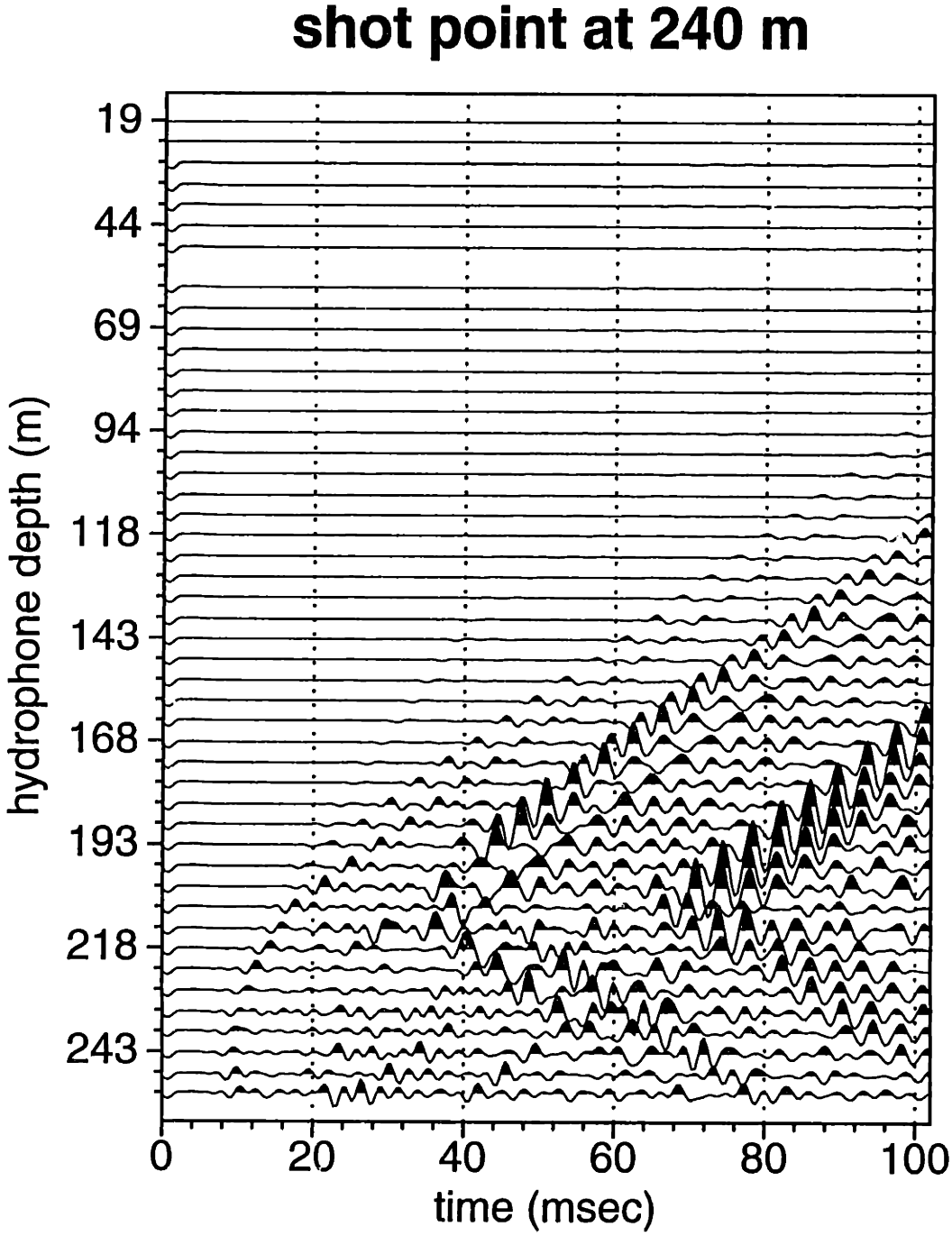

Figure 5-11: Real hydrophone data (common shot, 48 receivers) for a dynamite source in borehole fluid at a depth of 240 meters. The data shown are the filtered version of the original recording with a trapezoidal band-pass filter. Four corner frequencies are 0-100-600-800 Hz.

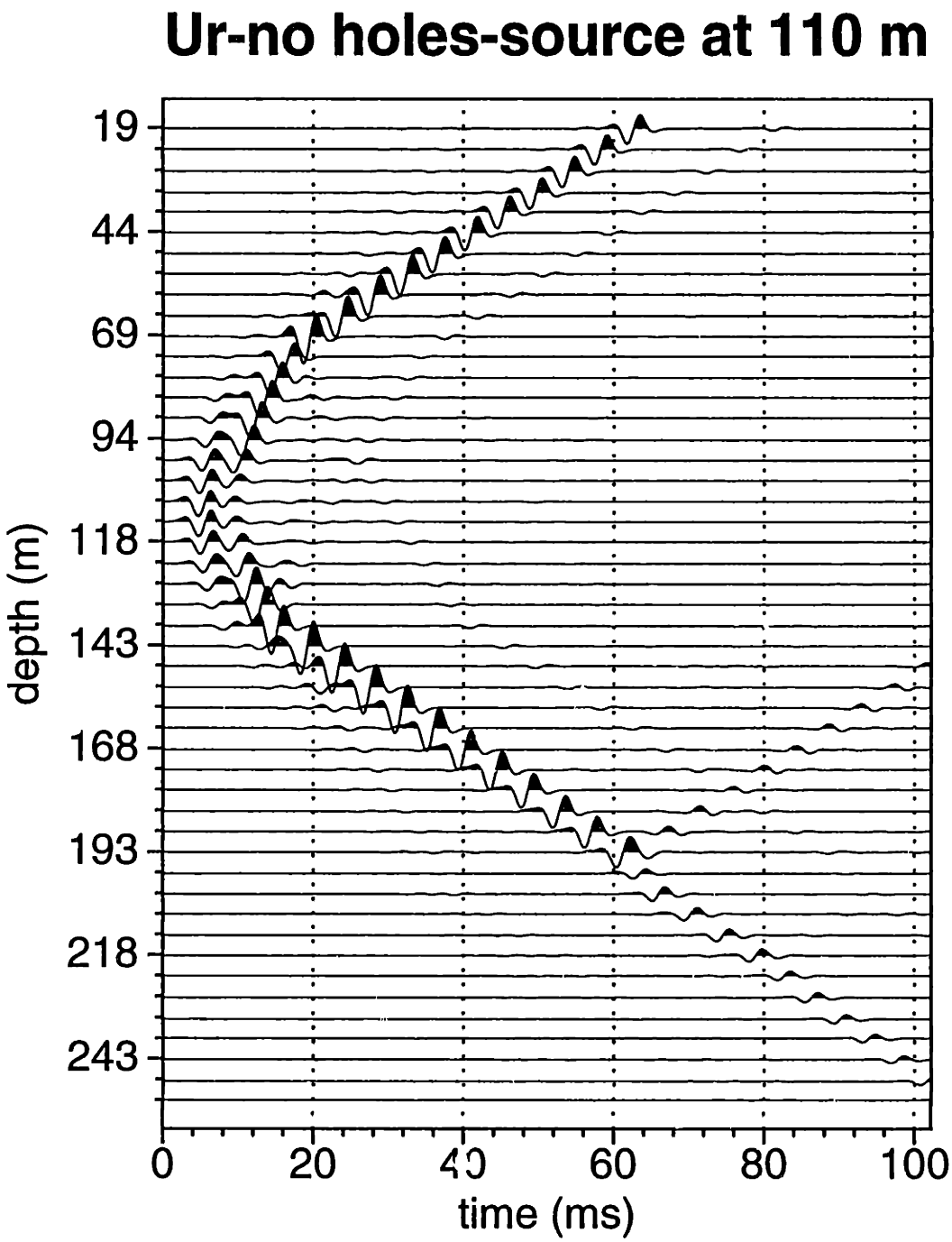

Figure 5-12: Synthetic data (U_r) for radial ring force inside formation and at a depth of 110 meters. Both source and receiver boreholes are absent from the modeling.

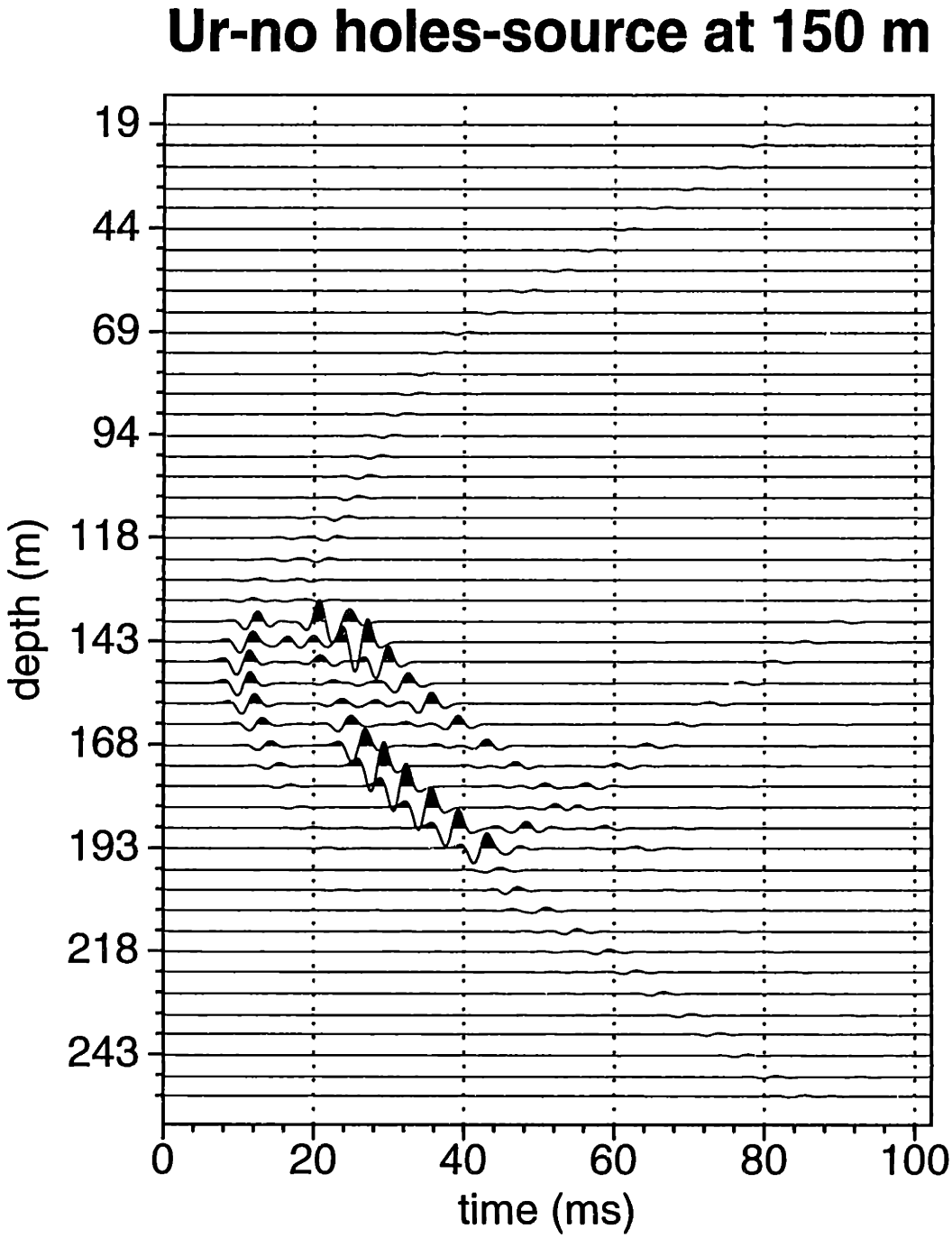

Figure 5-13: Synthetic data (U_r) for radial ring force inside formation and at a depth of 150 meters. Both source and receiver boreholes are absent from the modeling.

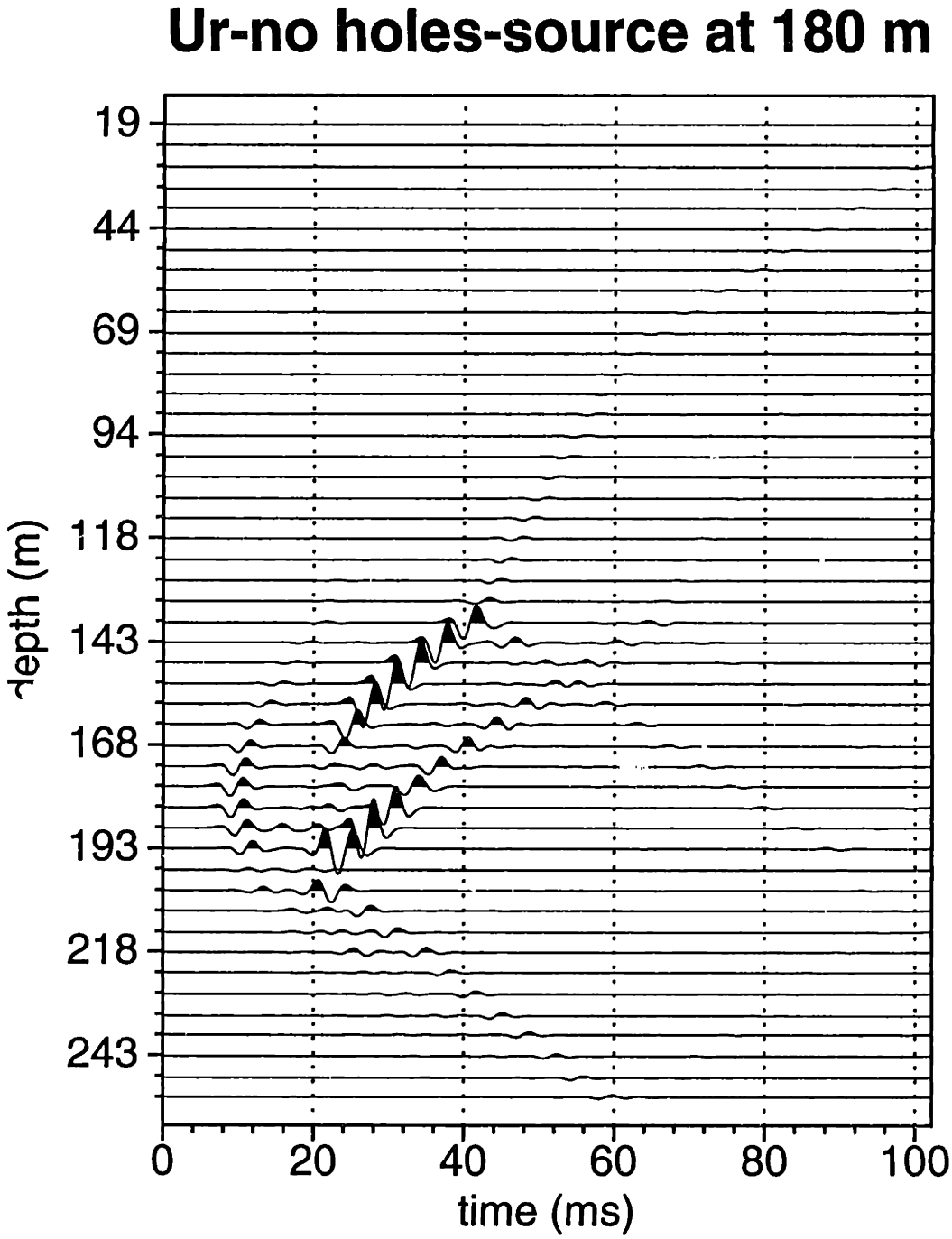

Figure 5-14: Synthetic data (U_r) for radial ring force inside formation and at a depth of 180 meters. Both source and receiver boreholes are absent from the modeling.

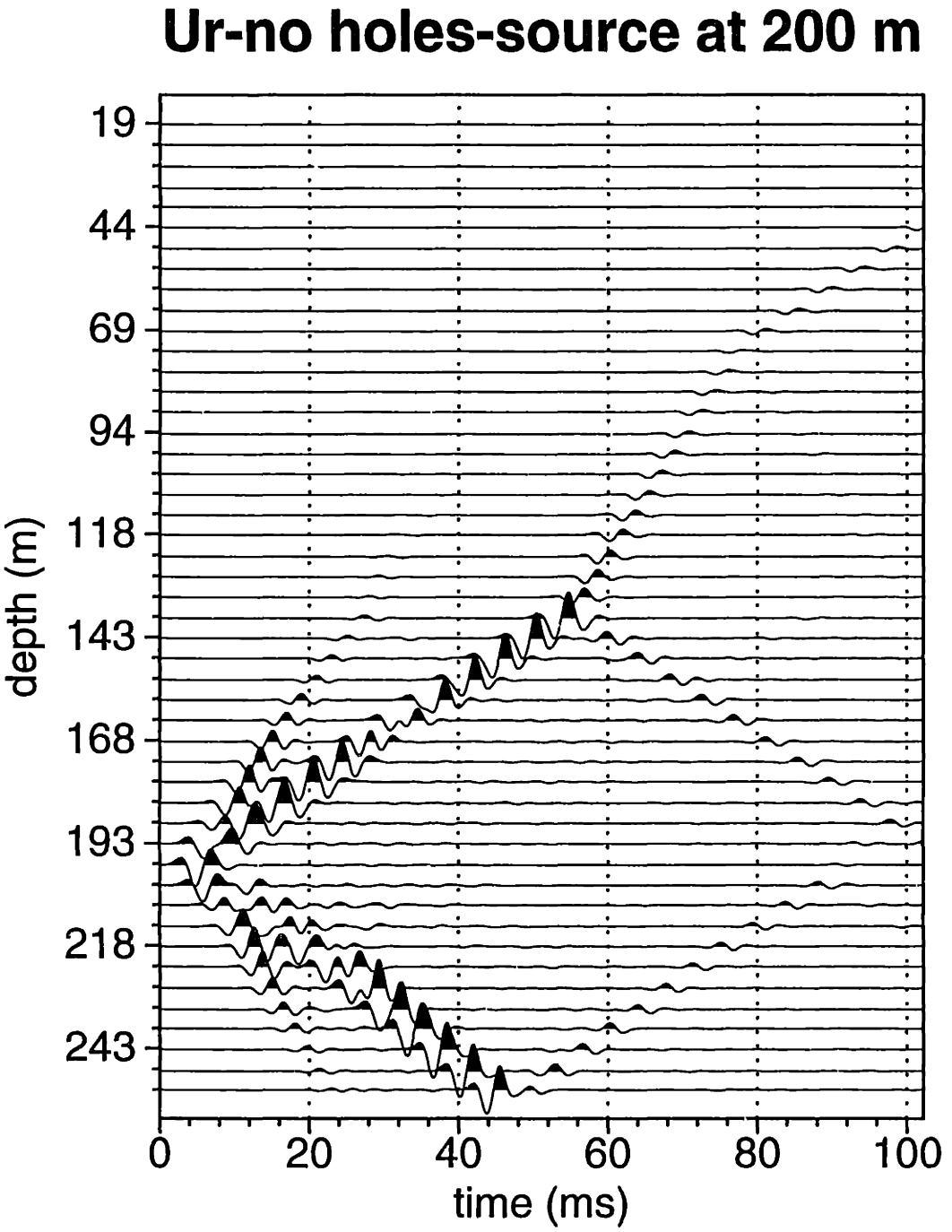

Figure 5-15: Synthetic data (U_r) for radial ring force inside formation and at a depth of 200 meters. Both source and receiver boreholes are absent from the modeling.

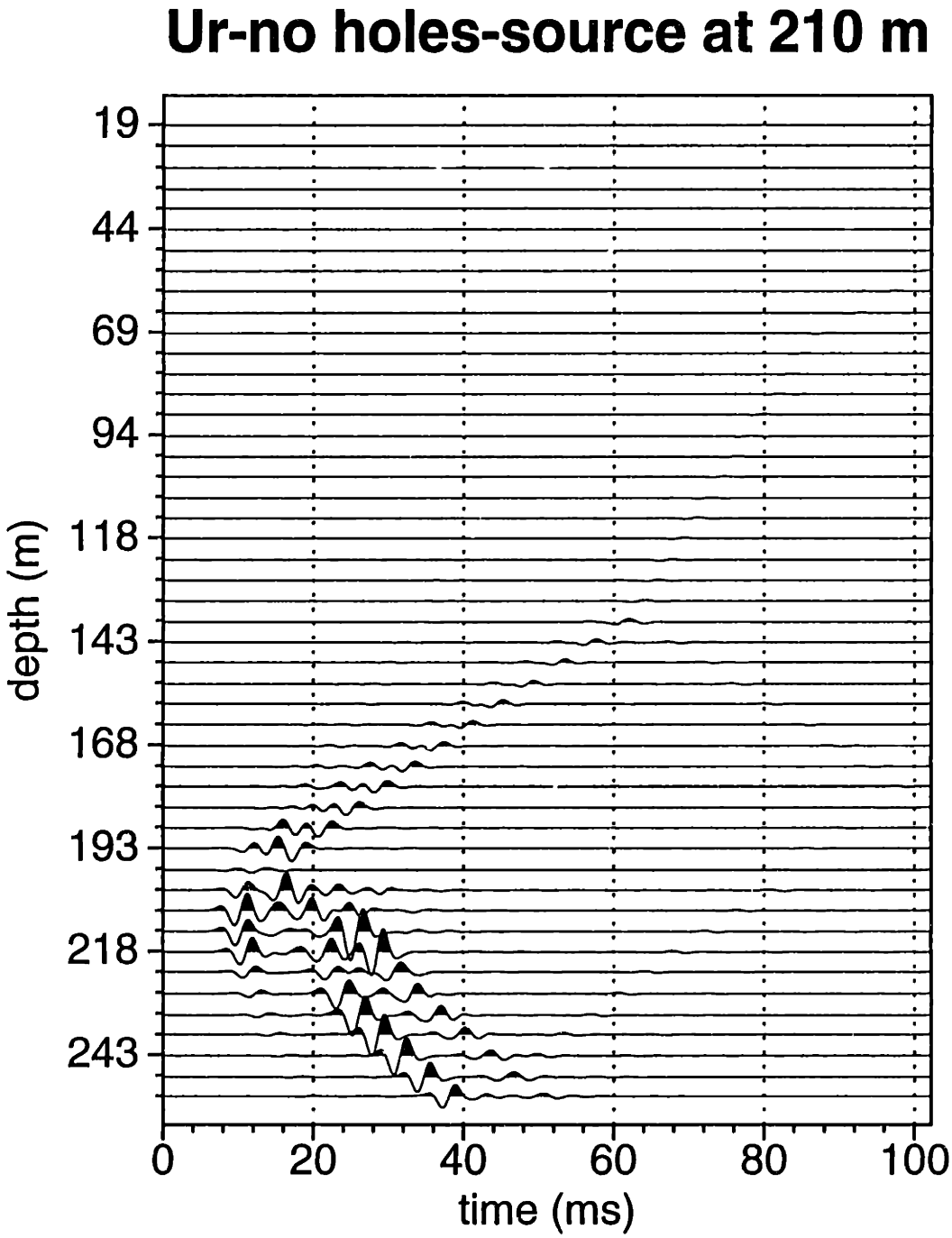

Figure 5-16: Synthetic data (U_r) for radial ring force inside formation and at a depth of 210 meters. Both source and receiver boreholes are absent from the modeling.

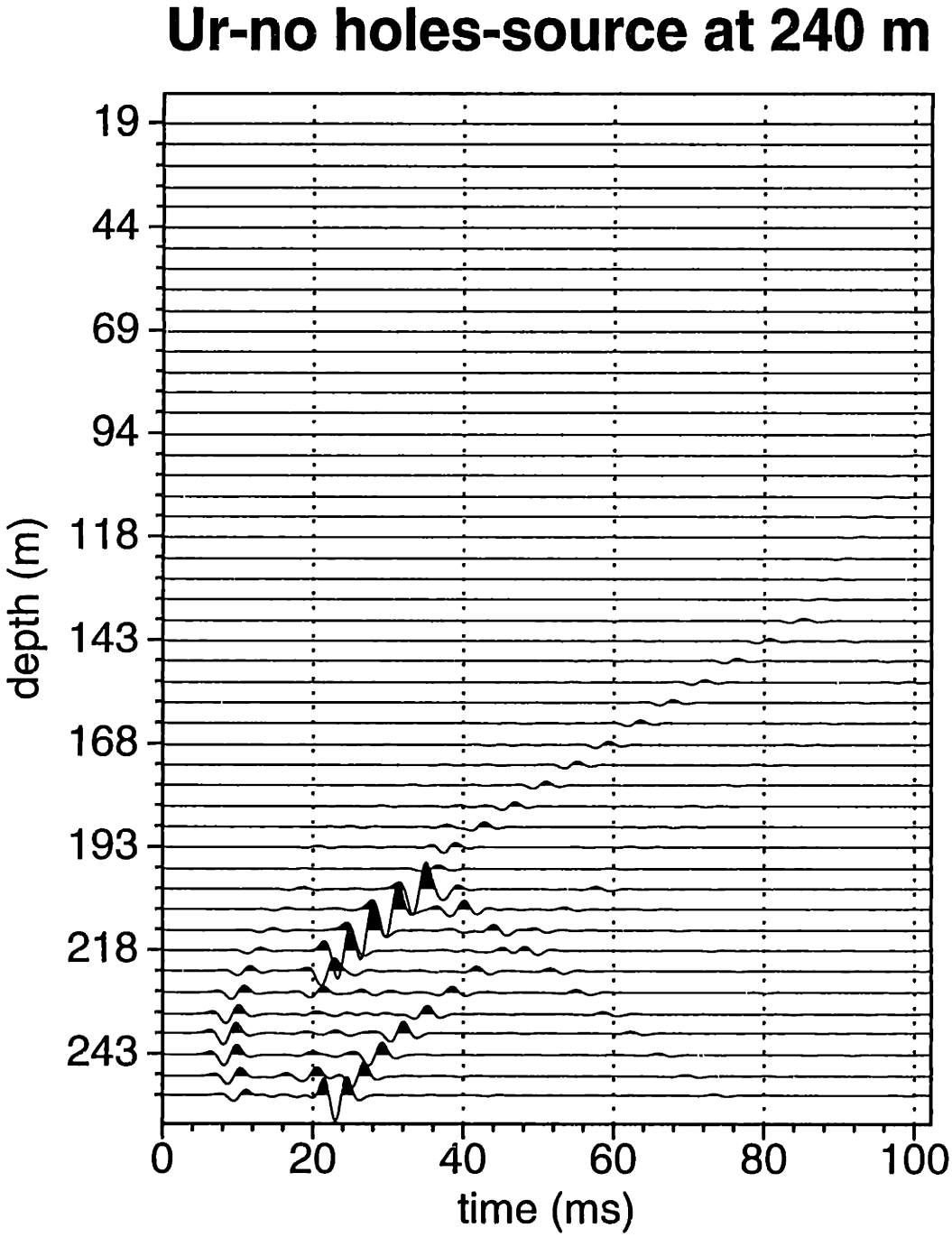

Figure 5-17: Synthetic data (U_r) for radial ring force inside formation and at a depth of 240 meters. Both source and receiver boreholes are absent from the modeling.

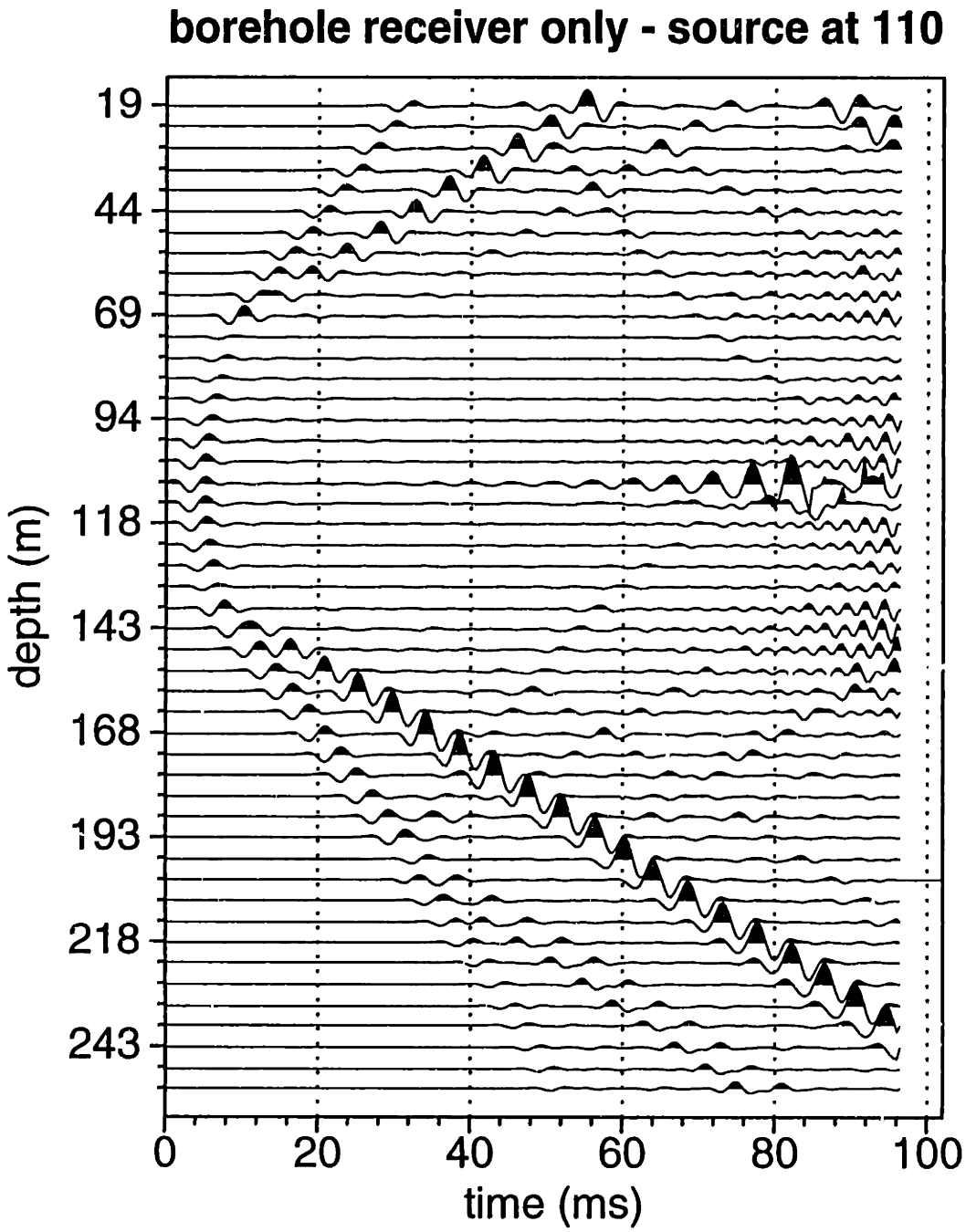

Figure 5-18: Synthetic data (hydrophone pressure) for explosion source inside formation and at a depth of 110 meters. Only the receiver borehole is considered in the modeling. Noises at the later times (80 *ms*) in the limestone layer are caused by insufficient sampling in wave number.

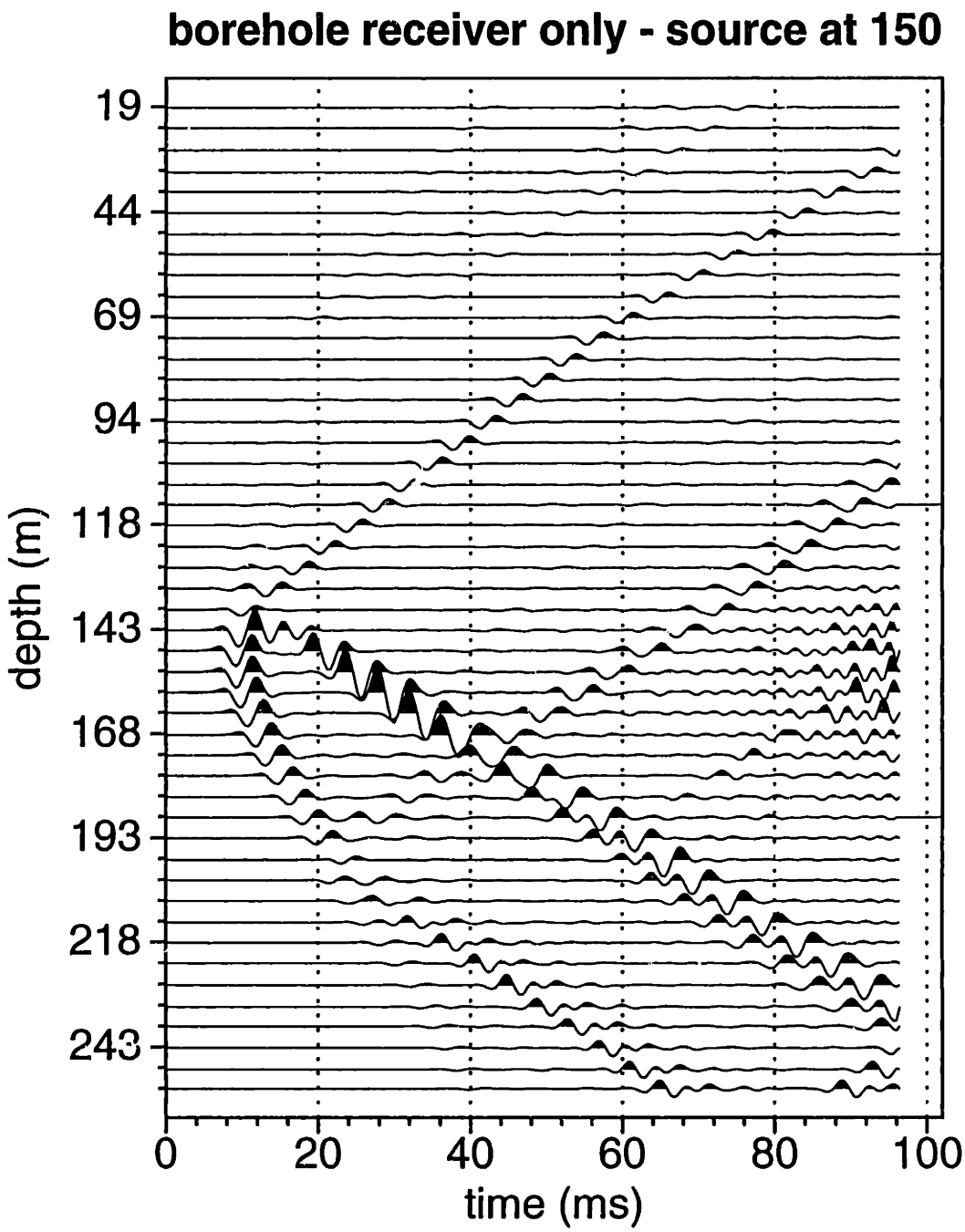

Figure 5-19: Synthetic data (hydrophone pressure) for explosion source inside formation and at a depth of 150 meters. Only the receiver borehole is considered in the modeling.

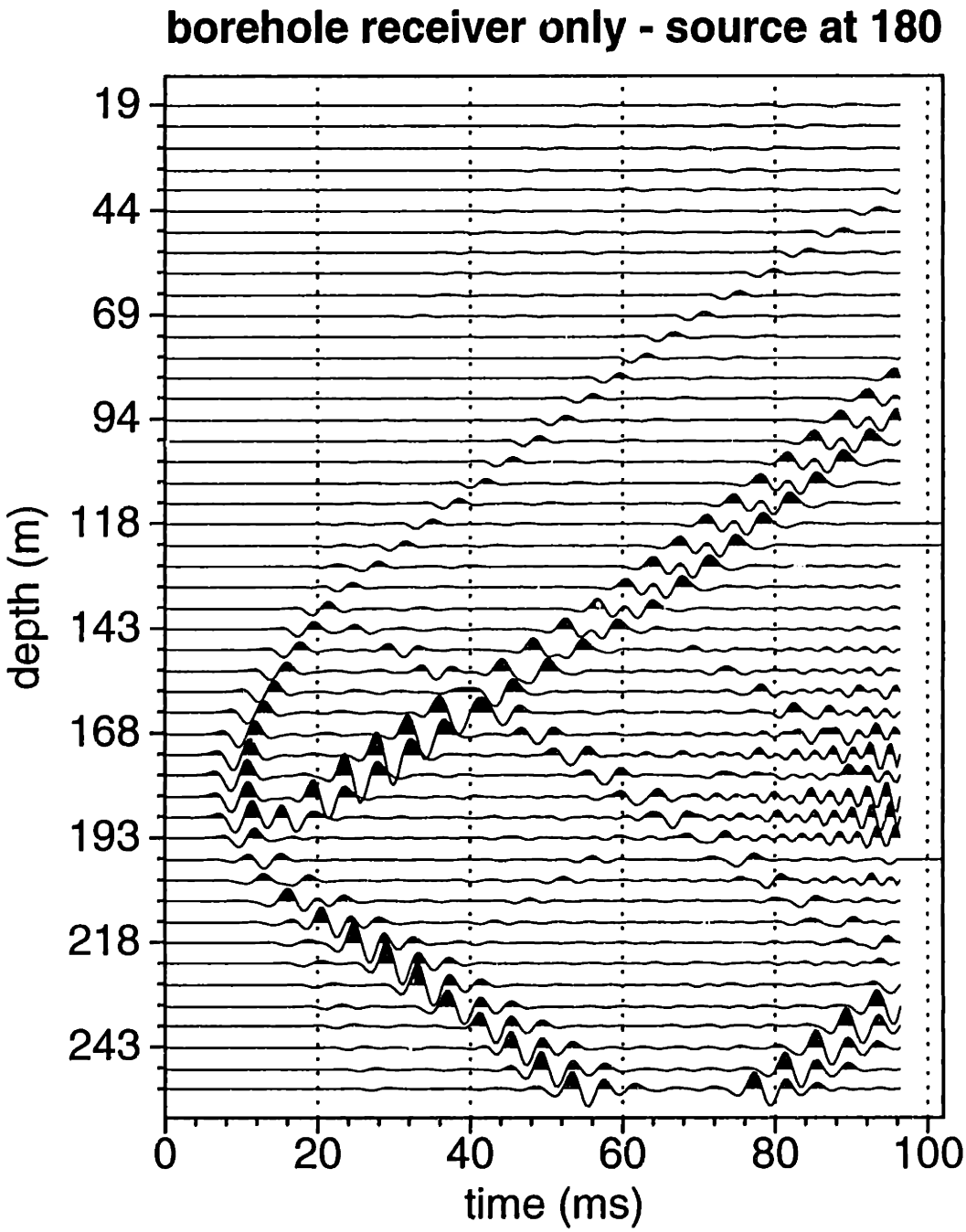

Figure 5-20: Synthetic data (hydrophone pressure) for explosion source inside formation and at a depth of 180 meters. Only the receiver borehole is considered in the modeling.

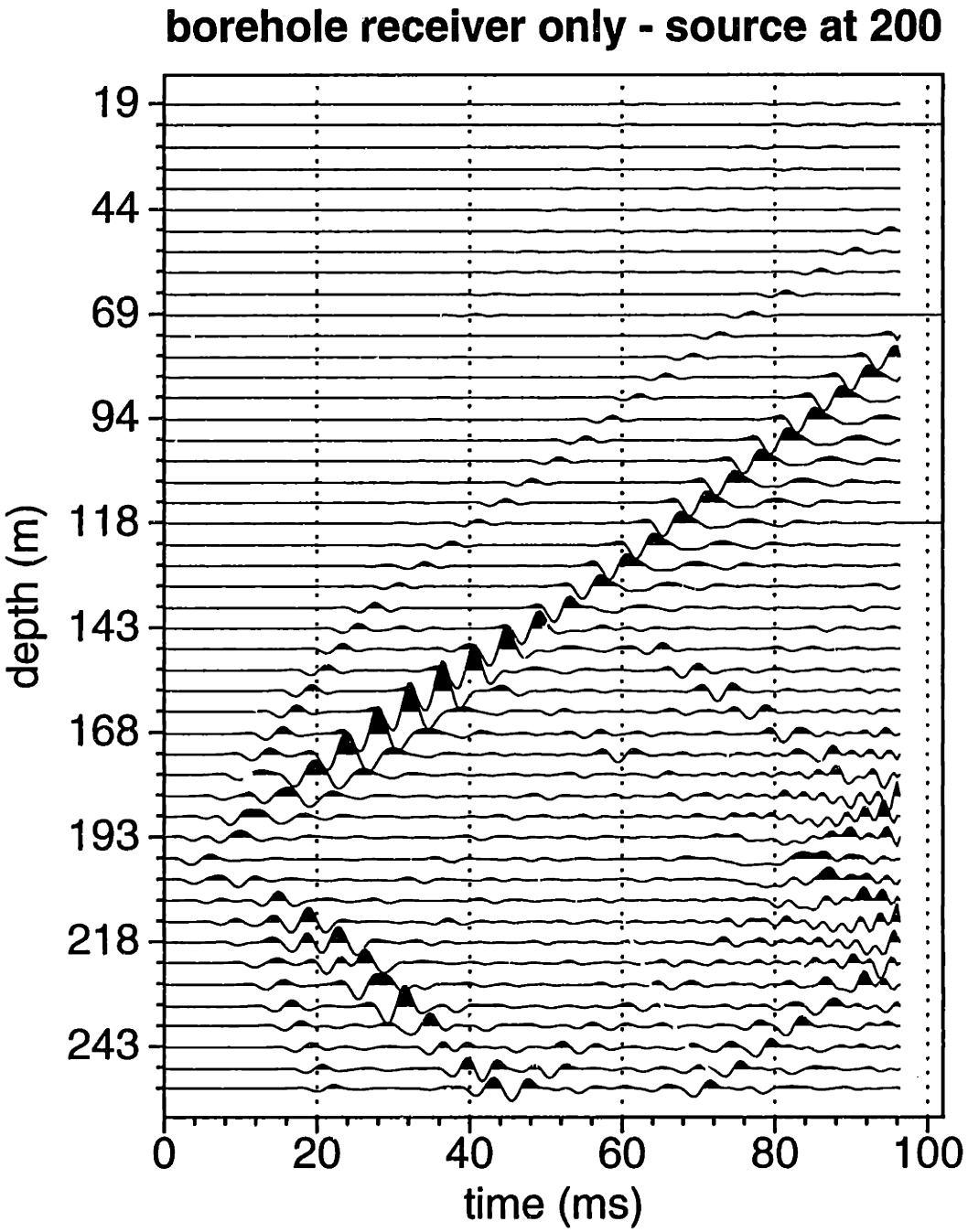

Figure 5-21: Synthetic data (hydrophone pressure) for explosion source inside formation and at a depth of 200 meters. Only the receiver borehole is considered in the modeling.

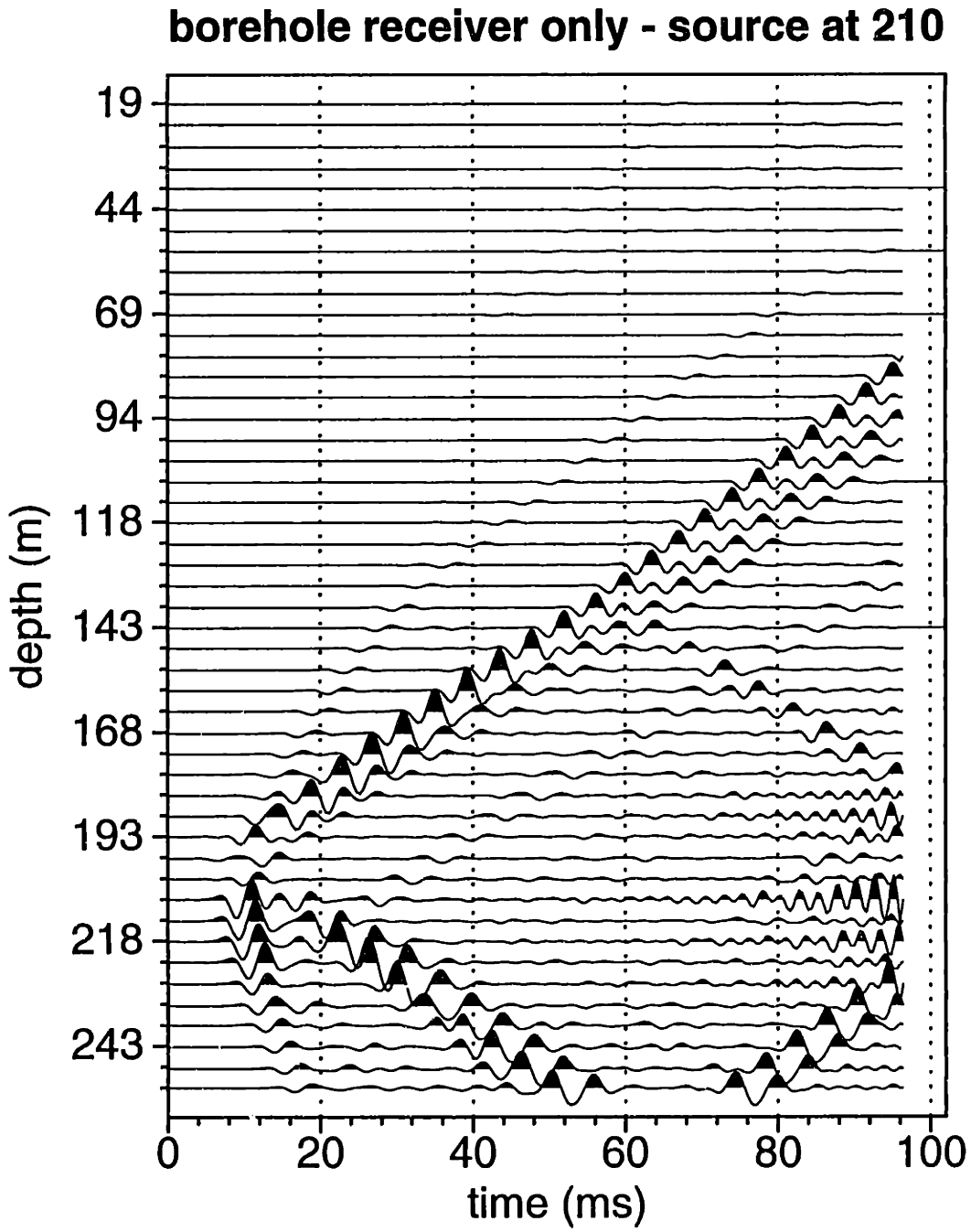

Figure 5-22: Synthetic data (hydrophone pressure) for explosion source inside formation and at a depth of 210 meters. Only the receiver borehole is considered in the modeling.

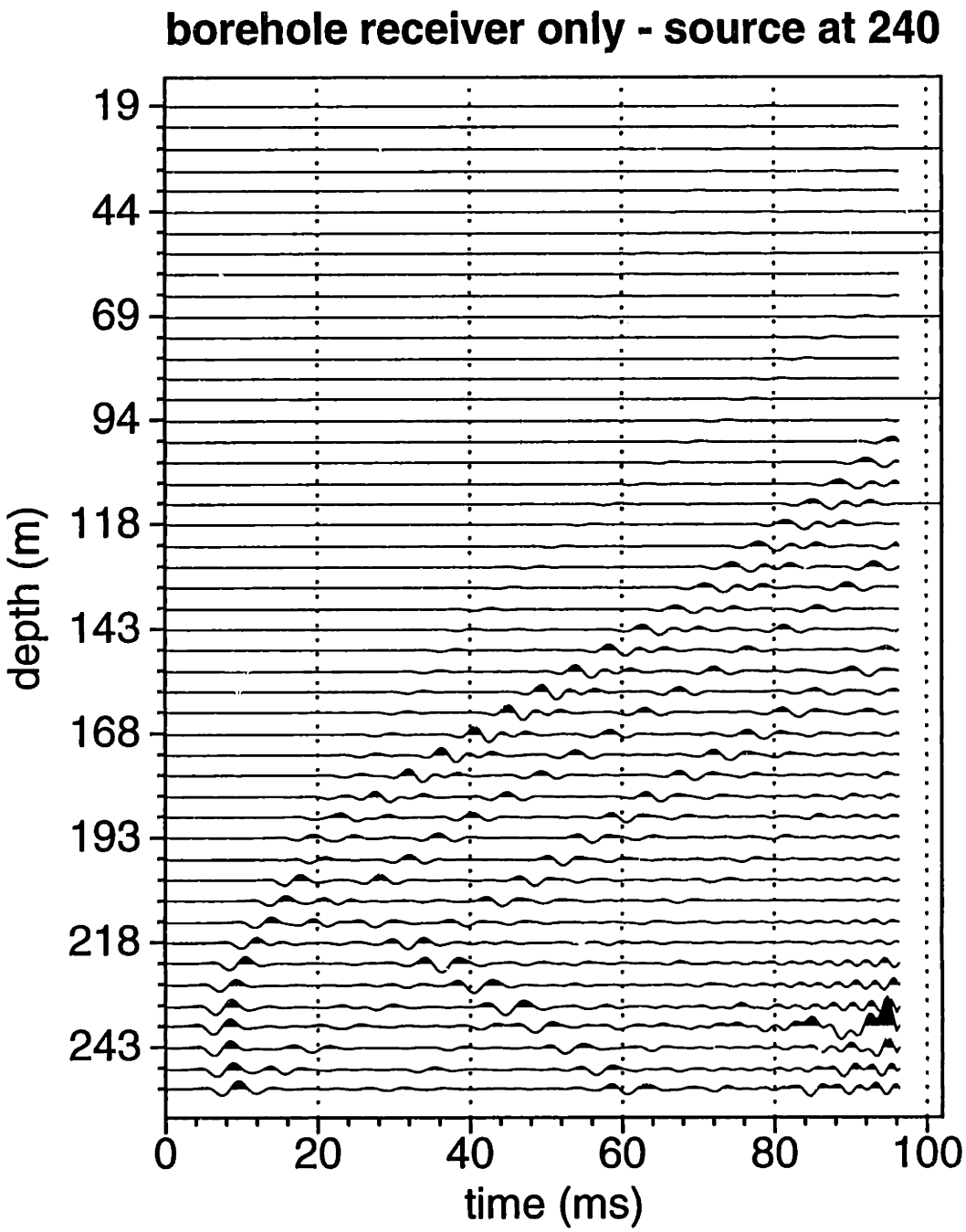

Figure 5-23: Synthetic data (hydrophone pressure) for explosion source inside formation and at a depth of 240 meters. Only the receiver borehole is considered in the modeling.

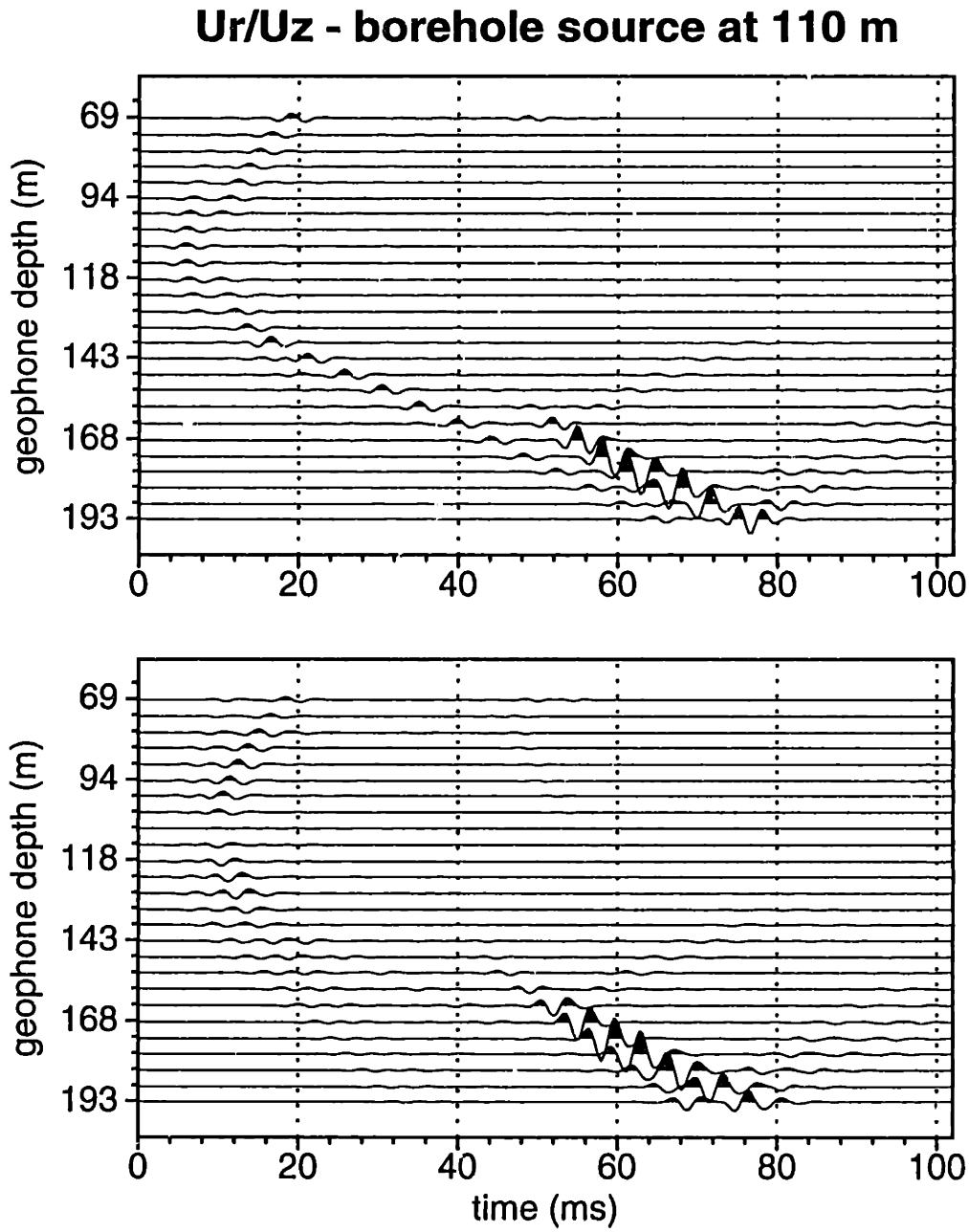

Figure 5-24: Synthetic data for a borehole explosion source at a depth of 110 meters. Only the source borehole is considered in the modeling.

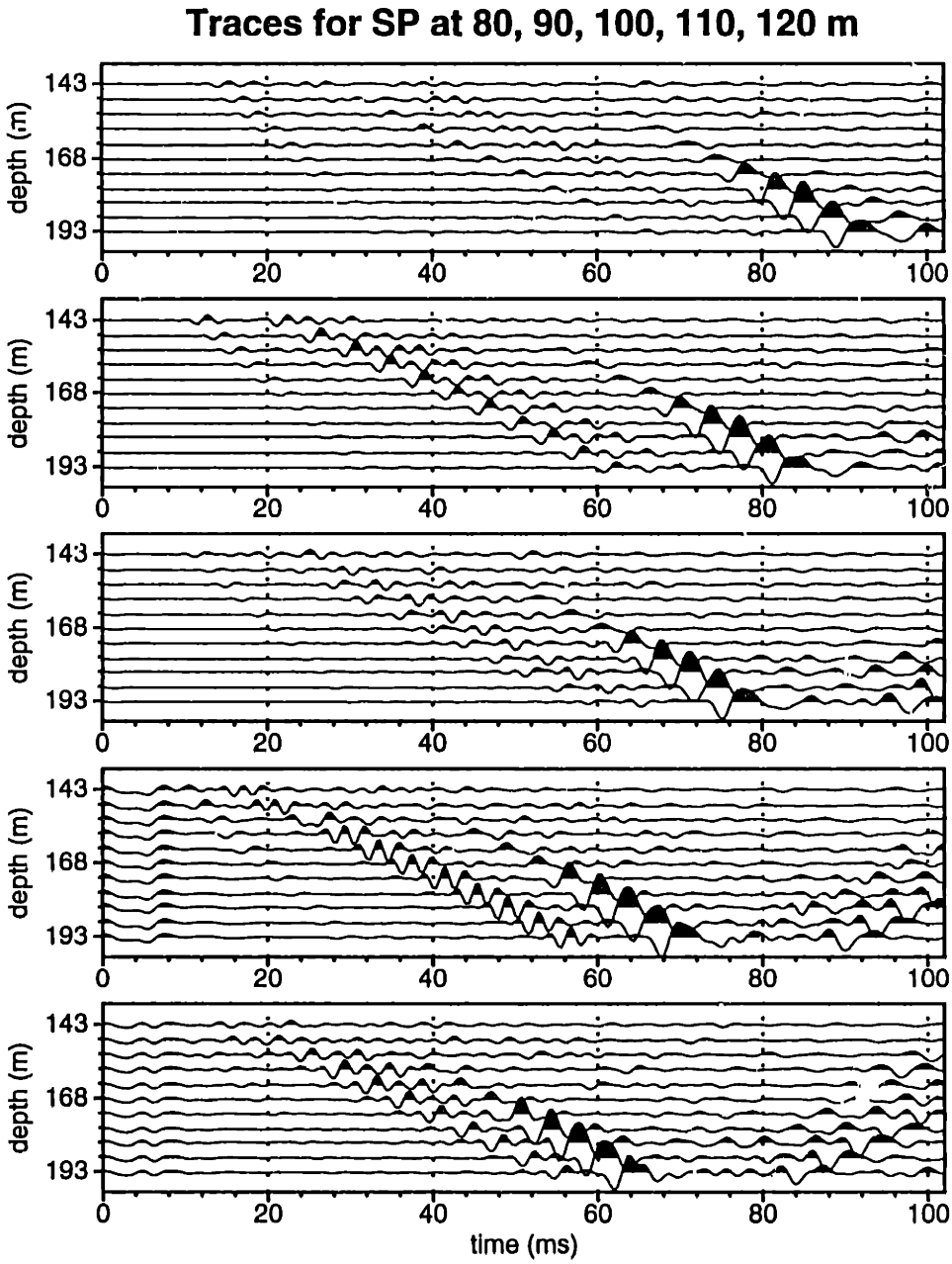

Figure 5-25: Traces from five different common-shot sections showing the relative arrival time for the strong event following the shear wave.

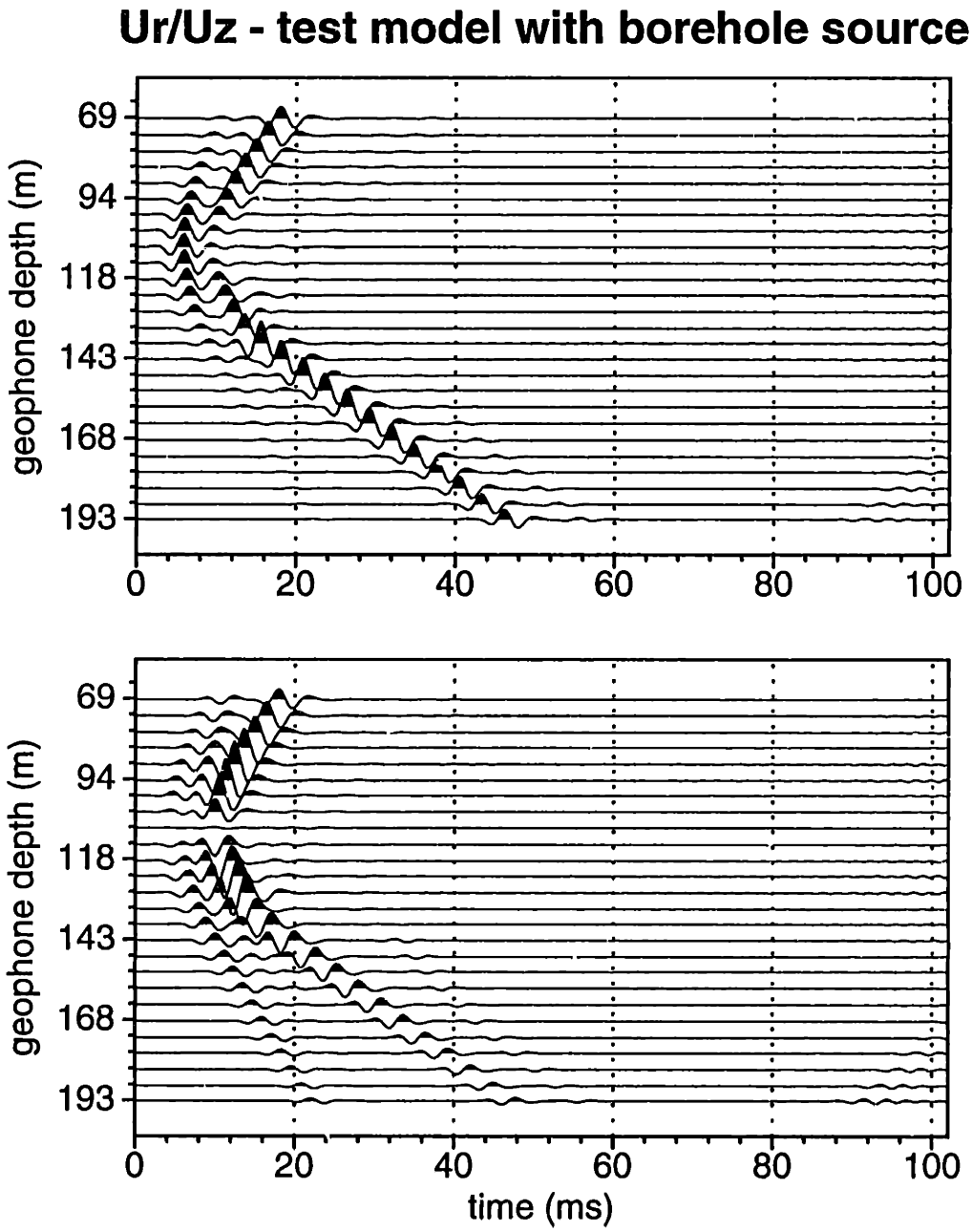

Figure 5-26: Displacements for a borehole source at 110 meters, but with one interface only (at 137 m). The parameters for the lower medium are: $V_p = 3600$, $V_s = 1700$, and $\rho = 2.1$.

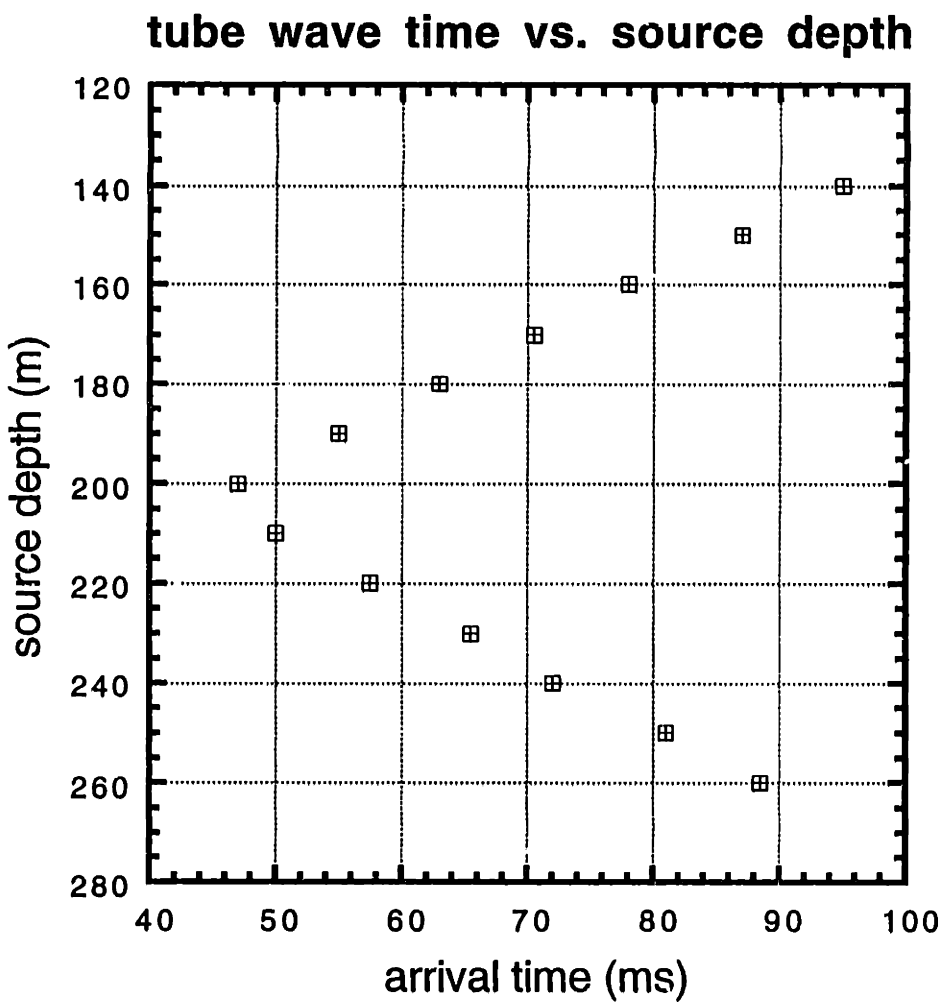

Figure 5-27: The arrival time of the late arriving tube wave at its apex (the hydrophone at 203 m), plotted as a function of shot point depth.

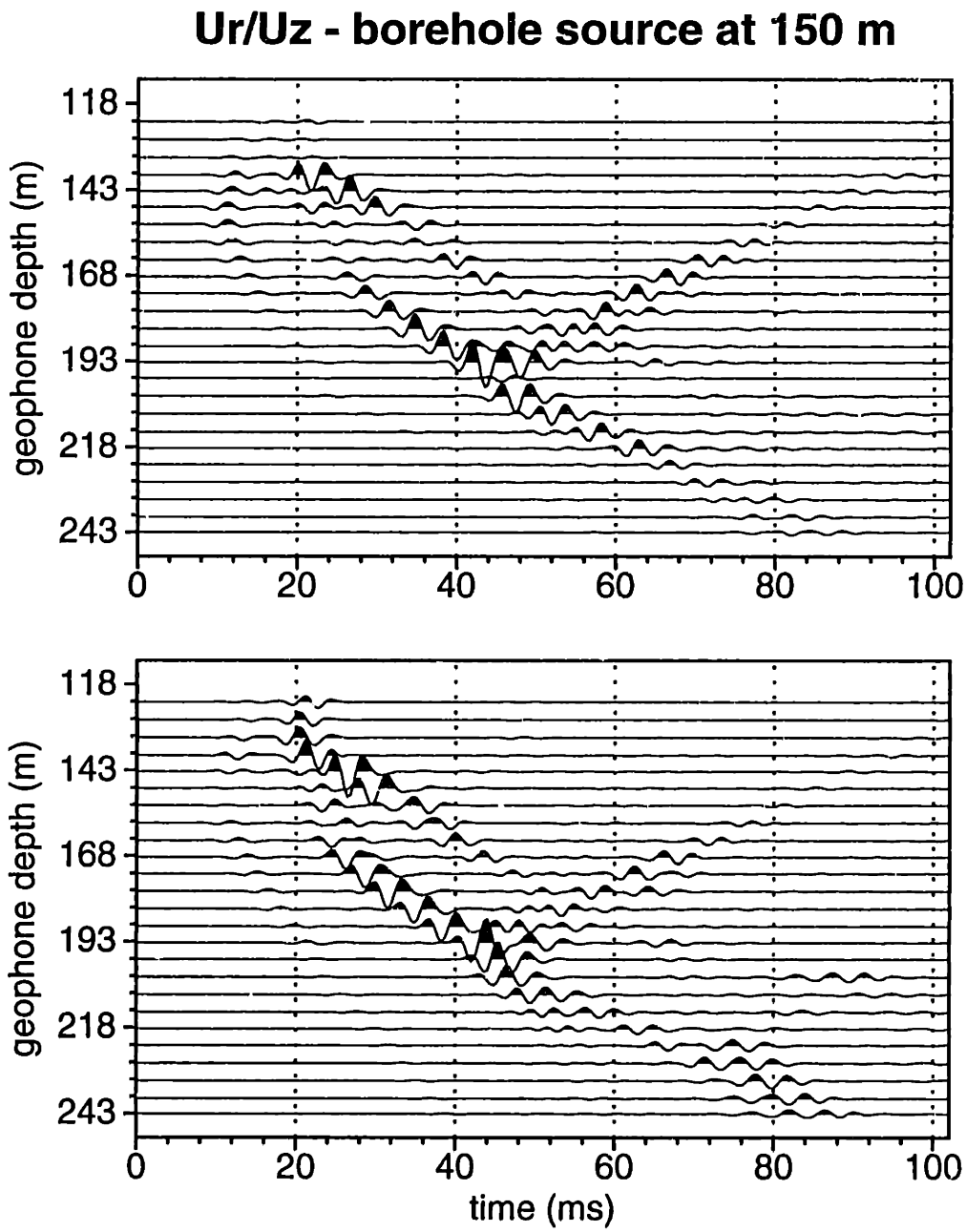

Figure 5-28: Synthetic data for a borehole explosion source at a depth of 150 meters. Only the source borehole is considered in the modeling.

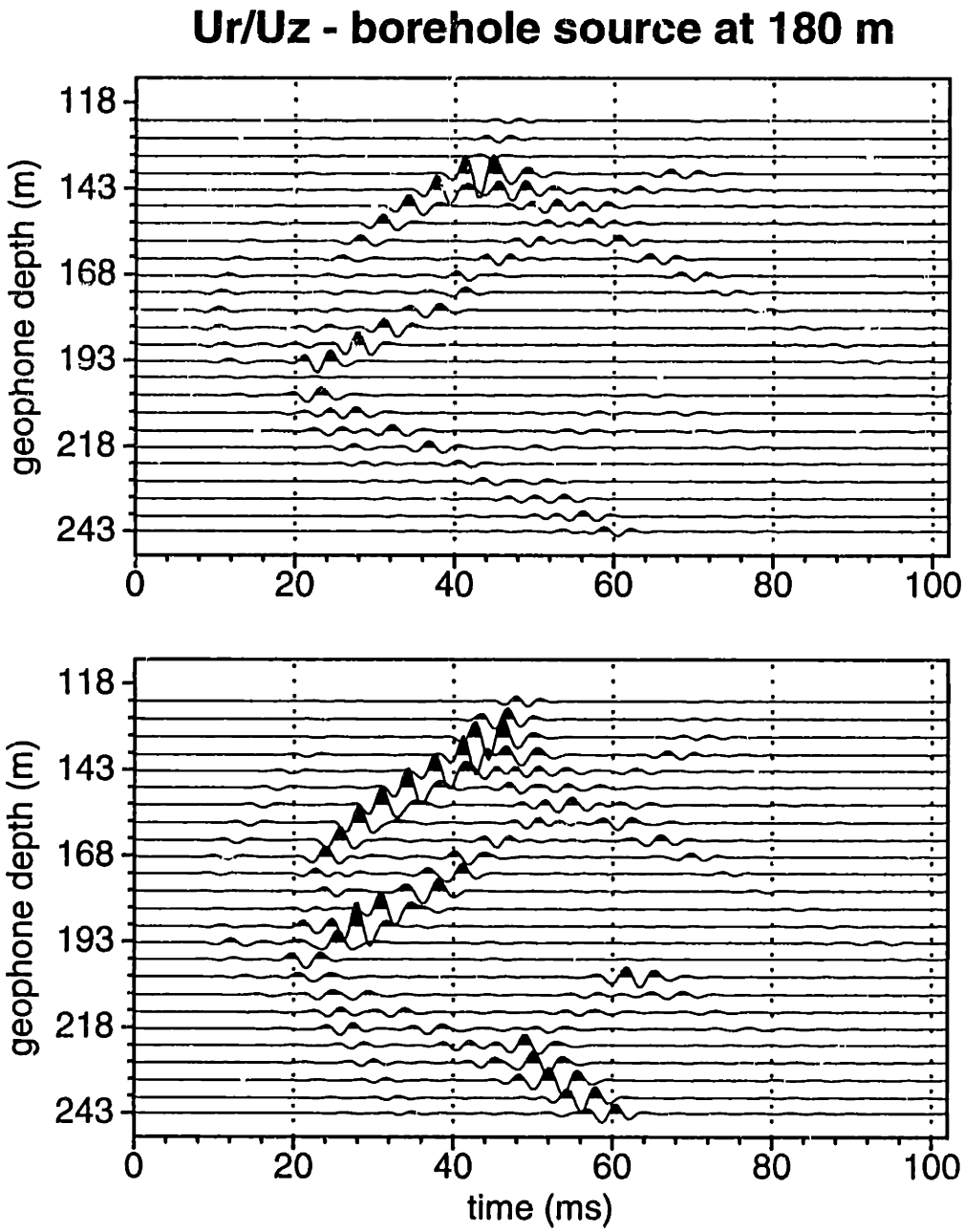

Figure 5-29: Synthetic data for a borehole explosion source at a depth of 180 meters. Only the source borehole is considered in the modeling.

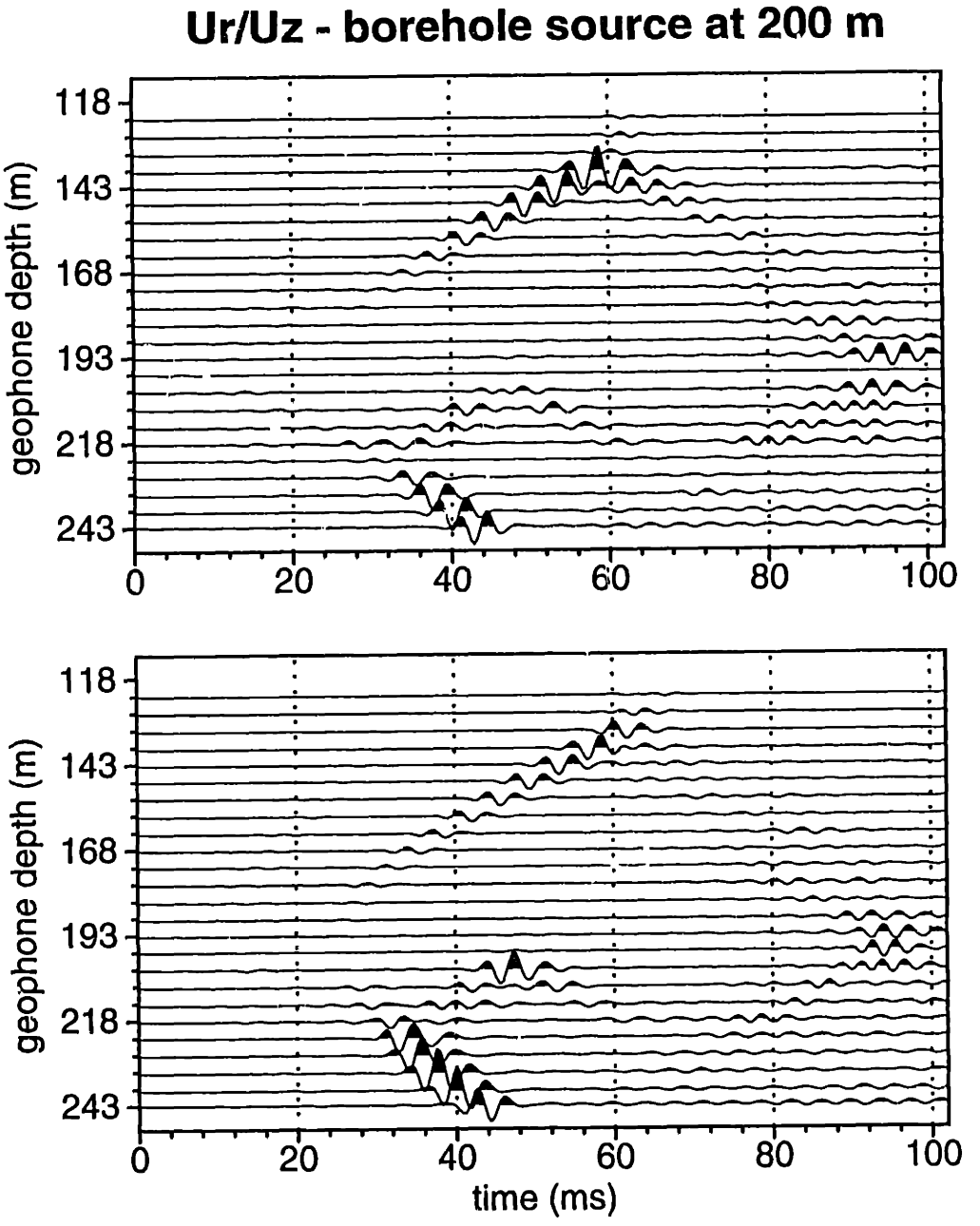

Figure 5-30: Synthetic data for a borehole explosion source at a depth of 200 meters. Only the source borehole is considered in the modeling.

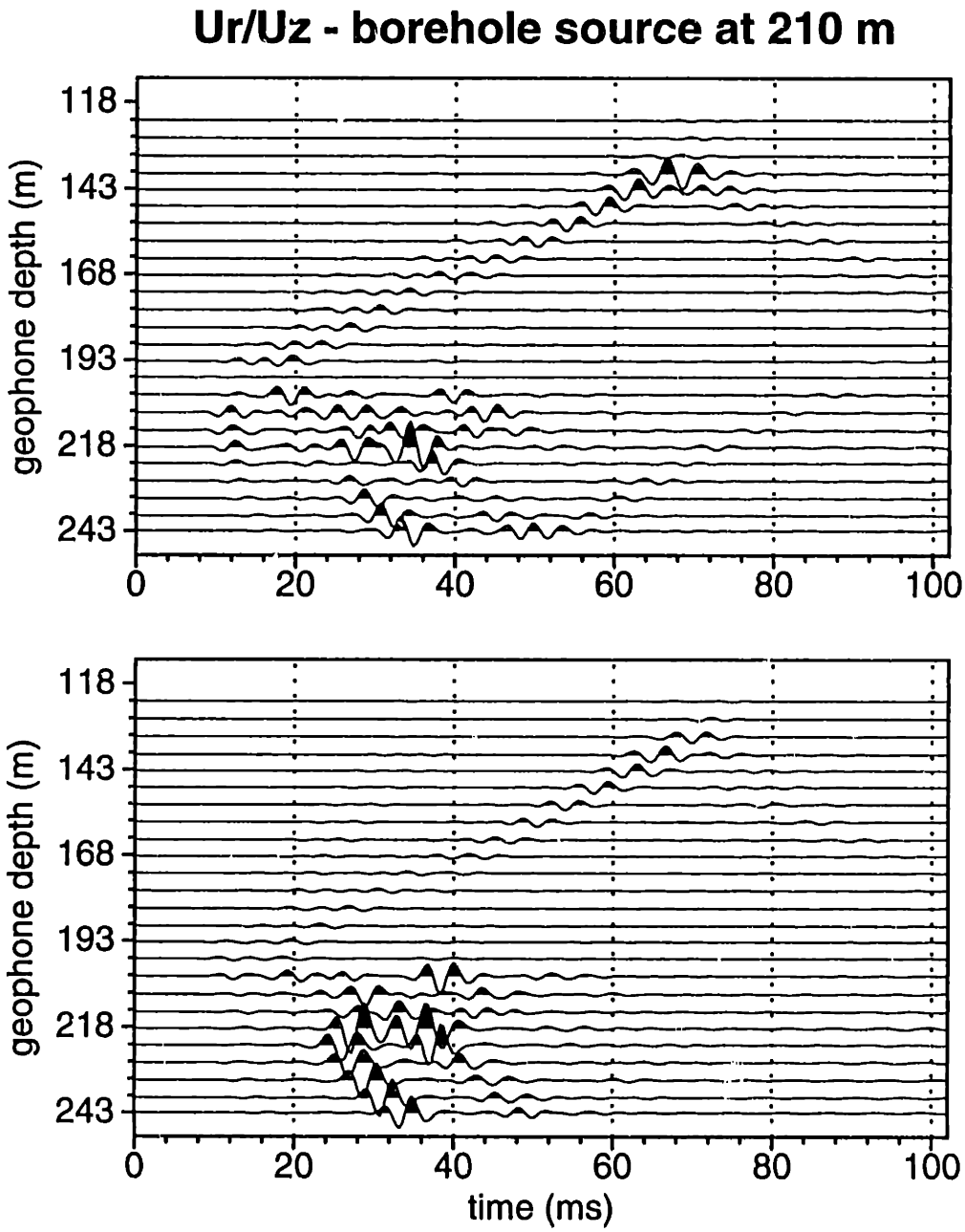

Figure 5-31: Synthetic data for a borehole explosion source at a depth of 210 meters. Only the source borehole is considered in the modeling.

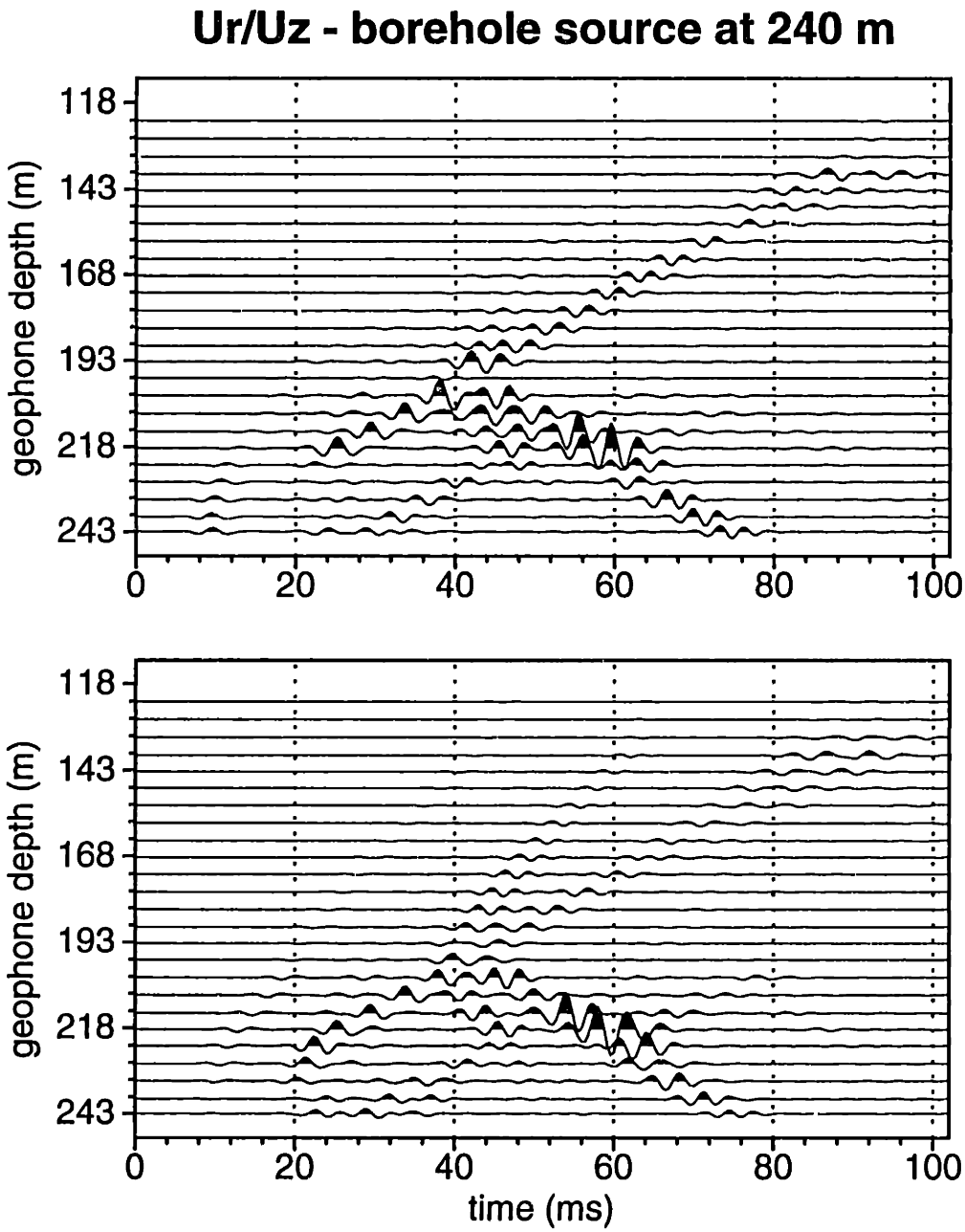

Figure 5-32: Synthetic data for a borehole explosion source at a depth of 240 meters. Only the source borehole is considered in the modeling.

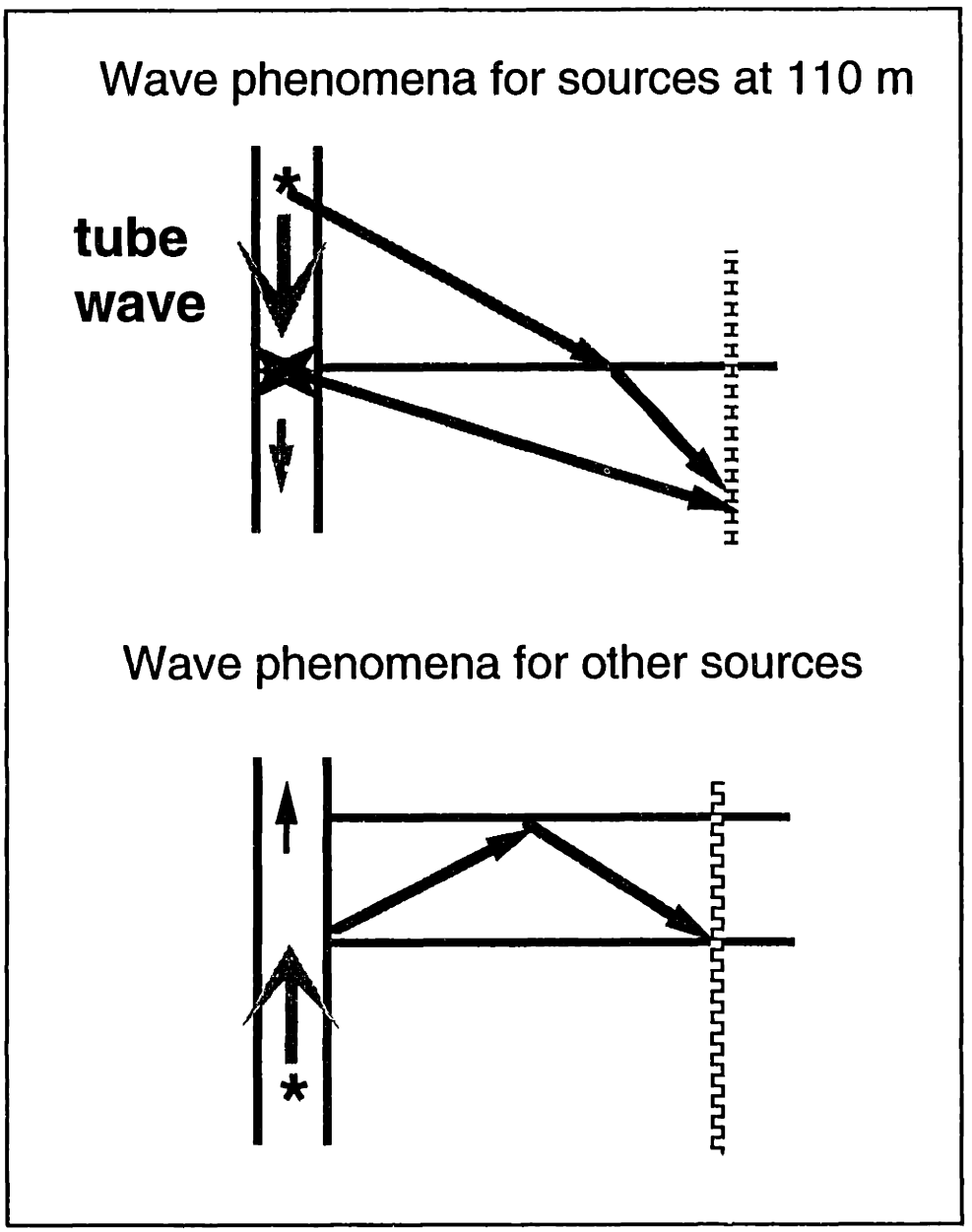

Figure 5-33: A schematic showing of the wave phenomena associated with borehole source at 110 m and other depths.

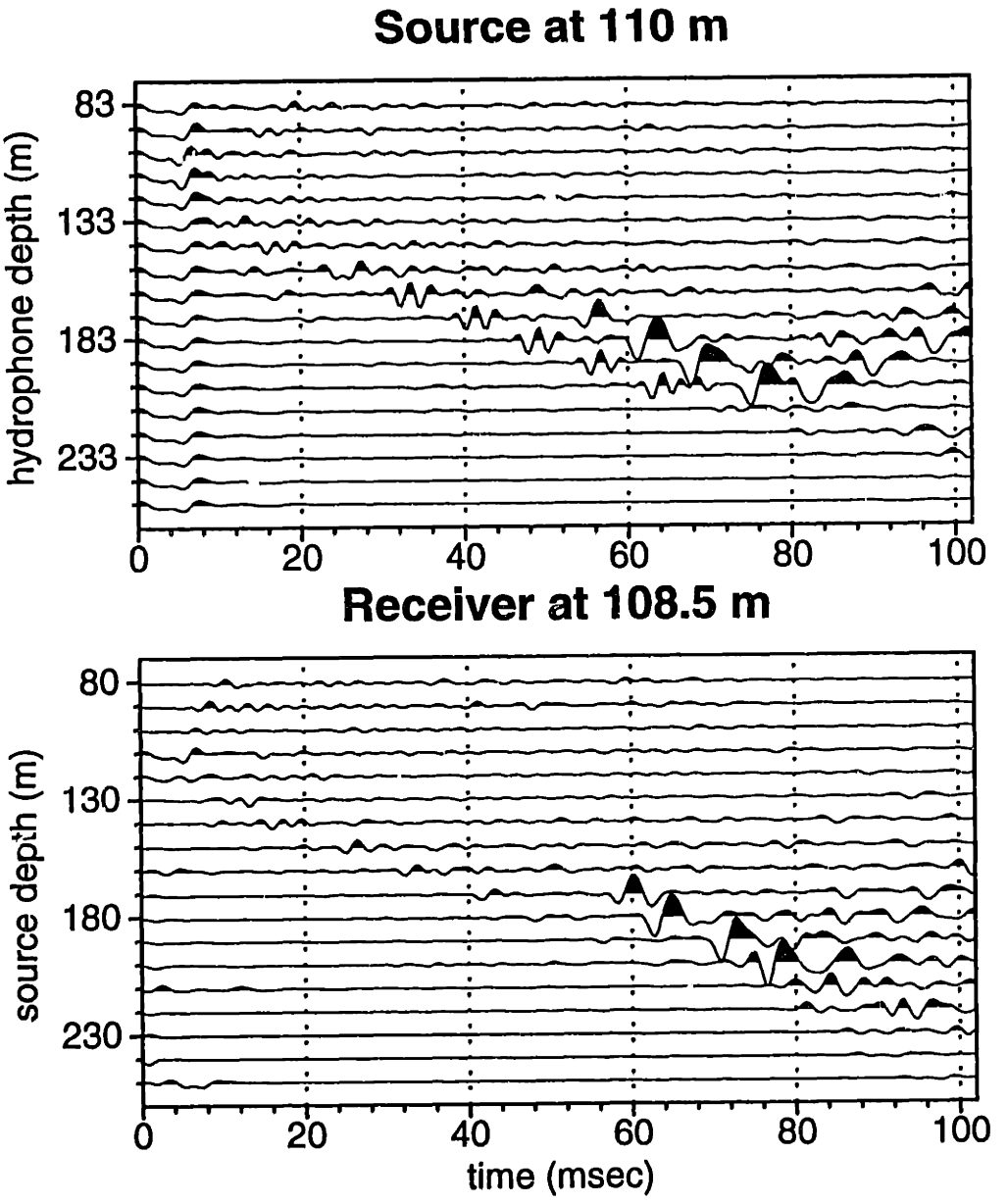

Figure 5-34: The common-shot (top) and common-receiver (bottom) sections at or near the depth of 110 meters. The strong later arrival in the common-shot gather reflects the effect of the source borehole; While the similar event in the common-receiver gather reflects the receiver borehole effect.

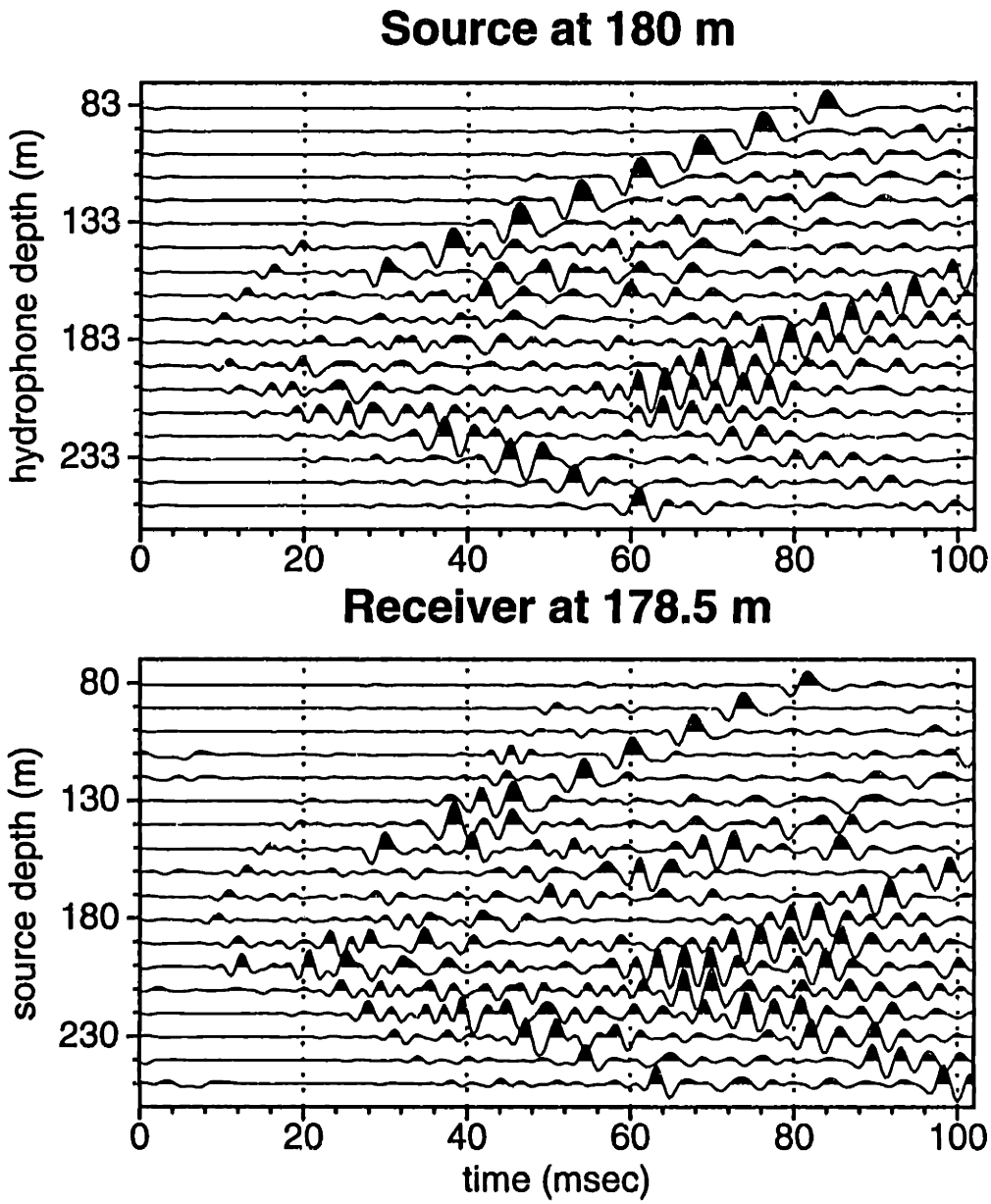

Figure 5-35: The common-shot (top) and common-receiver (bottom) sections at or near the depth of 180 meters.

Chapter 6

Models for Two Special Borehole Sources

6.1 Introduction

Routine use of cross-well techniques depends heavily on the further advent of downhole source technology. The desirable source should be powerful and easy to deploy, should have a wide range of operating frequency, and should not damage the borehole. In the previous chapters, models for the dynamite source, the vertical wall-clamped vibrator, and the bender source have been described. In this chapter we consider two special downhole sources. Conoco's Downhole Orbital Vibrator is commonly used as a SH wave source. We'll show through a mathematical model that this source is an efficient 3-D source. Potentially, it can be used to detect and to measure the shear wave anisotropy of a rock formation. We also discuss some aspects of modeling Seismic-While Drilling, which uses a drill-bit as a downhole source.

6.2 Downhole Orbital Vibrators

Conoco Inc. has patented a borehole seismic source technology that uses one or two DC motors to spin internal eccentric masses in the fluid column and to excite elastic disturbances in the surrounding formation (Cole, 1989). The source operates as a free-hanging device in a borehole fluid column and is not wall-clamped. Since this vibrator does not have to be clamped and unclamped at each source location, cross-well and reverse VSP data can be recorded at high production rates. It is claimed that robust P and S waves are created which have ideal radiation patterns for cross-well profiling and that almost no tube wave disturbances are observed in the far-field. In the following subsection, we first briefly describe the source and its specifications. A mathematical model is then offered for this increasingly popular source.

6.2.1 Description of the source

Figure 6-1 shows a dual motor Downhole Orbital Vibrator (DOV). The mechanics of these sources is simple. The original single-motor and the newer dual-motor DOV have similar devices consisting of single or double DC motors which spin internal eccentric masses attached to the motor shaft. After a voltage is applied to the motor(s), the angular velocity of the rotating masses increases with the duration time of the voltage. This is the up-sweep time. When the motor(s) voltage is switched off, the rotational velocity decreases until the masses spin down to a dead stop. This is the down-sweep time. Thus, a DC voltage pulse of a certain time duration produces a continuous frequency up-sweep followed immediately by a down-sweep. This frequency characteristic is very similar to the surface Vibroseis source. To correlate the wavefield with the source signal, a horizontal motion sensor, which records the movement of the eccentric mass, is provided. The source operates with a standard logging cable.

The internal spinning eccentric masses produce a centrifugal force vector which

causes the entire source to be radially displaced in phase with the angular position of the rotating force vector. This rotating radial movement of the source couples through the borehole fluid to produce P and S body waves at every point around the circumference of the well (Queen and Cole, 1992; personal communication). The maximum frequency of the source depends directly on its maximum number of operating spins per second. The effective bandwidth of the source is approximately 50 to 450 Hz.

The whole tool weighs 11 kilograms, is 76 centimeters long, and has a diameter of 10 centimeters. The outside material is aluminum capable of withstanding pressure up to 5000 *psi* and temperature to 180^o F. The peak input power is 800 watts and the sustained power is 550 watts.

6.2.2 A mathematical model

The actual rotation of the mass covers a different angle for a fixed time interval at a different moment. The mass can revolve many hundreds of rounds in a second. We consider an *effective* source that resembles the wavelet after the sweep correlation between tool sensor and actual receiver recordings. This is because sweep correlation changes the source signature.

In the time domain, the correlated wavelet can be regarded as due to a phase-delayed summation of a rotating radial point force which has a certain waveform. The rotation has a constant angle of coverage during each spin and the rate is increased for successive rotations, but remains constant for each spin. In the frequency domain, this effective source amounts to rotating the mass a full 360^o only once, but, at each position, the applied force has a certain spectrum. Let's assume that the maximum force density generated by the rotating mass is one *Newton/meter*. Then, for a specific moment, a radial force at angle φ_0 can be expressed as

$$F(\mathbf{x}) = e^{-i\varphi_0}[\hat{r}\cos(\varphi - \varphi_0) - \hat{\varphi}\sin(\varphi - \varphi_0)]\delta(r - r_0)\delta(z - z'). \qquad (6.1)$$

The first term, $e^{-i\varphi_0}$, accounts for the time delay of the rotating mass whose rotation was started at time 0 (t=0) at angle $\varphi_0 = 0$. In the time domain, the delay is

$$t_0 = \frac{\varphi_0}{\omega} = \frac{\varphi_0}{2\pi} T. \tag{6.2}$$

That is, the time delay depends on the frequency of the tool rotation, which is the case in reality. With φ being the observation angle, the terms inside the square bracket are the radial and tangential components, relative to the observation direction, contributed by any radial point force at φ_0. The Kronical delta functions represent the location of the radial point force.

The above is not yet the full model for the DOV source. We have to superpose all the different radial forces at different positions. This amounts to an integration of the single force (Eq. 6.1) over the source position angle φ_0 from 0 to 2π. To simplify later integration, the expression in Eq. 6.1 can be rewritten as

$$\begin{aligned} F(\mathbf{x}) &= e^{-i\varphi} e^{i(\varphi-\varphi_0)} [\hat{r}\cos(\varphi-\varphi_0) - \hat{\varphi}\sin(\varphi-\varphi_0)]\delta(r-r_0)\delta(z-z'), \quad (6.3) \\ &= \frac{1}{2} e^{-i\varphi} \{\hat{r} - i\hat{\varphi} + \hat{r}\cos 2(\varphi-\varphi_0) - \hat{\varphi}\sin 2(\varphi-\varphi_0) \\ &\quad + i[\hat{r}\sin 2(\varphi-\varphi_0) + \hat{\varphi}\cos 2(\varphi-\varphi_0)]\} \, \delta(r-r_0)\delta(z-z'). \quad (6.4) \end{aligned}$$

This is an important result as it decomposes the actual source into summations of other sources. A closer observation and comparison with the results in the previous chapters leads to the following remarks.

1. The net result of the integration of the first term in Eq. 6.4 is a force at the *center* of the borehole in the direction of the observation, while the second term produces a force at the *center*, that is perpendicular to the observation direction and has a $\pi/2$ phase delay relative to the force in the observation direction.

2. Integrations of the third and fourth term yield collectively a radial source that applies radial forces *simultaneously* to the borehole wall. It is similar to the radial sources considered in the previous chapters. The only difference now is

that the argument of the trigonometric functions has a factor of two, that later is seen to yield different Bessel functions.

3. Integrations of the fifth and sixth term produce collectively a torsional source that applies tangential forces *simultaneously* to the borehole wall, and has a $\pi/2$ phase advance relative to the radial force from the third and fourth term.

Thus, the Downhole Orbital Vibrator can be effectively approximated by the combination of the above mentioned basic sources. Equation 6.4 also states that a wave arrives at the observation points with different azimuthal angles at different times, and that the time delay depends on the angle.

6.2.3 Displacements in isotropic media

To obtain the displacements due to a DOV source, we dot-multiply the expression in Equation 6.4 by the Green's function of the isotropic medium

$$\overline{\mathbf{G}}(\mathbf{x},\mathbf{x}') = \frac{1}{\rho\omega^2}\left\{k_b^2\overline{\mathbf{I}}g_b(\mathbf{x},\mathbf{x}') + \nabla\nabla\left[g_b(\mathbf{x},\mathbf{x}') - g_a(\mathbf{x},\mathbf{x}')\right]\right\}. \tag{6.5}$$

where, g_a and g_b are the scalar Green's functions for the P and S wave and take the form

$$g_{a,b} = \frac{i}{4\pi}\sum_{m=0}^{\infty}\varepsilon_m \cos m(\varphi-\varphi_0)\int_0^{\infty}\frac{k}{\nu_{a,b}}J_m(kr_0)J_m(kr)e^{i\nu_{a,b}|z-z'|}dk. \tag{6.6}$$

Integration over φ_0 determines the integer value of m according to the orthogonality of trigonometric functions in the range of 0 to 2π. Due to their complexity, we list the displacements for the individual forces as follows.

1. force $\hat{r}$:

$$\begin{aligned}
U_\varphi &= 0 \\
U_r &= \frac{i}{2\mu}\int_0^{\infty}\frac{kr_0}{\nu_b}J_0(kr_0)J_0(kr)e^{i\nu_b|z-z'|}dk \\
&\quad -\frac{i}{2\rho\omega^2}\int_0^{\infty}k^3r_0J_0(kr_0)J_1'(kr)\left[\frac{e^{i\nu_b|z-z'|}}{\nu_b}-\frac{e^{i\nu_a|z-z'|}}{\nu_a}\right]dk, \\
U_z &= \frac{\mathrm{sgn}(z-z')}{2\rho\omega^2}\int_0^{\infty}k^2r_0J_0(kr_0)J_1(kr)[e^{i\nu_a|z-z'|}-e^{i\nu_b|z-z'|}]dk
\end{aligned} \tag{6.7}$$

2. force $\hat{\varphi}$:

$$\begin{aligned} U_\varphi &= \frac{i}{2\mu}\int_0^\infty \frac{kr_0}{\nu_b} J_0(kr_0)J_0(kr)e^{i\nu_b|z-z'|}dk, \\ U_r &= 0, \\ U_z &= 0, \end{aligned} \tag{6.8}$$

3. force $\hat{r}\cos 2(\varphi-\varphi_0) - \hat{\varphi}\sin 2(\varphi-\varphi_0)$:

$$\begin{aligned} U_\varphi &= 0. \\ U_r &= \frac{i}{2\mu}\int_0^\infty \frac{kr_0}{\nu_b} J_2(kr_0)J_2(kr)e^{i\nu_b|z-z'|}dk \\ &\quad + \frac{i}{2\rho\omega^2}\int_0^\infty k^3 J_2(kr_0)J_1'(kr)\left[\frac{e^{i\nu_b|z-z'|}}{\nu_b} - \frac{e^{i\nu_a|z-z'|}}{\nu_a}\right]dk, \\ U_z &= \frac{\mathrm{sgn}(z-z')}{2\rho\omega^2}\int_0^\infty k^2 r_0 J_2(kr_0)J_1(kr)[e^{i\nu_a|z-z'|} - e^{i\nu_b|z-z'|}]dk \end{aligned} \tag{6.9}$$

4. force $\hat{r}\sin 2(\varphi-\varphi_0) + \hat{\varphi}\cos 2(\varphi-\varphi_0)$:

$$\begin{aligned} U_\varphi &= \frac{i}{2\mu}\int_0^\infty \frac{kr_0}{\nu_b} J_2(kr_0)J_2(kr)e^{i\nu_b|z-z'|}dk \\ &\quad - \frac{i}{\rho\omega^2}\int_0^\infty k^2\frac{r_0}{r} J_2(kr_0)J_1(kr)\left[\frac{e^{i\nu_b|z-z'|}}{\nu_b} - \frac{e^{i\nu_a|z-z'|}}{\nu_a}\right]dk, \\ U_r &= 0, \\ U_z &= 0, \end{aligned} \tag{6.10}$$

Integrating the above in z' over the length of the DOV source (typically 0.76 m), and grouping the results according to Equation 6.4, yields the total displacement components.

The above results suggest that, instead of being treated as a pure SH-wave source, the Downhole Orbital Vibrator is in reality a 3-D source. It generates all three wave types in an isotropic medium. Figures 6-2 and 6-3 show the three displacements due to a DOV source in an isotropic Pierre shale. The borehole radius r_0 is equal to 0.1 m, and the length of the source is equal to 0.76 m. The 31 receivers, vertically and symmetrically distributed at a spacing of 2 m above and below the source, are 20

meters away from the source. Normally, if the source is truly torsional, there is no radial displacement for the SV wave at source level. As it will become evident in the following subsection, the observed S wave near the source level is from the SH-wave contribution. This phenomenon is specifically related to the DOV source.

6.2.4 Displacements in anisotropic media

Displacements of the DOV source in anisotropic media are obtained by dot-multiplying the TI Green's function by the force in Equation 6.4 and by integrating the results over φ_0 from 0 to 2π. The Green's function in a transversely isotropic medium is obtained in Chapter 2 and is

$$\overline{\mathbf{G}} = g\bar{\mathbf{I}}_t + \hat{z}\hat{z}L_z\phi - (c_{13}+c_{44})(\nabla_t\hat{z}+\hat{z}\nabla_t)\frac{\partial\phi}{\partial z} + \nabla_t\nabla_t\psi. \tag{6.11}$$

The displacements are given as follows.

1. force $\hat{r}$:

$$\begin{aligned} U_\varphi &= 0 \\ U_r &= \frac{i}{2c_{44}}\int_0^\infty \frac{e^{i\nu_c|z-z'|}}{\nu_c} kr_0 J_0(kr_0)[J_0(kr) - J_1'(kr)]dk \\ &\quad + \frac{i}{2}\int_0^\infty \left[T_a e^{i\nu_a|z-z'|} - T_b e^{i\nu_b|z-z'|}\right] kr_0 J_0(kr_0)J_1'(kr)dk \\ U_z &= \frac{\mathrm{sgn}(z-z')}{2}\int_0^\infty S_{ab}k^2 r_0 J_0(kr_0)J_1(kr)[e^{i\nu_a|z-z'|} - e^{i\nu_b|z-z'|}]dk \end{aligned} \tag{6.12}$$

2. force $\hat{\varphi}$:

$$\begin{aligned} U_\varphi &= \frac{i}{2c_{44}}\int_0^\infty \frac{e^{i\nu_c|z-z'|}}{\nu_c} kr_0 J_0(kr_0)J_0(kr)dk \\ U_r &= 0 \\ U_z &= 0 \end{aligned} \tag{6.13}$$

3. force $\hat{r}\cos 2(\varphi-\varphi_0) - \hat{\varphi}\sin 2(\varphi-\varphi_0)$:

$$U_\varphi = 0.$$

$$
\begin{aligned}
U_r &= \frac{i}{2c_{44}} \int_0^\infty \frac{e^{i\nu_c|z-z'|}}{\nu_c} kr_0 J_2(kr_0)[J_2(kr) - J_1'(kr)]dk \\
&\quad -\frac{i}{2} \int_0^\infty \left[T_a e^{i\nu_a|z-z'|} - T_b e^{i\nu_b|z-z'|}\right] kr_0 J_2(kr_0) J_1'(kr) dk \qquad (6.14) \\
U_z &= \frac{\mathrm{sgn}(z-z')}{2} \int_0^\infty S_{ab} k^2 r_0 J_2(kr_0) J_1(kr)[e^{i\nu_a|z-z'|} - e^{i\nu_b|z-z'|}]dk
\end{aligned}
$$

4. force $\hat{r}\sin 2(\varphi - \varphi_0) + \hat{\varphi}\cos 2(\varphi - \varphi_0)$:

$$
\begin{aligned}
U_\varphi &= -\frac{i}{2c_{44}} \int_0^\infty \frac{kr_0}{\nu_c} J_2(kr_0) J_0(kr) e^{i\nu_c|z-z'|} dk \\
&\quad -\frac{i}{2} \int_0^\infty kr_0 J_2(kr_0)[J_2(kr) + J_0(kr)] \left[T_b e^{i\nu_b|z-z'|} - T_a e^{i\nu_a|z-z'|}\right] dk \qquad (6.15) \\
U_r &= 0, \\
U_z &= 0,
\end{aligned}
$$

Integrating the above in z' over the length of the DOV source (typically 0.76 m), and grouping the results according to Equation 6.4, one obtains the total displacement components.

An important observation is that the SH wave contributes to the horizontal displacement (U_r) for a DOV source. With the U_r contribution of the *quasi-SV* wave, formation shear wave anisotropy will be clearly indicated on the horizontal displacement recording, due to the different traveltime of the SH and SV wave. Figures 6-4 and 6-5 show the phenomena for an anisotropic Pierre shale. The elastic parameters of the rock are: $c_{11} = 11.81$, $c_{33} = 9.68$, $c_{13} = 7.11$, $c_{44} = 1.70$, $c_{66} = 2.26$, in GPa, and $\rho = 2.25\ g/cm^3$. One sees that two waves are clearly separated near the source level. The later arrival on the U_r section is the *quasi-SV* wave, the middle one is the SH wave. As the figures indicate, there is no SV wave contribution to U_r near the source level. On the other hand, the SH wave is stronger near the source level. The difference in traveltime suggests the well-known phenomena of *shear wave splitting*. The extent of the separation also indicates the degree of shear wave anisotropy of the formation.

The splitting of shear waves should also be observable on a recorded pressure section, if a hydrophone is used in the receiver borehole. Using a DOV source and hydrophones, a rapid survey of the formation anisotropy is feasible and attractive. This may present a technique of direct shear wave anisotropy estimation of the rock formations.

6.3 Drill-Bit as a Downhole Seismic Source

A drill-bit used as a downhole seismic source, Tomex Survey^{TM} or Seismic-While-Drilling (SWD), has attracted some attention in recent years (see Rector *et al*, 1988). The advantages of SWD lie mainly in its economical value. Using the drill-bit impact vibration as the source of seismic disturbances, inverse VSP surveys can be continuously recorded while drilling, and no interruption nor lost rig time are incurred. The processing of these VSP data *on site* presents a potential for drilling engineers to *look* ahead of the bit, and for geophysicists to image the surrounding subsurface of the area. This technique is especially attractive in a geothermal area where conventional downhole instruments break down very easily.

In spite of its potential and the attention this technique attracted, many questions remain to be answered, such as what is the source mechanism, what frequency content should one expect from drill-bit vibration, how can one obtain good reverse VSP data, etc.? Two most recent Ph.D theses have devoted their entire attention to answering these questions. The thesis by Rector (1990) describes the technique from a broad view. He presented detailed processing procedures on correlating geophone recordings with drill-pipe sensor recordings. Radiation patterns of the typical tri-cone bit was discussed and case studies were given. The thesis by Lee (1991) focuses on the theoretical and experimental investigation of the boundary conditions at the top and at the bottom of a drill-string. By comparing theory to experiment, he concluded that the drill-bit impact can be modeled either as a vertical stress discontinuity, or as

a displacement discontinuity at bit/formation contact. Lee (1991) also described the drill-string filtering effect using real data. These two theses contribute significantly to our understanding of this emerging SWD technology.

In accordance with the focus of this thesis, the purpose of this section is to point out that the aforementioned BEM modeling technique can be used to model an idealized SWD experiment, in layered isotropic or anisotropic media. The only complication in modeling SWD using BEM comes from the fact the borehole now is semi-infinite.

To apply BEM, the borehole bottom is discretized into concentric ring-shaped disks, named *bottom elements*, as shown in Figure 6-6. Similar to the previous *wall elements*, three fictitious sources of unknown magnitudes are assumed on each of these bottom elements: an explosion source for the fluid side of the element, and radial and vertical forces for the solid side of the element. The three boundary conditions of bottom element are the continuity of U_z and σ_{zz} and the vanishing of σ_{zr}. That is, when computing the contribution of other elements on a bottom element, the vertical displacement, the vertical stress, and the tangential stress are the quantities to calculate. The formula for U_z and σ_{zz} have been given along with U_r, σ_{rr}, and σ_{rz} in Section 4.3 and Section 4.4.

To compute the contribution of a radiating bottom element to other elements, the surface integration for the bottom element is required. Since displacements and stresses are given for ring sources, the surface integration of the bottom element amounts to integrating the ring source results with respect to the radius of the ring source, r_i. Basically, two types of integrals are involved in the end: $\int r_i J_0(kr_i)dr_i$ and $\int r_i J_1(kr_i)dr_i$. For the element parameters in Figure 6-6, these integrals are

$$\int_{r_1}^{r_2} r_i J_0(kr_i)dr_i = \frac{1}{k}[r_2 J_1(kr_2) - r_1 J_1(kr_1)], \tag{6.16}$$

and

$$\int_{r_1}^{r_2} r_i J_1(kr_i)dr_i = \frac{\pi}{2k} r_2 [J_1(kr_2)H_0(kr_2) - J_0(kr_2)H_1(kr_2)]$$

rock and fluid type	V_p (m/s)	V_s (m/s)	ρ (g/cm^3)	σ
Berea sandstone	4206	2664	2.14	0.165
Test sediment	2100	1212	2.00	0.250
Borehole fluid	1500	0	1.00	0.500

Table 6.1: Parameters for two formation rocks and the borehole fluid.

$$-\frac{\pi}{2k} r_1 \left[J_1(kr_1) H_0(kr_1) - J_0(kr_1) H_1(kr_1) \right]. \qquad (6.17)$$

where H_0 and H_1 are the Struve functions of the zeroth and the first order (Abramowitz and Stegun, 1964). Their definition and computation are discussed in Appendix D.3.

The BEM technique is applied to generate the radiation patterns for a drill-bit (modeled as an unit stress discontinuity) in two formations. Their parameters are listed in Table 6.1. Figures 6-7 and 6-8 show the radiation pattern for the horizontal and vertical displacements recorded by a circular receiver array. A 10 cm borehole radius was used for both figures. Each point on the plots is the measured maximum amplitude for the P and S pulses in the seismogram. For hard rock (Berea sandstone), the drill-bit radiation pattern is basically the same as that of a vertical point force in an infinite Berea sandstone. Borehole fluid influence on the radiation pattern is negligible. However, the drill-bit radiation pattern in the test rock is visibly affected by the borehole fluid. A stronger shear wave is radiated downward, which is plausible for the purpose of looking-ahead-of-the-bit. The radiation patterns suggest that, three component geophones should be deployed on the earth surface, in order to utilize the strong shear wave radiation.

6.4 Conclusions

A mathematical model for Conoco's Downhole Orbital Vibrator is presented. The model incorporates the rotational effect of the forces radially exerted on the borehole wall. The source is shown to be a 3-D source. It emits all three waves in an elastic

medium: P or *quasi-P* wave, SV or *quasi-SV* wave, and SH wave. Due to the rotation of applied forces on the wall, these three waves can be observed together on the horizontal component of the displacement. In an anisotropic medium, the *quasi-SV* and SH waves arrive at different times, thus presenting a potential for direct detection and measurement of shear wave anisotropy of the formation.

Drill-bit source and sources in finite boreholes can be easily modeled using the BEM technique in isotropic and in TI media. The radiation pattern of the drill-bit is basically the same as that of a vertical force. In hard and moderately hard formations, the effect of the borehole on drill-bit radiation is negligible.

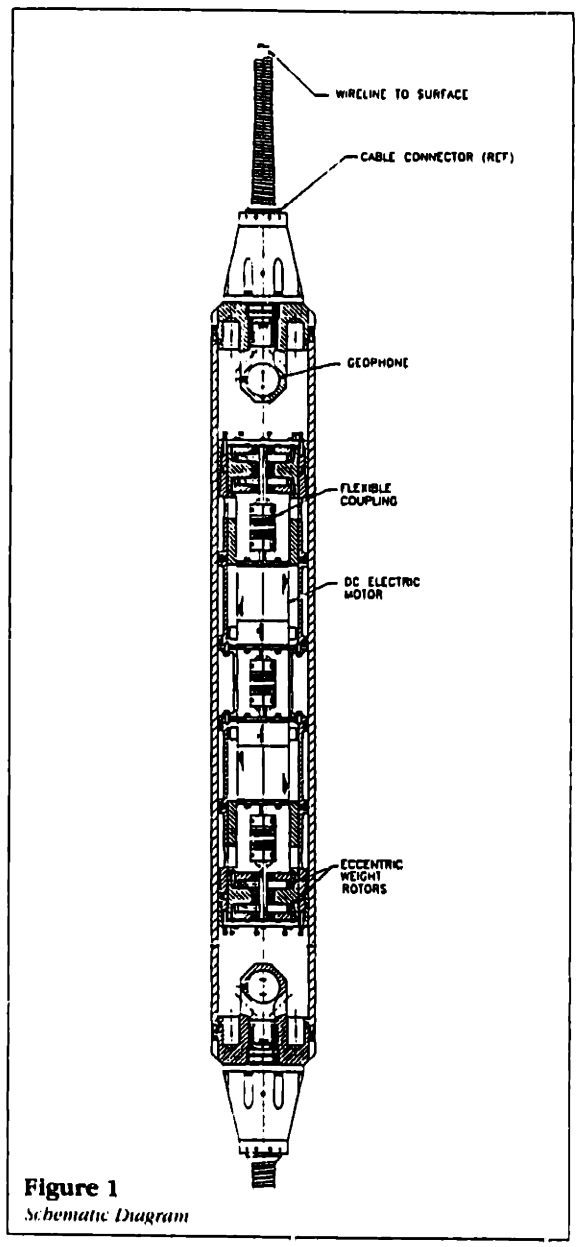

Figure 6-1: A schematic look at the dual-motor Downhole Orbital Vibrator source (from OYO Geospace). Two DC motors spin two eccentric masses to create radial forces to the borehole wall. Typical length: 0.76 m, Frequency range: 40-450 Hz.

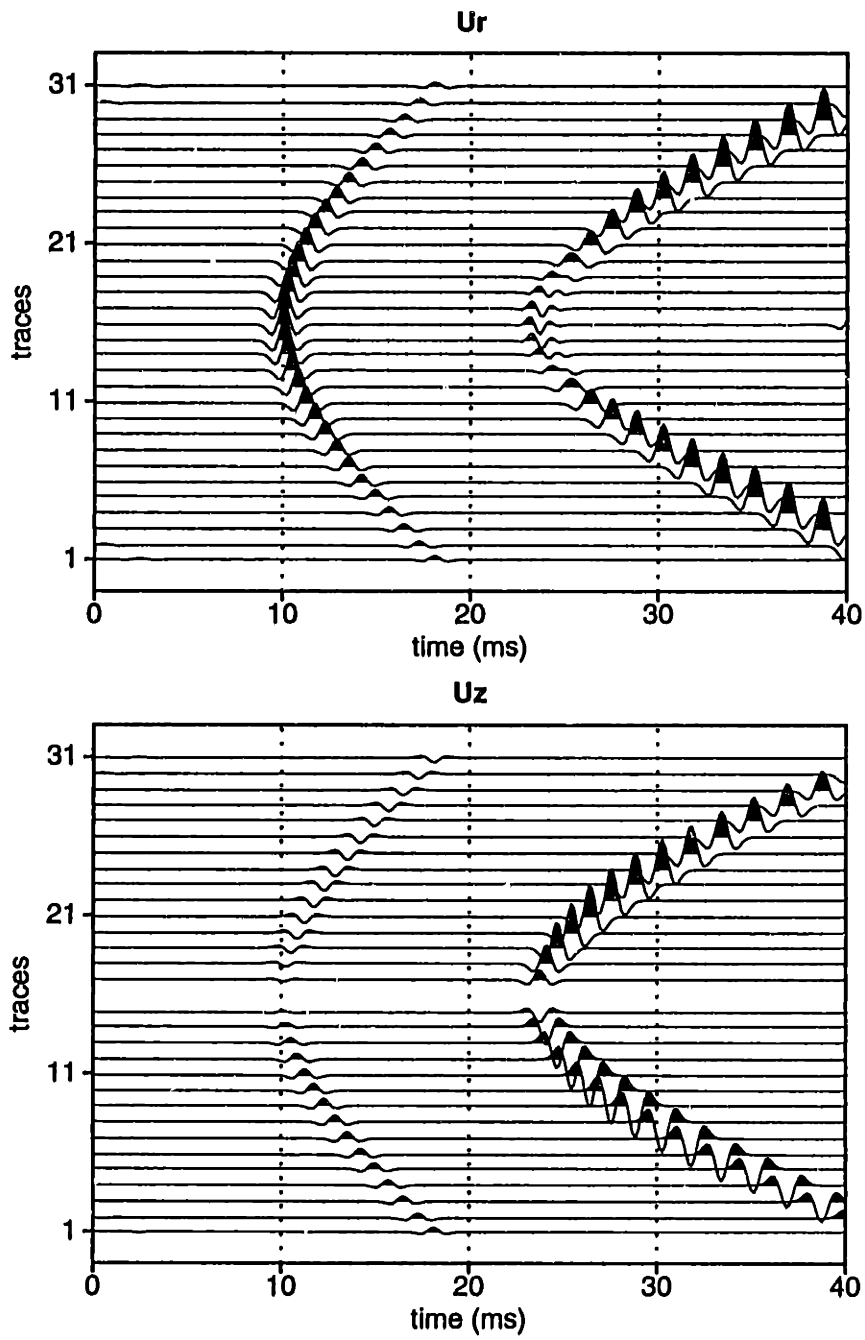

Figure 6-2: The horizontal (U_r) and vertical (U_z) components at receivers 20 meters away from a DOV source in an isotropic Pierre shale ($V_p = 2\ km/s$, $V_s = 0.85\ km/s$, $\rho = 2\ g/cm^3$). Receiver spacing: 2 meters.

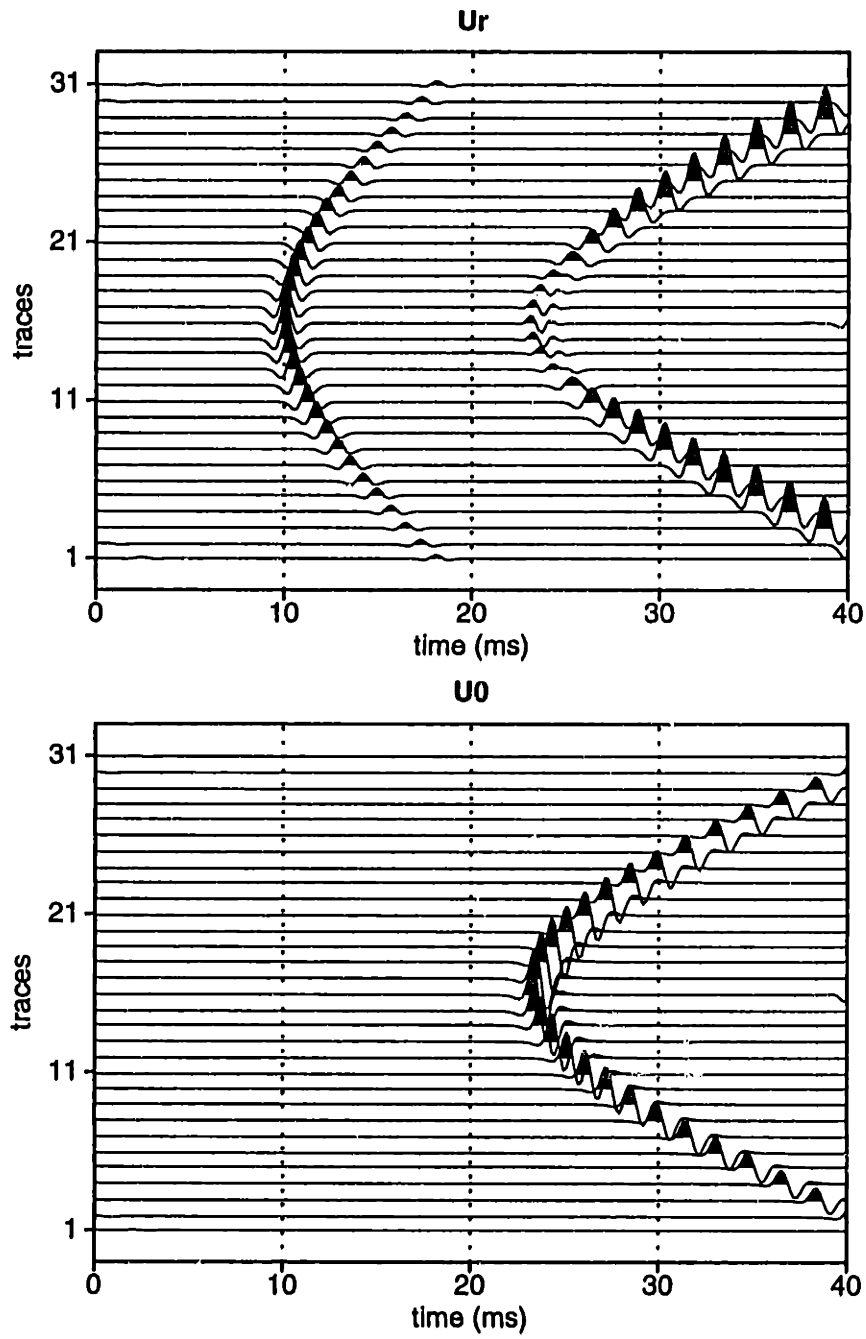

Figure 6-3: The horizontal (U_r) and torsional ($U\theta$) components at receivers 20 meters away from a DOV source in an isotropic Pierre shale ($V_p = 2\ km/s$, $V_s = 0.85\ km/s$, $\rho = 2\ g/cm^3$). Receiver spacing: 2 meters.

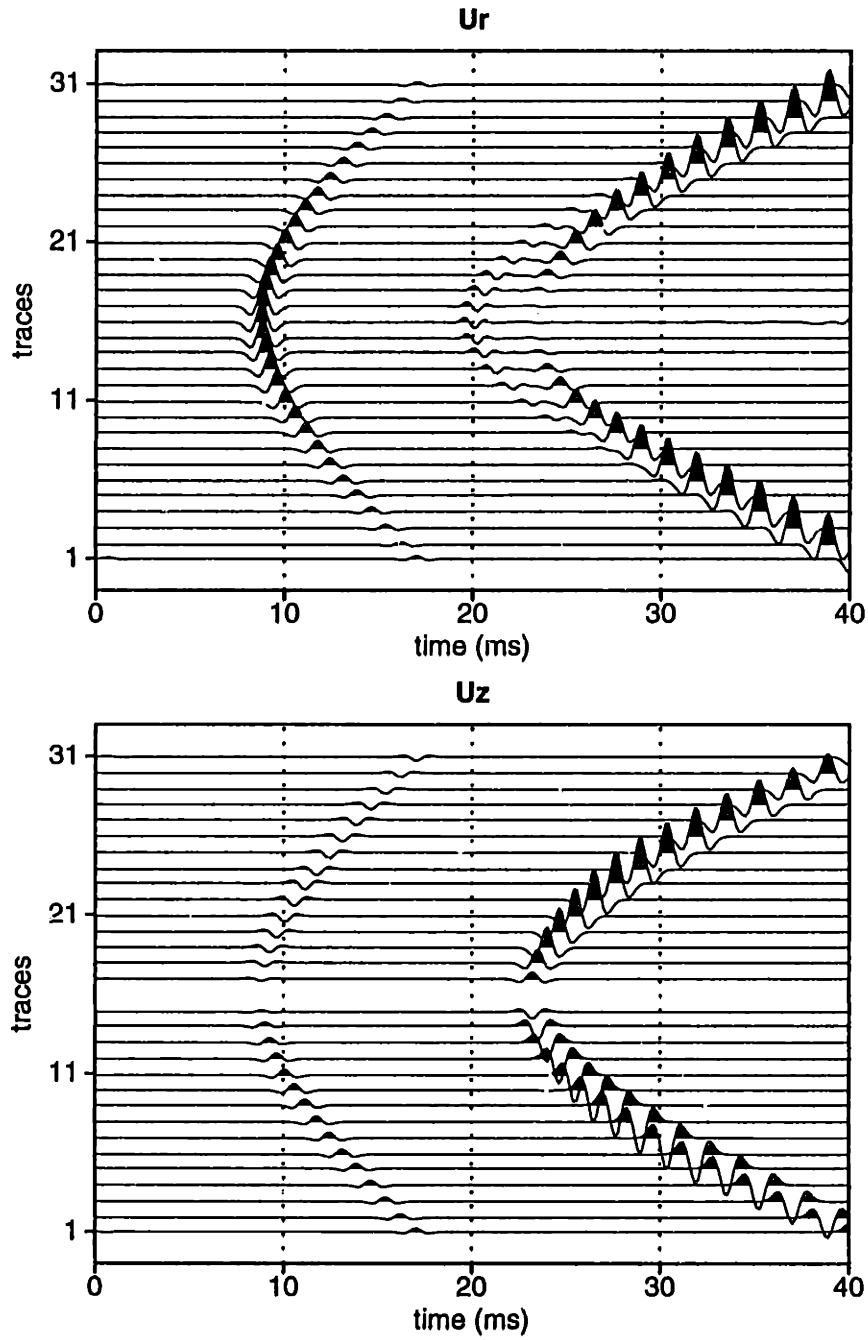

Figure 6-4: The horizontal (U_r) and vertical (U_z) components at receivers 20 meters away from a DOV source in an anisotropic Pierre shale ($c_{11} = 11.81$, $c_{33} = 9.68$, $c_{13} = 7.11$, $c_{44} = 1.70$, $c_{66} = 2.26$, in GPa, and $\rho = 2.25\ g/cm^3$). Receiver spacing: 2 meters.

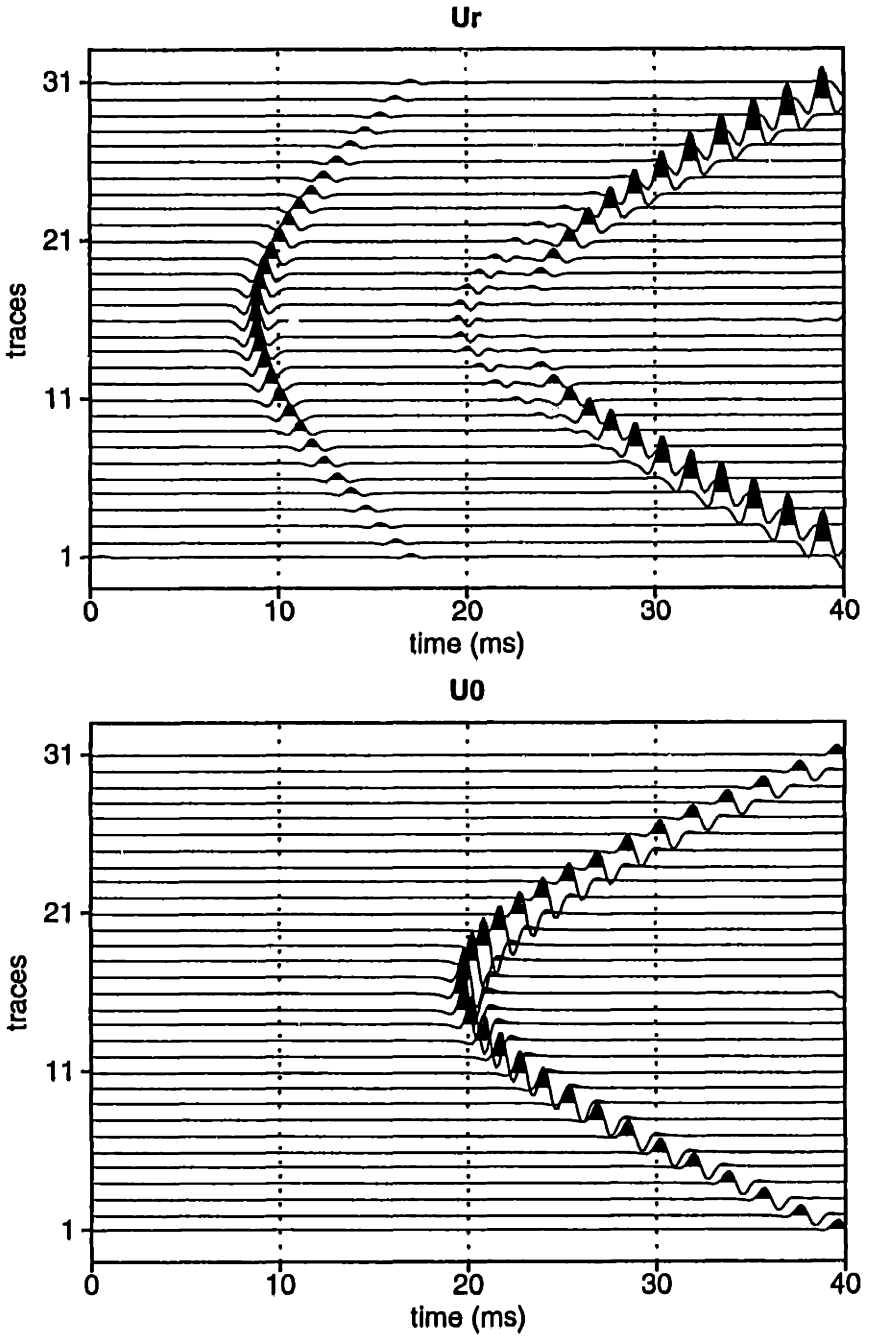

Figure 6-5: The horizontal (U_r) and torsional ($U\theta$) components at receivers 20 meters away from a DOV source in an anisotropic Pierre shale ($c_{11} = 11.81$, $c_{33} = 9.68$, $c_{13} = 7.11$, $c_{44} = 1.70$, $c_{66} = 2.26$, in GPa, and $\rho = 2.25\ g/cm^3$). Receiver spacing: 2 meters.

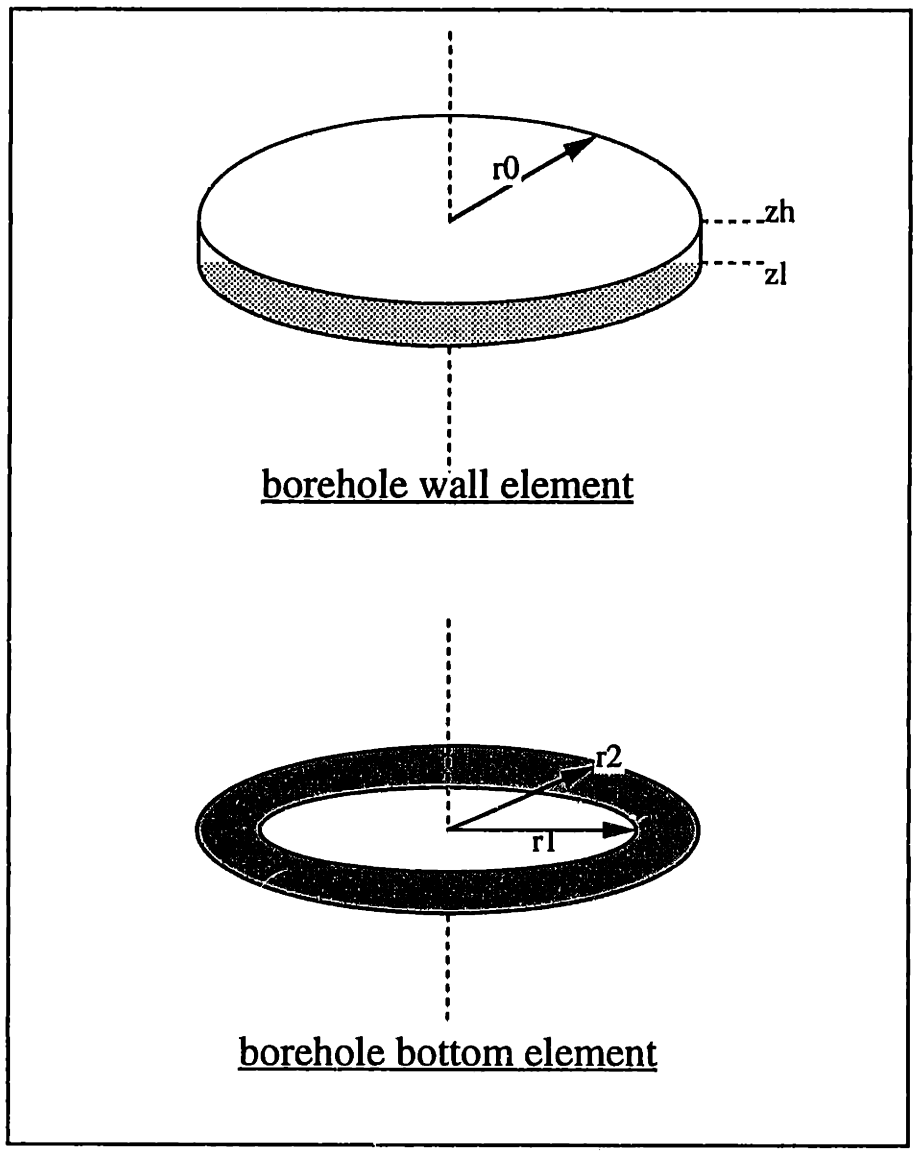

Figure 6-6: Borehole wall and bottom elements for a semi-infinite borehole.

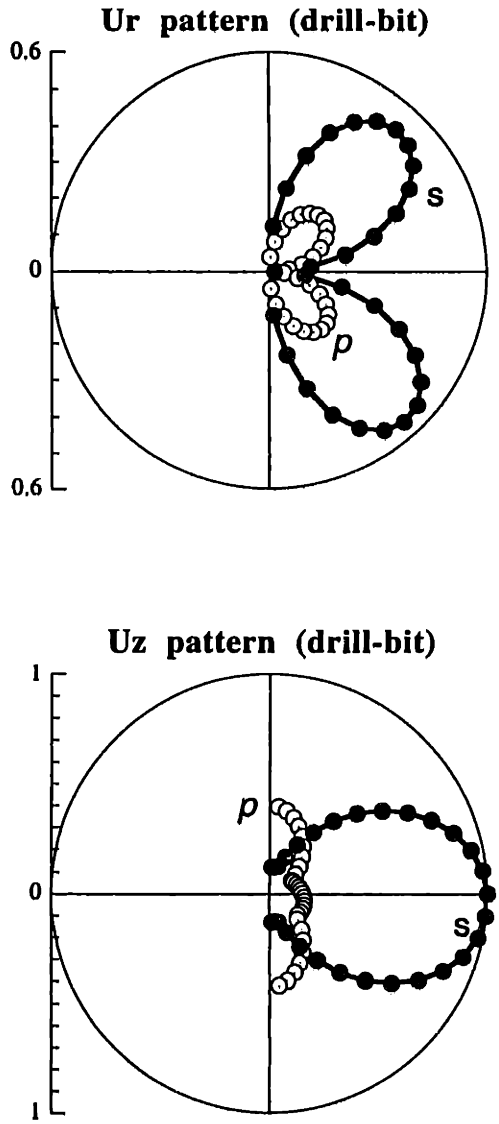

Figure 6-7: Radiation patterns of P and SV wave horizontal and vertical displacements for a drill-bit source in Berea sandstone (hard rock). Parameters: $V_p = 4206\ m/s$, $V_s = 2664\ m/s$, $\rho = 2.14\ g/cm^3$.

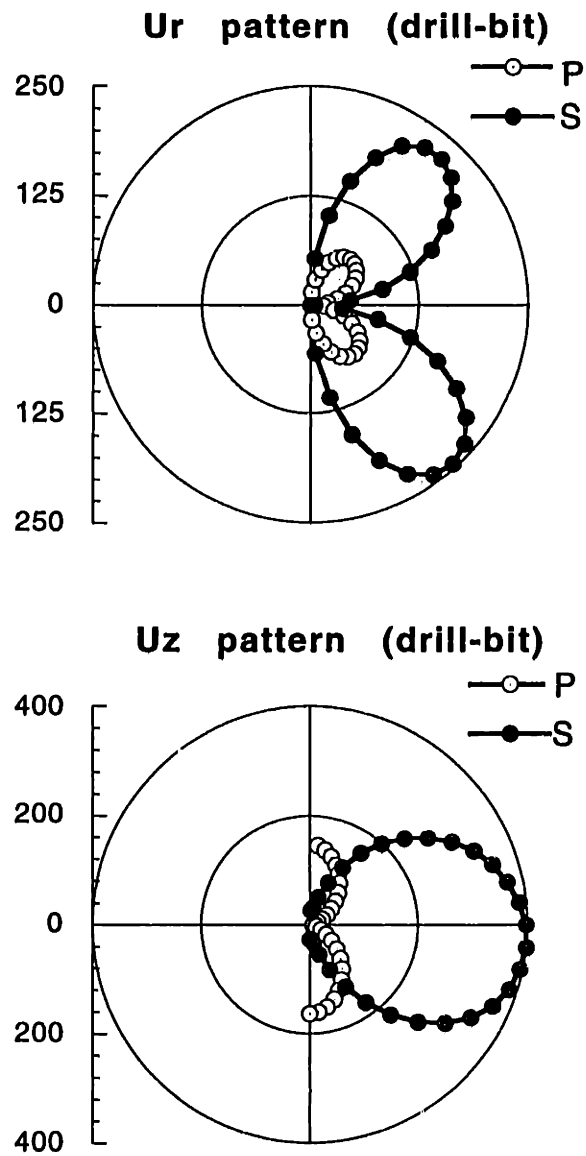

Figure 6-8: Radiation patterns of P and SV wave horizontal and vertical displacements for a drill-bit source in a softer test rock. Parameters: $V_p = 2100\ m/s$, $V_s = 1212\ m/s$, $\rho = 2.0\ g/cm^3$.

Chapter 7

Summary and Conclusions

The objective of the thesis was to understand the influence of the borehole on the elastic waves radiated from downhole seismic sources. As all previous studies on the subject were for borehole sources in a homogeneous isotropic medium, this thesis focused its attention on the more general problem: borehole sources in homogeneous and layered transversely isotropic (TI) media. To this end, the thesis addressed three major issues: wave radiation and propagation in TI media, analytical radiation patterns of borehole sources, and a boundary element method (BEM) to model borehole sources in layered TI media.

The dynamic and static Green's functions of a TI solid are obtained using a general solution method - the Kupradze method. The term involving a 2-D inverse Laplacian operator is evaluated without limiting it to special cases. This results in analytically and numerically feasible Green's functions that are valid for sources at any location and are directly applicable to BEM implementations. Though the displacement Green's functions are well defined (zero) under surface integration when the source and receiver points coincide, surface integration of the stress Green's functions in the same limit yields contributions due to the higher order singularities. When stress σ_{xx} for a horizontal force or stress σ_{xz} for a vertical force are integrated over a half elliptical surface, the singular contribution is shown to be the negative one-half of the

applied force. Explicit displacements for three basic sources are evaluated for two TI media. Results agree with those obtained from different approaches.

From the dynamic Green's function, the displacement potentials for a TI medium can be easily derived. From the potentials and by matching boundary conditions between the fluid and the TI medium, displacement integrals for three borehole sources are obtained. Asymptotic evaluation of these integrals yields the far-field radiation patterns for the three sources. These patterns are expressed in slowness components or in ray parameters, thus they can be readily incorporated into existing ray-based modeling or tomography codes to account for the source borehole effect on wave amplitudes.

Tests show that anisotropy effect on S-wave radiation is dramatic, even for a medium with a small degree of anisotropy. The results show that positive δ^* anisotropy broadens the radiation angle of the S-wave, while negative δ^* beams together the S-wave radiation. Thus, δ^* can be used as an indicator for the S-wave radiation pattern. Because energy distribution is determined by δ^*, and traveltime difference by ϵ and γ, the three anisotropy parameters are all important in cross-borehole seismology.

Examination of radiation from a cased borehole show that the effect of casing and cement for a hard formation is relatively frequency independent when the source frequency is not very high. The amplitude reduction for a radial source is more severe than for the explosion and vertical sources. For a relatively soft formation, casing and cement introduce a frequency dependent radiation pattern, even if the source frequency is relatively low.

To model wave radiation from open or cased boreholes in layered TI media, a BEM-based modeling algorithm is presented. Its main advantages lie in the semi-analytical nature and the perfect handling of the scale problem. The cylindrical isotropic layers (casing, cement, and fluid) inside the borehole, and the horizontal layers outside, are treated as separated systems in terms of wave propagation. They are tied together at the borehole boundary through matching boundary conditions. This

connection sets up a system of equations to determine the fictitious (or equivalent) boundary sources for each system. Once these equivalent sources are known, wave propagations in the two systems are achieved through their Green's functions. The examples validate the theoretical background and the implementation procedures.

The importance of the source borehole in understanding data is demonstrated through modeling and analyzing a real cross-well data set from Buckhorn, Illinois. The complicated wave phenomena in the data are shown to be caused by the presence of a fluid-filled borehole for the dynamite sources. Tube waves in the source borehole, the presence of soft formations (low velocity layers), and a highly contrasted local stratigraphy, are the important factors responsible for these waves. In the presence of interfaces between hard and soft formations, if the source is in the hard formation, 99% of the source energy propagates as tube waves. When the tube wave propagates through the interface, it not only looses speed, but also leaks energy to the formation because a soft formation confines energy less efficiently. This sudden drop of speed and loss of energy create a secondary shear wave source, strong enough to generate a shear wave that dominates the recorded primary waves. We have shown that this new shear wave is not of Mach wave origin.

Later arriving tube waves in the receiver well hydrophone data have been identified as due to a tube wave-converted shear wave, guided by a soft shale layer right beneath the oil-producing Kankakee limestone. Their energetic characteristic is caused by the fact that most of the dynamite explosion energy is trapped by the source borehole. A low percent conversion from source borehole tube wave to shear wave in a soft formation will result in significant shear-to-tube wave conversion at the receiver borehole. Since the shale layer has a shear wave velocity of 1000 m/s, a Mach wave phenomena may be responsible for the tube-to-shear wave conversion, as the tube wave speed is about 1200 m/s.

A mathematical model for Conoco's Downhole Orbital Vibrator is presented. The model incorporates the rotational effect of the forces radially exerted on the borehole

wall. The source is shown to be a 3-D source. It emits all three waves in an elastic medium: a P or *quasi-P* wave, a SV or *quasi-SV* wave, and a SH wave. Due to the rotation of applied forces on the wall, these three waves can be observed together on the horizontal component of the displacement. In an anisotropic medium, the *quasi-SV* and SH waves arrive at different times, thus presenting a potential for direct detection and measurement for the shear wave anisotropy of the formation. Drill-bit source can be easily modeled by the BEM technique, in isotropic or in TI media. The radiation pattern of a drill-bit is basically the same as that of a vertical force. In a hard and moderately hard formation, the effect of the borehole on the drill-bit radiation is negligible.

For future work, the BEM modeling technique in the thesis can be coupled with White's borehole coupling theory to model hydrophone data, both kinematically and dynamically. It may also be possible to extend the technique to model borehole sources in an azimuthally isotropic medium (TI medium with a horizontal axis of symmetry). For azimuthal isotropy, the important requirement on the axial symmetry of the formation is violated. Some of the theoretical developments and basic assumptions in this thesis no longer apply, such as the ring source results. However, for a monopole source on the borehole axis, the system still remains highly symmetric, which may lead to a simple algorithm.

In any event, the complexity associated with the wave phenomena in cross-well experiments is clearly demonstrated in the thesis. In order to fully understand and utilize the information carried by the data, detailed analysis of any cross-well recording should be a necessary step, *prior* to any kind of processing.

References

Abramowitz M. and I.A. Stegun, 1964, *Handbook of mathematical functions with formulas, graphs, and mathematical tables*: Dover, New York.

Aki, K. and P.G. Richards, 1980, *Quantitative Seismology*, W.H. Freeman and Co., New York.

Backus, G.E., 1962, Long-wave elastic anisotropy produced by horizontal layering: *J. Geophs. Res.*, **67**, 4427-4440.

Banerjee, P.K. and R. Butterfield, 1981, *Boundary element methods in engineering science*, McGraw-Hill Book Co. Ltd., London.

Ben-Menahem, A. and S.J. Singh, 1981, *Seismic Waves and Sources*, Springer-Verlag New York Inc., New York.

Ben-Menahem, A. and A.G. Sena, 1990. Seismic source theory in stratified anisotropic media, *J. Geophys. Res.*, **95**, 15,395-15,427.

Berryman, J.G., 1979, Long-wave elastic anisotropy in transversely isotropic media: *Geophysics*, **44**, 896-917.

Bleistein, N., 1984, *Mathematical methods for wave phenomena*: Academic Press, New York.

Bleistein, N. and R.A. Handelsman, 1975, *Asymptotic expansions of integrals*, Dover Publications, Inc., New York.

Bouchon, M., 1993. A numerical simulation of the acoustic and elastic wavefields radiated by a source in a fluid-filled borehole embedded in a layered medium: *Geophysics*, **58**, 475-481.

Bouchon, M. and K. Aki, 1977, Discrete wave-number representation seismic-source wave fields: *Bull. Seis. Soc. Am.*, **67**, 259-277.

Bouchon, M. and D.P. Schmitt, 1989, Full-wave acoustic logging in an irregular borehole: *Geophysics*, **54**, 758-765.

Brebbia, C.A. and J. Dominguez, 1989, Boundary elements: an introductory course, McGraw-Hill Inc., New York.

Buchwald, V.T., 1959. Elastic waves in anisotropic media, *Proc. R. Soc. London, Ser. A*, **253**, 563-580.

Cheng, C.H. and M.N. Toksöz, 1981, Elastic wave propagation in a fluid -filled borehole and synthetic acoustic logs: *Geophysics*, **46**, 1042-1053.

Chew, W.C., 1990, *Waves and Fields in Inhomogeneous Media*, Van Nostrand Reinhold, New York.

Cicerone, R.D., 1991, Detection and characterization of in-situ fractures in the Earth from vertical seismic profiling data: Ph.D thesis, MIT.

Cole, J.H., 1989, Downhole orbital seismic source: U.S. Patent No. 4,874,061.

Crampin, S., 1984, Effective anisotropic elastic-constants for wave propagation through a cracked solid, *in* Proc. of the First Internat. Workshop on Seismic Anisotropy, Crampin, S., Hipplin, R.G., and Chesnokov, E.M., eds: Geophys. J. Roy. Astr. Soc., **76**, 135-145.

Crampin, S., 1985. Evaluation of anisotropy by shear wave splitting, *Geophysics*, **50**, 383-411.

de Bruin, J. and W. Huizer, 1989, Radiation from waves in boreholes, *Scientific Drilling*, **1**, 3-10.

Dong, W., M. Bouchon, and M.N. Toksöz, 1992. Modeling downhole source radiation by boundary element and discrete wave number method, SEG Expanded Abstracts, 1337-1340.

Ellefsen, K.J., 1990, Elastic wave propagation along a borehole in an anisotropic medium: Ph.D thesis, MIT.

Fedorov, F.I., 1968. *Theory of Elastic Waves in Crystals*, Plenum, New York.

Fehler, M. and C. Pearson, 1981, Acoustic radiation patterns for borehole sources: *Trans., Soc. Prof. Well Log Anal.*, paper MM.

Fehler, M. and C. Pearson, 1984, Cross-hole seismic surveys: applications for studying subsurface fracture systems at a hot dry rock geothermal site, *Geophysics*, **49**, 37-45.

Gibson, R.L., 1993, Radiation from seismic sources in cased and cemented boreholes, *Geophysics*, in press.

Gibson, R.L. and M.N. Toksöz, 1990, Permeability estimation from velocity anisotropy in fractured rock, *J. Geophys. Res.*, **95**, 15643-15655.

Gilbert F., S.J. Laster, M.M. Backus, and R. Shell, 1962, Observation of pulses on an interface: *Bull. Seismo. Soc. of America*, **52**, No. 4, 847-868.

Greenfield, R.J., 1978, Seismic radiation from a point source on the surface of cylindrical cavity: *Geophysics*, **43**, 1071-1082.

Harris, J.M., 1988, Cross-well seismic measurements in sedimentary rocks: SEG Expanded Abstracts, 147-150.

Heelan, P.A., 1953, Radiation from a cylindrical source of finite length: *Geophysics*, **18**, 685-696.

Ingram, J., 1963, On the elastodynamic response of a fluid filled borehole: Presented at the 33rd Annual International SEG Meeting, in New Orleans.

Kawase, H., 1988, Time domain response of a semicircular canyon for incident SV, P, and Rayleigh waves calculated by the discrete wavenumber boundary element method: *Bull. Seism. Soc. Am.*, **79**, 1361-1382.

Kazi-Aoual, M.N., G. Bonnet, and P. Jouanna, 1988, Response of an infinite elastic transversely isotropic medium to a point force. An analytical solution in Hankel space, *Geophys. J.*, **93**, 587-590.

Kennet, B.L.N., 1983, *Seismic Wave Propagation in Stratified Media*, Cambridge University Press, Cambridge.

Kong, J.A., 1990, *Electromagnetic Wave Theory*, John Wiley & Sons, Inc., New York.

Krohn, C.E., 1990, Cross-well continuity logging using seismic guided waves: 60th Ann. Internat. Mtg., SEG Expanded Abstracts, 43-46.

Kupradze, V.D., 1963, *Dynamical Problems in Elasticity*, Volume III in PROGRESS IN SOLID MECHANICS, North-Holland, Amsterdam.

Kupradze, V.D., 1979, *The Three-Dimensional Problems of the Mathematical Theory of Elasticity and Thermoelasticity*, North-Holland, Amsterdam.

Kurkjian, A.L., H. Schmidt, T.L. Marzetta, J.E. White, and C. Chouzenoux, 1992, Numerical modeling of Cross-Well Seismic Monopole Sensor data: SEG Expanded Abstracts, New Orleans, 141-144.

Larner, K., 1993, Dip-moveout error in transversely isotropic media with linear velocity variation in depth: *Geophysics*, **58**, 1442-1453.

Larner, K. and J.K. Cohen, 1993, Migration error in transversely isotropic media with linear velocity variation in depth: *Geophysics*, **58**, 1454-1467.

Lee, M.W. and A.H. Balch, 1982, Theoretical seismic wave radiation from a fluid-filled borehole: *Geophysics*, **47**, 1308-1314.

Lee, H.Y., 1991, Drillstring axial vibration and wave propagation in boreholes: Ph.D thesis, MIT.

Lee, J.M., 1990, In situ seismic anisotropy and its relationship to crack and rock fabrics: Ph.D thesis, Pennsylvania State University.

Lee S.W., J. Boersma, C.L. Law, and G.A. Deschamps, 1980, Singularity in Green's function and its numerical evaluation: *IEEE Transac. on Antennas and Communication*, Vol. AP-28, No. 3.

Levin, F.K., 1979, Seismic velocities in transversely isotropic media: *Geophysics*, **44**, 918-936.

Lines, L.R., K.R. Kelly, and J.H. Queen, 1992, Channel waves in cross-borehole data: *Geophysics*, **57**, 334-342.

Lo, T.W., K.B. Coyner, and M.N. Toksöz, 1986, Experimental determination of elastic anisotropy of Berea sandstone, Chicopee shale, and Chelmsford granite, *Geophysics*, **51**, 164-171.

Love, A.E.H., 1944, *A Treatise on the Mathematical Theory of Elasticity* (4th edition). Dover, New York, N.Y., 643 pp.

Mandal, B., 1991, Reflection and transmission properties of elastic waves on a plane interface for general anisotropic media, *J. Acoust. Soc. Am.*, **90**, 1106-1118.

Mandal, B. and M.N. Toksöz, 1990, Computation of complete waveforms in general anisotropic media - Results from an explosion source in anisotropic medium, *Geophys. J. Int.*, **103**, 33-45.

Marzetta, T.L., 1992, Inverse borehole coupling theory and its application to hydrophone vertical seismic profiling: SEG Expanded Abstracts, 145-147.

McMechan, G.A., 1983, Seismic tomography in boreholes: *Geophys. J. Roy. Astr. Soc.*, **74**, 601-612.

Meredith, J.A., 1990, Numerical and analytical modeling of downhole seismic sources: the near and far field: Ph.D thesis, MIT.

Meredith, J.A., M.N. Toksöz, and C.H. Cheng, 1993, Secondary shear waves from source boreholes: *Geophysical Prospecting*, **41**, 287-312.

Morse, P. and H. Feshbach, 1953, *Methods of theoretical physics*, McGraw Hill.

Müller, G., 1985, The reflectivity method: A tutorial: *J. Geophys.*, **58**, 153-174.

Musgrave, M.J.P., 1954, On the propagation of elastic waves in aelotropic media, II, media of hexagonal symmetry, *Proc. R. Soc. London, Ser. A, 226*, 356-366.

Nur, A. and G. Simmons, 1969, Stress-induced velocity anisotropy in rock: An experimental study: *J. Geophs Res.*, **74**, 6667-6674.

Pan, Y.C. and T.W. Chou, 1976. Point source solution for an infinite transversely isotropic solid, *Transac. Amer. Soc. Mechan. Engineers*, December, 608-612.

Peng, C., M.N. Toksöz, and J.M. Lee, 1993, Pressure in fluid-filled borehole due to a source in stratified formation: SEG Expanded Abstracts, 321-324.

Postma, G.W., 1955, Wave propagation in a stratified medium: *Geophysics*, **20**, 780-806.

Pratt, R.G. and C.H. Chapman, 1992, Traveltime tomography in anisotropic media: application. *Geophysical Journal International*, **109**, 20-37.

Pratt, R.G. and N.R. Goulty, 1991, Combining wave-equation imaging with traveltime tomography to form high-resolution images from crosshole data: *Geophysics*, **56**, 208-224.

Randall, C.J., D.J. Scheibner, and P.T. Wu, 1991, Multipole borehole acoustic waveforms: Synthetic logs with beds and borehole washouts: *Geophysics*, **56**, 1757-1769.

Rector, J.W., 1990, Utilization of drill-bit vibrations as a downhole seismic source: Ph.D thesis, Stanford University.

Rector, J.W., B.P. Marion, and B. Widrow, 1988, Use of drill-bit energy as a downhole seismic source: SEG Expanded Abstracts, 161-164.

Riggs, E., 1955, Seismic wave types in a borehole: *Geophysics*, **20**, 53-67.

Robertson, J.D. and D. Corrigan, 1983, Radiation patterns of a shear-wave vibrator in near surface shale, *Geophysics*, **48**, 19-26.

Rutledge, J.T., J.N. Albright, W.S. Phillips, M.C. Fehler, and D.L. Howlett, 1992, Observation of Mach waves at the McKittrick oil field: SEG Expanded Abstracts, 151-154.

Saito, H., T. Takahashi, T. Imayoshi, and S. Sakashita, 1991, High resolution cross-hole seismic tomography at the Buckhorn Test Facility in Illinois, U.S.A., EAEG Meeting Abstracts, 154-155.

Saito, H., 1991, Anisotropic traveltime tomography at the Buckhorn Test Facility in Illinois: SEG Expanded Abstracts, 123-126.

Schmitt, D.P., 1989, Acoustic multipole logging in transversely isotropic poroelastic formations: *J. Acoust. Soc. Am.*, **86**, 2397-2421.

Schmitt, D.P. and M. Bouchon, 1985, Full-wave acoustic logging: Synthetic micro-seismograms and frequency-wavenumber analysis: *Geophysics*, **50**, 1756-1778.

Schoenberg, M., 1986, Fluid and solid motion in the neighborhood of a fluid-filled borehole due to the passage of a low-frequency elastic plane wave, *Geophysics*, **51**, 1191-1205.

Schoenberg, M., T. Marzetta, J. Aron, and R. Porter, 1981, Space-time dependence of acoustic waves in a borehole: *J. Acoust. Soc. Am.*, **70**, 1496-1507.

Sena, A.G., 1992, Elastic wave propagation in anisotropic media: source theory, traveltime computations and migration, Ph.D thesis, MIT.

Stephen, R.A., F. Cardo-Casas, and C.H. Cheng, 1985, Finite difference synthetic acoustic logs: *Geophysics*, **50**, 1588-1609.

Takahashi, T., H. Saito, and H. Shima, 1991, Field study on geophysical imaging techniques at the Buckhorn test facility in Illinois: SEG Expanded Abstracts, 460-463.

Takeuchi, H. and M. Saito, 1972, Seismic surface waves, in *Methods in Computational Physics*, Academic Press, New York, 11, 217-295.

Thomsen, L., Weak elastic anisotropy: *Geophysics*, **51**, 1954-1966.

Tongtaow, C., 1982, Wave propagation along a cylindrical borehole in a transversely isotropic formation: Ph.D thesis, Colorado School of Mines.

Track, A., Daube, F., and Oristaglio, F., 1992, 3-D cross-well simulations and applications: SEG Expanded Abstracts, New Orleans, 75-78.

Tsang, L. and D. Rader, 1979, Numerical evaluation of the transient acoustic waveform due to point source in a fluid-filled borehole: *Geophysics*, **44**, 1706-1720.

Tubman, K.M., C.H. Cheng, and M.N. Toksöz, 1984, Synthetic full-waveform acoustic logs in cased boreholes: *Geophysics*, **49**, 1051-1059.

Watson, G.N., 1944, *A Treatise on the Theory of Bessel Functions*, Cambridge Univ. Press, 2nd edition, 1966.

White, J.E., 1953, Signals in a borehole due to plane waves in the solid, *J. Acoust. Soc. Amer.*, **25**, 906-915.

White, J.E. and R.L. Sengbush, 1963, Shear waves from explosive sources: *Geophysics*, **28**, 1101-1019.

White, J.E., 1965, *Seismic waves, radiation, transmission and attenuation*, McGraw-Hill.

White, J.E. and C. Tongtaow, 1981, Cylindrical waves in transversely isotropic media: *J. Acous. Soc. Amer.*, **70**, No. 4, 1147-1155.

White, J.E., 1982, Computed waveforms in transversely isotropic media: *Geophysics*, **47**, 771-783.

White, J.E., 1983, *Underground sound: application of seismic waves*, Elsevier.

Winbow, G.A., 1991, Seismic sources in open and cased boreholes: *Geophysics*, **28**, 1001-1019.

Winterstein, D.R., 1986, Anisotropy effects in P-wave and SH-wave stacking velocities containing information on lithology, *Geophysics*, **51**, 661-672.

Winterstein, D.F. and B.N.P. Paulsson, 1990, Velocity anisotropy in shale determined from crosshole seismic and vertical seismic profile data: *Geophysics*, **55**, 470-479.

Yaghjian, A.D., 1980, Electric dyadic Green's functions in the source region: *Proceedings of the IEEE*, Vol. 68, No. 2.

Appendix A

Proof of Zero Integrals

In this appendix, we prove that integrating the second term in Equation 2.97 over a half elliptical surface results in zero. According to Equation 2.90 and Equation 2.91, we have

$$\begin{aligned} I &= \int dy\,dz \left(\frac{x-x'}{R_a D_a^2} - \frac{(x-x')(y-y')^2}{D_a^2 R_a^3} - \frac{2(x-x')(y-y')^2}{R_a^2 D_a^3} \right) \\ &= \frac{1}{\nu_a} \int_0^{\pi} \sin\theta d\theta \int_{-\pi/2}^{\pi/2} d\varphi \left(\frac{R_a^2}{D_a^2} - \frac{(y-y')^2}{D_a^2} - \frac{2R_a(y-y')^2}{D_a^3} \right) \\ &= \frac{1}{\nu_a} \int_0^{\pi} d\theta \int_{-\pi/2}^{\pi/2} d\varphi \left(\frac{\sin\theta}{(1+|\cos\theta|)^2} - \frac{\sin^3\theta \sin^2\varphi}{(1+|\cos\theta|)^2} - \frac{2\sin^3\theta\sin^2\varphi}{(1+|\cos\theta|)^3} \right) \\ &= \frac{\pi}{\nu_a} \int_0^{\pi} d\theta \left(\frac{\sin\theta}{(1+|\cos\theta|)^2} - \frac{\sin^3\theta}{2(1+|\cos\theta|)^2} - \frac{\sin^3\theta}{(1+|\cos\theta|)^3} \right). \end{aligned}$$

If we divide the θ integral into two regions, 0 to $\pi/2$ and $\pi/2$ to π, and combine the first and the third term, we obtain

$$\begin{aligned} I &= \frac{\pi}{\nu_a} \int_0^{\pi/2} \frac{\sin\theta\,\cos\theta}{(1+\cos\theta)^2} d\theta - \frac{\pi}{\nu_a} \int_{\pi/2}^{\pi} \frac{\sin\theta\,\cos\theta}{(1-\cos\theta)^2} d\theta \\ &\quad - \frac{\pi}{2\nu_a} \int_0^{\pi/2} \frac{\sin^3\theta}{(1+\cos\theta)^2} d\theta - \frac{\pi}{2\nu_a} \int_{\pi/2}^{\pi} \frac{\sin^3\theta}{(1-\cos\theta)^2} d\theta \\ &= \frac{2\pi}{\nu_a} \int_0^{\pi/2} \frac{\sin\theta\cos\theta}{(1+\cos\theta)^2} d\theta - \frac{\pi}{\nu_a} \int_0^{\pi/2} \frac{\sin^3\theta}{(1+\cos\theta)^2} d\theta \\ &\overset{\theta=2t}{=} -\frac{4\pi}{\nu_a} \int_0^{\pi/4} \frac{\sin^3 t}{\cos t} dt + \frac{2\pi}{\nu_a} \int_0^{\pi/4} \left(\frac{\sin t}{\cos t} - \frac{\sin^3 t}{\cos^3 t} \right) dt \end{aligned}$$

$$
\begin{aligned}
&= -\frac{4\pi}{\nu_a}[\cos^2 t/2 - \ln\cos t]_0^{\pi/4} + \frac{2\pi}{\nu_a}[-\ln\cos t]_0^{\pi/4} \\
&\quad -\frac{2\pi}{\nu_a}[\frac{1}{2\cos^2 t} + \ln\cos t]_0^{\pi/4} \\
&= 0.
\end{aligned}
$$

The same result is obtained for the fourth and fifth terms in Equation 2.97.

Appendix B

Other Green's Functions

The previous chapters have demonstrated the pivotal importance of the Green's functions in the integral formulations. The Green's functions are defined in an infinite homogeneous medium and they satisfy the Sommerfeld radiation conditions. This appendix presents a comprehensive and consistent derivation of the Green's functions for the acoustic wave equation, the electromagnetic wave equation, the elastic equilibrium equation, and the elastic wave equation. Properties that pertain to BEM implementation are described.

B.1 The Acoustic Green's Function

The acoustic wave equation with a point source of strength $V_0\delta(\mathbf{x}-\mathbf{x}')$ is

$$\nabla^2\phi(\mathbf{x},\mathbf{x}')+k_f^2\phi(\mathbf{x},\mathbf{x}')=V_0\delta(\mathbf{x}-\mathbf{x}'), \tag{B.1}$$

the solution is of the well known form

$$\phi(\mathbf{x},\mathbf{x}')=-V_0 g(\mathbf{x},\mathbf{x}')=-V_0\frac{e^{ik_f|\mathbf{x}-\mathbf{x}'|}}{4\pi|\mathbf{x}-\mathbf{x}'|}. \tag{B.2}$$

The above displacement potential has dimension m^2. Since delta function has dimension m^{-3}, source V_0 must have dimension m^3, which is a volume point source.

In the above $g(\mathbf{x},\mathbf{x}')$ denotes the scalar Green's function, having dimension m^{-1}. Displacement and pressure produced by this volume source are

$$\mathbf{u}(\mathbf{x},\mathbf{x}') = -V_0 \nabla g(\mathbf{x},\mathbf{x}') = -V_0 \nabla \left(\frac{e^{ik_f|\mathbf{x}-\mathbf{x}'|}}{4\pi|\mathbf{x}-\mathbf{x}'|} \right), \tag{B.3}$$

$$p(\mathbf{x},\mathbf{x}') = \lambda k_f^2 V_0 \frac{e^{ik_f|\mathbf{x}-\mathbf{x}'|}}{4\pi|\mathbf{x}-\mathbf{x}'|}. \tag{B.4}$$

The point source potential and pressure have first order singularities at $\mathbf{x} = \mathbf{x}'$. Integration of potential and pressure over a infinitesimal spherical surface around $\mathbf{x} = \mathbf{x}'$ approach zero as the surface shrinks to a point. Therefore, these singularities are removable. However, the point displacement involves a second order singularity due to the gradient of Green's function. Integration of the displacement over spherical surface centered at $\mathbf{x} = \mathbf{x}'$ approaches to a constant as the radius of the sphere tends to zero. As this constant plays a very important role in BEM algorithm, we derive it here. For a local spherical coordinates centered at $\mathbf{x}'$, the displacement vector is along radial direction for a point source at $\mathbf{x}'$. Integrating over a sphere surface of radius r, and as r approaches to zero, we have

$$\begin{aligned}
\lim_{r\to 0} \oint_S u_r dS &= -\lim_{r\to 0} \frac{V_0}{4\pi} \oint_S dS \hat{r} \cdot \nabla \left(\frac{e^{ik_f r}}{r} \right) \\
&= \lim_{r\to 0} -\frac{V_0}{4\pi} \int_0^{2\pi} d\varphi \int_0^{\pi} d\theta r^2 \sin\theta \frac{\partial}{\partial r} \left(\frac{e^{ik_f r}}{r} \right) \\
&= \lim_{r\to 0} -\frac{V_0}{4\pi} 4\pi [ik_f r e^{ik_f r} - e^{ik_f r}] \\
&= V_0.
\end{aligned} \tag{B.5}$$

B.2 Isotropic Electromagnetic Green's Functions

Shear wave propagation in elastic media is very similar to the electromagnetic wave propagation in dielectric media. Study of the electromagnetic Green's function will set the stage for the derivation of the dynamic elastic Green's function.

The three independent Maxwell's equations in frequency domain are

$$\nabla \times \mathbf{E} = i\omega\mu \mathbf{H}, \tag{B.6}$$

$$\nabla \times \mathbf{H} = \mathbf{J} - i\epsilon\omega\mathbf{E}, \tag{B.7}$$

$$\nabla \cdot \mathbf{J} = i\omega\rho. \tag{B.8}$$

The first equation expresses the Faraday's law, the second the Maxwell-Ampere law, and the third the equation of continuity. From these equations the magnetic and electric Gauss's laws are

$$\nabla \cdot \mathbf{H} = 0, \quad \nabla \cdot \mathbf{E} = \frac{\rho}{\epsilon}. \tag{B.9}$$

By eliminating $\mathbf{H}$ or $\mathbf{E}$ between Equation B.6 and Equation B.7, one obtains two inhomogeneous vector wave equations

$$\nabla \times \nabla \times \mathbf{E} - \omega^2\mu\epsilon\mathbf{E} = i\omega\mu\mathbf{J}, \tag{B.10}$$

$$\nabla \times \nabla \times \mathbf{H} - \omega^2\mu\epsilon\mathbf{H} = \nabla \times \mathbf{J}. \tag{B.11}$$

Using the method of potentials, we assume the electric field having the form

$$\mathbf{E} = \mathbf{A} - \nabla\psi, \tag{B.12}$$

where, $\mathbf{A}$ and ψ are vector and scalar potentials. Substitution of Equation B.12 into Equation B.10 yields

$$\nabla \times \nabla \times \mathbf{A} - \omega^2\mu\epsilon + \omega^2\mu\epsilon\nabla\psi = i\omega\mu\mathbf{J}. \tag{B.13}$$

Using the vector identity $\nabla \times \nabla \times \mathbf{A} = \nabla\nabla \cdot \mathbf{A} - \nabla^2\mathbf{A}$, and imposing a gauge condition

$$\nabla \cdot \mathbf{A} = -\omega^2\mu\epsilon\psi, \tag{B.14}$$

we obtatin

$$\nabla^2\mathbf{A} + \omega^2\mu\epsilon\mathbf{A} = -i\omega\mu\mathbf{J}. \tag{B.15}$$

From the gauge condition (B.14), equation (B.12), and the Gauss's law on electric field, another equation is obtained

$$\nabla^2\psi + \omega^2\mu\epsilon\psi = -\frac{\rho}{\epsilon}. \tag{B.16}$$

Thus, Maxwell's equations reduce to Equations B.15 and B.16. Once $\mathbf{A}$ and ψ are known, the electric and magnetic fields are readily available.

Equations B.15 and B.16 have the form of scalar wave equation, thus can be solved using the known Green's function for this equation. Applying the Green's theorem, we obtain

$$\mathbf{A} = i\omega\mu \int_{V_J} g(\mathbf{x}, \mathbf{x}')\mathbf{J}(\mathbf{x}')dV', \tag{B.17}$$

$$\psi = \frac{1}{\epsilon} \int_{V_\rho} g(\mathbf{x}, \mathbf{x}')\rho(\mathbf{x}')dV'. \tag{B.18}$$

Substitution of the continuity equation (B.8) to Equation B.18 yields

$$\psi = \frac{1}{i\omega\epsilon} \int_{V_J} g(\mathbf{x}, \mathbf{x}')\nabla \cdot \mathbf{J}(\mathbf{x}')dV'. \tag{B.19}$$

According to (B.12), (B.17), and (B.19), the elctric field for the EM wave is

$$\mathbf{E} = i\omega\mu \int_{V_J} \left[g(\mathbf{x}, \mathbf{x}')\mathbf{J}(\mathbf{x}') - \frac{1}{\omega^2\mu\epsilon} \nabla g(\mathbf{x}, \mathbf{x}')\nabla \cdot \mathbf{J}(\mathbf{x}') \right] dV'. \tag{B.20}$$

From (B.12) and (B.6), the magnetic field is

$$\mathbf{H} = \int_{V_J} \nabla \times [g(\mathbf{x}, \mathbf{x}')\mathbf{J}(\mathbf{x}')]dV' \tag{B.21}$$

Now, using the following vector identities,

$$\begin{aligned} \nabla g \nabla \cdot \mathbf{J} &= \nabla \cdot (\nabla g \mathbf{J}) - \nabla\nabla g \cdot \mathbf{J}, \\ (\nabla \times \mathbf{J})g &= \nabla \times (\mathbf{J}g) - \nabla g \times \mathbf{J}, \\ \nabla g \times \mathbf{J} &= (\nabla \times g\mathbf{I}) \cdot \mathbf{J}. \end{aligned}$$

and transforming the volume integral to surface integral for those having total differential form and noticing that surface integral vanishes due to the nature of volume source, we obtain

$$\mathbf{E} = i\omega\mu \int_{V_J} \left[g(\mathbf{x}, \mathbf{x}')\bar{\mathbf{I}} + \frac{1}{\omega^2\mu\epsilon} \nabla\nabla g(\mathbf{x}, \mathbf{x}') \right] \cdot \mathbf{J}(\mathbf{x}')dV'. \tag{B.22}$$

The magnetic field is

$$\mathbf{H} = -\int_{V_J} \nabla \times [g(\mathbf{x},\mathbf{x}')\bar{\mathbf{I}}] \cdot \mathbf{J}(\mathbf{x}')dV'. \tag{B.23}$$

Thus, the Green's functions for the electric and magnetic field for a given current source are

$$\overline{\mathbf{G}}_E(\mathbf{x},\mathbf{x}') = \left[g(\mathbf{x},\mathbf{x}')\bar{\mathbf{I}} + \frac{1}{\omega^2\mu\epsilon}\nabla\nabla g(\mathbf{x},\mathbf{x}')\right], \tag{B.24}$$

$$\overline{\mathbf{G}}_H(\mathbf{x},\mathbf{x}') = -\nabla \times [g(\mathbf{x},\mathbf{x}')\bar{\mathbf{I}}]. \tag{B.25}$$

One has to be careful when applying the electric Green's function. The problem lies in the undetermined nature of the volume integral involving the term $\nabla\nabla g$. Since this term contains a thrid order pole when the receiver point coincides with the source point, which renders the volume integral not well-defined. Two papers have devoted much attention to the explicit evaluation of the volume integral at the source region (Lee et al., 1980; Yaghjian, 1980). They found that the value of the volume integral at the source region depends on the shape of the exclusion volume chosen. For spheric cavity, the value is $\frac{1}{3}$ of the applied current. Thus, the complete electric Green's function has to include the source region contribution. For the magnetic Green's function, such problem does not appear because the second order pole is removable under the volume integral. The corresponding physics is that when the source and the receiver coincide, the wave propagation problem degenerates to a static problem, and steady charges emit electric field but not magnetic field.

For the elastic problem, fortunately, the singularities associated with $\nabla\nabla g_a$ and $\nabla\nabla g_b$ for the P and SV parts cancel out and leave a well defined Green's function, even in the source region. This is discussed in Section B.5.

B.3 Anisotropic Electromagnetic Green's Function

The electric field in an uniaxial anisotropic medium satisfies the following wave equation

$$\nabla \times \nabla \times \mathbf{E} - \omega^2 \epsilon_0 \mu_0 \begin{bmatrix} \epsilon & 0 & 0 \\ 0 & \epsilon & 0 \\ 0 & 0 & \epsilon_z \end{bmatrix} \cdot \begin{bmatrix} E_x \\ E_y \\ E_z \end{bmatrix} = i\omega\mu_0 \mathbf{J}. \tag{B.26}$$

Applying the identity $\nabla \times \nabla \times g = \nabla\nabla g - \nabla^2 g$, and following the derivation procedures for the anisotropic elastic case, we rewrite Equation B.26 as

$$\nabla_t \nabla_t \cdot \mathbf{E}_t - (\nabla^2 + k_0^2 \epsilon)\mathbf{E}_t + \nabla_t \frac{\partial E_z}{\partial z} = \mathbf{J}_t, \tag{B.27}$$

$$\partial_z \nabla_t \cdot \mathbf{E}_t - (\nabla_t^2 + k_0^2 \epsilon) E_z = J_z, \tag{B.28}$$

where, $k_0^2 = \omega^2 \mu_0 \epsilon_0$. Similarly, taking the transverse curl, transverse divergence, and the z-derivative, we have

$$(\nabla^2 + k_0^2 \epsilon)\nabla_t \times \mathbf{E}_t = -\nabla_t \times \mathbf{J}_t \tag{B.29}$$

$$\begin{bmatrix} (\partial_z^2 + k_0^2 \epsilon) & -\nabla_t^2 \\ -\partial_z^2 & (\nabla_t^2 + k_0^2 \epsilon_z) \end{bmatrix} \begin{bmatrix} \nabla_t \cdot \mathbf{E}_t \\ \partial_z E_t \end{bmatrix} = \begin{bmatrix} -\nabla_t \cdot \mathbf{J}_t \\ -\partial_z J_z \end{bmatrix}. \tag{B.30}$$

The solution for Equation B.29 corresponds to the so-called *ordinary* wave (Kong, 1990). Its electric field is always perpendicular to the optical axis (axis of symmetry). This ordinary EM wave in an uniaxial medium is similar to the SH wave in an anisotropic elastic medium.

Solution for Equation B.30 can be obtained following the extended Kupradze method used in Chapter 2. In $f-k$ domain, the scalar quantity ϕ is

$$\phi(k_z, k, \omega) = \frac{1}{k_0^2} \frac{1}{\epsilon_z k_z^2 + \epsilon k^2 - k_0^2 \epsilon \epsilon_z}. \tag{B.31}$$

The singularity in ϕ corresponds to the wavenumber of the so-called *extraordinary EM wave* (Kong, 1990). Evaluating the k_z integral, we obtain

$$\phi(r, z, \omega) = \frac{i}{4\pi k_0^2 \epsilon_z} \int_0^\infty \frac{k}{\nu_e} J_0(kD) e^{i\nu_e |z - z'|} dk, \tag{B.32}$$

where, $\nu_e = \sqrt{k_0^2\epsilon - k^2\epsilon/\epsilon_z}$, is the vertical wavenumber for the extraordinary EM wave.

In the end, the Green's function for EM waves in uniaxial media has the form

$$\overline{\mathbf{G}} = g\bar{\mathbf{I}} + \hat{z}\hat{z}(L_z\phi - g) + \partial_z(\nabla_t\hat{z} + \hat{z}\nabla_t)\phi + \frac{\nabla_t\nabla_t}{\nabla_t^2}(L_t\phi - g), \tag{B.33}$$

where,

$$L_z = (\partial_z^2 + k_0^2\epsilon), \tag{B.34}$$

$$L_t = (\nabla_t^2 + k_0^2\epsilon_z), \tag{B.35}$$

$$g = \frac{i}{4\pi}\int_0^\infty \frac{e^{i\nu_o|z-z'|}}{\nu_o} kJ_0(kD)dk. \tag{B.36}$$

Removing the inverse Laplacian by the procedures used in Chapter 2, one has

$$\overline{\mathbf{G}} = g\bar{\mathbf{I}} + \hat{z}\hat{z}(L_z\phi - g) + \partial_z(\nabla_t\hat{z} + \hat{z}\nabla_t)\phi + \nabla_t\nabla_t\psi, \tag{B.37}$$

where,

$$\psi = \frac{i}{4\pi k_0^2\epsilon}\int_0^\infty \left[-\frac{\nu_e}{k^2}e^{i\nu_e|z-z'|} + \frac{k_0^2\epsilon}{k^2\nu_o}e^{i\nu_o|z-z'|}\right] kJ_0(kD)dk. \tag{B.38}$$

Equation B.37 is the final form of the Green's function for the electric field in an uniaxial medium. One can easily verify that, in the isotropic limit, $\epsilon = \epsilon_z$ and $\nu_o = \nu_e$, the isotropic Green's function of previous section is recovered. The aforementioned singularity problem still applies to the anisotropic EM Green's function.

B.4 Isotropic Elastic Green's Function: Static

The equilibrium equation in a homogeneous isotropic medium is

$$\mu\nabla^2\mathbf{U} + (\lambda + \mu)\nabla\nabla\cdot\mathbf{U} + \mathbf{F} = 0. \tag{B.39}$$

It can be rewritten as

$$\nabla^2\mathbf{U} = -\frac{\mathbf{F}}{\mu} - \frac{\lambda + \mu}{\mu}\nabla\nabla\cdot\mathbf{U}. \tag{B.40}$$

Taking the divergence on both sides of equation B.40, we have

$$(\lambda + 2\mu)\nabla^2 \nabla \cdot \mathbf{U} = -\nabla \cdot \mathbf{F}. \tag{B.41}$$

Then, applying the Green's theorem, we obtain

$$\nabla \cdot \mathbf{U} = \frac{1}{\lambda + 2\mu} \int_{V_z} \frac{1}{4\pi R(\mathbf{x}, \mathbf{z})} \nabla_z \cdot \mathbf{F}(\mathbf{z}) dV_z, \tag{B.42}$$

where,

$$R(\mathbf{x}, \mathbf{z}) = |\mathbf{x} - \mathbf{z}| = \sqrt{(x_1 - z_1)^2 + (x_2 - z_2)^2 + (x_3 - z_3)^2}. \tag{B.43}$$

Then,

$$\begin{aligned} \nabla\nabla \cdot \mathbf{U} &= \frac{1}{\lambda + 2\mu} \nabla_x \int_{V_z} \frac{1}{4\pi R(\mathbf{x}, \mathbf{z})} \nabla_z \cdot \mathbf{F}(\mathbf{z}) dV_z \\ &= \frac{1}{4\pi(\lambda + 2\mu)} \int_{V_z} \nabla_x \frac{1}{R(\mathbf{x}, \mathbf{z})} \nabla_z \cdot \mathbf{F}(\mathbf{z}) dV_z. \end{aligned} \tag{B.44}$$

Using Love's equality (Love, 1944)

$$\nabla_x \frac{1}{R(\mathbf{x}, \mathbf{z})} = \frac{1}{2} \nabla_x^2 (\nabla_x R), \tag{B.45}$$

we have

$$\nabla\nabla \cdot \mathbf{U} = \frac{1}{8\pi(\lambda + 2\mu)} \nabla_x^2 \int_{V_z} \nabla_x R(\mathbf{x}, \mathbf{z}) \nabla_z \cdot \mathbf{F}(\mathbf{z}) dV_z. \tag{B.46}$$

Now, substituting equation B.46 into B.40 and moving the second term to the left of equation B.40, we obtain

$$\nabla^2 \left[\mathbf{U} + \frac{\lambda + \mu}{8\pi\mu(\lambda + 2\mu)} \int_{V_z} \nabla_x R(\mathbf{x}, \mathbf{z}) \nabla_z \cdot \mathbf{F}(\mathbf{z}) dV_z \right] = -\frac{\mathbf{F}}{\mu}. \tag{B.47}$$

The above is just the Possion's equation. Applying Green's theorem again to Possion's equation yields

$$\mathbf{U} = \frac{1}{4\pi\mu} \int_{V_z} \frac{\mathbf{F}}{R(\mathbf{x}, \mathbf{z})} dV_z + \frac{\lambda + \mu}{8\pi\mu(\lambda + 2\mu)} \int_{V_z} \nabla_z R(\mathbf{x}, \mathbf{z}) \nabla_z \cdot \mathbf{F}(\mathbf{z}) dV_z. \tag{B.48}$$

In the above, $\nabla_x = -\nabla_z$ is used. Using the vector identity

$$[\nabla_z \cdot \mathbf{F}(\mathbf{z})] \nabla_z R(\mathbf{x}, \mathbf{z}) = \nabla \cdot [\mathbf{F}(\mathbf{z}) \nabla_z R(\mathbf{x}, \mathbf{z})] - \mathbf{F}(\mathbf{z}) \cdot \nabla_z \nabla_z R(\mathbf{x}, \mathbf{z}), \tag{B.49}$$

and the Gauss's theorem on the divergence part, which is zero because of the volume source, we then have

$$\int_{V_z} \nabla_z \cdot \mathbf{F}(\mathbf{z}) \nabla_z R(\mathbf{x},\mathbf{z}) dV_z = -\int_{V_z} \mathbf{F}(\mathbf{z}) \cdot \nabla_z \nabla_z R(\mathbf{x},\mathbf{z}) dV_z. \tag{B.50}$$

The integrand of the above integral can be rewritten

$$\begin{aligned} \nabla_z \nabla_z R(\mathbf{x},\mathbf{z}) &= \nabla_z \left[-\frac{(x_1 - z_1)\hat{x} + (x_2 - z_2)\hat{y} + (x_3 - z_3)\hat{z}}{R(\mathbf{x},\mathbf{z})} \right] \\ &= \frac{\bar{\mathbf{I}}}{R(\mathbf{x},\mathbf{z})} - \frac{\nabla R \nabla R}{R(\mathbf{x},\mathbf{z})}. \end{aligned} \tag{B.51}$$

Thus, we obtain

$$\begin{aligned} \mathbf{U}(\mathbf{x}) &= \frac{1}{4\pi\mu} \int_{V_z} \frac{\mathbf{F}(\mathbf{z})}{R(\mathbf{x},\mathbf{z})} dV_z + \frac{\lambda+\mu}{8\pi\mu(\lambda+2\mu)} \int_{V_z} \mathbf{F}(\mathbf{z}) \cdot \left[\frac{\bar{\mathbf{I}}}{R(\mathbf{x},\mathbf{z})} - \frac{\nabla R \nabla R}{R(\mathbf{x},\mathbf{z})} dV_z \right] \\ &= \int_{V_z} \left[\frac{\lambda+3\mu}{8\pi\mu(\lambda+2\mu)} \bar{\mathbf{I}} + \frac{\lambda+\mu}{8\pi\mu(\lambda+2\mu)} \nabla R \nabla R \right] \frac{1}{R(\mathbf{x},\mathbf{z})} \cdot \mathbf{F}(\mathbf{z}) dV_z. \end{aligned} \tag{B.52}$$

This is the Green's theorem for the equilibrium equation of a homogeneous isotropic medium. Therefore, the static Green's function for the isotropic elastic medium is

$$\overline{\mathbf{G}} = \frac{1}{8\pi\mu(\lambda+2\mu)} \left[(\lambda+3\mu)\bar{\mathbf{I}} + (\lambda+\mu)\nabla R \nabla R \right] \frac{1}{R(\mathbf{x},\mathbf{z})}. \tag{B.53}$$

B.5 Isotropic Elastic Green's Function: Dynamic

For infinite homogeneous isotropic elastic medium, the well-known Navier equation is

$$(\lambda+2\mu)\nabla\nabla\cdot\mathbf{u} - \mu\nabla\times\nabla\times\mathbf{u} + \rho\omega^2\mathbf{u} + \mathbf{F} = 0, \tag{B.54}$$

where, λ and μ are the Lamé constants. F is an external body force of dimension N/m^3. The solution of the Navier equation was first given by Stokes and later generalized by Love for a concentrated force. Textbooks on elastic wave theory (e.g. Aki and Richard, 1980; Ben-Menahem and Singh, 1981) presented the solution based on vector, scalar and force potentials. Due to the importance of the solution, and

in order to avoid repeating, we derive the solution using a different but a simpler approach.

Assume

$$\mathbf{u} = \mathbf{A} - \nabla\phi, \tag{B.55}$$

where, A is an arbitrary vector and ϕ an arbitrary scalar. Substitution of (B.55) into (B.54) yields

$$(\lambda + 2\mu)\nabla\nabla \cdot \mathbf{A} - (\lambda + 2\mu)\nabla\nabla^2\phi - \mu\nabla \times \nabla \times \mathbf{A} + \mathbf{F} = -\rho\omega^2\mathbf{A} + \rho\omega^2\nabla\phi. \tag{B.56}$$

Using the gauge condition

$$\nabla \cdot \mathbf{A} = \nabla^2\phi + k_\alpha^2\phi, \tag{B.57}$$

we obtain from (B.56)

$$\nabla \times \nabla \times \mathbf{A} - k_\beta^2\mathbf{A} = \frac{1}{\beta^2}\mathbf{F}, \tag{B.58}$$

where, k_α and k_β are wave numbers for dilatational (P) and shear waves (S), with $\alpha = \sqrt{(\lambda + 2\mu)/\rho}$ and $\beta = \sqrt{\mu/\rho}$ being the P-wave and S-wave velocity. From (B.55) and (B.57), we obtain

$$\nabla \cdot \mathbf{u} = k_\alpha^2\phi. \tag{B.59}$$

Upon substituting (B.59) into the resultant equation of taking the divergence of (B.54), we have

$$\nabla^2\phi + k_\alpha^2\phi = -\frac{1}{\rho\omega^2}\nabla \cdot \mathbf{F}. \tag{B.60}$$

Therefore, in solving Equation B.54 we are in fact solving equations (B.58) and (B.60). Equation B.60 is the familiar scalar wave equation governing pressure wave propagation in fluid. Its source term states that only the divergent part of force $\mathbf{F}$ excites dilatational waves. Equation B.58 governs the propagation of shear waves. It says that any given force produces shear waves. This equation is exactly the same as the equation governing electromagnetic wave propagation in electromagnetic wave theory (see Section B.2). Its solution is

$$\mathbf{A} = \frac{1}{\rho\omega^2}\int_V d^3\mathbf{x}'[k_\beta^2\bar{\mathbf{I}} + \nabla\nabla]g_\beta(\mathbf{x}, \mathbf{x}') \cdot \mathbf{F}(\mathbf{x}'), \tag{B.61}$$

where, g_β is the scalar Green's function satisfying scalar wave equation with shear wave number k_β. Solution to (B.60) is

$$\begin{aligned}\phi(\mathbf{x}) &= \frac{1}{\rho\omega^2}\int_V d^3\mathbf{x}' g_\alpha(\mathbf{x},\mathbf{x}')\nabla'\cdot\mathbf{F} \\ &= \frac{1}{\rho\omega^2}\int_V d^3\mathbf{x}'\nabla g_\alpha(\mathbf{x},\mathbf{x}')\cdot\mathbf{F}(\mathbf{x}'). \end{aligned} \tag{B.62}$$

Here g_α is the dilatational scalar Green's function. In the second equation of (B.62), we used integration by parts and the facts that $\nabla g_\alpha = -\nabla' g_\alpha$ and $\mathbf{F}(\mathbf{x}')$ is only supported in V. Then solution to the Navier equation is, according to (B.55),

$$\mathbf{u} = \frac{1}{\rho\omega^2}\int_V d^3\mathbf{x}'[k_\beta^2\bar{\mathbf{I}}g_\beta(\mathbf{x},\mathbf{x}') + \nabla\nabla[g_\beta(\mathbf{x},\mathbf{x}') - g_\alpha(\mathbf{x},\mathbf{x}')]\cdot\mathbf{F}(\mathbf{x}'). \tag{B.63}$$

The above is the Green superposition theorem, the integrand is the Green's dyadic or Green's tensor

$$\overline{\mathbf{G}}(\mathbf{x},\mathbf{x}') = \frac{1}{\rho\omega^2}\left\{k_\beta^2\bar{\mathbf{I}}g_\beta(\mathbf{x},\mathbf{x}') + \nabla\nabla\left[g_\beta(\mathbf{x},\mathbf{x}') - g_\alpha(\mathbf{x},\mathbf{x}')\right]\right\}. \tag{B.64}$$

We see that Green's function for elastic medium is a second rank tensor or matrix operator. Given point force $\mathbf{F} = \hat{a}\delta(\mathbf{x}-\mathbf{x}')$, the resultant displacement is

$$\mathbf{u}(\mathbf{x}) = \overline{\mathbf{G}}\cdot\hat{a} = \frac{1}{\rho\omega^2}[k_\beta^2 g_\beta\hat{a} + \nabla\nabla(g_\beta - g_\alpha)\cdot\hat{a}]. \tag{B.65}$$

The stress dyadic can be obtained by substituing (B.63) into stress and displacement relation. Upon using the two scalar wave equations for g_β and g_α to simplify the resultant equation, we have

$$\overline{\mathbf{T}} = \frac{\lambda}{\lambda+2\mu}\bar{\mathbf{I}}\frac{\partial}{\partial a}g_\alpha + [\nabla g_\beta\hat{a} + g_\beta\hat{a}\nabla] + \frac{\mu}{\rho\omega^2}\nabla[\nabla\frac{\partial}{\partial a}(g_\beta - g_\alpha) + \frac{\partial}{\partial a}(g_\beta - g_\alpha)\nabla]. \tag{B.66}$$

Then, stress along direction $\hat{c}$ at a surface whose normal is $\hat{b}$, with a concentrated force at $\mathbf{x}'$ applied in direction $\hat{a}$, T_{bc} is

$$\begin{aligned} T_{bc} &= \hat{c}^t\cdot\overline{\mathbf{T}}\cdot\hat{b} \\ &= \hat{c}\cdot\hat{b}\frac{\lambda}{\lambda+2\mu}\frac{\partial g_\alpha}{\partial a} + \hat{a}\cdot\hat{b}\frac{\partial g_\beta}{\partial c} + \hat{c}\cdot\hat{a}\frac{\partial g_\beta}{\partial b} + \frac{2\mu}{\rho\omega^2}\frac{\partial}{\partial c}\frac{\partial}{\partial b}\frac{\partial}{\partial a}(g_\alpha - g_\beta). \end{aligned} \tag{B.67}$$

If a, b and c are chosen as three mutually perpendicular coordinates, then, stress along direction $\hat{a}$ at a surface whose normal is $\hat{a}$, with a concentrated force at $\mathbf{x}'$ applied in direction $\hat{a}$, T_{aa}, is

$$T_{aa} = \frac{\partial g_\alpha}{\partial a} - \frac{\partial}{\partial a}\left(\frac{\partial^2}{\partial b^2} + \frac{\partial^2}{\partial c^2}\right)(g_\alpha - g_\beta). \tag{B.68}$$

Stress at point $\mathbf{x}$ along direction $\hat{a}$ on a surface whose normal is in $\hat{b}$ direction, with a concentrated force applied at $\mathbf{x}'$ in direction $\hat{a}$, T_{ba}, is

$$T_{ba} = \frac{\partial g_\beta}{\partial b} + \frac{2\mu}{\omega^2}\frac{\partial}{\partial b}\left(\frac{\partial^2}{\partial a^2}(g_\beta - g_\alpha)\right). \tag{B.69}$$

Stress in $\hat{c}$ with surface normal in $\hat{b}$ and force applied in $\hat{a}$ is

$$T_{bc} = \frac{2\mu}{\omega^2}\frac{\partial}{\partial c}\frac{\partial}{\partial b}\frac{\partial}{\partial a}(g_\beta - g_\alpha). \tag{B.70}$$

It can be shown that the Green's dyadic displacement has a first order singularity as $r \to 0$. Therefore, integration of it over a small half spherical surface in the limit $r \to 0$ is zero. However, the stress dyadic has a second order singularity. Integrating the above three stresses over a small half spherical surface centered at source point $\mathbf{x}'$, and by noticing that the second parts of (B.68) and (B.69) and right part of (B.70) do not contribute to the integral because integration over angle results zero, and in the limit that radius of this spherical surface goes to zero, we obtain

$$T_{aa} = -\frac{1}{2}; \quad T_{ba} = -\frac{1}{2}; \quad T_{bc} = 0; \tag{B.71}$$

Physically, these values result from static force balance at the source point because in the limit of observation point at source point the dynamic problem degenerates to static problem.

Appendix C

Rigorous Description of the Boundary Element Method in Borehole Environment

The boundary element method (BEM) has been thoroughly discussed by many authors (e.g., Banerjee and Butterfield, 1981; Brebbia and Dominguez, 1989; Chew, 1990). In this appendix, following a rigorous mathematical development of the direct BEM formulation in borehole fluid and in the elastic solid, the corresponding indirect formulation of boundary integral equations is derived. The indirect formulations are used in the BEM implementation for the fluid inside a borehole and the solid formation outside. The direct and indirect formulations are shown to be equivalent.

C.1 Boundary Integrals for the Fluid

C.1.1 The direct formulation

Waves in an incompressible and non-viscous fluid satisfy the scalar Helmholtz wave equation in terms of displacement potential (unit=m^2), $\phi(\mathbf{x},\omega)$. i.e.

$$\nabla^2\phi(\mathbf{x},\omega) + k_f^2\phi(\mathbf{x},\omega) = -S(\mathbf{x},\omega), \tag{C.1}$$

where, $k_f^2 = \omega^2/c^2$ and $S(\mathbf{x},\omega)$ is source signature (dimensionless) and c the sound speed in the fluid. Displacement vector and pressure field in the fluid are given by

$$\mathbf{u}(\mathbf{x},\omega) = \nabla\phi(\mathbf{x},\omega), \quad p(\mathbf{x},\omega) = -\lambda\nabla^2\phi(\mathbf{x},\omega), \tag{C.2}$$

where, $\lambda = \rho_f c^2$ is the bulk modulus of the fluid and ρ_f density of the fluid.

Assume without loss of generality that borehole fluid is separated by the borehole wall from another fluid instead of an elastic medium. The total displacement potential inside the borehole (subscript 1) and outside the borehole (subscript 2) satisfy (frequency dependence is omitted from now on)

$$(\nabla^2 + k_{f1}^2)\phi_1(\mathbf{x}) = -S(\mathbf{x}), \tag{C.3}$$

$$(\nabla^2 + k_{f2}^2)\phi_2(\mathbf{x}) = 0. \tag{C.4}$$

We consider two auxiliary displacement potential density functions (dimension = m^{-1}) satisfying the following equations:

$$(\nabla^2 + k_{f1}^2)g_1(\mathbf{x},\mathbf{x}') = -\delta(\mathbf{x}-\mathbf{x}'), \tag{C.5}$$

$$(\nabla^2 + k_{f2}^2)g_2(\mathbf{x},\mathbf{x}') = -\delta(\mathbf{x}-\mathbf{x}'). \tag{C.6}$$

In the above equations, delta functions have dimension m^{-3}. On multiplying Equation C.3 by $g_1(\mathbf{x},\mathbf{x}')$ and Equation C.5 by $\phi_1(\mathbf{x})$, substracting the two resultant equations, intgerating over borehole fluid volume, V_b, and applying Gauss' theorem by

recognizing $\nabla \cdot (g\nabla\phi - \phi\nabla g) = g\nabla^2\phi - \phi\nabla^2 g$, we have the following equation

$$\int_B dS\hat{n} \cdot [g_1(\mathbf{x},\mathbf{x}')\nabla\phi_1(\mathbf{x}) - \phi_1(\mathbf{x})\nabla g_1(\mathbf{x},\mathbf{x}')] = -\int_{V_b} dV g_1(\mathbf{x},\mathbf{x}')S(\mathbf{x}) + \gamma_1(\mathbf{x}')\phi_1(\mathbf{x}'). \tag{C.7}$$

The parameter function γ_1 depends on the position of $\mathbf{x}'$ and has the following form

$$\gamma_1(\mathbf{x}') = \begin{cases} 1 & \text{if } \mathbf{x}' \in V_b, \\ 0.5 & \text{if } \mathbf{x}' \in B \text{ except corners}, \\ 0 & \text{if } \mathbf{x}' \notin V_b + B\ . \end{cases} \tag{C.8}$$

The volume integral in (C.7) is the incident field generated by source and is denoted by ϕ_i. Upon changing the role of source position $\mathbf{x}'$ and receiver position $\mathbf{x}$, Equation C.7 becomes

$$\gamma_1(\mathbf{x})\phi_1(\mathbf{x}) = \phi_i + \int_B dS'\hat{n}' \cdot [g_1(\mathbf{x}',\mathbf{x})\nabla'\phi_1(\mathbf{x}') - \phi_1(\mathbf{x}')\nabla' g_1(\mathbf{x}',\mathbf{x})]. \tag{C.9}$$

The above is the mathematical statement of Huygen's principle. It says that if a receiver is inside a borehole ($\mathbf{x} \in V_b$), the total displacement potential received is the sum of the incident potential (ϕ_i) and the potentials generated by surface sources ($\hat{n}' \cdot \nabla'\phi_1(\mathbf{x}')$ and $\phi_1(\mathbf{x}')$) on S. If the receiver is outside the borehole, the total potential is zero or the potential generated by surface sources exactly cancels out the incident potential. If the receiver is on the borehole wall, the total potential is twice the sum of the incident and the secondary potentials.

Following the same line as above, but noticing the surface normal direction change, we have for the fluid outside the borehole

$$\gamma_2(\mathbf{x})\phi_2(\mathbf{x}) = -\int_{B+S_\infty} dS'\hat{n}' \cdot [g_2(\mathbf{x}',\mathbf{x})\nabla'\phi_2(\mathbf{x}') - \phi_2(\mathbf{x}')\nabla' g_2(\mathbf{x}',\mathbf{x})], \tag{C.10}$$

here,

$$\gamma_2(\mathbf{x}) = \begin{cases} 0 & \text{if } \mathbf{x} \in V_b\ , \\ 0.5 & \text{if } \mathbf{x} \in B \text{ except corners}, \\ 1 & \text{if } \mathbf{x} \notin V_b + B\ . \end{cases} \tag{C.11}$$

S_∞ refers to the surface enclosing the fluid at infinity. Although boundary conditions of the two auxiliary equations (C.5) and (C.6) are at our disposal, the Sommerfeld radiation condition (boundary condition at infinity) is used to eliminate the surface integral over S_∞. The solutions of (C.5) and (C.6) then are the unbounded, homogeneous medium scalar Green's functions. Symmetry of the Green's functions can be used. Thus, Equation C.10 becomes

$$\gamma_2(\mathbf{x})\phi_2(\mathbf{x}) = -\int_B dS'\hat{n}' \cdot [g_2(\mathbf{x},\mathbf{x}')\nabla'\phi_2(\mathbf{x}') - \phi_2(\mathbf{x}')\nabla' g_2(\mathbf{x},\mathbf{x}')]. \qquad \text{(C.12)}$$

Equations (C.9) and (C.12) yield two boundary integral equations of the second kind for $\mathbf{x} \in B$,

$$\phi_i = 0.5\,\phi_1(\mathbf{x}) - \int_B dS'\hat{n}' \cdot [g_1(\mathbf{x},\mathbf{x}')\nabla'\phi_1(\mathbf{x}') - \phi_1(\mathbf{x}')\nabla' g_1(\mathbf{x},\mathbf{x}')], \qquad \text{(C.13)}$$

$$0 = 0.5\,\phi_2(\mathbf{x}) + \int_B dS'\hat{n}' \cdot [g_2(\mathbf{x},\mathbf{x}')\nabla'\phi_2(\mathbf{x}') - \phi_2(\mathbf{x}')\nabla' g_2(\mathbf{x},\mathbf{x}')], \qquad \text{(C.14)}$$

which can be solved for the two unknown sources, $\hat{n}' \cdot \nabla'\phi_1(\mathbf{x}')$ and $\phi_1(\mathbf{x}')$, with the help of two boundary conditions for $\mathbf{x} \in B$

$$\rho_{f1}\phi_1(\mathbf{x}) = \rho_{f2}\phi_2(\mathbf{x}), \qquad \text{(C.15)}$$

$$\hat{n} \cdot \nabla\phi_1(\mathbf{x}) = \hat{n} \cdot \nabla\phi_2(\mathbf{x}). \qquad \text{(C.16)}$$

The above system of integral equations can only be solved by discretizing the boundary surface or the borehole wall. A system of linear equations are then solved to obtain unknowns at every element. After determining $\hat{n} \cdot \nabla\phi_1(\mathbf{x})$ and $\phi_1(\mathbf{x})$ and substituting them into (C.9), displacement potential inside the borehole can be calculated at every point. Since we solve for ϕ_1 and $\nabla\phi_1$ on the boundary explicitly, this method is termed *direct formulation* of BEM.

C.1.2 The indirect formulation

The direct formulation requires simultaneous treatment of the fluids inside and outside the borehole. Two Green's functions and their gradients are required to calculate

the potential inside the borehole. Although mathematically rigorous and obvious, this approach demands extra work when digitized on a computer. However, a more physically intuitive and computational simple approach can be obtained with equal mathematical rigor. This approach is termed *indirect formulation* of BEM.

Since the region of our present interest is the fluid volume inside borehole, we cannot care less about what kind of fluid (or elastic medium) there is outside the region of our interest as long as the effect of the outside fluid (or elastic medium) is reflected on the boundary of the region (borehole wall). Therefore, we can replace the fluid outside the borehole by the fluid inside and shift the influence of the outside fluid to the borehole wall. Then, we obtain from Equation C.12

$$\gamma_2(\mathbf{x})\phi_2(\mathbf{x}) = -\int_B dS' \hat{n} \cdot [g_1(\mathbf{x},\mathbf{x}')\nabla'\phi_2(\mathbf{x}') - \phi_2(\mathbf{x}')\nabla' g_1(\mathbf{x},\mathbf{x}')]. \tag{C.17}$$

If $\phi_2(\mathbf{x})$ is specified to be the solution that, in the region outside the borehole, produces on B exactly the same boundary displacement potentials as those inside the borehole, i.e. $\phi_2(\mathbf{x}) = \phi_1(\mathbf{x})$ for $\mathbf{x} \in B$, then substituting $\phi_2(\mathbf{x})$ by $\phi_1(\mathbf{x})$ in equation (above) and adding it to Equation C.9 yields

$$\phi_1(\mathbf{x}) = \phi_i + \int_B dS' g_1(\mathbf{x},\mathbf{x}')\psi(\mathbf{x}'); \quad \text{for } \mathbf{x} \in V_b + B, \tag{C.18}$$

where, $\psi(\mathbf{x}') = \hat{n} \cdot [\nabla'\phi_1(\mathbf{x}') - \nabla'\phi_2(\mathbf{x}')]$. This equation says that the displacement potential inside the borehole is the sum of the incident potential and the potential due to a fictitious source distribution. The sources are fictitious because no physical meaning can be attached to $\psi(\mathbf{x}')$). Notice the above equation is valid on the borehole wall as well as inside the borehole. Uniqueness of $\phi_1(\mathbf{x})$ is guaranteed because $\phi_1(\mathbf{x})$ not only satisfies the scalar wave equation in the region of interest but also the boundary conditions (i.e. the continuity of potential and difference in normal derivative is offset by surface sources). Thus, once the fictitious source distributions are determined, displacement potential everywhere inside the borehole and on its wall is obtained by the above equation. It is also clear that only the Green's function for the borehole fluid is involved in Equation C.18.

Although we presented in this section the boundary integral equations by considering two fluid regions, the fundamental idea is the same for fluid and elastic medium contact problem. In fact, the indirect formulation remains the same as we can attribute the effect of an elastic medium into fictitious sources on the boundary. In the following section, the direct and indirect formulation for elastic medium is presented.

C.2 Boundary Integrals for the Elastic Medium

The derivation of direct and indirect formulations for elastic medium is very similar to that of fluid. However, we are now dealing with vector wave equation, instead of scalar equation. To present the solution of this vector equation either index notation or dyadic notation has to be used. We choose the dyadic notation for its conciseness. A dyadic is defined as the *algebraic product* of two vectors as opposite to scalar and vector product. Therefore, given vector $\mathbf{A}$ and vector $\mathbf{B}$, $\mathbf{AB}$ and $\mathbf{BA}$ are dyadics. A dyadic is in fact a second ranked tensor, comparing to a vector from cross product and a scalar from a dot product. Hence, elastic stress and strain tensors can be denoted by dyadic symbols.

C.2.1 The direct formulation

Wave propagation in a general elastic medium absent of source is governed by the vector wave equation

$$\nabla \cdot \overline{\mathbf{T}}(\mathbf{u}) + \rho\omega^2\mathbf{u}(\mathbf{x}) = 0, \tag{C.19}$$

where, $\overline{\mathbf{T}}(\mathbf{u})$ is the stress dyadic and $\mathbf{u}$ is the displacement vector. The stress dyadic and the displacement vector are related through Hooke's law and strain-dispacement relation.

We now assume that two different elastic solids, instead of two fluids as in previous section, occupy the inner borehole and outer borehole regions (denoted as 1 and 2) separated by the borehole wall. Assume no source is present in both regions. Total

displacement fields inside and outside the borehole satisfy

$$\nabla \cdot \overline{\mathbf{T}}_1(\mathbf{u}_1) + \rho_1 \omega^2 \mathbf{u}_1(\mathbf{x}) = 0, \tag{C.20}$$

$$\nabla \cdot \overline{\mathbf{T}}_2(\mathbf{u}_2) + \rho_2 \omega^2 \mathbf{u}_2(\mathbf{x}) = 0. \tag{C.21}$$

We also consider two dyadic Green's functions satisfying equations

$$\nabla \cdot \overline{\mathbf{T}}_1(\overline{\mathbf{G}}_1) + \rho_1 \omega^2 \overline{\mathbf{G}}_1(\mathbf{x}, \mathbf{x}') = -\rho_1 \bar{\mathbf{I}} \delta(\mathbf{x} - \mathbf{x}'), \tag{C.22}$$

$$\nabla \cdot \overline{\mathbf{T}}_2(\overline{\mathbf{G}}_2) + \rho_2 \omega^2 \overline{\mathbf{G}}_2(\mathbf{x}, \mathbf{x}') = -\rho_2 \bar{\mathbf{I}} \delta(\mathbf{x} - \mathbf{x}'). \tag{C.23}$$

On dot multiplying Equation C.20 by $\overline{\mathbf{G}}_1$ from left and Equation C.22 by $\mathbf{u}_1$ from right, subtracting the two resultant equations, integrating over borehole volume (V_b), we have

$$\gamma_1(\mathbf{x}')\mathbf{u}_1(\mathbf{x}') = \int_{V_b} dV [\overline{\mathbf{G}}_1(\mathbf{x}, \mathbf{x}') \cdot \nabla \cdot \overline{\mathbf{T}}_1(\mathbf{u}_1) - \nabla \cdot \overline{\mathbf{T}}_1(\overline{\mathbf{G}}_1) \cdot \mathbf{u}_1(\mathbf{x})]. \tag{C.24}$$

The volume integral can be reduced to surface integral through integration by parts and by using symmetry property of elastic constant ($C_{ijkl} = C_{klij}$). Interchanging the $\mathbf{x}$ and $\mathbf{x}'$ and applying symmetry property of the dyadic Green's function, we have

$$\gamma_1(\mathbf{x})\mathbf{u}_1(\mathbf{x}) = \int_B dS' \hat{n}' \cdot [\overline{\mathbf{G}}_1(\mathbf{x}, \mathbf{x}') \cdot \overline{\mathbf{T}}_1(\mathbf{u}_1) - \overline{\mathbf{T}}_1(\overline{\mathbf{G}}_1) \cdot \mathbf{u}_1(\mathbf{x}')]. \tag{C.25}$$

This equation is the vector form of Huygen's principle. It states that displacement vector inside the borehole is the displacement field generated by boundary vector sources. If we apply the same manipulations to equations (C.21) and (C.23), we obtain the following for the region outside the borehole

$$\gamma_2(\mathbf{x})\mathbf{u}_2(\mathbf{x}) = -\int_B dS' \hat{n}' \cdot [\overline{\mathbf{G}}_2(\mathbf{x}, \mathbf{x}') \cdot \overline{\mathbf{T}}_2(\mathbf{u}_2) - \overline{\mathbf{T}}_2(\overline{\mathbf{G}}_2) \cdot \mathbf{u}_2(\mathbf{x}')]. \tag{C.26}$$

The direct formulation is to solve two second kind Fredholm integral equations (C.25) and (C.26) on the boundary with six boundary conditions

$$\mathbf{u}_1(\mathbf{x}) = \mathbf{u}_2(\mathbf{x}); \quad \text{for } \mathbf{x} \in B, \tag{C.27}$$

$$\hat{n} \cdot \overline{\mathbf{T}}_1(\mathbf{u}_1) = \hat{n} \cdot \overline{\mathbf{T}}_2(\mathbf{u}_2); \quad \text{for } \mathbf{x} \in B. \tag{C.28}$$

The six unknowns (boundary source components) can then be substituted into (C.25) to obtain displacement for any point inside or on borehole wall.

As we argued before, the direct formulation is computationally complicated because two sets of integral equations are solved. Complication also comes from one of the integrands in (C.25) which involves the differentiation of dyadic Green's function.

C.2.2 Indirect formulation

The difficulty associated with direct formulation can be overcome by reformulate the resultant integral equations of the two regions (C.25) and (C.26). Since we are only interested in the region outside the borehole, we may replace the inside region by the elastic medium of the outside region and shift the influence of original medium to the boundary. Then, from Equation C.25

$$\gamma_1(\mathbf{x})\mathbf{u}_1(\mathbf{x}) = \int_B dS'\hat{n}' \cdot [\overline{\mathbf{G}}_2(\mathbf{x},\mathbf{x}') \cdot \overline{\mathbf{T}}_1(\mathbf{u}_1) - \overline{\mathbf{T}}_1(\overline{\mathbf{G}}_2) \cdot \mathbf{u}_1(\mathbf{x}')]. \tag{C.29}$$

If $u_1(\mathbf{x})$ is specified to be that solution satisfying the boundary condition $\mathbf{u}_1(\mathbf{x}) = \mathbf{u}_2(\mathbf{x})$ for $\mathbf{x} \in B$, Then addition of equation (C.26) and (C.29) yields the indirect formulation

$$\mathbf{u}_2(\mathbf{x}) = \int_B dS'\overline{\mathbf{G}}_1(\mathbf{x},\mathbf{x}') \cdot \Psi(\mathbf{x}') \quad \text{for } \mathbf{x} \in V_e + B, \tag{C.30}$$

where, $\Psi(\mathbf{x}') = [\overline{\mathbf{T}}_1(\mathbf{u}_1) - \overline{\mathbf{T}}_2(\mathbf{u}_2)] \cdot \hat{n}'$, is the vector fictitious source distributions on the boundary. Equation C.30 says that displacement in the region outside the borehole is due to the fictitious sources distributed along boundary. Once again, the uniqueness of this solution is guaranteed by the equivalence principle and more fundamentally by the uniqueness theorem.

Appendix D

Relations in Cylindrical Coordinates and Struve Function

D.1 Hooke's Law

In cylindrical coordinates (r, z, φ), strain has the following form

$$\begin{aligned}
\epsilon_{rr} &= \frac{\partial u_r}{\partial r}, \\
\epsilon_{\varphi\varphi} &= \frac{u_r}{r} + \frac{\partial u_\varphi}{r\partial\varphi}, \\
\epsilon_{zz} &= \frac{\partial u_z}{\partial z}, \\
\epsilon_{r\varphi} &= \frac{1}{r}\frac{\partial u_r}{\partial \varphi} - \frac{u_\varphi}{r} + \frac{\partial u_\varphi}{\partial r}, \\
\epsilon_{\varphi z} &= \frac{1}{r}\frac{\partial u_z}{\partial \varphi} + \frac{\partial u_\varphi}{\partial z}, \\
\epsilon_{zr} &= \frac{\partial u_z}{\partial r} + \frac{\partial u_r}{\partial z}.
\end{aligned} \tag{D.1}$$

The stresses for an isotropic solid are

$$\begin{aligned}
\sigma_{rr} &= (\lambda + 2\mu)\epsilon_{rr} + \lambda\epsilon_{\varphi\varphi} + \lambda\epsilon_{zz}, \\
\sigma_{\varphi\varphi} &= \lambda\epsilon_{rr} + (\lambda + 2\mu)\epsilon_{\varphi\varphi} + \lambda\epsilon_{zz}, \\
\sigma_{zz} &= \lambda\epsilon_{rr} + \lambda\epsilon_{\varphi\varphi} + (\lambda + 2\mu)\epsilon_{zz},
\end{aligned}$$

$$
\begin{aligned}
\sigma_{\varphi z} &= \mu\epsilon_{\varphi z}, \\
\sigma_{zr} &= \mu\epsilon_{zr}, \\
\sigma_{r\varphi} &= \mu\epsilon_{r\varphi}.
\end{aligned} \tag{D.2}
$$

The stresses for a transversely isotropic solid are

$$
\begin{aligned}
\sigma_{rr} &= c_{11}\epsilon_{rr} + (c_{11} - 2c_{66})\epsilon_{\varphi\varphi} + c_{13}\epsilon_{zz}, \\
\sigma_{\varphi\varphi} &= (c_{11} - 2c_{66})\epsilon_{rr} + c_{11}\epsilon_{\varphi\varphi} + c_{13}\epsilon_{zz}, \\
\sigma_{zz} &= c_{13}\epsilon_{rr} + c_{13}\epsilon_{\varphi\varphi} + c_{33}\epsilon_{zz}, \\
\sigma_{\varphi z} &= c_{44}\epsilon_{\varphi z}, \\
\sigma_{zr} &= c_{44}\epsilon_{zr}, \\
\sigma_{r\varphi} &= c_{66}\epsilon_{r\varphi}.
\end{aligned} \tag{D.3}
$$

D.2 Divergence and Gradient

The divergence and gradient operator in cylindrical coordinates have the following form

$$
\nabla \cdot \mathbf{A} = \frac{1}{r}\frac{\partial}{\partial r}(rA_r) + \frac{1}{r}\frac{\partial A_\varphi}{\partial \varphi} + \frac{\partial A_z}{\partial z}, \tag{D.4}
$$

and

$$
\nabla\phi = \frac{\partial\phi}{\partial r}\hat{r} + \frac{1}{r}\frac{\partial\phi}{\partial\varphi}\hat{\varphi} + \frac{\partial\phi}{\partial z}\hat{z}. \tag{D.5}
$$

D.3 Struve Function

Struve function $H_\nu(z)$ is a particular solution of the inhomogeneous Bessel equation

$$
z^2\frac{d^2w}{d^2z} + z\frac{dw}{dz} + (z^2 - \nu^2)w = \frac{4(\frac{1}{2}z)^{\nu+1}}{\sqrt{\pi}\Gamma(\nu + \frac{1}{2})}. \tag{D.6}
$$

Struve function of the zeroth and first order have the following power series expansion for small argument

$$H_0(z) = \frac{2}{\pi}\left[z - \frac{z^3}{1^2\cdot 3^2} + \frac{z^5}{1^2\cdot 3^2\cdot 5^2} - \frac{z^7}{1^2\cdot 3^2\cdot 5^2\cdot 7^2} + \frac{z^9}{1^2\cdot 3^2\cdot 5^2\cdot 7^2\cdot 9^2} - \ldots\right], \tag{D.7}$$

and

$$H_1(z) = \frac{2}{\pi}\left[\frac{z^2}{1^2\cdot 3} + \frac{z^4}{1^2\cdot 3^2\cdot 5} - \frac{z^6}{1^2\cdot 3^2\cdot 5^2\cdot 7} + \frac{z^8}{1^2\cdot 3^2\cdot 5^2\cdot 7^2\cdot 9} - \ldots\right]. \tag{D.8}$$

For large argument, these two functions have the following asymptotic expansions

$$H_0(z) \sim Y_0(z) + \frac{2}{\pi}\left[\frac{1}{z} - \frac{1}{z^3} + \frac{1^2\cdot 3^2}{z^5} - \frac{1^2\cdot 3^2\cdot 5^2}{z^7} + \ldots\right], \tag{D.9}$$

and,

$$H_1(z) \sim Y_1(z) + \frac{2}{\pi}\left[1 + \frac{1}{z^2} - \frac{1^2\cdot 3}{z^4} + \frac{1^2\cdot 3^2\cdot 5}{z^6} + \ldots\right]. \tag{D.10}$$

In the above, $Y_0(z)$ and $Y_1(z)$ are the zeroth and first order Bessel functions of the second kind. In our calculation, the power series expansions are used for $z < 17$ and for $z \geq 17$ the asymptotic expansions are used. For more detail, consult Abramowitz and Stegun (1964).